Università degli studi di Genova

DIPARTIMENTO DI SCIENZE DELLA TERRA, DELL'AMBIENTE E DELLA VITA

Scuola di Scienze e tecnologie per l'Ambiente e il Territorio

Dottorato di Ricerca in Scienze della Terra

XXXII ciclo

s.d. GEO/07

Elastic thermobarometry: methods and applications to ultrahigh-pressure metamorphic rocks

Candidate:
Nicola Campomenosi

Supervisors:
Prof. Scambelluri M. (University of Genova)
Prof. Alvaro M. (University of Pavia)
Dr. Angel R. J. (CNR of Padova)
Prof. Hermann J. (University of Bern)

Table of content

Abstract

Ultra-High Pressure (UHP) metamorphic rocks represent the evidence we have for the detailed reconstruction of deep-seated tectonic processes, which are the source of natural hazards like deep-focus earthquakes and volcanic eruptions.

Mineral inclusions are often the only proof of ultrahigh pressure metamorphism and their study provides insights into the mechanisms of subduction and subsequent exhumation of metamorphic rocks. The most frequently used approach for this purpose is the application of equilibrium thermodynamics assuming a linear relationship between the inferred Pressure (P) and the depth of formation of metamorphic mineral assemblages. For instance, coesite or diamond-bearing systems suggest that rocks can be exhumed from depths even greater than 100 km. However, a major current controversy is whether high-pressure minerals actually indicate such great depths of subduction or whether they are the result of tectonic overpressure during subduction. If tectonic overpressure were effective, coesite- and diamond-bearing rocks could come from shallower domains of the lithosphere and a revaluation of the current knowledge of plate tectonics would be necessary.

So far, there are no available techniques to constrain the amount of deviatoric paleo-stress present during metamorphic processes. A first attempt has been recently proposed combining mineral physics and petrology: the elastic thermobarometry. The advantage of this technique is that it is not based on the equilibrium thermodynamic assumption but, rather, on the contrast in the elastic properties of two crystals that are constrained within a confined space such as a mineral inclusion and its surrounding host.

The analysis of solid inclusions that are fully buried within their hosts by non-destructive techniques, such as Raman spectroscopy or single crystal X-ray diffraction, reveals pressures that can considerably deviate from the external (ambient) one. This is the so-called residual pressure and it arises as a response to the contrast in the thermo-elastic properties between the host and the inclusion if, for example, the entrapment of the inclusion occurred at high P-T conditions. Importantly, the amount of residual pressure is linked to the entrapment pressure and knowing the physical properties of the two crystals (i.e. their equations of state), using theoretical models it is possible to back-calculate the P-T conditions of inclusion entrapment. The current theoretical models for interpreting the residual pressure are based on simplified assumptions and ideal host-inclusion systems (e.g. isotropic elasticity for both

the host and the inclusion crystals, shape of the inclusions are spherical and infinite in size for the host crystal).

In this regard, this PhD Thesis has two main objectives: (i) to understand, from an experimental point of view, how much the deviations from the ideal host-inclusion system can actually influence the thermobarometric estimates and (ii) to apply the new theoretical and experimental developments of the elastic thermobarometry to a natural case of study.

The first point focuses on the use of Raman spectroscopy to measure and determine the strain state of natural (i.e. non-ideal) mineral inclusions while the second one develops the application of this technique to the famous UHP metamorphic rocks of the Dora-Maira Massif (Western Alps).

This study allowed the development of experimental protocols devoted in selecting reliable mineral inclusions for elastic-thermobarometric purposes. Backbone of this work are zircon inclusions because they represent one of the most common accessory minerals in metamorphic rocks and, furthermore, can give also age information on the metamorphic processes. Finally, the application of the elastic thermobarometric method to a natural case of study, shows the possibility in considering the presence of deviatoric stresses during inclusion entrapment starting from experimental measurements of stress field in host-inclusion mineral systems. Although this last point remains currently difficult to confirm, the aim of this work is also to give some perspectives that, eventually, can be used to describe metamorphic processes at a higher level than has ever been envisaged before.

Chapter 1

Introduction and Scope

1.1 The role of stress in equilibrium thermodynamics and pressure distribution from micro to macroscale during metamorphism

To retrieve pressure and temperature (*P-T*) conditions of rock recrystallization during tectonic processes in the Earth's interiors, metamorphic petrology relies on equilibrium thermodynamics. In many cases however, the textural features and the compositional zoning of minerals suggest that metamorphic rock recrystallization is not controlled by equilibrium thermodynamics alone; rather, they can be the result of kinetically-favoured processes (Carpenter and Putnis 1985). In this regard, reasonable assumptions such as *local equilibrium* attainment, coupled with careful micro-textural analysis of metamorphic mineral assemblages, help to obtain correct interpretations of the tectono-metamorphic rock histories (Lanari and Engi, 2017). Recently, a growing number of studies discussed the limitations of the equilibrium thermodynamic approach by emphasizing, in particular, the fact that hydrostatic stress conditions may not be dominant during metamorphism (Mancktelow, 2009). The planar anisotropic structures (e.g. foliations, shear zones) developed in metamorphic rocks from macro- to micro- scales provide a convincing observational basis that significant deviatoric stress components can be involved during metamorphism and crystal growth (Brodie and Rutter, 1985). In his classic paper on thermodynamics, Gibbs (1906) considered the effect of non-hydrostatic stress on phase equilibria. He noticed that the chemical potential between solids and adjacent fluids vary according to the orientation of the solid surfaces and showed that the magnitude of such a variation depends on the degree to which the stress departs from hydrostatic conditions along

the solid-fluid boundaries. After Gibbs, numerous scientific articles have dealt with this topic. As an example, Coe and Paterson (1969) suggested that the temperature of α–β transition in single quartz crystals strongly depends on the crystallographic orientation of quartz with respect to the principal axes of a non-hydrostatic stress field. More recently, Wheeler (2014) pointed out the "dramatic effect of stress on metamorphic reactions" for which, for example, garnet and clinopyroxene breakdown might be offset by the equivalent of 0.5 GPa for a 0.05 GPa differential stress. However, Hobbs and Ord (2015), commenting the work of Wheeler, concluded that deviatoric stresses have small effects on phase equilibria, pointing out that the major flaw in Wheeler's (2015) argumentation is that the stress is treated as a thermodynamic state variable. Hobbs and Ord (2015) stated that the shift in the breakdown reaction modelled by Wheeler (2015) is not dramatic, and pointed out that a temperature shift of just 1K requires a deviatoric stress of 1.4 GPa.

Another consequence of the assumption of hydrostatic stress conditions during metamorphism is the linear relationship between the formation pressure of a mineral and the corresponding depth within the Earth:

$$P = \rho g h \quad (1.1)$$

where P is the pressure, g the gravity acceleration constant, h the depth and ρ the density of the overlying rock column. Following equation 1.1, coesite or diamond-bearing rocks, whose minimum formation pressure is estimated at about 3 and 4.5 GPa should be exhumed from depths exceeding 80 and 100 km, respectively. Differently, numerical simulations (e.g. Schmalholz et al., 2014), suggest the possibility to reach deviatoric stresses as high as 2 GPa during crustal tectonics and metamorphism: therefore, the mean normal stress and then the P affecting phase equilibria, could be significantly different at same depths.

Nowadays, many sessions at international conferences focus on the above subjects trying to shed light on a major debated issue: can we measure deviations from hydrostatic conditions in terms of paleo-stress recorded by metamorphic rocks within the Earth? Given the controversy about equilibrium thermodynamics that I have described, the advent of the practical implementation of elastic thermobaromtery is especially valuable as it provides a completely independent method to determine stresses and pressures acting in a rock at the time of metamorphism.

1.2 Elastic thermobarometry

Basic concepts

Let us consider the entrapment of a mineral inclusion within a growing, coarser, mineral host (Figure 1.1).

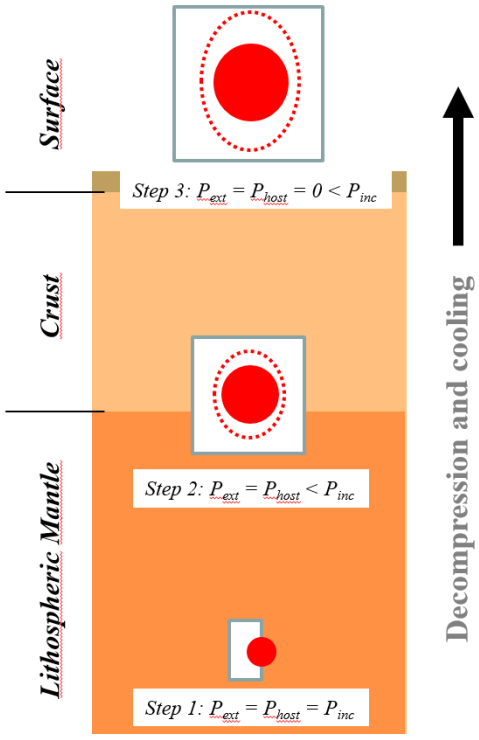

Figure 1.1. Schematic step-representation of inclusion (red) entrapment in a mineral host (white) and development of a residual pressure at room conditions. The red dashed line represents the volume of the inclusion as it would be if it was free to expand. Note that, in this case the inclusion is anisotropic, i.e. it would expand more along one direction (vertical) with respect the other (horizontal).

Under such a circumstance the two minerals record the same external *P-T* conditions. However, once the entrapment is completed and the host has grown a sufficient amount, the inclusion is physically (elastically) isolated from the surrounding rock environment. Therefore, any later modification of the external conditions will be recorded in a different way by the two minerals (the inclusion and the host). Importantly, if the host-inclusion system is tectonically exhumed, the two minerals will expand in a different amount due to their different thermo-elastic properties. If the inclusion is softer than the host, it will want to expand more than the stiffer host which, in turn, inhibits the volume expansion of the inclusion: this contrast in the physical properties of the two adjacent minerals brings the development of an elastic stress field that the inclusion transmits to the host walls (e.g. Angel et al. 2015 and reference therein).

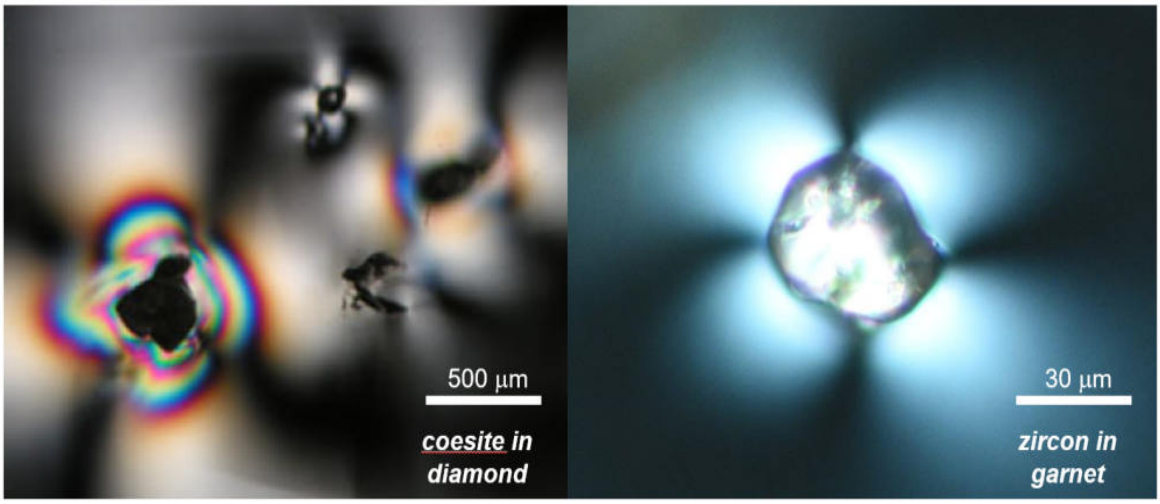

Figure 1.2. Stress-induced birefringent haloes in cubic crystals (diamond and garnet) surrounding stressed inclusions. To the left: coesite inclusion in diamond by Howell et al. (2010). To the right: zircon inclusion in garnet from by Campomenosi et al. (2018).

Key evidence of this process in natural samples are stress-induced birefringent haloes (Figure 1.2) in cubic minerals hosting stressed inclusions (e.g. Rosenfeld and Chase, 1961; Howell et al. 2010; Nasdala et al. 2003; Campomenosi et al., 2020). This stress field, generated by the inclusion, is usually referred as *residual pressure* since it is still detectable

at room conditions. The quantification of this property represents the starting point of any elastic barometric estimate (e.g. Angel et al. 2015)**.**

The residual pressure built-up in host-inclusion systems can be measured by means of Raman spectroscopy and by single crystal X-ray diffraction (see Chapter 2). The basic principle consists of (i) measuring the stress state of the inclusion taking a free crystal as reference standard and, (ii) to calculate the corresponding residual pressure by means of reliable calibrations (e.g. Murri et al. 2018).

The main point of elastic barometry is to back calculate the entrapment P and T conditions starting from this residual pressure by using the combination of the *equations of state* (EoS) of the two crystals and their mutual elastic relaxation (e.g. Angel et al. 2015).

Isomeke: a "mechanical" univariant line

From a thermodynamic point of view, the possible entrapment conditions of a specific host-inclusion pair are defined by a line within the P-T space whose slope, for a constant fractional volume between the host and the inclusion (i. e. $V^I - V^H = constant$), is given by:

$$\left(\frac{\partial P}{\partial T}\right)_{(V^I - V^H)} = \frac{\alpha^I - \alpha^H}{\beta^I - \beta^H} \quad (1.2)$$

where α and β are the coefficients of thermal expansion and of compressibility for the host (H) and the inclusion (I), respectively. Along this line there is no pressure gradient between the host and the inclusion (indeed they are at the same P-T conditions, including at the time of entrapment). Note that the equation 1.2 is different from that of an isochor of a single mineral because it considers the properties of the host and of the inclusion simultaneously (Figure 1.3).

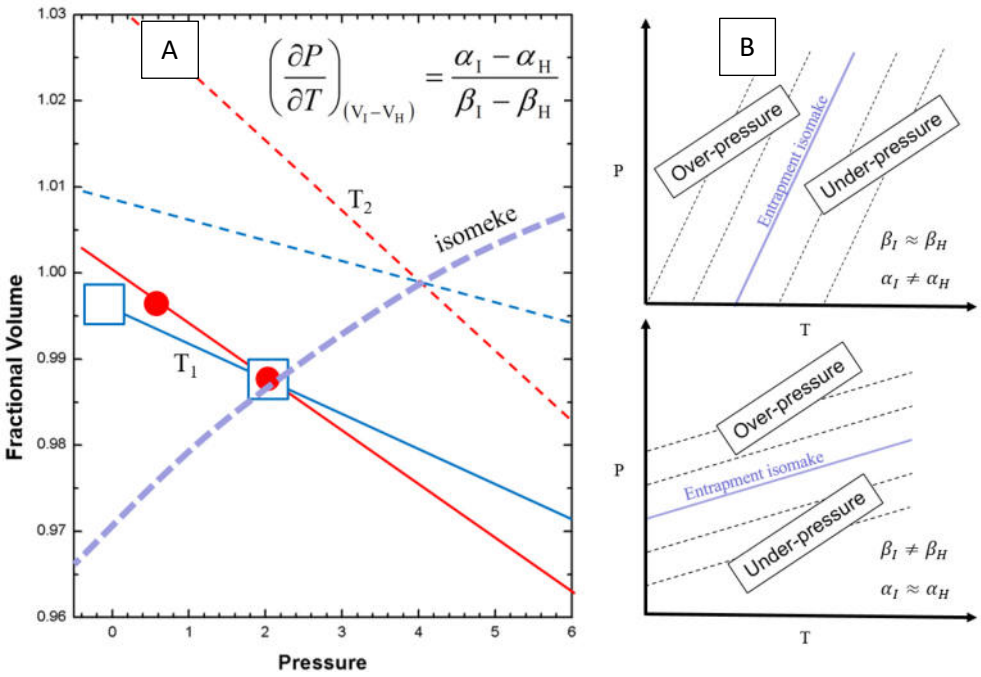

Figure 1.3. (A): how to construct an isomeke (dashed violet line?) using the equations of state (EoS) of the host (blue line) and of the inclusion (red line) at two different temperatures (T_1 and T_2). (B) The effect of the difference in the thermal expansion and compressibility coefficients between the host and the inclusion. Note that, in both cases, the inclusion has larger bulk moduli (i.e. smaller compressibility) with respect the host, i.e. the inclusion is stiffer than the host. On the other hand, if the inclusion would have smaller bulk modulus with respect to the host, the over-pressure and under-pressure domains are inverted.

The concept of isomeke is fundamental in elastic thermo-barometry because this line divides P-T space in two domains (Figure 1.3): one defined by under-pressure conditions of the inclusion with respect to the host and the other by over-pressure conditions. In P-T space, the relative position of these two domains with respect to the isomeke line depends if the host is stiffer or softer than the inclusion (i.e. higher or lower bulk modulus respectively) and on the isomeke slope. In this regard, different minerals have different physical properties and consequently the isomeke slope will change for different host-inclusion systems. In particular, as shown in Figure 1.3, a larger difference between the thermal expansion coefficients of the host and of the inclusion will define an isomeke line that is more sensitive to T changes (a geo-thermometer), while a larger difference in the compressibility coefficients defines a line more sensitive to P changes (a geo-barometer). Then, based on the same principle of classic geo-thermobarometry, this allows us to use different host-inclusion

systems to define a unique point within P-T space (e.g. Kohn, 2014, Zhong et al., 2019). However, one major advantage of the elastic barometry is that, differently from the classic approach, it does not depend on the chemical equilibrium between the involved minerals.

First applications and issues

Rosenfeld and Chase (1961) were the first to exploit the contrast in the elastic properties in host-inclusion systems in metamorphic petrology. After their pioneering work, a large use of this technique has been applied to rocks where the use of classic geo-thermobarometric calibrations is difficult due to the lack of specified mineral assemblages that can be exploited as geo-thermometer and or geo-barometer.

So far, elastic barometry has been successfully applied to "simple systems" only, in which both the host and the inclusion display cubic symmetry and the strain field involved is essentially isotropic (e.g. Milani et al. 2015). In such cases, the principle used to calculate the residual pressure starting from the measured Raman shift is straightforward, and only a hydrostatic pressure calibration for the Raman shift as a function of pressure for that phase is needed. Usually, such calibrations are available for numerous minerals (e.g. Gillet et al. 1992): in such cases, if the variation in the Raman peak position ($\Delta\omega$) with respect to an unstressed free crystal is known, one can directly calculate the residual pressure. Despite this simple approach, however, it is important to realize that the stress field between the host and the inclusion can deviate from hydrostatic conditions due to the *intrinsic anisotropy* of the involved crystals. Strictly speaking, one can expect that the hydrostatic calibrations are good approximation if the host and the inclusion are both pseudoisotropic in terms of elastic properties. However, this is not true for many host-inclusion systems in metamorphic rocks, where elastically anisotropic minerals (e.g. quartz, coesite) occur because, by definition,

anisotropic crystals have different compressibility and thermal expansion coefficients along different crystallographic directions. Therefore, during exhumation, a crystal will expand more in one direction than another, and the developed stress field cannot be hydrostatic even if the host is a cubic crystal (e.g. Angel et al. 2015). Recently, Murri et al. (2018) developed the approach for measuring the strain state of quartz inclusions taking into account their intrinsic anisotropy. Indeed, they exploit the concept of the phonon mode Grueneisen tensor, relating the changes in the phonon wavenumber directly to the strain tensor.

Furthermore, the effect of the real geometry of the host-inclusion systems on the elastic mutual relaxation and, consequently, on the measured residual pressure has been quantified and modelled (Mazzucchelli et al., 2018). The results show that the inclusion shape, its mutual orientation with respect to the host (because of the intrinsic anisotropy), the distance from any kind of boundary affect the final residual pressure in the inclusion. Indeed, the results deviate from those obtained using the available models which consider that (i) inclusions are spherical, (ii) the host is infinite in size, (iii) host and inclusion are elastically isotropic (Zhang, 1998). For this purpose, it is worth considering that, strictly speaking, no mineral is elastically isotropic (e.g. Nye, 1985).

Another misconception, that has been largely applied to derive residual inclusion pressures, is to use the strain state of the mineral host, in terms of measured Raman peak position, to get the pressure of the inclusion entrapment (e.g. Israeli et al. 1999). Differently from the inclusion, the mineral host is at room pressure; therefore, the strain field within the host and the eventual Raman shift variation are only given by the change in the normal stress components transmitted by the inclusion. From force balance considerations, one can expect that only in a narrow zone at the host-inclusion boundary does the radial stress in the host match the one of the inclusion. However, this is difficult to quantify and for anisotropic stress fields (i.e. the majority of the cases) the radial stress does not correspond to the pressure in

the inclusion because, in this case, the mean normal stress will be different from the single stress components (i.e. radial stress).

1.3 Scope of this Thesis

This PhD thesis is part of an interdisciplinary research program focussed on theoretical aspects of the elastic barometry method and its application to natural anisotropic mineral inclusions. The metamorphic history of the ultrahigh-pressure (UHP) Dora-Maira unit is investigated here by exploiting the physical properties of anisotropic (zircon) inclusions in pyrope megablasts hosted by UHP whiteschists (Chopin, 1984). Petrology and mineral physics are combined to gain information on the physical conditions achieved during zircon entrapment in garnet including the nature (isotropic or deviatoric) of stress and strain fields acting on the zircon-pyrope couples. Up to now, different experimental techniques and approaches have been employed and applied to zircon inclusions and their garnet hosts. These include: high magnification optical and electron microscopy; Raman spectroscopy; single-crystal X-ray diffraction; cathodolumiscence of zircon inclusions; zircon trace element ICP-MS laser ablation analysis. These techniques have been combined with thermodynamic modelling and with numerical modelling. The latter branch has been developed in collaboration with other PhD students.

This PhD has been developed in a collaboration program between the Universities of Pavia and Genova, in the frame of the ERC project TRUE-DEPTH (Horizon 2020 714936), awarded to Prof. M. Alvaro (University of Pavia). The core of the ERC project is the theoretical development of the elastic barometry method considering elastically anisotropic inclusions and its application to natural metamorphic rocks, to reconstruct their metamorphic histories and determine if the pressure conditions revealed by thermo-barometry do

correspond to true depth conditions (i.e. hydrostatic pressures), or are generated by tectonic deviatoric stresses and overpressures.

In my PhD thesis, I developed experimental methodologies to confirm theoretical predictions on the anisotropic behaviour of crystals and I tested the effects of real (natural) host-inclusion geometries on the elastic relaxation and residual pressure estimates. Specifically, I have provided experimental evidence for the effect of the host inclusion geometry and anisotropy on the measured residual pressure using Raman spectroscopy. My observations and measurements, coupled with numerical models, helped to define an experimental protocol allowing reliable estimates and corrections of the residual pressure measured on anisotropic inclusions (see Chapter 5**).**

Further, I developed a simple protocol to select zircon inclusions in proper textural settings within their garnet hosts, whose Raman spectra are unaffected by metamictization and whose peak positions are only function of the residual elastic stress built up within the inclusion and at the interface between inclusion and garnet host. These investigations and data have provided a useful basis for a robust interpretation of zircon elastic behaviour, with the possibility to reconstruct even more detailed P-T-time paths in metamorphic rocks (see Chapter 6).

I also performed a detailed Raman spectroscopic study of the strain state of the host minerals surrounding stressed inclusions. I have tried to exploit, for the first time, the theory of the morphic effects in lattice dynamics in the quantification of the stress/strain amount in optically anomalous crystals. The theoretical considerations and preliminary experimental results demonstrate the possibility to use the intensity variation of fully symmetric phonons mode to better define and map strain fields in crystals (see Chapter 7).

Finally, taking advantage from these new protocols and from theoretical development of other PhD theses developed in the frame of the Truedepth ERC program, I have applied elastic barometry to the well-known case of the UHP metamorphic terrain of the Dora-Maira Massif (Western Alps) (see Chapter 8).

Chapter 2

Analytical techniques

In the following a description of the main analytical techniques, used during this PhD Thesis, is presented.

Electron microscopy and micro-analysis

Mineral chemistry of garnets was determined by means of a TESCAN Vega-3 electron microprobe at the University of Genova (DISTAV department), using an energy-dispersive technique (with an acceleration voltage of 15 kV, a beam current of 14 nA) and by means of a JEOL JXA 8200 electron microprobe at the University of Milan (Earth Science Institute). The electron microprobe analysis and chemical element mapping of some zircon inclusions were performed using a Cameca SX-100 SEM system electron microprobe available at the University of Hamburg (Earth Science department), using a wavelength-dispersive technique with an acceleration voltage of 15 kV and a beam current of 40 nA.

Polarized-(micro)Raman spectroscopy

Raman measurements were collected with two different Horiba Jobin-Yvon spectrometers: a T64000 triple-monochromator system operating in a subtractive mode and an Explora_Plus single-monochromator spectrometer. The first one was equipped with a symphony LN_2-cooled CCD detector, 1800-gr/mm holographic gratings, an Olympus BH-41 optical microscope and a Coherent Ar^+ laser, while the second with a Peltier-cooled CCD detector, a 2400 gr/mm grating, an Olympus BH-41 optical microscope, and Nd-YAG solid-state laser. In both cases the spectral resolution was approximately 2 cm^{-1} and therefore apparatus

corrections of the peak widths were not required (Nasdala et al. 2001). In order to avoid heating of the sample due to laser energy absorption (Zhong et al. 2019), Raman measurements were collected with a laser power lower than 15 mW. The instrumental accuracy in the peak position determination is of about 0.35 cm^{-1} for the T64000 spectrometer and of about 0.55 cm^{-1} for the Explora_Plus.

Origin Lab-Pro 2018 software package was used for data fitting and evaluation. The collected spectra were baseline corrected for the continuum luminescence background when necessary, temperature-reduced to account for the Bose-Einstein occupation factor (Kuzmany, 2009) and normalized to the acquisition time. Peak positions, full-widths at half maximum (FWHMs), and integrated intensities were determined from fits with pseudo-Voigt functions (PV = (1 – q)·Lorentz + q·Gauss, q is the weight coefficient). The criterion for the maximum number of fitted peaks was $\Delta I < I/2$, where I and ΔI are the calculated magnitude and uncertainty of each peak intensity, respectively.

Charge-Contrast (CC) imaging

CC images were acquired with a ZEISS EV050 scanning electron microscope at the Institute of Geological Sciences, University of Bern, at low vacuum conditions (18 Pa), 12 kV, a beam current of 100 mA and a working distance of 9.5 mm. CC images are obtained from well-polished, uncoated samples. It has been demonstrated that CC images correlate exactly to cathodoluminescence images and result from the complex interaction between the electron beam, the positive ions generated by electron-gas interactions in the chamber, a biased detector, and the sample (Griffin et al. 2000; Watt et al. 2000). Internal check in the Bern laboratory confirmed that CC images are virtually identical to panchromatic cathodoluminescence (CL) images.

Laser Ablation Inductively Coupled Plasma Mass Spectrometer (LA-ICP-MS)

Zircon and rutile inclusion as well as garnet hosts were measured by LA-ICP-MS with a Resonetics RESOlutionSE 193nm excimer laser system equipped with a S-155 large volume constant geometry chamber (Laurin Technic, Australia) at the Institute of Geological Sciences, University of Bern, Switzerland. The laser system was coupled to an Agilent 7900 quadrupole ICP-MS instrument. Samples were ablated in a He atmosphere and the aerosol mixed with Ar carrier gas before being transported to the ICP-MS. The ICP-MS was tuned for low oxide production (ThO/Th < 0.2%) and Th/U ratio close to one (Th/U > 97%). Measurement beam size was set from 20 to about 80 µm depending on grain size, and the surface area of each measurement spot was cleaned by pre-ablation for 3 pulses employing a larger spot size. Total acquisition time for each analysis was 70 s, consisting of 30 s of gas background acquired with the laser switched off, 10 s of washout after pre-ablation cleaning and 30 s of ablation signal. The laser was tuned to a repetition rate of 5 Hz and an energy output of 4 mJ (corresponding to an HV of about 26-27 kV). The ICPMS was tuned for maximum sensitivity and minimum production of molecular species, maintaining ThO^+/Th^+ at <0.5%. The spot size on the zircon crystals was 20 µm while those on rutile and garnet crystals was 64 µm. Analyses were standardized to glass NIST 612 and GSD-1g from USGS. Zircon 91500 was run as secondary standard to monitor accuracy for the zircon inclusions. Stoichiometric Si was employed as internal standard for both zircon (SiO_2: 31.6 wt%) and garnet (SiO_2: 43.9 wt%) while for rutile was employed stoichiometric TiO_2 (99 wt%). Reproducibility and accuracy were within 10 % or less across all analysed elements. The data were reduced with the freeware Iolite (Paton et al. 2011) and its data reduction scheme for trace elements (Woodhead et al. 2007).

Chapter 3

Ultrahigh Pressure (UHP) metamorphism in Western Alps: the Dora-Maira Massif (Italy)

3.1 UHP metamorphism: definition and occurrence

Following the definition by Carswell et al. (2005), UHP metamorphic rocks "*form at very high lithostatic pressures within the eclogite facies but above the stability field of quartz"*. The resulting rocks can contain crystals of coesite or, depending on the bulk chemistry of the protolith, other ultrahigh-pressure minerals (e.g. diamond, majoritic garnet) and mineral assemblages (Dobrzhinetskaya et al., 1995; Parkinson and Katayama, 1999; Ye et al., 2000; Hermann et al., 2001; Scambelluri et al., 2008; Katayama and Maruyama, 2009).

Christian Chopin (1984) wrote one of the first high impact paper on the occurrence of coesite in metamorphic rocks and the possible geo-tectonic implications. Chopin (1984) found coesite and quartz pseudomorphs after coesite as inclusions in pyrope-rich garnet within quartz-phengite schists (the so-called whiteschists) from the continental crust of the Dora-Maira Massif in the Western Alps (Italy). At that time, the work by Chopin had enormous echo in the petrologic and geo-tectonic community. Before Chopin's (1984) work, it was accepted that only the oceanic lithosphere could be subducted to mantle depths, while the continental crust either remained close to the Earth's surface or, in some cases, was obducted at the top of the oceanic crust. Chopin's discovery showed that the continental crust can be involved in deep subduction, reaching pressures in excess of 2.8 GPa for temperature values of about 700 °C. Conversion of such pressure values into depth suggested that subduction of continental crustal slices in the Alps reached and even went beyond depths of 90 kilometres

if hydrostatic forces were continuously acting on the Dora-Maira rocks during the formation of the relevant assemblage.

Consequently, in his 1984 paper, Chopin concluded with the statement *"the range of pressure endured by crustal rocks of continental derivation might be in fact much wider then presently thought. Some of our present concepts about earth tectonics might have to be modified by these coesite discoveries and other possible ones to come"*.

After Chopin's (1984) findings, coesite and, later on, diamond and majoritic garnet were shown to occur in metamorphic crustal rocks and ophiolites. Figure 3.1 reports, on a simplified global geotectonic map, the currently recognised UHP metamorphic terrains now exposed at the Earth's surface. These correspond to:

1) Dora-Maira Massif, Western Alps (Chopin, 1984; Chopin et al., 1991; Hermann, 2003)
2) Cignana Unit, Zermatt-Saas Zone, Western Alps (Reinecke, 1991; van der Klauw et al., 1997; Frezzotti et al., 2011)
3) Leaota Massif, South Carpathians (Sabau, 2000)
4) Rhodope Metamorphic Province, Northern Greece (Krohe and Mposkos, 2001)
5) Western Gneiss Region, Norwegian Caledonides (Smith, 1984; van Roermund, 1998)
6) Northeast Greenland Caledonides (Gilotti and Krogh Ravna, 2002)
7) Saxonian Erzgebirge, Germany (Nasdala and Massonne, 2000)
8) Sudetes Mountains, Poland (Bakun-Czubarow, 1991)
9) Maksyutov Complex, Southern Urals (Leech and Ernst, 1998)
10) Kokchetav Massif, Kazakhstan (Sobolev and Shatsky, 1990)
11) Tian Shan, Kyrghyzstan/China (Tagiri et al., 1995; Zhang et al., 2002)
12) Kaghan Valley, Pakistan Himalaya (O'Brien et al., 2001; Treloar et al., 2003)
13) Tso-Morari Complex, eastern Lakakh, Indian Himalaya (Sachan and Mukherjee, 2003)
14) Su-Lu Terrane, Eastern China (Zhang et al. 1995; Zhang and Liou, 1998)

15) Dabie Shan, Central China (Wang et al., 1989)
16) North Qinling, Central China (Liu et al., 2003)
17) North Qaidam, Tibet Plateau, China (Yang et al., 2002; Song et al., 2003)
18) South Altyn Tagh, China (Liu et al., 2001)
19) Bantimala Complex, Central Sulawezi, Indonesia (Parkinson et al., 1998)
20) Pan-African Nappes of Northern Mali (Caby, 1994)
21) Pan-African Nappes of Minas Gerais State, Brazil (Parkinson et al., 2001)
22) Lanterman Range, North Victoria Land, Antarctica (not shown on figure 3.1) (Ghiribelli et al., 2001; Palmieri et al., 2003)

Note that some of the above occurrences, such as the ones at points 3), 8), 9) and 22), are currently less certain with respect to the others and require further confirmation (Carswell et al. 2005).

Statistically, the majority of the UHP metamorphic remnants are preferentially preserved within mafic rocks. In particular, most UHP index minerals survive as inclusions within stiff host minerals such as garnet and zircon (see references listed above). These mafic rocks largely occur within continental crustal terrains consisting of large bodies of ortho- and para-gneisses, which are supposed to play a buoyant-geodynamic role in driving the exhumation of denser UHP mafic rocks (A-type continent-continent collision) (Carswell et al., 2005 and reference therein).

On the other hand, only two recognised UHP metamorphic terrains represent remnants of deeply subducted oceanic lithosphere (B-type continent-continent collision). These are the Zermatt-Saas Zone in the Western Alps and the Sulawesi terrain in Indonesia (Reinecke, 1991; Parkinson et al., 1998).

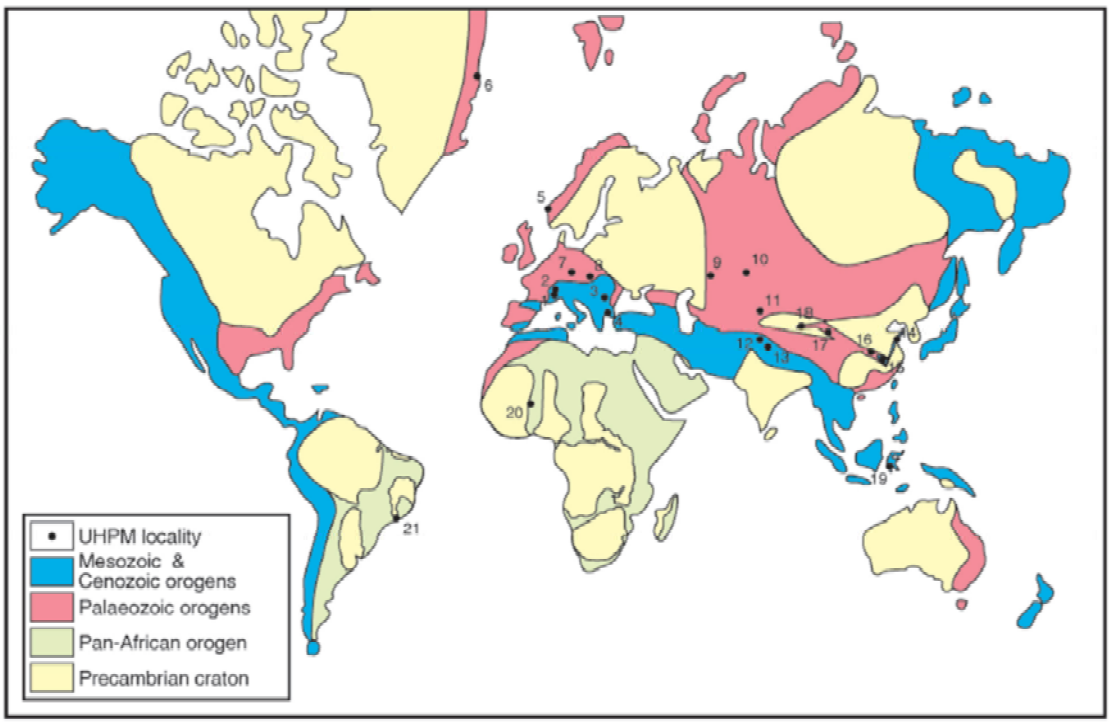

Figure 3.1 Simplified global tectonic map showing the UHP metamorphic terrains listed in the main text (the numbers are for reference to the list). After Carswell et al. 2005.

3.2 The Dora-Maira Massif: a type locality of UHP metamorphism in subducted continental crust

The Dora-Maira Massif (DMM) together with the Monte Rosa and the Gran Paradiso Massifs constitute the "Internal Crystalline Massifs" of the Pennine Domain in the Western Alps (Beltrando et al. 2010). The DMM as described in the review by Carswell et al. (2005) is a *nappe pile* composed of continent-derived tectonic units locally separated by thin ocean-derived units of the Piemonte Zone. Figure 3.2 reports a schematic tectonic map of the Western Alps.

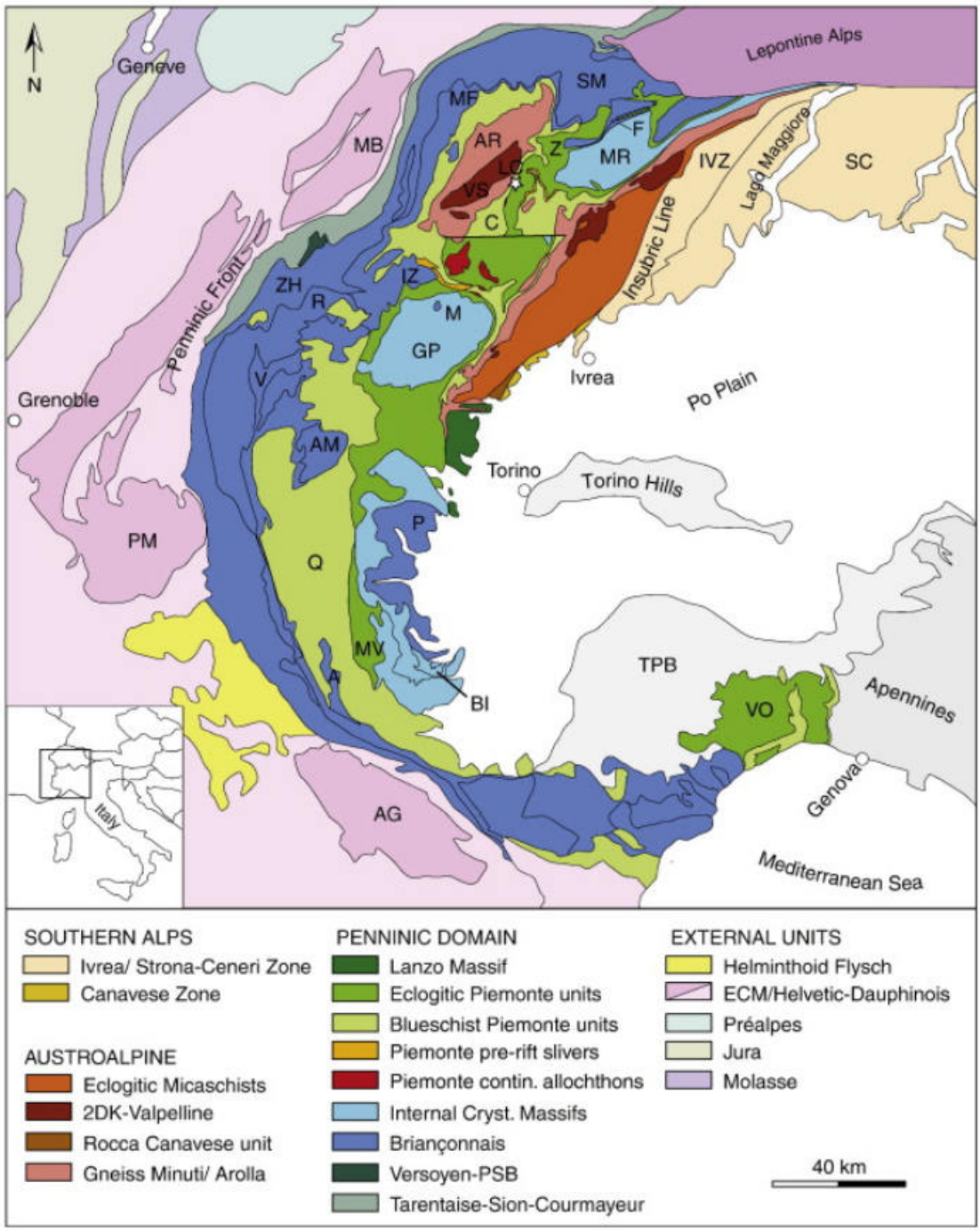

Figure 3.2 Tectonic map of the Western Alps (taken from Beltrando et al., 2010). A: Acceglio Zone; AG: Argentera Massif; AM: Ambin Massif; AR: Arolla Series; BI: Brossasco–Isasca UHP Unit; C: Combin Zone; ECM: External Crystalline Massifs; F: Furgg Zone; GP: Gran Paradiso Massif; IVZ: Ivrea Zone; IZ: Internal Zone; LC: Lago di Cignana UHP Unit; M: Money Unit; MB: Mont Blanc Massif; MF: Mont Fort Unit; MR: Monte Rosa Massif; MV: Monviso Massif; P: Pinerolo Unit; PM: Pelvoux Massif; Q: Queyras Schistes Lustrés; R: Rutor Massif; SL: Serie dei Laghi; SM: Siviez–Mischabel; TPB: Tertiary Piemonte Basin; VA: Vanoise; VO: Voltri Massif; VS: Valpelline Series; ZH: Zone Houillère; ZS: Zermatt–Saas Zone. Star indicates location of the UHP Lago di Cignana Unit.

Vialon (1966) carried out the first modern work on the Dora-Maira massif, describing it as representing the deep structural roots of the internal Western Alps exposed in a large tectonic window. It forms a broad half-dome delimited on the east by boundary faults and Tertiary fill of the Po basin and overlain by oceanic Penninic nappes on the west.

In general, the Dora-Maira tectonic units derive from reworking of former Variscan continental crust and of the associated Triassic cover, which experienced different metamorphic peak conditions during the Alpine subduction to HP and UHP conditions (e.g. Carswell et al., 2005).

The southern and most famous part of the DMM is composed by four metamorphic units described below: (1) San Chiaffredo (2) Rocca Solei; (3) Pinerolo; (4) Brossasco-Isasca.

The San Chiaffredo and Rocca Solei units

The San Chiaffredo and Rocca Solei Units are very similar: they both represent portions of pre-Alpine continental crust consisting of Variscan metamorphic basement equilibrated at amphibolite-facies conditions and subsequently intruded by Permian granitoid bodies. The metamorphic basement consists of a garnet-bearing micaschist with micaceous gneiss, marbles and eclogites. On the other hand, the granitoid bodies consist mainly of fine-grained orthogneiss and augen-gneiss (Matsumoto and Hirajima, 2000).

The analysis performed by Matsumoto and Hirajima (2000) on the garnet-bearing micaschists revealed a complex metamorphic evolution of this unit that, however, is consistent with the evolution of adjacent HP and UHP units (see below). The zoning pattern of large garnet crystals and the distribution of solid inclusions within them, suggest two main metamorphic stages of garnet growth. The first stage, interpreted as pre-Alpine in origin, leads to formation of garnet cores with low pyrope content that enclose staurolite inclusions;

the second stage, related to HP conditions during the Alpine metamorphism, leads to the formation of garnet richer in pyrope component and enclosing chloritoid inclusions. Finally, a last garnet growth event takes place during a low-pressure (LP) exhumation event characterized by a tiny Mn enrichment along the garnet external rim (Sandrone and Borghi 1992; Matsumoto and Hirajima 2000). Chopin et al. (1991) suggested that the peak conditions of these units, in the southern Dora-Maira, were probably close to the reaction curve of albite breakdown to give jadeite and quartz at about 1.5 GPa and 550 °C at the quartz-eclogite facies stability field. However, they also pointed out that further mineralogical studies on less deformed rocks are necessary to better define the maximum pressure conditions of these units. Recently, Groppo et al. (2019) suggested, on the base of pseudosection modelling and internally consistent thermobarometric estimates, an eclogite-facies metamorphism for these two units at about 500-520 °C and 2-2.4 GPa.

Finally, it is interesting to note that, as reported in a short note by Compagnoni et al. (2012), due to their similarities, the San Chiaffredo and Rocca Solei Units, located to the north and south of the UHP unit respectively, could possibly be the same unit just repeated by folds. However, according to these authors, it seems highly unlikely that such a geometry would allow the insertion between them of the UHP Brossasco-Isasca unit, which has been interpreted with a different peak metamorphic condition and subsequent exhumation history.

The Pinerolo unit

The Pinerolo unit (in some cases reported also as Sanfront-Pinerolo unit) is tectonically exposed below the UHP unit and it is a metasedimentary sequence with graphite-rich lenses, quartzite layers and local granitic intercalations. It represents the lowest structural unit exposed in the internal Western Alps and it has been interpreted as a distal part of the more external European Brianconnais platform (Avigad et al. 1993).

Several studies on this unit, mostly by Avigad and co-authors (1993; 2003), described two main metamorphic stages distinguished by the presence of solid inclusions and changes in the chemical composition of garnet porphyroblasts within the metapelitic rocks. The garnet cores display low Ca, Mg and Mn contents; the Spessartine component increases from the garnet cores towards the rims. The presence of staurolite solid inclusions in the early-formed garnet cores has been taken as evidence for pre-Alpine metamorphism. Differently, the garnet rims, containing phengite and chloritoid inclusions, have been related to a second stage of garnet growth, during Alpine blueschist-facies metamorphism. The coexistence of staurolite and chloritoid allowed Avigad et al. (2002) to estimates temperature of 500°C for this first metamorphic stage with a maximum pressure of 0.6-0.7 GPa. For the second metamorphic stage, Si-rich phengite in the matrix of the rocks, in equilibrium with the garnet rim, and the occurrence of chloritoid with a Fe/(Fe + Mg) ratio of about 0.8 gave P-T conditions of about 0.8 GPa and 530 °C which are within the epidote-blueschist facies conditions. More recently, however, Groppo et al. (2019) suggested notable different metamorphic condition of this unit suggesting, similarly to th San Chiaffredo and Rocca Solei units, a eclogite-facies metamorphism at T of about 500-520 °C and P of 2-2.4 GPa.

The Brossasco-Isasca UHP unit

The Brossasco-Isasca unit is the one in which Chopin (1984) firstly described the coesite inclusions in garnet from phengite- and garnet-bearing whiteschists. It consists of a portion of pre-Alpine continental crust (essentially paraschists) equilibrated under amphibolite-facies conditions and intruded by Permian granitoids. During the Alpine event, with respect to the other units, the Brossasco-Isasca reached the highest P and T conditions of re-equilibration with a metamorphic climax within the coesite/diamond stability field (e.g. Hermann, 2003) (see below).

The Brossasco-Isasca unit, as other UHP units, is usually described as "*tectonically sandwiched"* between the two lower-grade units Rocca Solei, at the top, and the Pinerolo, at the bottom (Figure 3.3), that record lower P and T conditions during the Alpine re-equilibration.

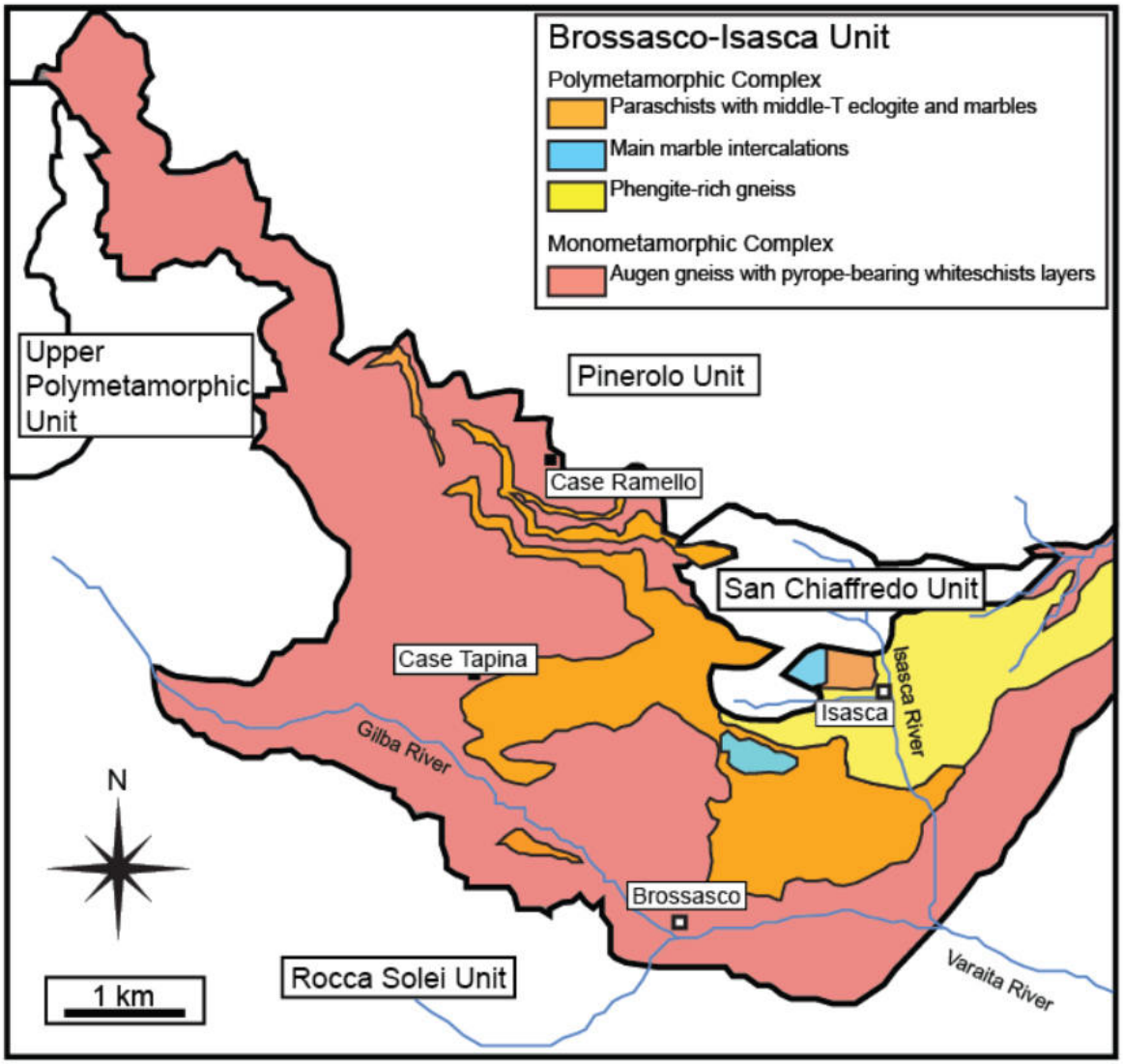

Figure 3.3 Tectono-metamorphic sketch map of the southern part of Dora-Maira Massif (modified from Castelli et al. 2007).

After the first paper by Chopin (1984), numerous structural and petrological studies have been carried out to clarify the petrologic and tectonic evolutionary frame of this UHP unit

(e.g. Michard et al. 1993; Compagnoni et al. 1994; Chopin and Schertl, 1999; Rubatto and Hermann, 2001; Hermann, 2003; Ferrando et al. 2009; Gautiez-Putallaz et al., 2016).

The Brossasco-Isasca UHP Unit consists of two main lithostratigraphic complexes (e.g. Compagnoni et al. 1995): (1) the Mono-metamorphic and (2) the Poly-metamorphic complexes. The first one consists of orthogneiss with local relics of meta-granitoids, hosting lens-shaped bodies and layers of pyrope-bearing whiteschist derived from metasomatic reworking of Variscan granitoids during the Alpine orogeny (Gebauer et al., 1997). Differently, the Poly-metamorphic complex consists of paragneiss and mica-schists with intercalations of eclogite and marble deriving from the Alpine reworking of Variscan, amphibolite-facies, metamorphic basement rocks, which therefore clearly retain the record of two superposed orogenic cycles, Variscan and Alpine (e.g. Compagnoni et al., 1995). It represents the metamorphic country-rock in which the granites, forming the Monometamorphic complex intruded during the Permina age (Compagnoni et al., 2005). Figure 3.3 reports a schematic geological map of the Brossasco-Isasca unit showing the spatial distribution of the main rock formations.

The poly-metamorphic complex

This complex mainly includes paragneiss with marble and eclogite layers that locally preserve relics of pre-Alpine parageneses and microstructures (Compagnoni et al. 1995; Carswell et al., 2005).

The most frequent rock-type in this complex is a kyanite and almandine-bearing micaschist, showing garnet crystals up to 2 cm in size. The main Alpine mineral association of these rocks consists of phengite, kyanite, quartz, jadeite with abundant accessory rutile and minor zircon and tourmaline (Compagnoni et al., 1995). Another generation of fine-grained

acicular kyanite appears to replace previous sillimanite crystals, or former andalusite in (meta-) hornfelses around the Permian (meta-)granitoid. Finally, a decompression event is attested by the replacement of jadeite crystals by albite and paragonite and of the garnet crystals by biotite and chlorite.

Porphyroblastic kyanite and garnet (almandine-rich in composition) bear plenty of solid inclusions which, in some instances, define a local foliation within the host crystals (Compagnoni et al. 1995). Garnet usually contains inclusions of chloritoid, rutile, staurolite, kyanite, jadeite, quartz and coesite. While the kyanite inclusions are ubiquitous, staurolite, quartz and chloritoid occur in the core and mantle of the garnet host only (Groppo et al. 2019). Coesite is also found only at the garnet rim (Compagnoni et al. 1995).

Ferraris et al. (2000) revealed the occurrence of nano-scale exsolutions of quartz + talc in large phengite flakes, which they interprete as the result of exhumation into the quartz stability field, producing a phengite increasingly depleted in celadonite component.

The eclogites within the poly-metamorphic complex form rare and small bodies likely derived from boudinage of previous concordant mafic layers (Castelli et al. 2010). At the contact with the country paragneiss, the eclogite often shows a thin garnetite layer. The eclogite is fine-grained and the main mineral association is represented by garnet, omphacite, phengite and quartz. Minor phases are zoisite, rutile, zircon and apatite. Omphacite and phengite, different from quartz, that shows granoblastic textures, line along a peak metamorphic foliation. However, the occurrence of coesite inclusions within omphacite crystals suggest that the quartz aggregate derives from previous coesite. Retrograde metamorphism of this eclogite is characterized by formation of fine-grained symplectitic intergrowths of diopside, albite and green amphibole after omphacite and of biotite and oligoclase after former phengite (Hermann, 2003; Groppo et al. 2007).

The marbles of the poly-metamorphic complex consist of calcite and dolomite-rich layers embedded within the paraschists. Marbles are locally associated with thin and discontinuous films of micaschists and eclogite. Two major lenses occurring close to Costa Monforte correspond to phengite-bearing calcite marbles. Locally, these lenses contain silicate-rich domains showing a mineral assemblage of garnet, pyroxene, phengite, epidote and titanite. These minerals display a preferred orientation within the marble that is parallel to the regional UHP foliation (Castelli et al. 2007). Detailed microstructural, petrological and crystallographic data suggest that the marbles underwent the same Alpine metamorphic evolution as the country paragneiss (Ferraris et al., 2005; Castelli et al., 2007).

The mono-metamorphic complex

This complex prevalently consists of *orthogneisses* that locally preserve the relics of their *(meta)granitoid* protolith: these rocks are associated with lenses of *pyrope-bearing whiteschists* and with rare, dyke-shaped, bands of a *garnet-jadeite-kyanite-quartz granofels* (Carswell et al., 2005). The orthogneiss constitutes over 90% of the Mono-metamorphic complex; the field appearance, depending on the strain distribution within the rock, can change from augen-gneiss textures into fine grained mylonites. Usually, the orthogneiss shows greenschist-facies assemblages including quartz, albite, biotite, chlorite, phengite with low celadonite content, epidote, titanite and other accessory minerals (see Carswell et al., 2005 for a detailed review). However, this rock locally retains the evidence of a former UHP event, as suggested by porphyroclastic, highly celadonitic, phengite and by aggregates of titanite associated with grossular rich garnet; no coesite has been found in the orthogneiss.

The metagranitoids are interpreted as the products of a static Alpine metamorphic transformation of Variscan protoliths (275 Ma), as suggested by zircon U/Pb dating (Gebauer et al., 1997). The metagranitoids still preserve the original igneous structure and are granitic to granodioritic in composition. They can locally include aplitic dykes together

with microgranular enclaves and cm to m sized xenoliths of the country rocks (Carswell et al., 2005). The static Alpine overprint of such metagranitoid occurs with development of garnet + phengite coronas around igneous biotite and with replacement of igneous plagioclase by symplectites of zoisite. Fine-grained sugary quartz aggregates after the igneous quartz suggested to Compagnoni et al. (1995) the possible replacement of former coesite. Evidence that this rock likely passed through UHP is provided by some coesite-bearing mafic enclaves (personal communication of David R. Snoeyenbos to C. Chopin).

Chopin (1984) described the garnet-jadeite-kyanite-quartz (previous coesite) granofels as "weathered bluish rock devoid of mica". They occur within the pyrope-bearing whiteschists as thin layers (from 10 to 20 cm in thickness and several meters long) and show UHP mineral assemblages such as coesite included in kyanite and jadeite. Schreyer et al. (1987) and Sharp et al. (1993) interpreted the origin of these rocks as the product of partial melting of the host whiteschists protolith. However, convincing evidence for this interpretation is still lacking (Hermann, 2003).

The pyrope-bearing whiteschists occur within the orthogneiss as lenses of variable size. Peculiarity of these rocks is the size of the garnets ranging from few mm up to megablasts 25 cm across, often showing a sub-idiomorphic habitus. They present an almost pure pyrope composition and most of them, especially the largest crystals, are quite homogeneous in composition across the entire volume of the grains (e.g. Schertl et al. 1991). However, Compagnoni and Hirajima (2001) reported the rare occurrence of super-zoned garnet in these rocks, which has been related to a metasomatic process taking place during the prograde path towards UHP conditions. Further detail on the pyrope-bearing whiteschists are discussed in the next section.

Pyrope-bearing whiteschists and their origin

At the outcrop scale, the whiteschists appear as a heterogeneous lenses with an apparent thickness of 1 to about 30 m and up to about 50-100 m length. They occur within the orthogneiss of the Mono-metamorphic complex. The contact with the surrounding rocks can be either sharp or transitional, with the interposition of phengite-rich gneiss locally presenting relics of K-feldspar. These contact layers can be of variable thickness, from few centimetres to metres across (e.g. Schertl et al., 1991; Compagnoni and Hirajima, 2001).

In general, the mineral assemblage mainly consists of quartz (previous coesite) + phengite + kyanite + garnet ± talc (e.g. Chopin, 1984). The whiteschists can therefore be described as garnet-bearing quartz-schist. Based on their bulk chemistry (Chopin, 1984; Hermann, 2003), they are divided in two groups: *SiO_2 saturated* (or, in terms of possible protolith, *chlorite poor*-) and *SiO_2 under-saturated* (or *chlorite rich*-) whiteschists. In SiO_2 under-saturated domains, quartz hardly reaches 5-10 vol% and the rock contains larger amount of phengite, garnet and kyanite (e.g. Gautiez-Putallaz et al. 2016). In the SiO_2 saturated variety, quartz reaches up to 40-50 vol% while phengite and garnet are less abundant. In particular, garnet changes slightly its composition and size as function of the bulk chemistry: it is larger (up to 25 cm across) with almost pure and homogeneous pyrope composition in under-saturated whiteschists, while in the SiO_2-saturated domains it is smaller and richer in almandine component (up to 15 wt% at the core). Compagnoni and Hirajima (2001) also documented few examples of super-zoned garnets showing up to 60% of almandine component at the core. Along with garnet, phengite is an important marker of the evolution of these rocks. Based on the microstructure and mineral chemistry of mica, Hermann (2003) found up to 5 evolution stages in whiteschists starting from the peak assemblage (stage A) and proceeding toward the retrograde processes (up to stage E) (Figure 3.4). The first recrystallization stage A consists of garnet, large phengite crystals (Si up to 3.60 a.p.f.u.), kyanite and coesite (now mainly quartz) with accessory rutile and zircon and represents the metamorphic climax of

these rocks. During the second stage B, a phengite + kyanite + talc ± quartz corona formed at the contact between phengite and garnet. Phengite shows an average Si-content of about 3.55 a.p.f.u., lower than phengite formed during stage A, locating this evolution stage at a lower metamorphic grade. Stage C, characterized by an even more reduced grain size, consists of biotite, phengite (Si ~3.39 a.p.f.u.) with minor talc and kyanite. In this stage, biotite reaches up to 3.02 a.p.f.u. of Si content. Stage D, found in contact with the garnet wall, consists of biotite (Si ~2.80 a.p.f.u.) and chlorite. Finally, stage E represents the garnet breakdown along cracks, where it is mainly replaced by chlorite and by minor amounts of biotite. In some cases, a retrograde overgrowth of pure muscovite on previous phengite has been documented.

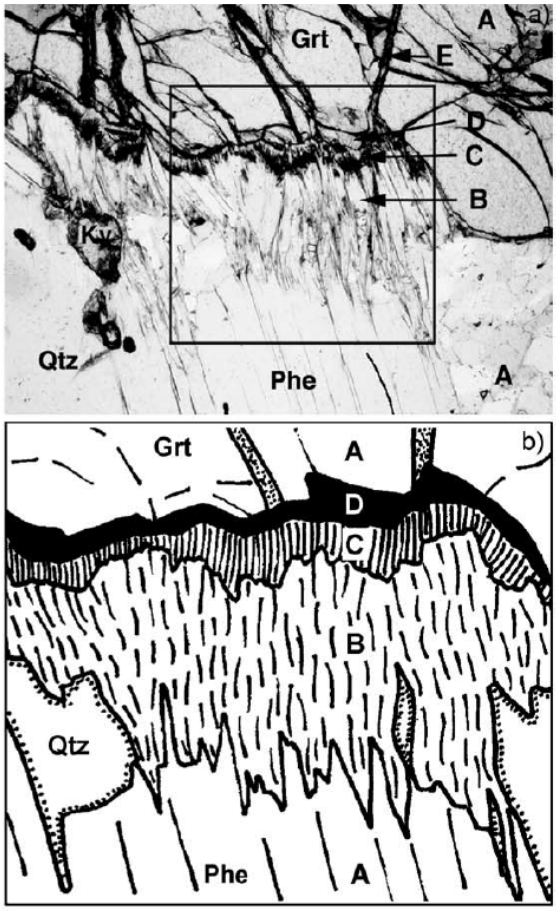

Figure 3.4. Microphotograph (on top) and a sketch drawing (bottom) of a whiteschist showing a multistage corona between peak metamorphic garnet and phengite with highlighted the different evolution stages (taken by Hermann, 2003). Capital letters (A, B, C, D and E) represent the different evolution stages as reported in the main text.

Another key feature of these rocks is represented by the index mineral inclusions found inside garnet and subordinately kyanite, that mainly correspond to rutile, zircon, kyanite (in garnet), chlorite, talc, coesite, and other subordinate phases such as ellenbergerite and Mg-dumortierite (e.g. Chopin, 1984). Chopin (1984) firstly described the occurrence of coesite inclusions in garnet from these rocks, showing partially preserved coesite cores surrounded by palisade quartz structures. Notably, these microstructures are often surrounded by radial cracks of the adjacent garnet host that (Chopin, 1984) interpreted as the result of volume increase during the coesite to quartz transition along the exhumation pathway of these rocks. The discovery of coesite inclusions in this subducted slice of continental material (Chopin, 1984) demonstrated, for the first time, that such rocks reached minimum pressures of about 3 GPa. In terms of depth of subduction, using the hydrostatic approximation, such a value would correspond to approximately 90 km. At the time of discovery, this evidence led the scientific community to consider new geodynamic concepts, such as the possible depths reached by subducted crustal materials, the processes driving the exhumation of eclogite facies rocks, the extent of crustal recycling in the deep Earth; processes that, after all, are still explored and debated nowadays.

The origin of whiteschist is still matter of debate. In his first paper, Chopin (1984) attributed these rocks to metasomatism of previous meta-evaporitic rocks. Several subsequent oxygen isotope studies demonstrated that the whiteschists represent a metasomatized granite (Schertl and Schreyer 2008; Ferrando et al. 2009; Gautiez-Putallaz et al., 2016). However, the origin and the tectonic context of this metasomatic event are still controversial. Several studies attributed the metasomatic event to a prograde Alpine event. As an example, Compagnoni and Hirajima (2001) attributed the metasomatic event to an early episode of fluid release during partial dehydration of serpentinites located to lower levels of the slab during initial

subduction. More recently, Gautiez-Putallaz et al. (2016) pointed out that such a scenario is difficult to reconcile with the observation that the surrounding gneisses appear unaffected by such a fluid influx. Therefore, they suggested, based on oxygen isotopes systematics combined with zircon dating and thermodynamic modelling, that the whiteschists had already acquired their Mg-rich and low $\delta^{18}O$ signature before subduction, concluding that the main metasomatic transformation took place before the HP and UHP metamorphism. Alternatively, they proposed an oceanic environment for the origin of this metasomatic event speculating that the continental sequence of the Dora-Maira could be a continental sliver that was part of hyper-extended margin during the Jurassic rifting, in agreement with the reconstruction given by Beltrando et al. (2010).

P-T path of the Brossasco-Isasca UHP unit

The oldest event, found within the Paraschist of the Polymetamorphic Complex, is the pre-Alpine recrystallization in amphibolite facies conditions represented by pseudomorphs after andalusite and sillimanite in association with pre-Alpine biotite and plagioclase which was later substituted by jadeite quartz and zoisite. Further, the presence of metatects within the paragneiss suggested an incipient melting during the Variscan HT metamorphism (Compagnoni et al., 1995; Groppo et al., 2007). On the other hand, the prograde path of the Brossasco-Isasca unit, during the Alpine orogeny, has been mainly constrained combining P-T index mineral inclusions with classical thermobarometric methodologies. In this regard, while there has been a general agreement in constraining the Alpine peak temperature around 730-750 °C since the first evaluations (e.g. Chopin 1984; Sharp et al. 1993), the peak pressure value has been more debated. Chopin (1984; 1987) gave a P value of about 3.3 GPa. Later, Schertl et al. (1991) found slightly higher P values around 3.7 GPa. Ferrando et al. (2009), from the whiteschists, inferred three prograde Alpine stages corresponding to: about

1.6 GPa at T lower than 600 °C the first, 2.1 GPa and 600 °C the second and about 2.8 GPa at 650 °C for the last one. However, Hermann (2003), combining experimental results in the KMASH system together with petrologic information, was the first to suggest that the BIU unit reached the diamond stability field with a metamorphic climax of about 4.3 GPa at 730 °C. Later, similar conditions were found by Castelli et al. (2007) even if diamond has never been recorded in these rocks. Finally, the retrograde path has been interpreted as a significant decompression followed by cooling. The major evidences of this stage are represented by symplectitic structures characterized by biotite (phlogopite-rich), kyanite and talc assemblages in replacing the contact between UHP phengite and garnet (Chopin, 1984; Schertl et al. 1991). Therefore, the whole Alpine evolution is defined by a clockwise path in the P-T space with an extremely narrow loop consistent with a fast exhumation (see Figure 3.5).

Timing of UHP metamorphism in the Dora-Maira Massif

From the first ^{39}Ar-^{40}Ar data (e.g. Monie & Chopin, 1991), the UHP metamorphism of the Brossasco-Isasca unit was Cretaceous in age. However, later geochronological studies have suggested different conclusions. For instance, Tilton et al. (1989) was the first to suggest a Tertiary age for the UHP metamorphism. They proposed, by means of conventional U–Pb and Sm-Nd systematics in zircon and garnet respectively that the growth of pyrope in the UHP whiteschists occurred at 38–40 Ma. Later, Gebauer et al. (1997) further supported these results constraining the age of the metamorphic zircon domains at 35.4 ± 1.0 Ma. This age was also confirmed by Duchene et al. (1997), who reported a Lu–Hf age of 32.8 ± 1.2 Ma, obtained on a garnet–whole-rock pair from a pyrope whiteschist.

Rubatto & Hermann (2001) further refined the P–T–t path of the Brossasco-Isasca unit using SHRIMP in situ dating on single growth zones of titanite crystals within calc-silicate nodules

in marbles. Their results suggested a mean age for the UHP at 35.1 ± 0.9 Ma with other two retrograde processes, developed during exhumation, at 32.9 ± 0.9 Ma, and at 31.8 ± 0.5 Ma. Combining these radiometric data with a zircon fission track age of about 30 Ma (Gebauer et al., 1997), and with the assumption about the conversion of pressure to depth, they estimated a maximum exhumation rate of 3.4 cm/year. This allowed the reconstruction of one of the best-documented exhumation paths for UHP terrains. Furthermore, these rates imply that exhumation acted at plate tectonic speeds similar to subduction, and was significantly faster than erosion, thus suggesting that exhumation is driven by a combination of tectonic processes involving buoyancy and normal faulting (Rubatto & Hermann, 2001).

Figure 3.5 reports selected Alpine and pre-Alpine (blue curve) P-T-t paths for the Brossasco-Isasca unit.

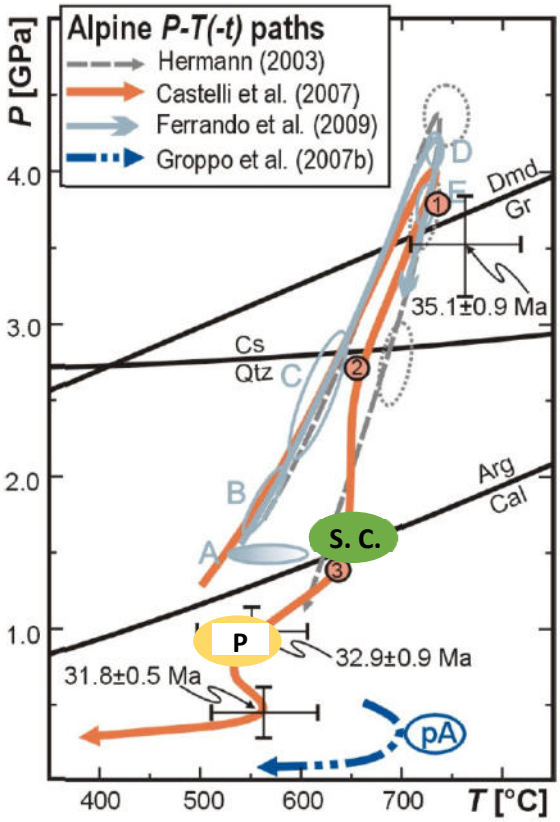

Figure 3.5. Selected P-T paths proposed for the Alpine and pre-Alpine (blue curve: pA) events recorded in the Brossasco-Isasca unit and the metamorphic climax for the San Chiaffredo (S.C.) and Pinerolo (P) units. Grey solid ellipses labelled A to E are the P-T conditions of prograde, peak and retrograde stages by Ferrando et al. (2009) for the

Brossasco-Isasca UHP unit, whereas grey dotted ellipses are those estimated by Hermann (2003) for the same unit. The error bars of ages refer to the geochronologically dated P-T estimates of Rubatto & Hermann (2001). Modified from Castelli et al., 2014.

Chapter 4

Sample description and characterization

The pyrope- and coesite-bearing whiteschists outcrop in two different classic localities, one next to Case Ramello, near Parigi at Martiniana Po, and the other one close to Case Tapina, near Canova, in the Gilba valley. Hereafter, they will be referred as Martiniana and Gilba, respectively. Figure 4.1 reports their position within the Brossasco-Isasca unit and two representative pictures of the rocks.

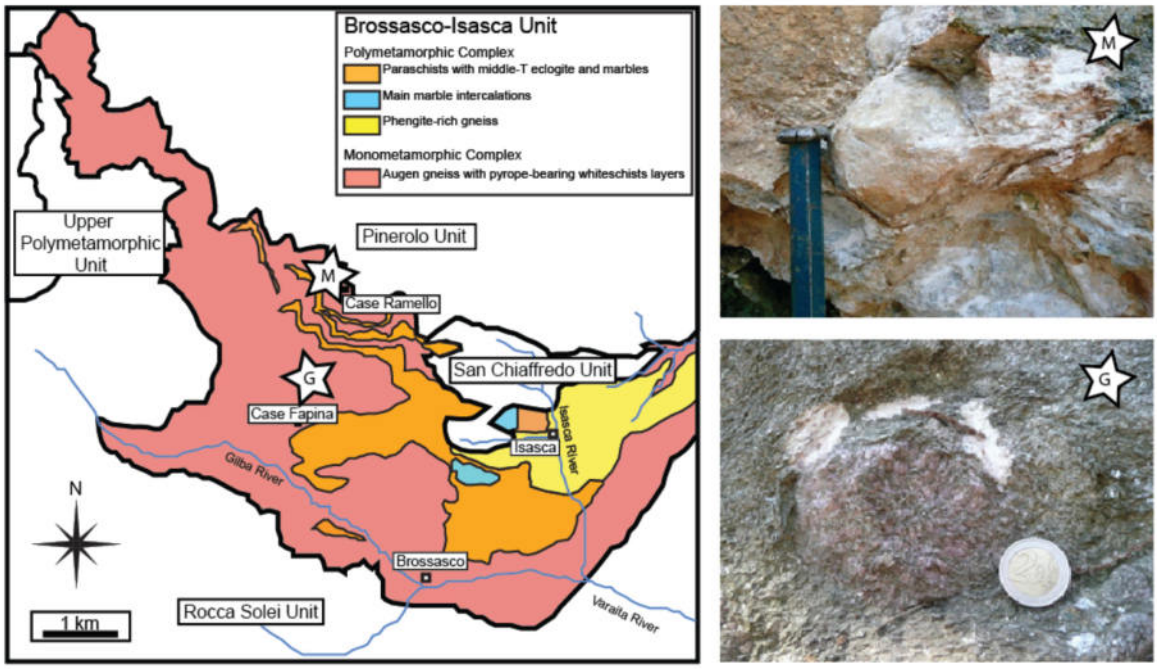

Figure 4.1. Tectono-metamorphic sketch map of the Brossasco-Isasca unit (modified from Castelli et al. 2007). The two white stars indicate the Gilba (G) and Martiniana (M) outcrops.

At a first glance, the main difference between them is the shape of the pyrope megablasts, occurring as idiomorphic single crystals in Martiniana and as rounded ones in Gilba (Fig. 4.1, M and G pictures).

The distinction between the two outcrops is maintained throughout the text and, even if this is a qualitative discrimination, it is interesting that such a difference seems to be reflected also by the microstructural features and by the abundance of solid inclusions.

4.1 Whiteschists: field occurrence and description

As described previously, the whiteschists occur as lenses within the country orthogneiss of the Monometamorphic complex. In the field, they can be recognized due to their pale colour with respect to the country rocks. The whiteschists display a discontinuous foliation defined by the iso-orientation of large white mica flakes and kyanite crystals. Petrographically, these rocks are garnet-bearing quartz-schists; the pyrope-rich garnet can be easily recognized at the field scale because of the pink colour and the size, ranging from few millimetres up to 25 cm across (i.e. garnet neoblasts and garnet megablasts respectively). The modal abundance of garnet is highly variable, suggesting local differences in the bulk chemistry of the protolith (i.e. *SiO_2-saturated* and *SiO_2-under-saturated* whiteschists as described in the previous chapter). Below a brief description of the main field-scale features of the two outcrops is reported.

The Martiniana outcrop

The Martiniana whiteschists display the largest modal abundance of idiomorphic pyrope megablasts. In some cases, for instance, it is possible to recognize the 4-fold axis (see Figure 4.2A). Locally, the modal amount of garnet megablasts can be as high as 80 % of the rock volume forming impressive clusters. Garnet megablasts and neoblasts usually present a greenish-to-yellowish external rim consisting of weathered chlorite and talc caused by partial

retrogression. Mesoscale polished sections of the garnet megablasts show that this alteration can be significantly developed, up to the complete replacement of garnet (Figure 4.2B).

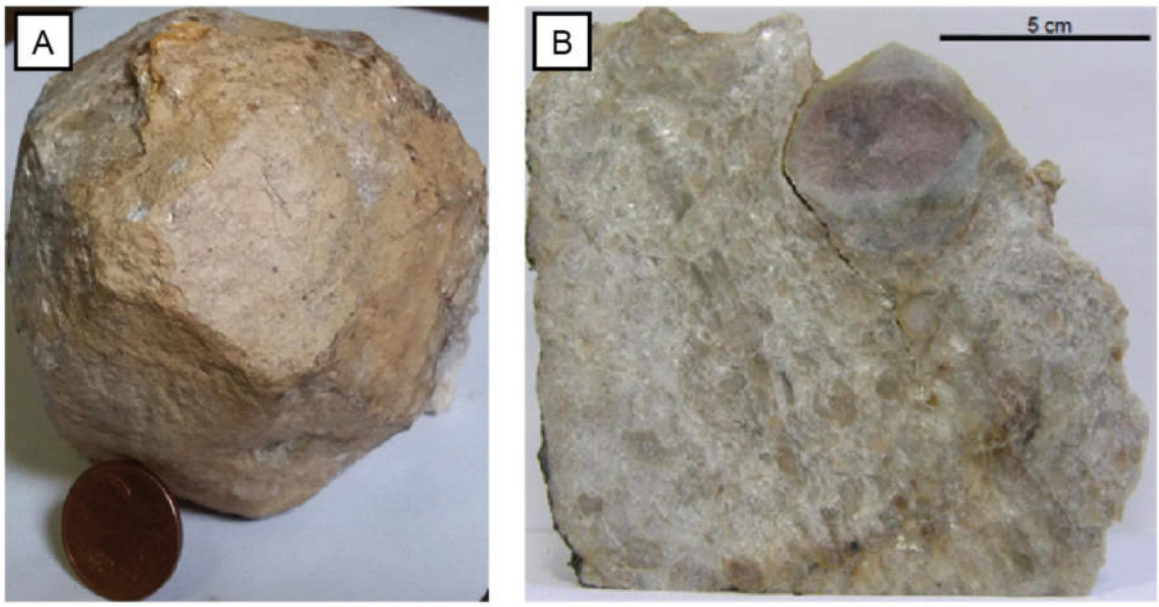

Figure 4.2. (A) Single pyrope megablast with idiomorphic shape. (B) Quartz-schist bearing a well shaped, partly chloritised pyrope megablast and anhedral centimetre-size very pale pink pyrope crystals in the quartz-phengite-kyanite groundmass Martiniana outcrop.

On the other hand, the freshly preserved rocks consist of pink garnet, transparent quartz, colourless kyanite and abundant white mica that, with talc, confers the rock the typical whitish colour. The small-sized garnets display irregular shapes, varying from rounded to slightly elongated crystals. Figure 4.2 B reports the cut mesoscopic section of a whiteschist sample from this specific outcrop.

The high to ultrahigh pressure foliation structuring the whiteschists is apparently unaffected by the strong greenschists mylonitization described by Henry et al. (1993) that brings multiple folding and transposition of the UHP structures. In many places however, a reconstruction of the structural patterns of whiteschists is hampered by the dense vegetation and by the fact that these rocks occur as loose blocks of variable dimensions.

The Gilba outcrop

The Gilba whiteschists are characterized by a slightly minor modal amount of garnet megablasts that, also in this case, reach dimensions up to 15-20 cm across. Differently from Martiniana, the Gilba garnet megablasts are usually rounded or irregular in shape. In general, the Gilba whiteschists are better preserved. The garnet megablasts are pinkish in colour, display a lower extent of retrograde reworking and are less affected by weathering. Figure 4.3 shows the mesoscopic section of a Gilba coarse-grained rock sample containing several garnet megablasts overgrowing a continuous rutile and biotite foliation whose orientation appears concordant with fracture systems inside the garnet megablasts.

The samples collected from this outcrop are from blocks that are not in place and a comparison with the local foliation is meaningless.

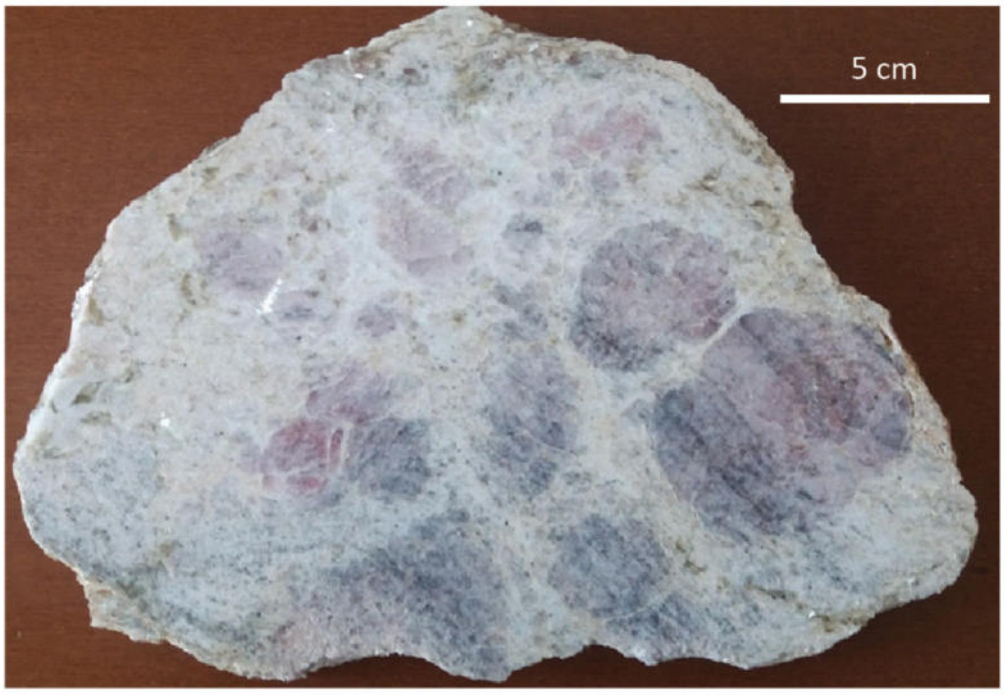

Figure 4.3. Coarse-grained pyrope-bearing quartz-schist from the Gilba locality

4.2 Petrography and chemistry of whiteschists

Whiteschists with garnet neoblasts (SiO_2-saturated)

Under the optical microscope, the rock mesoscale foliation visible in the field is difficult to follow (Figure 4.4 A).

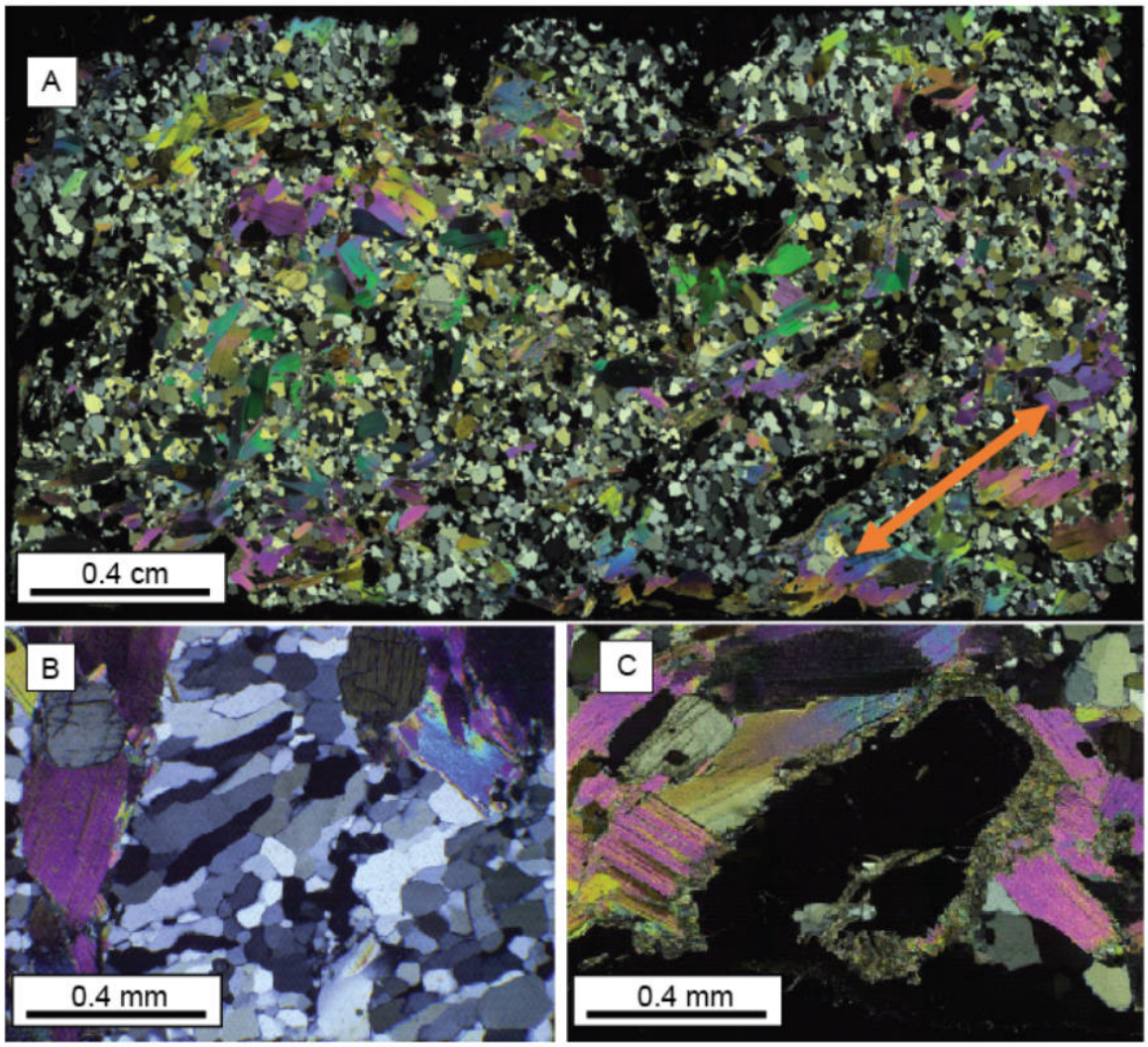

Figure 4.4. (A) Thin section of a SiO_2-saturated whiteschist under cross-polarized light. Phengite, garnet and quartz are easily distinguished. Locally a slight iso-orientation of phengite flakes is apparent along the NE-SW direction of the observation plane (high-lighted by the red arrow). (B), granoblastic and elongated textures of quartz constituting the rock matrix of SiO_2-saturated whiteschists. (C), retrogression corona around a garnet neoblast in contact with phengite crystals.

Quartz, the most abundant mineral in these rocks, display a granoblastic texture with triple junctions. In some cases, however, close to the interface with other minerals, the quartz appears stretched and elongated (Figure 4.4-B).

These particular textures resemble the coarse palisade structures developed around partially preserved coesite inclusion at the contact with the garnet host; in previous studies (e.g. Chopin,1984; Schertl et al., 1991) they have been interpreted as the retrograde products of former coesite. Indeed, these particular textures have been taken as evidence that these rocks, at metamorphic peak conditions, were *coesite-schists* that later retrogressed to quartz-schists.

In *SiO_2-saturated* whiteschists the garnets are small and display irregular shapes. These garnets are frequently replaced by retrograde assemblages.

Fresh garnet usually appears completely transparent, fractured and hosts different type of solid inclusions such as kyanite, rutile, zircon, coesite.

Table 4.1: Representative chemical analyses of garnet neoblasts

Label	**Line 1 DM17-8A2**	**Line 2 DM17-8A2**	**Line 4 DM17-8A2**	**Line 5 DM17-8A2**	**Line 12 DM17-8A2**	**Line 14 DM17-8A2**
note	*rim*	*rim*	*mantle*	*mantle*	*core*	*core*
SiO_2	44.08	44.20	44.06	43.87	43.88	44.08
TiO_2	0.00	0.03	0.00	0.00	0.00	0.00
Al_2O_3	25.63	25.97	25.63	25.55	25.20	25.24
Cr_2O_3	0.01	0.04	0.00	0.00	0.00	0.00
MgO	28.86	28.63	27.58	27.62	26.85	27.26
FeO	1.35	1.06	1.88	1.78	3.34	3.21
MnO	0.00	0.01	0.00	0.02	0.00	0.01
CaO	0.08	0.05	0.78	0.75	0.33	0.20
Total	*100.00*	*99.99*	*99.93*	*99.59*	*99.60*	*100.00*
Recalculated formula						
Si	2.98	2.98	2.99	2.98	3.00	3.00
Ti	0.00	0.00	0.00	0.00	0.00	0.00
Al	2.04	2.06	2.05	2.05	2.03	2.02
Cr	0.00	0.00	0.00	0.00	0.00	0.00
Mg	2.91	2.88	2.79	2.80	2.74	2.77
Fe2+	0.08	0.06	0.11	0.10	0.19	0.18
Mn	0.00	0.00	0.00	0.00	0.00	0.00
Ca	0.01	0.00	0.06	0.05	0.02	0.01
Total	*8.00*	*7.99*	*7.99*	*7.99*	*7.98*	*7.99*

Microprobe analyses of garnet show an almost pure pyrope composition. Element profiles and element mapping reveal a slight Mg-Fe zonation of these crystals ranging from 90% to 98% in pyrope component from core to rim respectively. Table 4.1 reports representative chemical analyses of garnet neoblasts while Figure 4.5 displays their chemical zonation.

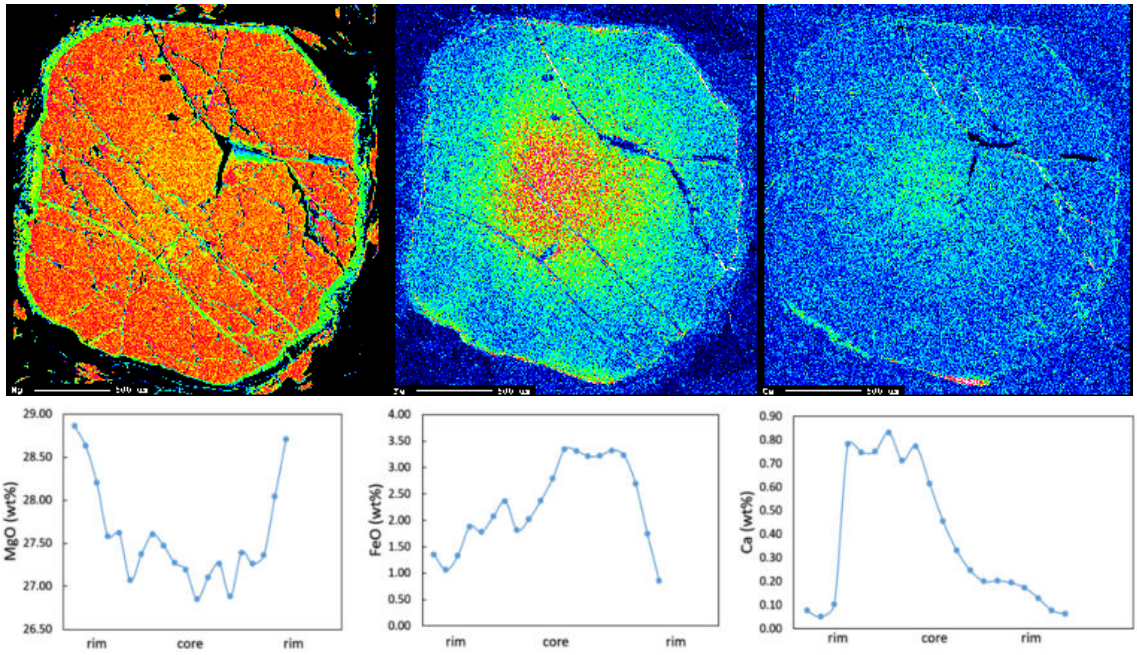

Figure 4.5 Chemical maps (top) and E-W measurements profiles (bottom) of MgO, FeO and CaO concentrations in garnet neoblasts.

After quartz, white mica is the most abundant mineral in these rocks; it mainly appears as large flakes that can reach several millimetres in size. The textural features suggest the presence of at least three main generations of mica: (1) a first generation consisting of large flakes defining the main rock foliation; (2) a second generation of tiny and randomly oriented grains growing in between the contacts of granoblastic quartz crystals in the rock matrix; (3) a third generation developed at contact with garnet crystals, where white mica develops retrograde symplectitic coronas, as reported by Hermann (2003) (Figure 4.4-C).

The chemical analysis of white mica (1) reveals high contents in celadonite component (Si ~ 3.48 a.p.f.u.) that decreases in the fine-grained mica (2). The fine-grained mica (3) consists mainly of phengite (coexisting with biotite) with the lowest Si content. Table 4.2 reports representative analyses of phengitic mica.

Table 4.2: Representative analyses of white mica

Stage	*1*	*2*	*3*
Mineral	Phe	Phe	Phe
SiO2	52.2	53.46	51.55
TiO2	0.08	0.28	0.1
Al2O3	25.61	24.8	28.94
FeO	0.13	0.12	0.12
MgO	5.33	5.09	4.21
CaO	0.12	0.06	0.06
Na2O	0.54	0.15	0.71
K2O	10.2	11.36	9.43
Total	94.21	95.32	95.12
Recalculated formula on 11 oxigens			
Si	3.48	3.53	3.10
Ti	0.00	0.01	0.00
Al(IV+VI)	2.01	1.93	2.05
Fe^{2+}	0.01	0.01	0.01
Mg	0.53	0.50	0.38
Ca	0.01	< 0.01	< 0.01
Na	0.07	0.02	0.08
K	0.87	0.95	0.72
Total	6.97	6.97	6.93

Kyanite is abundant in these rocks; it appears both as inclusion within garnet and as a free crystal in the rock matrix. In both cases, however, these crystals present a lot of solid inclusions (mainly talc, rutile and zircon) and stretched fluid inclusions that have not been characterized in this study.

Whiteschists with garnet megablasts (SiO_2-under-saturated)

These rock domains consist essentially of garnet megablasts mainly surrounded by large phengite crystals, kyanite and rare granoblastic quartz.

Phengite and quartz display the same textural and chemical features reported above. On the other hand, garnet megablasts display, on average, tiny but significant differences with respect to garnet neoblasts.

The garnet megablasts within silica undersaturated domains of the whiteschists host numerous inclusions of kyanite, rutile, zircon, rare coesite (only at the garnet rim), biotite, chlorite, tourmaline and subordinate rare phases like ellenbergerite and dumortierite (see also Chopin, 1984 and Schertl et al., 1991). Some minerals found as inclusions, such as biotite, have never been found in the rock matrix. In this regard, it is interesting to note that garnet megablasts coming from the Gilba locality tends to be better preserved than those of Martiniana and contain a large amount of rutile and zircon inclusions that in places are grouped in clusters. The Gilba megablasts display a notable fracture system extending along preferred direction within the crystal, a feature that is not shown by the Martiniana megablasts.

Microprobe profiles along the equatorial section of garnets megablasts (about 15 cm across) display little chemical variation from core to rim with an essentially pure pyrope composition; a tiny Fe-Mg variation has been documented by means of laser-ablation analysis. Appendix 1 and 2 report microprobe and trace elements analyses of garnet megablasts while Figure 4.6 shows the variations in major and trace elements measured by laser ablation transects.

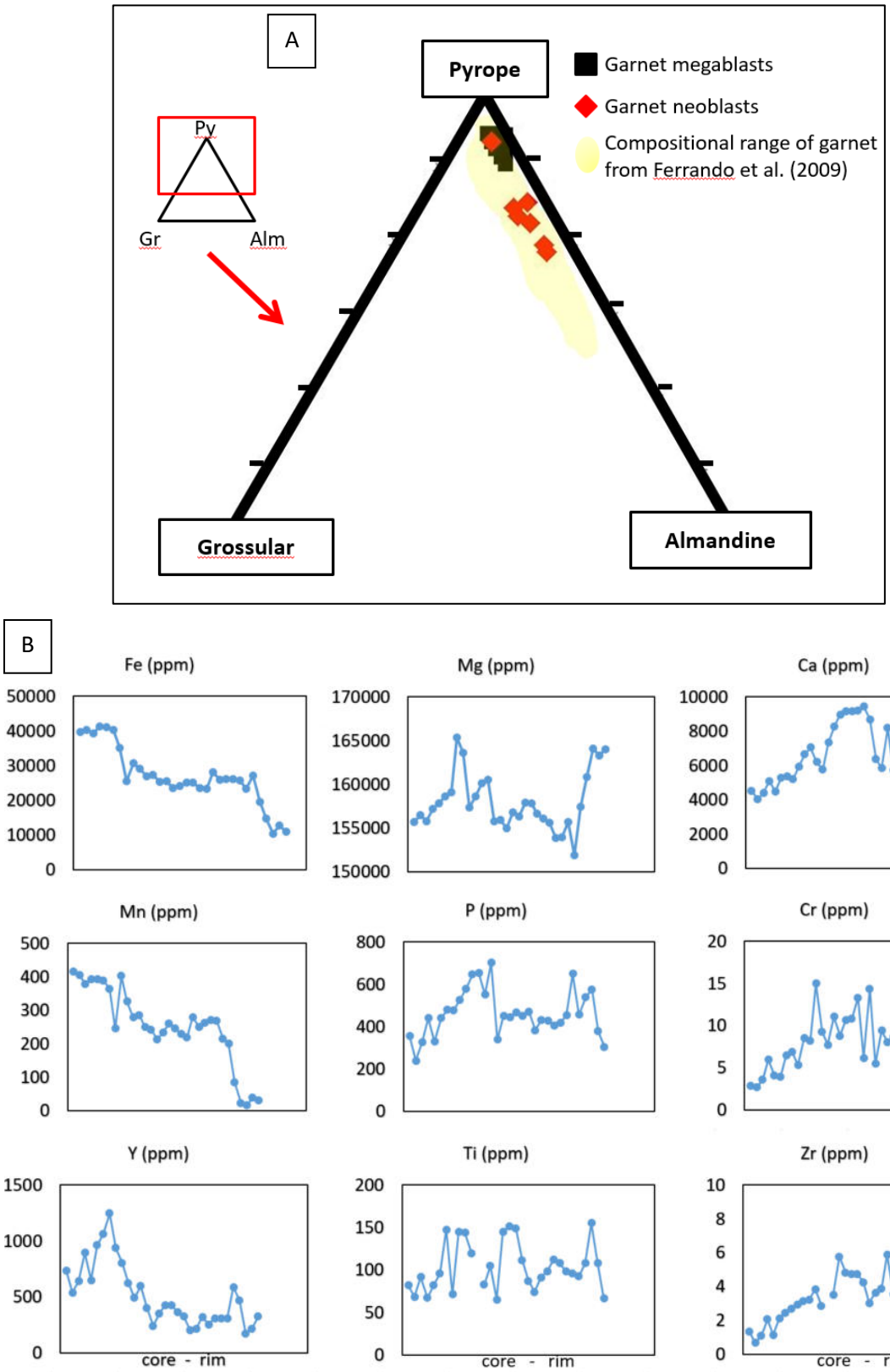

Figure 4.6 A) Ternary diagram showing the homogeneous chemical composition of pyrope megablasts with respect to the garnet neoblasts. B) Representative chemical transects from core (to the left) to rim (to the right) of a garnet megablast measured by means of laser ablation (sample DM17-13).

Moreover, the trace element analysis of garnet megablasts usually displays depletion in HREE from core to rim. In some cases, however, HREE increase has been measured in the Martiniana and Gilba garnets at the garnet external rim, probably as the result of partial garnet resorption (Figure 4.7).

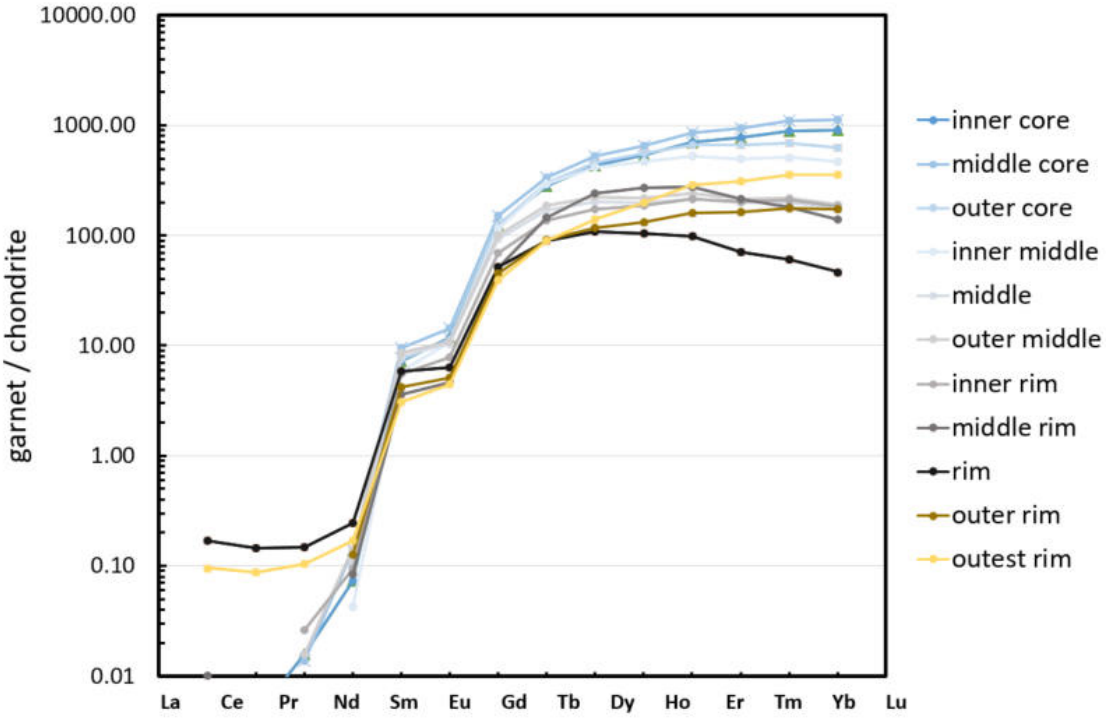

Figure 4.7 Representative HREE variation from core to rim of a garnet megablast (sample DM17-13)

Characterization, petrography and Raman spectra of the main solid inclusions

Index mineral inclusions have been of primary importance to reconstruct the P-T path of the Dora-Maira whiteschists. The clearest evidence of UHP metamorphism has been inferred, for the first time, by the discovery of coesite inclusions in garnet from these rocks (Chopin, 1984). In the present study the inclusions play a key role since they can be used for the purposes of the elastic thermobarometry. The description and characterization of mineral inclusions has been carried out by means of optical microscopy combined with Raman

spectroscopy. In the following, a description of the main solid inclusions, in terms of abundance and petrologic importance, and their Raman spectra is given.

Kyanite

Kyanite represents the largest inclusion type within the garnet megablasts; it ranges in size from 100-200 micrometres to a maximum of several millimetres. Kyanite usually presents a prismatic shape with twinned micro-structures. Kyanite inclusions often display a pronounced cleavage and contain many solid inclusions, mainly talc, chlorite, rutile, zircon and subordinated coesite (Figure 4.8).

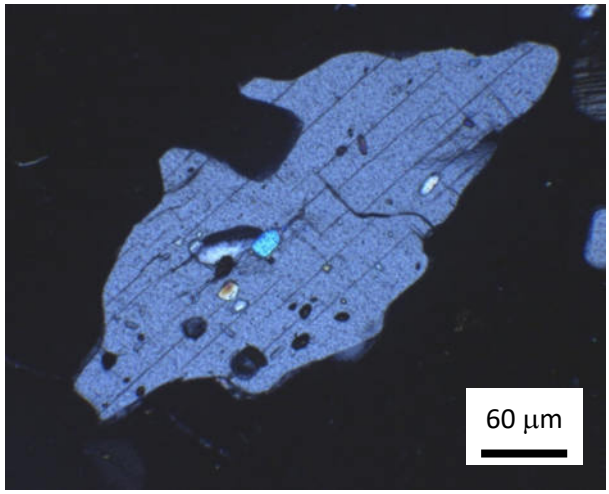

Figure 4.8. Inclusion of kyanite within a garnet megablast showing small inclusions of talc, white mica, rutile and zircon.

Figure 4.9 shows the Raman spectra and the wavenumbers of the main Raman peaks of a kyanite inclusion in garnet.

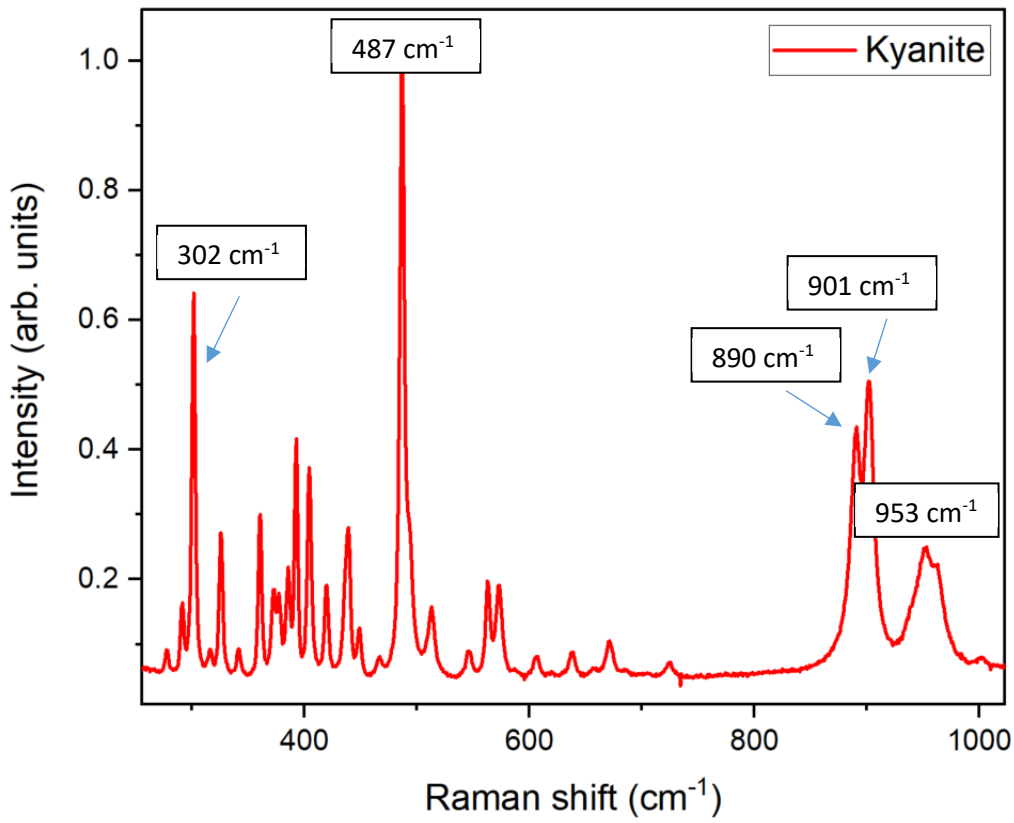

Figure 4.9 Raman spectra of a partially exposed kyanite inclusion

Rutile

Rutile inclusions are the most abundant inclusion in the Dora-Maira pyrope megablasts. Their size can range from a few to several hundred micrometres; they usually appear as single crystal although they can locally form inclusion clusters made of several grains. Most of the rutile inclusions display brownish colour and rounded shape that in some cases can appear as a strongly oblate ellipsoid (Figure 4.10 A). A few rutile inclusions show idiomorphic or sub-idiomorphic (prismatic) shape and appear as transparent in colour (Figure 4.10 B). Inside the garnet megablasts rutile can also occur as thin needles following a specific arrangement along the crystallographic planes of garnet, that could suggest an exsolution origin of TiO_2 lamellae (Figure 4.10 C).

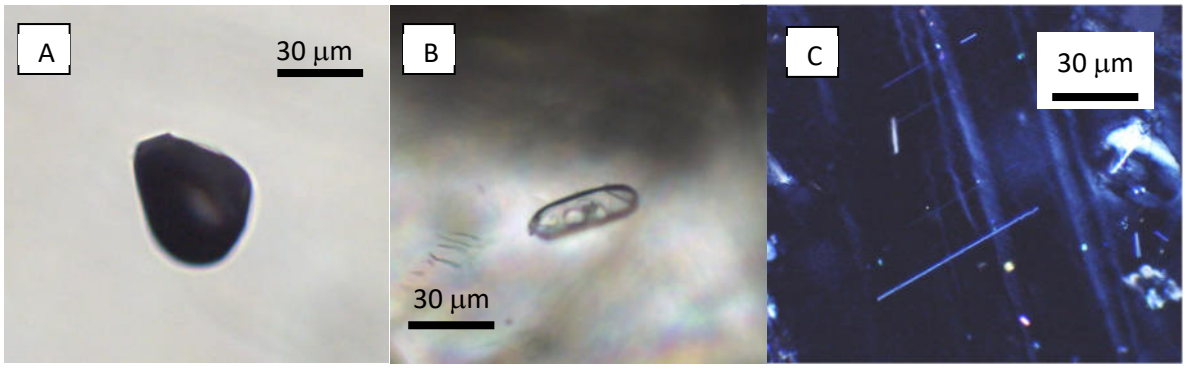

Figure 4.10. Rutile occurrences within garnet megablasts. (A) The most common occurrence of rutile is in the form of brownish rounded inclusion. (B) Example of a rare transparent sub-idiomorphic rutile inclusion. (C) Needles of rutile exsolution from the garnet structure.

Figure 4.11 reports the Raman spectra of a rutile inclusion within garnet with indicated the wavenumbers of the main Raman peaks. Note that the peak broadening of rutile phonon modes seems to be related to a strong phonon mode anharmonicity in rutile and to the presence of impurity elements such as Nb (Lan et al., 2012).

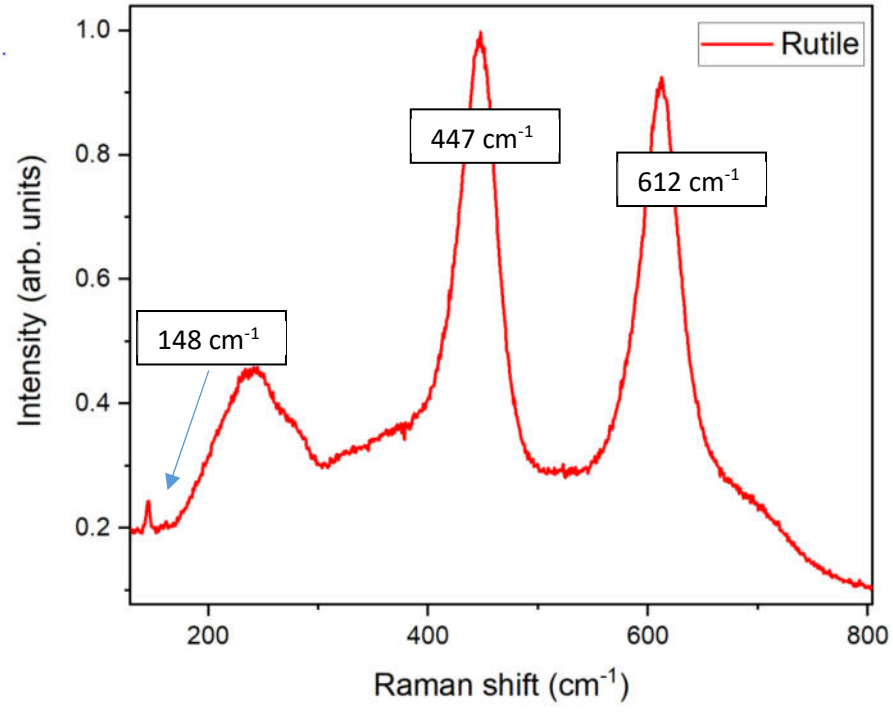

Figure 4.11 Raman spectrum of a partially exposed rutile inclusion. Note that the broad peak around 250 cm-1 is a second order effect and not a proper phonon mode of the crystal

Coesite

Coesite inclusions can be of different size, ranging from few to several hundreds of micrometres in size. The small ones are, on average, best preserved and optically they can appear as single pristine crystals. More frequently, large coesite inclusions display the typical palisade texture associated with impressive radial cracks of the garnet host (Figure 4.12).

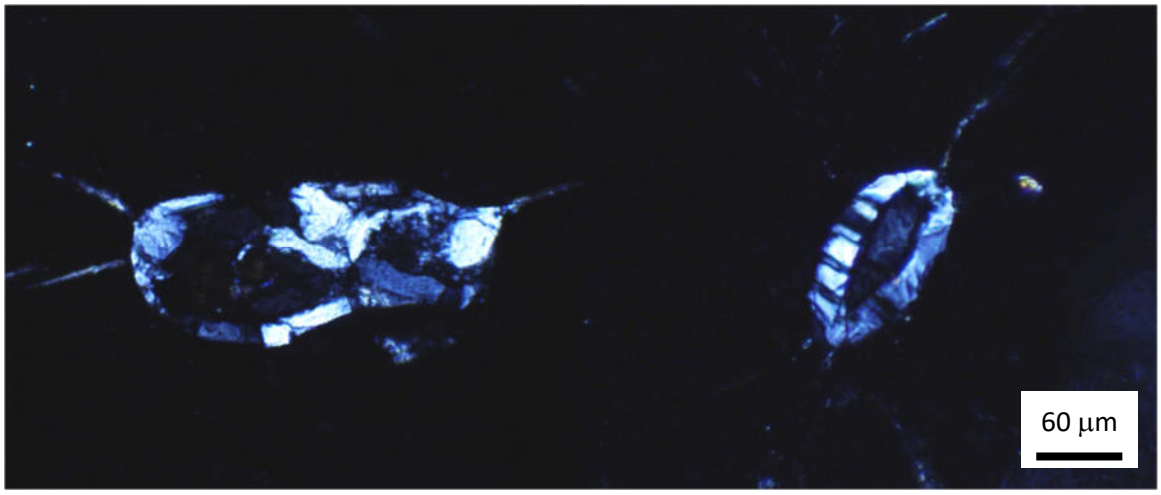

Figure 4.12. Example of coesite inclusions in garnet showing the typical palisade structure and radial cracks in the surrounding host due to the volume expansion of the inclusion during phase transition

In these domains, described for the first time in these rocks by Chopin (1984), coesite is partially preserved at the core of the inclusion structure with a higher relief with respect to the surrounding phase constituting the so-called palisade structure. Such palisade structures, can be easily recognized at the optical microscope by the typical partitioning of the optical extinction under cross-polarized light and consist of elongated quartz aggregates.

Coesite inclusions can be found mainly within the small garnets (i.e. garnet neoblasts) of the *SiO_2-saturated* whiteschists domains.

Within the garnet megablasts, coesite is less abundant and occurs only at the garnet rim. The best way to identify coesite is by means of Raman spectroscopic measurements. Figure 4.13 reports the Raman spectra of a coesite inclusion within a garnet.

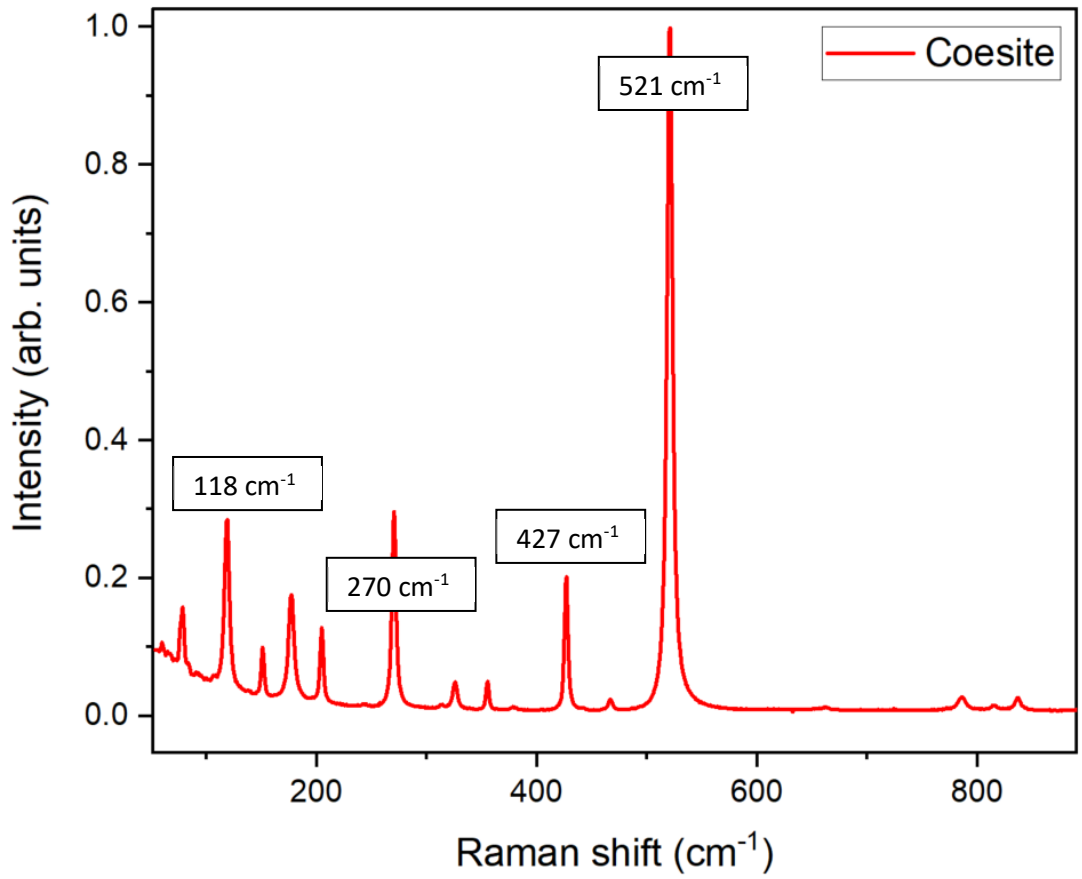

Figure 4.13 Raman spectrum of a partially exposed coesite inclusion

Raman spectroscopic measurements performed on single-crystal, apparently untransformed coesite inclusions revealed, despite the optical aspect, an incipient transition and retrogression from coesite to quartz of these crystals.

This interpretation is supported by the anomalous increase of the main Raman peak of quartz near 464 cm^{-1} along the rim and fractures of the inclusion (Figure 4.14).

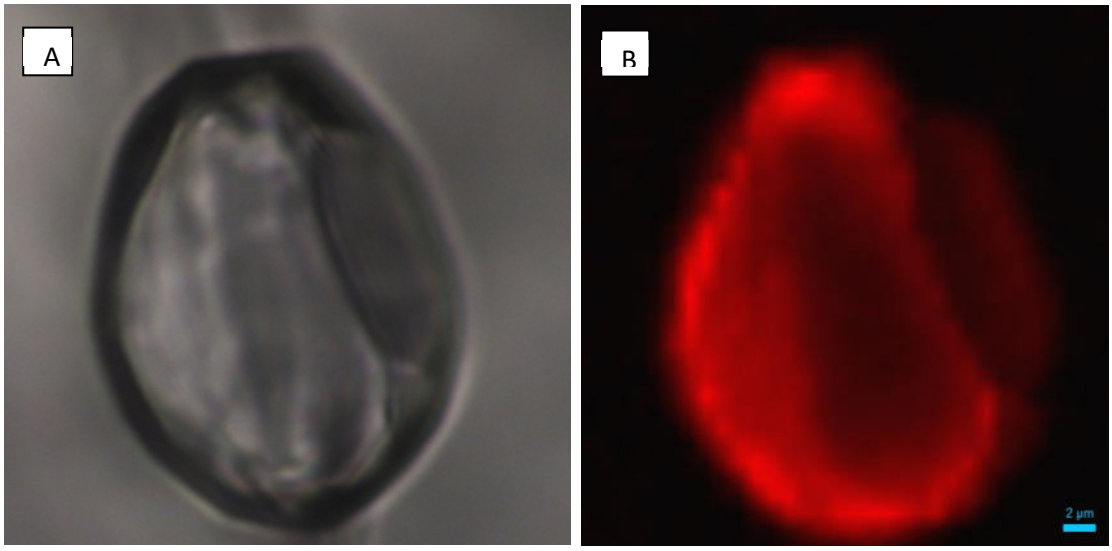

Figure 4.14. Single coesite inclusion, optically unperturbed, can show an anomalous increase in the Raman peak near 464 cm^{-1} along the rim and fractures probably due to the incipient retrogression from coesite to quartz.

An important feature of coesite inclusions is the presence of anomalous birefringent haloes in the adjacent surrounding host as shown in Figure 4.15.

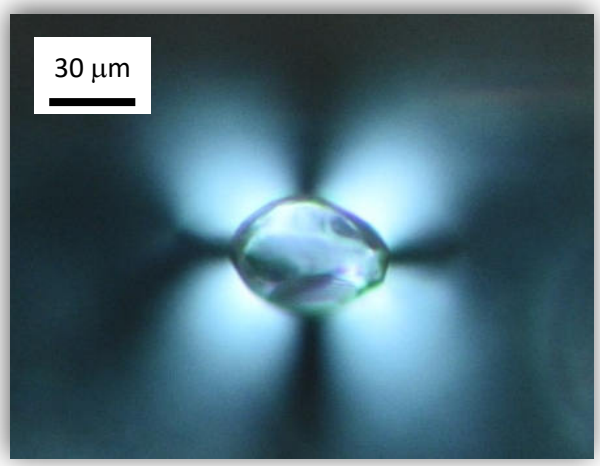

Figure 4.15 Coesite inclusion showing birefringent haloe in the surrounding host.

These birefringent haloes are the result of the contrast in physical properties between the host and the inclusion. At the optical microscope it appears in the form of a birefringent rosette where the cross shaped extinction pattern is controlled by the orientation of the microscope polarizers. These birefringent haloes have been largely used and characterized

in the literature (e.g. Howell, 2012) since they can give complementary information on the host-inclusion stress field and are used to identify potential inclusions to use for thermobarometric applications. In this thesis they represent the subject of a new Raman spectroscopy approach to determine and map strain fields in optically anomalous crystals, which I describe in Chapter 7.

Zircon

Zircon inclusions, the second in order of abundance after rutile, are widespread across the entire volume of both garnet megablasts and neoblasts; the inclusions range in size from a few to 500 micrometres in diameter, showing a high relief and transparent colour. Zircon inclusions display variable shape: from sphere-like to ellipsoidal and/or idiomorphic habits with sharp edges and corners (Figure 4.16).

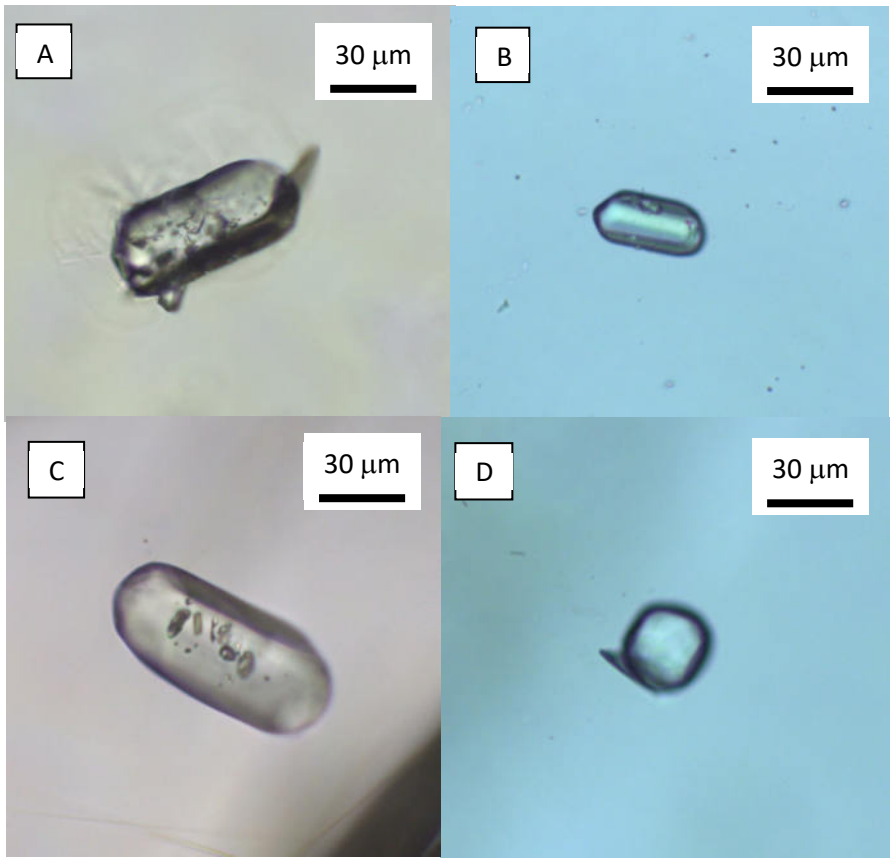

Figure 4.16. Zircon inclusions in garnet with different shape ranging from idiomorphic to spherical (from A to D respectively).

Most of them appear as single crystals, although clusters of inclusions in contact with each other can also be found. Zircon inclusions can contain brownish rutile grains and other inclusion phases such as coesite and layered silicates (see also Gautiez-Putallaz et al. 2016).

Figure 4.17 reports the Raman spectrum of a zircon inclusion. A detailed description of zircon Raman spectra relative to its structural and chemical features is provided in Chapter 6 which also provides a new protocol for the selection of reliable zircon inclusions to use for elastic thermobarometry applications.

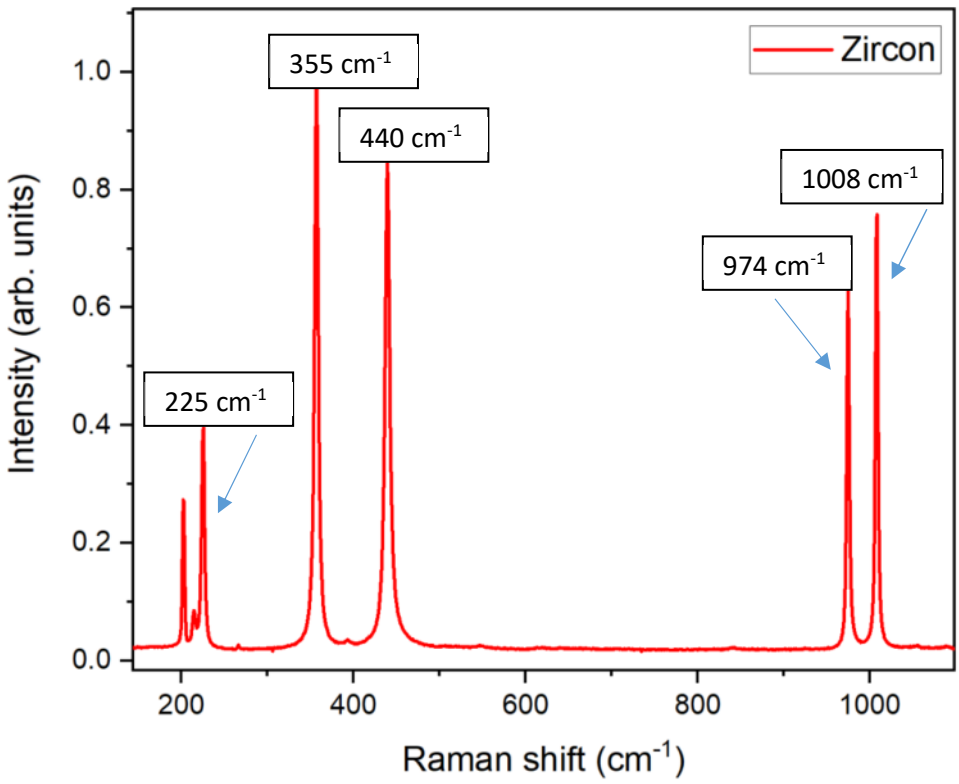

Figure 4.17 Raman spectrum of a partially exposed zircon inclusion

Also in this case, as seen for coesite inclusions, completely buried zircon inclusions display an anomalous birefringent rosette in the adjacent surrounding host (Figure 4.18).

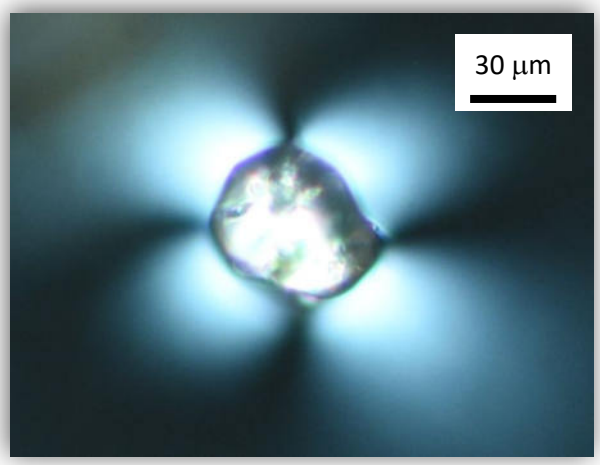

Figure 4.18 Zircon inclusion showing birefringent haloe in the surrounding host.

4.3 Phase relations and main rock-forming reactions in whiteschists

In the following, a description of the main reactions and paragenesis of whiteschists are described by thermodynamic modelling using pseudo-sections in the KFMASH system and ternary diagrams in the reduced MAS system with fluid and phengite being considered as excess phases. This computations are original and compared with petrographic observations and published results. Figure 4.19 reports the stability fields of different mineral assemblages for silica saturated and under-saturated whiteschists. Pseudo-sections have been computed by means of Gibbs free-energy minimization implemented within the software Perple_X (Connolly, 2005) with thermodynamic database from Holland and Powell (2002). The bulk chemistries used are taken from Gautiez-Putallaz et al. (2016): SiO_2 53 wt%, Al_2O_3 26 wt%, FeO 3.5 wt%, MgO 14 wt% and K_2O 6.6 wt% for silica undersaturated whiteschists and SiO_2 76 wt%, Al_2O_3 13 wt%, FeO 1.75 wt%, MgO 7 wt% and K_2O 3 wt% for silica saturated whiteschists. Water has been considered in excess in both cases.

The main result is that in Si-rich whiteschists, quartz and / or coesite are ubiquitous over all the considered P-T range while in Si-poor whiteschists quartz is completely consumed at relatively low P and T to appear again in the form of coesite only at UHP conditions.

This is in agreement with the experimental results of Hermann (2003) and with the fact that in garnet megablasts from Si-poor whiteschists no quartz inclusions have been found while it is possible to find coesite inclusions only along their external rims. A coesite inclusion has been found at the rim of a garnet megablast from the Martiniana outcrop. The absence of quartz in garnet megablasts can be explained as the consequence of the difference in the local bulk chemistry of the rocks.

This issue is clarified in the ternary MgO-Al_2O_3-SiO_2 compatibility diagrams of Figure 4.20, calculated here to explain the different parageneses (see Fig. 4.19) developed in whiteschists as a function of their SiO_2-saturated and undersaturated bulk compositions. In Figure 4.19 the mineral assemblages developed at about 16 kbar and 600 °C in both Si-rich and Si-poor whiteschists consist of *chlorite* + *kyanite* + *quartz* (blue area in Figure 4.20). After this stage, along the prograde P-T path, talc forms in both chemical systems.

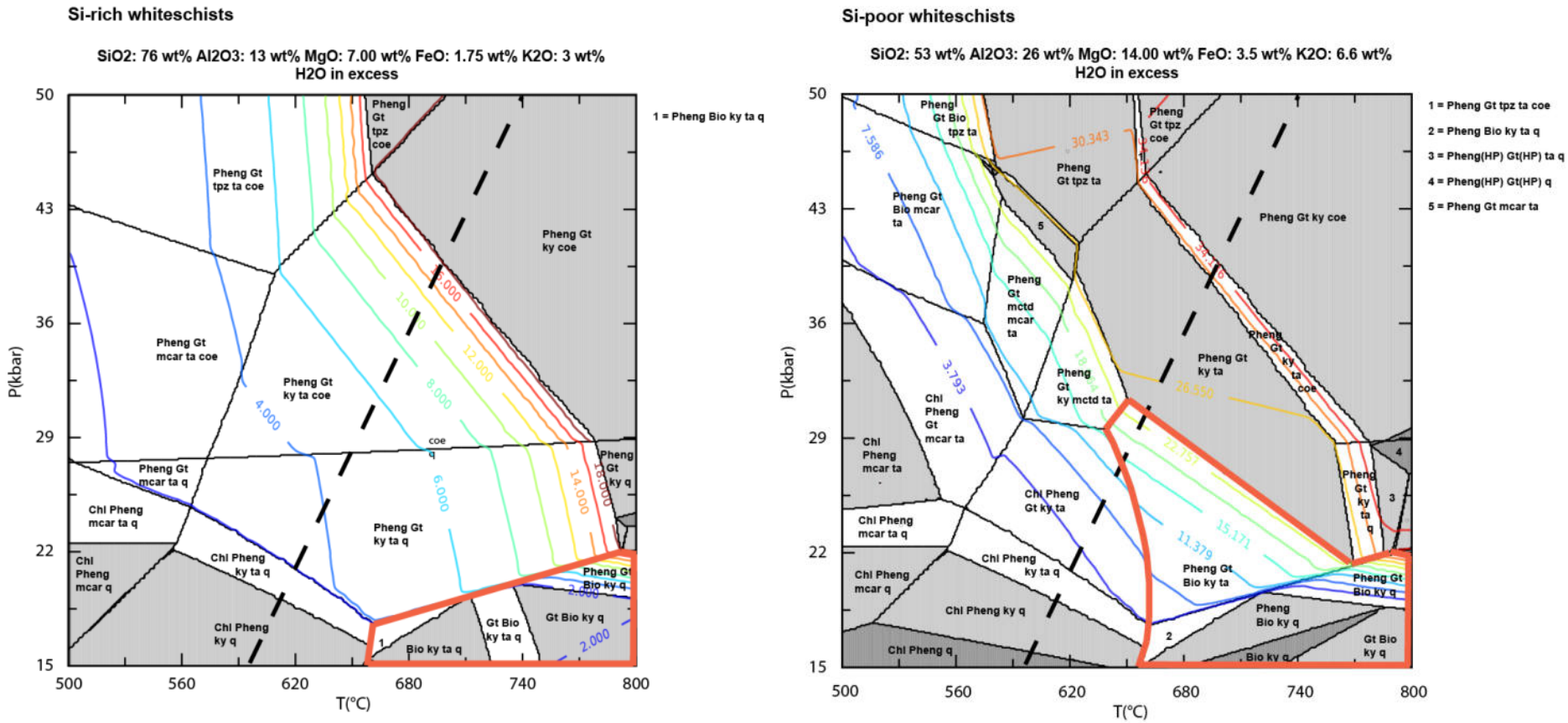

Figure 4.19. Pseudosection modelling of Si-rich (to the left) and Si-poor (to the right) whiteschists with highlighted the biotite stability field (Bio, in red) and the coloured iso-lines indicating the modal amount of garnet. Black dashed line is the indicative P-T trajectory showing changes in mineral assemblages in the whiteschists.

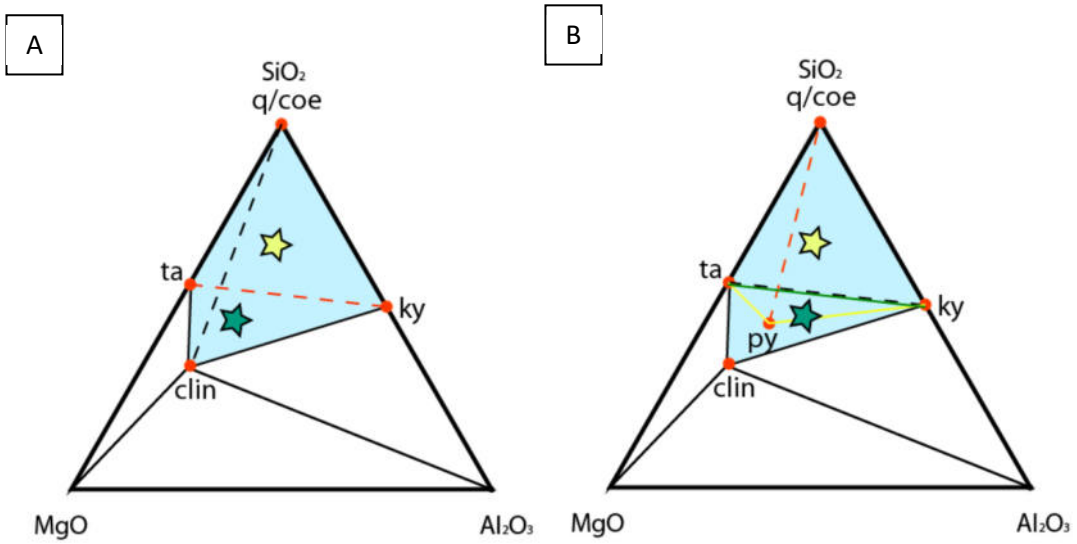

Figure 4.20. Indicative chemography in the simplified MASH system showing the differences in the mineral assemblages due to two different starting bulk chemistry (stars for Si-rich and Si-poor whiteschist). Dashed lines represent the minerals involved in metamorphic reaction (in red the reaction products and in black the reactants). Clin = clinochlore (chlorite).

The compatibility diagram (Figure 4.20 A) clearly displays that talc formation occurs by the reaction:

quartz + chlorite → talc + kyanite (+ fluid in excess)

Schreyer (1988) described this reaction as the index reaction for the whiteschists formation. In the Si-rich whiteschists (yellow star in Fig. 4.20) the reaction took place until chlorite (the less abundant reactant) was fully consumed. Differently, in Si-poor whiteschists (green star) the reaction took place until quartz was consumed. The different bulk compositions thus led to formation of two parageneses: one consiststing of *quartz + talc + kyanite* in the Si-rich whiteschists and another consisting of *talc + chlorite + kyanite* in the Si-poor variety (Figure 4.20 A).

As a consequence, the garnet-forming reactions have been different in the Si-rich and in the Si-poor whiteschists (Figure 4.20 B). In the first case, garnet enters into the system by the forming reaction:

kyanite + talc → pyrope + coesite (+ fluid in excess)

that proceeded until complete consumption of talc. Experimental results suggest that in the MASH system this reaction takes place at UHP conditions (Schreyer, 1988; Hermann, 2003) since talc and kyanite have a large stability field.

Nevertheless, following the proposed P-T path in the computed pseudo-sections (KFMASH system), garnet starts growing at lower pressure. Note that the robust formation of garnet (i.e. its modal amount) is restricted only at UHP conditions over the quartz-coesite phase boundary. This could be a good point in interpreting the origin of garnet neoblasts displaying inclusions of coesite also at the garnet-core**.**

The compatibility diagram for Si-poor whiteschists, suggests that the most likely reaction forming the garnet megablasts was:

chlorite + kyanite + talc → pyrope (+ fluid in excess)

that proceeded until chlorite was fully consumed, leading to a *kyanite + talc + pyrope* assemblage (delimited above by the green line in Figure 4.20 B). In this case the reaction generated up to 15 vol% garnet below the quartz-coesite phase boundary (see Figure 4.19-B) covering an important role at lower pressure with respect to the reaction that occurred in the Si-rich whiteschists. It is interesting to note that once the Si-poor whiteschists reached UHP conditions, talc was no longer stable with kyanite and reacted with it to produce pyrope and coesite according to the same reaction described above for the Si-rich whiteschists (see Figure 4.19-B and 4.20-B). Therefore, in the MASH system, the garnet forming reactions in Si-poor whiteschists are two rather than one. This evidence could explain formation of large amounts of garnet during the prograde evolution of the Dora-Maira whiteschists resulting in the

formation of impressive megablast clusters and also that, in the pyrope megablasts, coesite inclusions only occur in the outer rim.

In general, the character of the reactions represent the process governing the chemical zonation of garnet, mainly recorded in Si-rich whiteschists domains. As an indicative example,

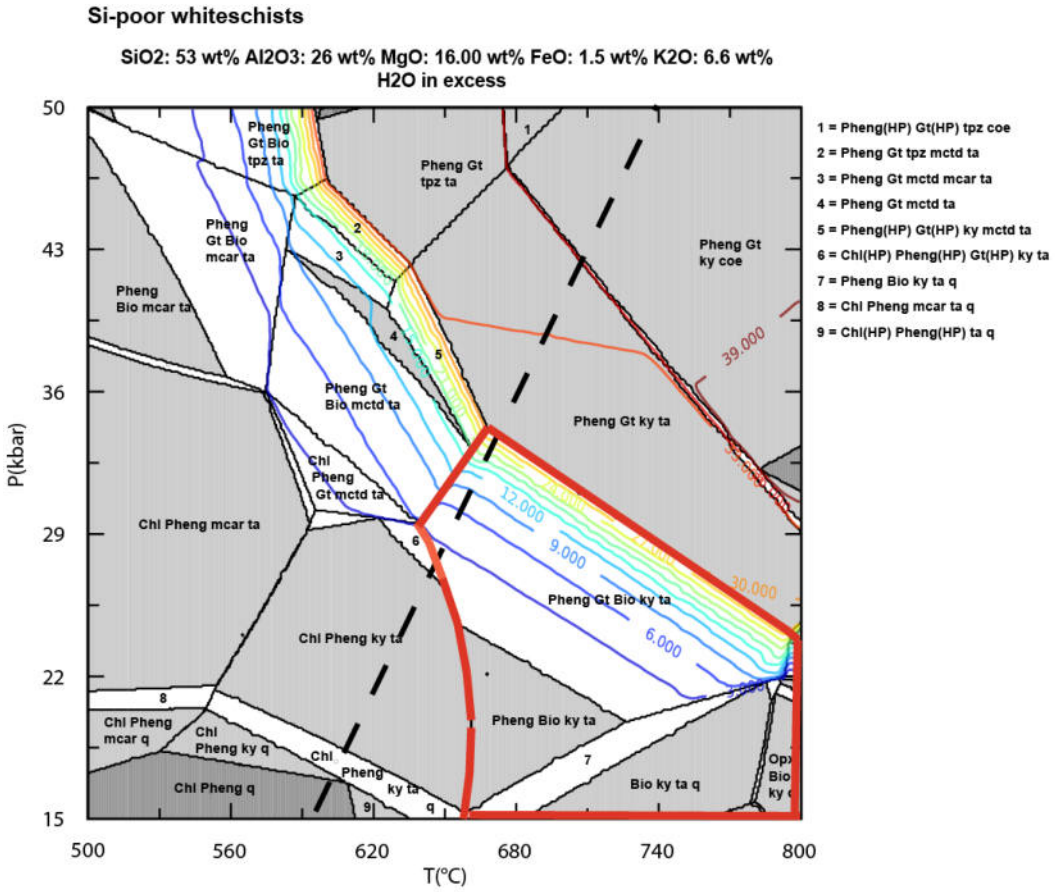

Figure 4.21. Pseudosection modelling of a Si-poor whiteschists with enriched Mg composition. Black dashed line is the indicative P-T path by Gautiez-Putallaz et al. (2016).

Figure 4.21 reports the effect of decreasing Fe content in the bulk chemistry of a Si-poor whiteschist, resulting in an almost ideal KMASH system (i.e. MgO = 16 wt% and FeO = 1.5 wt% respectively).

The major effects of Fe-deficiency are a shift of the garnet stability field to higher pressure conditions that is coupled with an even more significant increase in its modal amount. Indeed, garnet passes through an indicative initial value of 6 vol% to a value of about 30 vol% in a range of pressure between 30 to 36 kbar. The calculation of garnet isopleths shows that this increment of garnet abundance corresponds to garnet compositions close to pure pyrope (from 0.1 to 0.07% in almandine mole fraction).

A further difference between Si-rich and Si-poor whiteschists is represented by the stability of biotite (Bio), highlighted in red in Figure 4.19. While in the Si-rich variety biotite is not involved in the rock forming reactions, it can cover an important role in Si-poor whiteschists, where its stability field expands across higher pressure conditions intersecting the indicative P-T path followed by these rocks.

The biotite-forming reaction within the KFMASH system is:

Phengite + chlorite → biotite + talc + kyanite (+ fluid in excess)

These product minerals occur as solid inclusions within garnet megablasts. However, at high pressure biotite is no longer stable and breaks down through the garnet-forming reaction:

Biotite + talc + kyanite → phengite + garnet (+ fluid in excess)

in good agreement with natural occurrences where biotite has been found only within core-mantle regions of garnet megablasts. No biotite inclusions appear along the garnet rim (see also Hermann, 2003). In this regard, such results can be interpreted as responsible for the large modal amount of rutile inclusions in garnet megablasts. Indeed, biotite can be a good carrier of TiO_2 during metamorphism.

Finally, it must be pointed out that the most important reaction in whiteschists is the one involving the continuous exchange between celadonite and muscovite phase components within phengite in equilibrium with garnet and coesite:

Kyanite + *celadonite* → *coesite* + *muscovite* + *pyrope*

This exchange-reaction occurs along a large P range and, different from the dehydration reactions presented above, is a water-preserving reaction. Indeed the major uncertainty in constraining the P-T position of dehydration univariant lines arises from the difficulty in constraining the activity of water. However, this last reaction occurs under fluid-absent conditions, thus making its application useful to ascertain UHP conditions (See Hermann et al. 2003). In this regard, Hermann (2003) provided by means of selected new experimental results a calibration of the phengite-barometer using the Si content (i.e. celadonite molecule) of phengite solid solution as a function of pressure. Coupling the experimental results with the composition of natural phengite, Hermann (2003) firstly proposed diamond-facies conditions for the metamorphic peak of the Dora-Maira whiteschists.

4.4 Sample preparation and inclusion selection for elastic thermobarometry purposes

This section reports the specific methodology used for the selection of solid inclusions to use for elastic thermobarometry applications.

Sample collection and preparation

Sample collection has been focused mainly on the garnet megablasts and neoblasts of whiteschists from the UHP Brossasco-Isasca unit.

Rock fragments and garnet megablasts, when possible, have been collected taking into account their original orientation with respect the foliation of the rock.

Each collected garnet megablast has been cut in several slices each of which has been carefully polished using diamond paste (Figure 4.22 A).

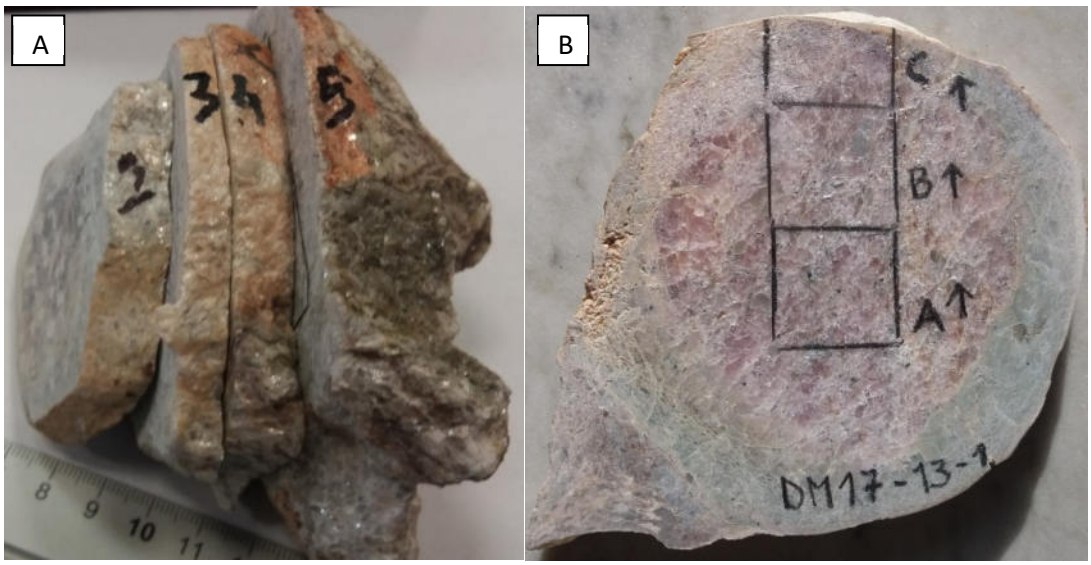

Figure 4.22 A) Garnet megablast cut in several slices. B) Selected portion from core to rim of a garnet slice for thin section preparation.

Afterward, using a stereoscopic microscope, the selection of well-preserved portions of garnet megablast has been performed. These portions show the lowest degree of retrograde transformation and the lowest level of garnet fracturing. Indeed, one of the main issue in the elastic thermobarometric method is the presence of fracture or any other kind of discontinuity that can potentially influence the residual stress in the inclusion (Zhang, 1998; Mazzucchelli et al., 2018). For each garnet megablast, the selected portions have been chosen and carefully oriented in order to spatially cover the entire volume of the garnet megablast along its equatorial plane from core to rim (Figure 4.22 B).

Finally, at least one (in some cases also two or three) thick polished section was prepared of each garnet portion. These sections were prepared starting from 200-250

to 500 μm thickness in order to obtain the largest possible of safely isolated inclusions.

Inclusion selection

The selection of reliable solid inclusions has been carried out by means of optical polarized microscopy and Raman spectroscopy.

The prerequisite for each inclusion is that, as stated above, it has to be isolated from any kind of discontinuity (i.e. fractures, section surfaces, other inclusions). In more quantitative terms (Zhang, 1998; Mazzucchelli et al., 2018), the inclusion must be isolated from other surfaces by at least 3 times the inclusion radius (or the longer axis for non-spherical inclusions). Furthermore, each selected inclusion must be single crystal and well crystalline with a homogeneous composition across the entire grain volume. For instance, inclusion such as pyroxenes, amphiboles or any other inclusion that can display a large range of chemical substitution (i.e. solid solution) should be avoided or carefully selected. This is because the position of Raman peaks, representing the frequency of vibration of each phonon mode, expressed in wavenumber, depend also on mineral composition. In the case of this study, solid inclusions such as coesite, rutile, zircon and so on, usually, display a very short or absent degree of chemical mixing with other isomorphous phases and then, the change in the Raman shift due to this effect is negligible. The only available, and largely used, inclusion presenting a usually small but significant degree of chemical mixing is zircon. Hf replacing Zr in the dodecahedral site of the zircon structure is a typical example. Chapter 6 discuss in detail this problem and shed light also on other important factors that can strongly influence Raman spectra of zircon inclusions such as metamictization and inherited structural heterogeneity, suggesting a protocol for the selection of reliable zircon inclusion to use for elastic thermobarometric purposes.

Table 4.3 reports, as a reference, the bulk moduli and thermal expansion coefficients of the main mineral inclusions (taken from Holland and Powell, 2011).

Table 4.3

Mineral phase	K_0 (GPa)	α ($\cdot 10^{-4}$)
coesite	97.9	0.12
zircon	230	0.12
kyanite	160	0.19
rutile	222	0.22
pyrope	174.3	0.24

Chapter 5

How host-inclusion geometry and anisotropy affects *residual pressure* estimates

This chapter reports the results and discussions from the published paper:

Campomenosi, N., Mazzucchelli, M. L., Mihailova, B., Scambelluri, M., Angel, R. J., Nestola, F., Reali, A., Alvaro, M. (2018) *How geometry and anisotropy affect residual strain in host-inclusion systems: coupling experimental and numerical approaches.* American Mineralogist, 103, 2032-2035.

Original Abstract

Raman spectroscopy provides information on the residual strain state of host-inclusion systems that, coupled with the elastic geobarometry theory, can be used to retrieve the P-T conditions of inclusion entrapment. In-situ Raman measurements of zircon and coesite inclusions in garnet from the Ultrahigh-pressure Dora Maira Massif show that rounded inclusions exhibit constant Raman shifts throughout their entire volume. In contrast, we demonstrate that Raman shifts can vary from the center to the edges and corners of faceted inclusions. Step-by-step polishing of the garnet host show that the strain in both rounded and prismatic inclusions is gradually released as the inclusion approaches the free surface of the host. More importantly our experimental results coupled with selected numerical simulations demonstrate that the magnitude and the rate of the strain release depends also on the contrast in elastic properties between the host and the inclusion and on the inclusion crystallographic orientation with respect to the external surface. These results allowed us to give new methodological guidelines for determining the residual strain in host inclusion systems.

5.1 Introduction and motivation

Models for elastic thermobarometry only apply to the simple case of elastically isotropic host-inclusion pairs with a simple ideal geometry where a small spherical inclusion is trapped within an infinite host (Angel et al., 2015). Recent numerical models showed that any deviations from this idealized geometry can significantly affect the estimation of "residual pressure" (Mazzucchelli et al., 2018). Indeed, strain gradients in non-spherical inclusions have been already reported (e.g. Zhukov and Korsakov, 2015; Murri et al., 2018). Moreover, several studies pointed out the effects on the residual "pressure" determination of the inclusion size and its partial exposure with respect to the mineral host surface (e.g. Rosenfeld and Chase, 1961; Enami et al., 2007; Zhang, 1998; Mazzucchelli et al. 2018). Nevertheless, open questions still remain, including:

1) what is the effect of the inclusion anisotropy on the residual strain release?

2) How much can the contrast in properties between the host and the inclusion and their geometry influence the residual strain?

Therefore, as an alternative way to test the effect of the geometry of the host-inclusion system on the Raman signal and on the calculated residual pressure, it is proposed to collect spectra from selected inclusions with different shape, size and crystallographic orientation, while performing several steps of polishing of the rock thick section to bring the inclusion closer to the external surface of the host.

This Chapter reports the effects on the Raman spectra of rounded and elongated zircon inclusions and a rounded coesite inclusion in pyrope from the ultrahigh-pressure (UHP) unit of the Dora-Maira Massif measured before and after several subsequent steps of polishing. The measured "*residual pressures*" are then compared with the results of a selected set of Finite Element models following the approach of

Mazzucchelli et al. (2018). This work provides new methodological guidelines and examples of correction curves to adjust measurements carried out on faceted and anisotropic inclusions and/or close to the host surface.

5.2 Specific methodology: the *step-by-step* polishing approach

As pointed out previously (Zhang, 1998; Mazzucchelli et al., 2018), only small isolated inclusions far from any free surface of the garnet thick sections (e.g. distance > 3 radii of the inclusion) do not suffer potential strain release. Therefore, for this study, as described above, polished sections of 250-260 μm thickness have been prepared. Raman spectroscopic measurements were carried out only on inclusions at the center of the section with a mean linear dimension smaller than 50 μm, (i.e. considerably less than the distance to the host surface). The selected inclusions all show a characteristic birefringent halo (Figure 5.1) within the surrounding host which is given by the stress field that the inclusion is transmitting to the host walls (see Chapter 7 for more details).

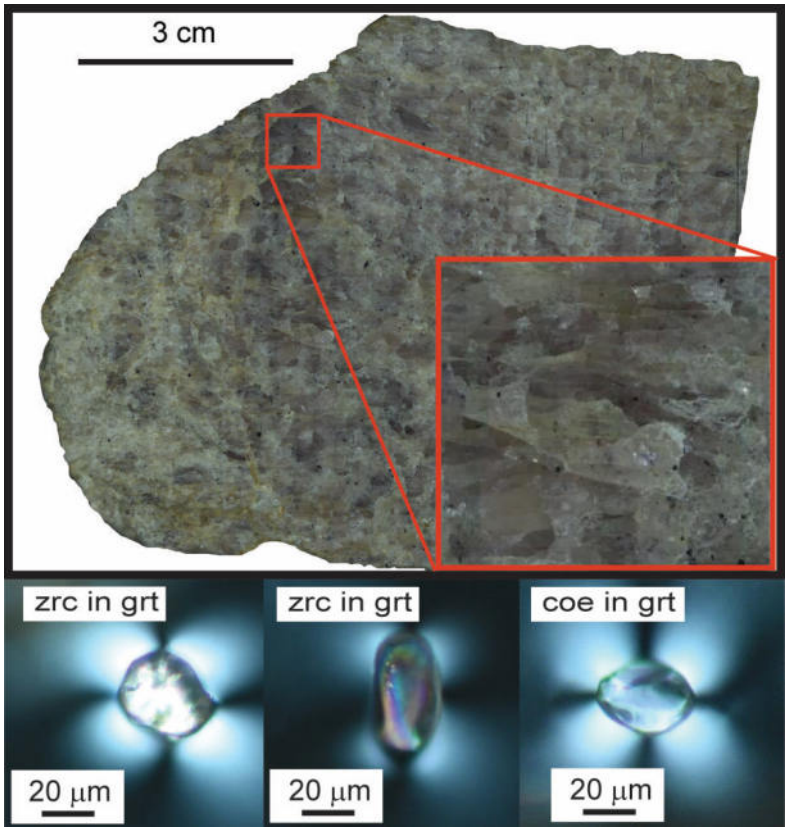

Figure 5.1. A polished pyrope megablast section with partial talc + chlorite alteration along fractures and rims. The red square shows an example of a mm-sized fracture-free garnet area selected for this study, in which zircon and coesite crystalline inclusions exhibiting strain-induced birefringent haloes in the surrounding host have been found.

Micro-Raman scattering measurements and processing were conducted as reported in Chapter 2. Furthermore, in this case of study, for each inclusion, a series of spot measurements were carried out along the equatorial plane of the inclusion.

Raman spectra were collected before and after polishing steps of the garnet hosts by known amounts. The inclusion distance from the surface (i.e. the distance between the equatorial plane of the inclusion and the host external surface) was estimated by means of optical focus coupled with the controlled z-position motorized microscope stage. The polishing and measuring cycle was repeated until the inclusion was half-exposed. In this way, it was possible to observe the "real time" evolution of the strain inside the inclusions in terms of changes in the Raman wavenumbers. This chapter

reports the examples of single crystals of zircon: one rounded (~20 μm radius) and one prismatic (~80 μm along the long axis), labelled S2 and S3, respectively and one rounded single crystal of coesite (~15 μm radius, sample S24) in the garnet megablasts and neoblasts, respectively. No prismatic or idiomorphic coesite inclusions have been found. Since these inclusions are elastically anisotropic, their orientation with respect to the polishing surface is critical for the interpretation of the results by means of numerical simulations. The idiomorphic zircon grain S3 has the *c* axis inclined with respect to the polishing surface by approximately 20° (estimated optically). Analysis of the peak intensities in the polarized Raman spectra suggests that the rounded zircon grain S2 has its *c* axis almost perpendicular to the surface. The coesite crystal S24 was rounded and the absence of pronounced changes in the Raman intensities measured in different scattering geometries makes it impossible to determine its orientation and therefore it was not possible to perform numerical simulations for this inclusion.

Finite element simulations have been carried out to support the measurements of zircon inclusions S2 and S3 and to evaluate the effect of the proximity of the inclusion to the external surface of the thick section on the residual strain of the inclusion (technical details are given in Mazzucchelli et al., 2018). Elastic anisotropy has been incorporated in the model for the zircon inclusions. We have used a commercially available engineering package, Abaqus Standard v.2016 (Dassault Systèmes, Simulia, Providence), to create and analyze 3D finite-element models following the same procedures outlined in Mazzucchelli et al. (2018). The models reproduce the geometry and the crystallographic orientations of our zircon inclusions in pyrope (samples S2 and S3), at several steps of distance of the inclusion from the external surface of the host.

All of our 3D models have at least one mirror plane, therefore only half of the selected shape was created and the full model was obtained by reflection through that mirror plane. Since the mirror plane of the model corresponds to the (1 0 0) crystallographic plane, it does not restrict the deformation of zircon that is tetragonal. The resulting model consisted of more than 400000 10-node quadratic tetrahedral elements (element C3D10 in the Abaqus library). Material properties and boundary conditions were assigned, and then a mesh convergence analysis was performed. The mesh was refined in the areas with higher stress gradients until the calculated stress distribution appeared smooth. To simulate the external pressure, face loads were applied to the 3D elements on the external boundaries of the host. Boundary conditions were placed on the appropriate edges and faces of the models to avoid rigid body rotation and translation in the x, y and z directions.

The constitutive equation used by Abaqus for anisotropic linear elasticity is:

$$\sigma_{ij} = C_{ijkl}\epsilon_{kl} \quad (5.1)$$

where σ_{ij} and ϵ_{kl} are the stress and the strain tensor respectively, and C_{ijkl} are the elastic stiffness moduli. For the zircon inclusion the elastic stiffness moduli at room conditions reported by Ozkan et al. (1974) were used in FE analysis (Table 5.1). The pyrope host was treated as isotropic because its universal anisotropic index (Ranganathan and Ostoja-Starzewski, 2008) is only 9 x 10^{-4}, essentially zero, based on the elastic moduli reported by Sinogeikin and Bass (2002). The isothermal bulk modulus at room conditions was derived from Milani et al. (2015) while the shear modulus was obtained from the elastic moduli reported by Sinogeikin and Bass (2002).

Table 5.1. Elastic parameters at room conditions for zircon and pyrope used for finite element calculations

Zircon (anisotropic elastic properties)	C11	C33	C44	C66	C12	C13
	(GPa)					
	423.7	490	113.6	48.5	70.3	149.5
Pyrope (isotropic elastic properties)	K_{0T} (GPa)				G_{0T} (GPa)	
	163.7				94.0	

The use of isotropic elastic properties for the host allows us to neglect the mutual crystallographic orientation of the host and the inclusion. For the purposes of this work, the only relevant orientation is that of the inclusion with respect to the surface of the petrographic section.

5.3 Selection rules for phonon modes in zircon and coesite

Zircon has tetragonal symmetry with space group $I4_1/amd$. According to group theory analysis, the optic phonons at the Brillouin-zone center of zircon are (Kroumova et al., 2003):

$$\Gamma_{opt} = 2A_{1g} + A_{1u} + A_{2g} + 3A_{2u} + 4B_{1g} + B_{1u} + B_{2g} + 2B_{2u} + 5E_g + 4E_u$$

The A_{1g}, B_{1g}, B_{2g} and E_g modes are Raman-active and therefore a total of 12 Raman peaks can be observed in the spectrum of a randomly oriented zircon.

According to previous experimental results (Knittle and Williams, 1993; Binvignat et al., 2018) the B_{1g} mode near 1008 cm^{-1}, the A_{1g} mode near 975 cm^{-1} and the E_g mode near 357 cm^{-1} are the most pressure-sensitive peaks. For this reason, our discussion is mainly focused on these vibrational modes. Note that the B_{1g} modes are symmetry allowed in $\bar{y}(xx)y$ scattering geometry (Porto's notation), A_{1g} in $\bar{y}(xx)y$, $\bar{y}(zz)y$, and $\bar{z}(xx)z$, whereas E_g in $\bar{y}(xz)y$, with x, y, z along the a, b and c crystallographic axes, respectively.

Coesite is a monoclinic crystal with space group *C*2/*c* (unique axis *b*). The irreducible representation of the optical vibrations is (Kroumova et al., 2003):

$\Gamma_{opt} = 16A_g + 18A_u + 17B_g + 18B_u$

The A_g and B_g modes are Raman-active and therefore a total of 33 Raman peaks can be theoretically observed in the spectrum of a randomly-oriented coesite crystal. Experimental results by Hemley (1987) suggest that the A_g mode near 119 cm^{-1}, near 183 cm^{-1} and near 521 cm^{-1} are the most pressure-sensitive Raman peaks and they were used as our "sensors" for the polishing effect in coesite. However not all of the peaks predicted by group theory were observed in our spectra because of their weak intensities or because of partial overlap with the main garnet peaks.

5.4 Results and discussion

Both rounded and idiomorphic inclusions close to the center of the section display Raman peak positions shifted toward higher wavenumbers compared to free reference crystals. Within the instrumental precision (±0.35 cm^{-1}), the rounded zircon inclusion S2 and the rounded coesite inclusion S24 showed no spatial variation of the Raman peak positions within the inclusions. On the other hand, for idiomorphic crystals (zircon inclusion S3 with well-developed corners and edges) there is a steady increase in the peak positions of about 1 cm^{-1} from the center towards the edges of the inclusions (Figure 5.2).

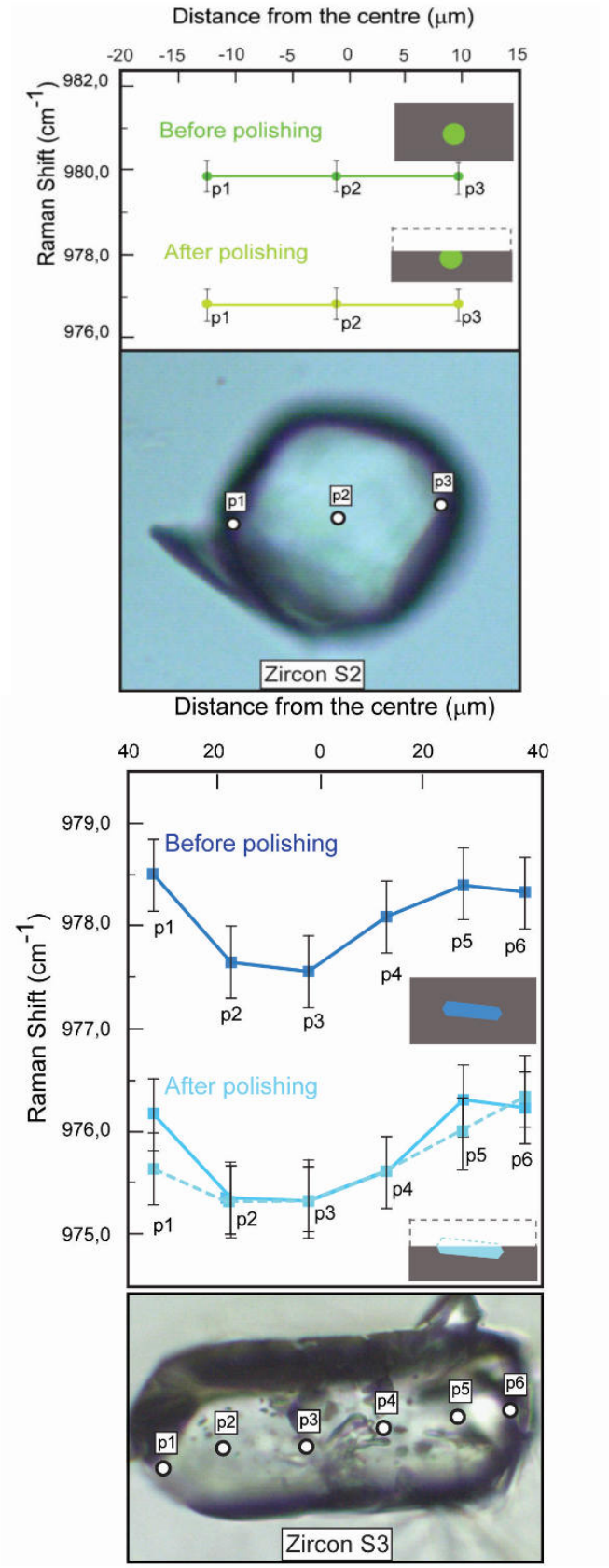

Figure 5.2. Position of the Raman peak A_{1g} ~ 975 cm^{-1} in a rounded (top) and an idiomorphic (bottom) zircon crystal before and after the final step of polishing. The solid lines in the plots are guides for the eye; the dashed line in (bottom) traces the data points measured after two days of final exposure of the grain.

This is a direct consequence of strain heterogeneity in the inclusion, which can be caused by chemical zonation, zoned radiation-induced damage and/or an imposed strain gradient. The substitution of elements such as Th, U, or Hf for Zr, may cause expansion (U, Th) or contraction (Hf) of the zircon unit cell (Nasdala et al., 1998), leading to a change in the phonon wavenumbers. However, compositional analysis of the exposed grain performed after the final step of polishing did not reveal any chemical zonation (see Table 5.2).

Radioactive decay of elements such as U and Th can induce structural damage, leading to Raman peak broadening and a shift towards lower wavenumbers (e.g. Binvignat et al., 2018). However, the full-width-at-half-maximum (FWHM) of a given phonon mode for totally entrapped S3 remains the same throughout the entire grain and within the instrumental spectral resolution and is equal to that of well crystalline zircon (Binvignat et al., 2018), thus indicating a high degree of crystallinity throughout the entire grain bulk. Since the zircon inclusion S3 is chemically homogeneous (see Table 5.2) and well-crystalline, the variable Raman shift in it is due to its faceted shape (Eshelby, 1957), because the edges and corners act as stress concentrators (Zhang, 1998; Mazzucchelli et al., 2018). After polishing the Raman spectra of S3 became homogeneous within the fully exposed part of the sample (Figure 5.2 b), confirming that the variation in the peak position in a single crystal for all bands was caused by the shape of the crystal (Table 5.3).

A decrease in the Raman wavenumbers was measured at the center of the inclusions upon polishing for all the investigated samples of zircon and coesite. As an example, Figure 5.3a shows the B_{1g} mode near 1008 cm^{-1} measured on zircon sample S3 at three different steps of polishing. Strictly speaking, the phonon wavenumbers are directly related to the strain, rather than to the applied pressure (Murri et al., 2018;

Angel et al., 2018). Moreover, for elastically anisotropic materials the same relative volume change can be obtained by different strains, for example as induced by hydrostatic or deviatoric stress. Therefore, the commonly used direct proportionality between the Raman peak positions and residual pressure is a strongly oversimplified assumption (Murri et al., 2018). Nonetheless, if we assume that the change in Raman wavenumber ω is linear with mean stress *P* (i.e. $\frac{\partial \omega}{\partial P}$ is constant), we can introduce the normalized change in the peak position $\Delta\omega_{norm}$ as a parameter to express the relative release in "pressure" as the inclusion becomes closer to the external surface of the host during polishing:

$$\Delta\omega_{norm} = \frac{\left(\left(\omega_{I,d} - \omega_{I,0}\right)\frac{\partial P}{\partial \omega} - \left(\omega_{I,\infty} - \omega_{I,0}\right)\frac{\partial P}{\partial \omega}\right)}{\left(\omega_{I,\infty} - \omega_{I,0}\right)\frac{\partial P}{\partial \omega}} = \frac{\left(\omega_{I,d} - \omega_{I,\infty}\right)}{\left(\omega_{I,\infty} - \omega_{I,0}\right)} = \Gamma \tag{5.2}$$

Where $\omega_{I,0}$ is the wavenumber for a free crystal measured at ambient conditions, $\omega_{I,\infty}$ and $P_{I,\infty}$ are the wavenumber and the corresponding pressure for an inclusion in an infinitely large host (i.e. before the polishing, when the inclusion was far from the surface of the host), while $\omega_{I,d}$ and $P_{I,d}$ are the wavenumber measured on the inclusion and its pressure after each polishing step and associated to a specific normalized distance *d* (i.e. the distance from the inclusion center to the host external surface divided by the corresponding inclusion radius).

Table 5.2. Representative chemical analysis of zircon sample s3 and garnet megablasts and porphyroblasts from whiteschists

Mineral	Zircon						mineral	garnet megablast		garnet porphyroblasts	
p. analysis	p1	p2	p3	p4	p5	p6	p. analysis	core	rim	core	rim
oxide	(wt%)	(wt%)	(wt%)	(wt%)	(wt%)	(wt%)	oxide	(wt%)	(wt%)	(wt%)	(wt%)
Al_2O_3	0.01	0.00	0.00	0.00	0.00	0.01	SiO_2	42.50	42.85	42.14	42.83
SiO_2	32.85	32.42	32.74	32.50	32.40	31.60	TiO_2	b.d.l.	b.d.l.	0.16	0.00
P_2O_5	0.23	0.40	0.27	0.27	0.35	0.09	Al_2O_3	25.11	25.00	24.64	25.23
CaO	0.02	0.02	0.01	0.02	0.02	0.02	Cr_2O_3	b.d.l.	b.d.l.	b.d.l.	b.d.l.
MnO	0.01	0.02	0.01	b.d.l.	0.01	b.d.l.	Na_2O	b.d.l.	b.d.l.	b.d.l.	b.d.l.
Fe_2O_3	0.10	0.17	0.12	0.14	0.11	0.20	FeO	2.80	3.36	8.98	2.82
Y_2O_3	b.d.l.	0.00	b.d.l.	b.d.l.	b.d.l.	b.d.l.	MgO	28.16	28.13	23.04	28.30
ZrO_2	66.11	64.04	65.44	64.55	65.17	66.51	MnO	b.d.l.	b.d.l.	b.d.l.	0.09
Ce_2O_3	b.d.l.	b.d.l.	0.01	b.d.l.	b.d.l.	b.d.l.	CaO	0.86	0.73	1.31	0.93
HfO_2	1.49	1.64	1.45	1.43	1.52	1.69	H_2O+	b.d.l.	b.d.l.	b.d.l.	b.d.l.
PbO	b.d.l.	b.d.l.	b.d.l.	0.03	0.01	b.d.l.	H_2O-	b.d.l.	b.d.l.	b.d.l.	b.d.l.
ThO_2	0.02	b.d.l.	b.d.l.	0.03	b.d.l.	b.d.l.	Sum	99.43	100.07	100.27	100.20
UO_2	0.07	0.14	0.03	0.09	0.07	0.04					
Nd_2O_3	b.d.l.	0.02	0.03	b.d.l.	0.01	0.03					
Sum	100.91	98.87	100.10	99.07	99.68	100.19					
Occupancy	moles	moles	moles	moles	moles	moles	occupancy	moles	moles	moles	moles
Zr	3.92	3.86	3.90	3.89	3.91	4.01	Si	2.92	2.93	2.95	2.92
Hf	0.05	0.06	0.05	0.05	0.05	0.06	Al	0.08	0.07	0.05	0.08
U	-	0.01	-	-	-	-	Sum site IV	3.00	3.00	3.00	3.00
Th	-	-	-	-	-	-	Al	1.95	1.95	1.99	1.95
Y	-	-	-	-	-	-	Fe^{3+}	0.05	0.05	0.01	0.05
Al	-	-	-	-	-	-	Cr^{3+}	-	-	-	-
Ca	-	-	-	-	-	-	Sum site VI	2.00	2.00	2.00	2.00
Mn	-	-	-	-	-	-	Fe^{2+}	0.11	0.14	0.51	0.11
Fe^{3+}	0.01	0.02	0.01	0.01	0.01	0.02	Mg	2.88	2.87	2.41	2.88
Sum VIII site	3.98	3.94	3.97	3.96	3.98	4.09	Mn^{2+}	-	-	-	0.01
P	0.02	0.04	0.03	0.03	0.04	0.01	Ca	0.06	0.05	0.10	0.07
Si	3.99	4.01	4.00	4.01	3.98	3.90	Na2O	-	-	-	-
Sum IV site	4.01	4.05	4.03	4.04	4.02	3.91	Sum site VIII	3.06	3.06	3.01	3.06

Table 5.3. Raman shift heterogeneity inside one zircon single crystal

p. analysis*	B_{1g} (cm^{-1})	FWHM (cm^{-1})	A_{1g} (cm^{-1})	FWHM (cm^{-1})	E_g (cm^{-1})	FWHM (cm^{-1})
p6	1011.90(1)	5.30(2)	978.51(8)	4.84(12)	360.07(1)	7.44(8)
p5	1012.09(2)	5.61(3)	977.66(9)	5.35(16)	358.90(2)	8.07(9)
p4	1011.60(2)	6.02(3)	977.56(9)	5.34(16)	358.77(2)	7.82(9)
p3	1011.18(2)	6.18(3)	978.10(7)	5.28(12)	359.65(2)	7.30(7)
p2	1011.26(2)	6.31(5)	978.41(7)	5.15(12)	359.98(2)	7.51(6)
p1	1012.18(2)	5.72(4)	978.34(7)	4.79(11)	360.08(2)	6.94(6)

p. analysis†	B_{1g} (cm^{-1})	FWHM (cm^{-1})	A_{1g} (cm^{-1})	FWHM (cm^{-1})	E_g (cm^{-1})	FWHM (cm^{-1})
p6	1010.03(1)	5.71(3)	976.23(5)	4.86(8)	358.37(1)	7.50(2)
p5	1010.05(2)	6.38(3)	976.30(5)	5.50(8)	358.25(1)	7.77(3)
p4	1009.37(2)	5.86(3)	975.60(5)	4.97(9)	357.51(1)	7.36(2)
p3	1009.05(2)	6.63(4)	975.32(8)	5.39(16)	357.13(1)	8.08(3)
p2	1008.99(2)	6.23(4)	975.37(8)	5.23(15)	357.17(1)	7.68(4)
p1	1009.92(2)	5.92(4)	976.18(9)	4.77(14)	357.96(1)	6.78(4)

p. analysis§	B_{1g} (cm^{-1})	FWHM (cm^{-1})	A_{1g} (cm^{-1})	FWHM (cm^{-1})	E_g (cm^{-1})	FWHM (cm^{-1})
p6	1009.58(2)	6.07(5)	976.40(5)	5.39(9)	358.23(2)	7.97(8)
p5	1009.53(1)	6.50(1)	975.86(3)	5.54(5)	357.18(1)	7.75(2)
p4	1009.01(1)	6.49(2)	975.61(4)	5.87(7)	357.31(1)	8.26(3)
p3	1008.94(1)	7.34(2)	975.39(4)	6.40(7)	357.09(1)	8.86(4)
p2	1008.85(1)	7.47(3)	975.33(5)	6.32(10)	356.60(9)	8.51(3)
p1	1009.18(1)	7.25(2)	975.65(4)	6.07(7)	357.06(1)	8.14(4)

Note: the errors in bracket are referred to the fit
*Value measured before polishing
† Value mesured just after polishing
§ Value measured two days after polishing end

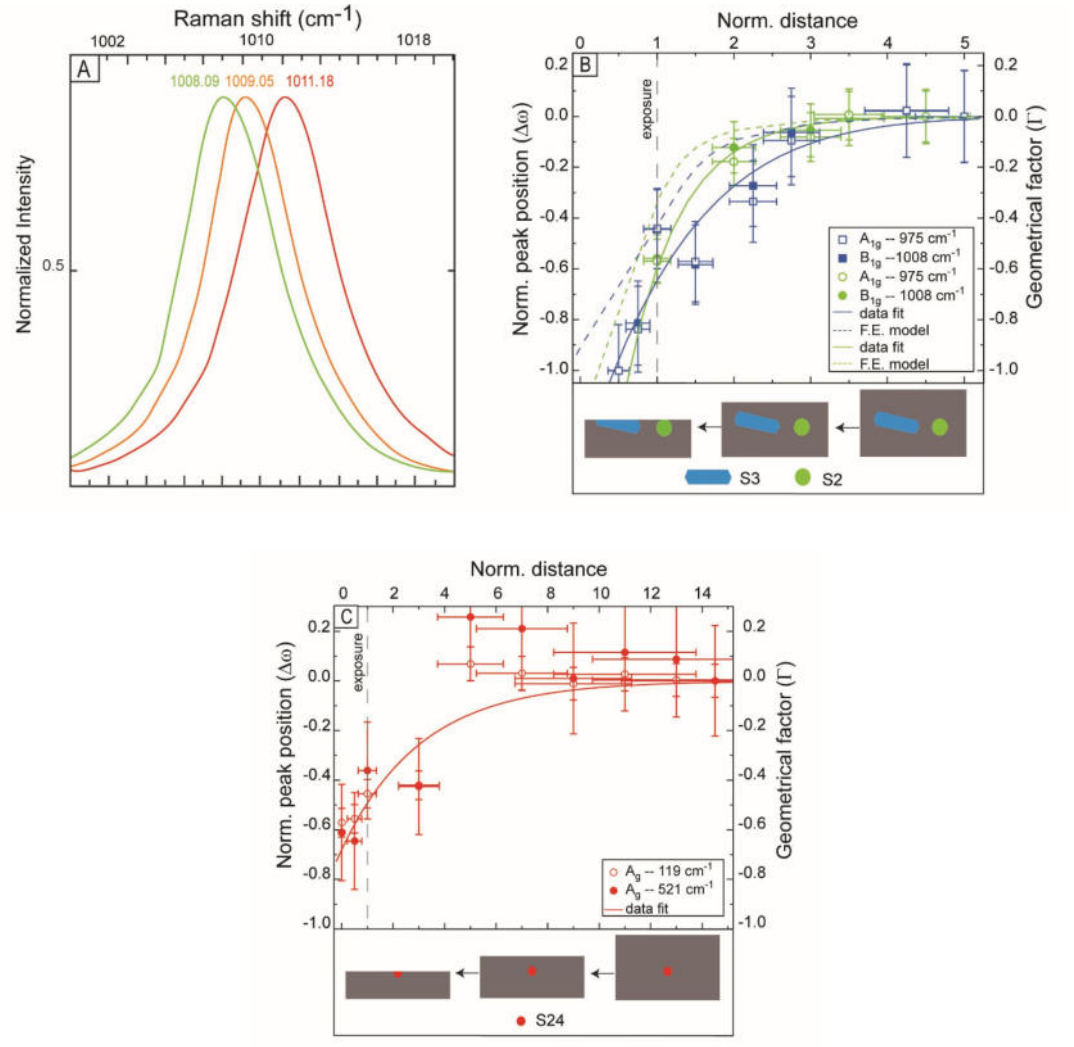

Figure 5.3. (A) Raman scattering arising from the antisymmetric SiO_4 stretching (the B_{1g} crystal phonon mode ~ 1008 cm^{-1}) measured when the grain S3 was fully entrapped (red line), at an intermediate stage of polishing (yellow), and when the inclusion was exposed at the final stage of polishing (green line). The numbers are the measured Raman shifts. (B) Measured normalized wavenumber shifts $\Delta\omega_{norm}$ for zircon S2 (green circles) and zircon S3 (blue squares) versus the normalized distance d to the host surface along with gaussian fits to the corresponding data A_{1g} ~ 975 and B_{1g} ~ 1008 cm^{-1} data sets (solid lines) as well as the calculated geometrical factor Γ (dashed lines) from the FE model; $\Delta\omega_{norm}(d)$ and $\Gamma(d)$ show the same trend within uncertainties. (C) Measured $\Delta\omega_{norm}(d)$ (red circles) and a Gaussian fit to A_{1g} ~ 119 and ~ 521 cm^{-1} (solid line) for S24 coesite inclusion

Under these assumptions, equation (5.2) shows that $\boldsymbol{\Delta\omega_{norm}}$ becomes equivalent to the geometrical factor $\boldsymbol{\Gamma}$ defined by Mazzucchelli et al. (2018).

As can be seen in Figure 5.3 b and c, the normalized change in the peak position $\Delta\omega_{norm}$ decreases progressively towards -1 (i.e. the Raman shift becomes equal to that of a free crystal), when the inclusion approaches the host surface (see also Table 5.4 for the two zircons and Table 5.5 for coesite). The trends of "pressure" release estimated from the Raman spectra measured on our zircon samples show the same pattern with those calculated from numerical simulations performed on similar geometries and crystallographic orientations (e.g. see the dotted lines in Figure 5.3 b). However, the experimental data suggest a greater amount of stress release compared to the numerical simulations. For example, at a normalized distance of 1 (inclusion just in contact with the external surface), the calculated stress release is approximately 50%, whereas that obtained from experimental data is about 70% (Figure 5.3 a).

There are at least two contributions to this discrepancy: (i) for non-cubic inclusions, direct conversion of Raman shifts into pressures using a hydrostatic calibration is incorrect; (ii) when the inclusion is close to the surface, strain gradients may be relaxed through plasticity or micro-fractures that are not considered in our purely elastic numerical models. Interestingly, our experiments show that even after partial exposure of the inclusion (i.e. for normalized distances ≤ 1) the Raman shift does not record full strain release which means that the inclusion is not at ambient conditions! In Figure 5.3 c, for example, the polished coesite inclusion still shows 40% of its original residual strain. Finally, the difference in the strain release between zircon and coesite inclusions is probably due to the different contrast in properties with respect the host garnet. Indeed, since coesite is softer than zircon, the host garnet can still retain a greater amount of its residual strain even if half of the inclusion is exposed.

Table 5.4

POLISHING EFFECT ON ZIRCON SAMPLE S3									
P. analysis	Shift (cm^{-1})	Normalized shift	Uncertainty norm. shift	Shift (cm^{-1})	Normalized shift	Uncertainty norm. shift	Distance (μm)	Normalized Distance	Uncertainty norm. distance
p0	1011.28	0.00	0.18	977.56	0.00	0.18	100	5.00	0.52
p7	1011.34	0.02	0.18	977.63	0.02	0.18	85	4.25	0.44
p13	1011.11	-0.06	0.17	977.31	-0.09	0.17	55	2.75	0.30
p16_bis	1010.53	-0.27	0.16	976.65	-0.34	0.16	45	2.25	0.26
p19	1009.68	-0.58	0.16	976.01	-0.57	0.16	30	1.50	0.20
p36	1010.06	-0.44	0.16	976.36	-0.44	0.16	20	1.00	0.16
p53	1009.04	-0.81	0.17	975.29	-0.84	0.17	15	0.75	0.15
reference	*1008.53*	*-1.00*	*0.18*	*974.85*	*-1.00*	*0.18*			

POLISHING EFFECT ON ZIRCON SAMPLE S2									
P. analysis	Shift (cm^{-1})	Normalized shift	Uncertainty norm. shift	Shift (cm^{-1})	Normalized shift	Uncertainty norm. shift	Distance (μm)	Normalized distance	Uncertainty nom. distance
2	1013.16	0.00	0.11	979.80	0.00	0.10	90	4.50	0.47
6	1013.13	-0.01	0.11	979.84	0.01	0.10	70	3.50	0.37
8	1012.91	-0.05	0.10	979.40	-0.08	0.10	60	3.00	0.33
9	1012.60	-0.12	0.10	978.92	-0.18	0.09	40	2.00	0.24
27	1010.57	-0.56	0.09	976.98	-0.57	0.09	20	1.00	0.16
reference	1008.53	-1.00	0.18	974.85	-1.00	0.18			

Table 5.5

P. analysis	Shift (cm^{-1})	Norm. shift	uncertainty norm. shift	Shift (cm^{-1})	Norm. shift	uncertainty norm. shift	Shift (cm^{-1})	Norm. shift	uncertainty norm. shift	Distance (μm)	Norm. Distance	uncertainty norm. distance
	POLISHING EFFECT ON COESITE SAMPLE S24											
p0	127.21	0.00	0.07	183.84	0.00	0.091	524.18	0.00	0.22	145	14.5	2.9
p1	127.01	-0.03	0.07	183.41	-0.08	0.088	524.03	-0.07	0.22	140	14	2.8
p2	127.20	0.00	0.07	184.09	0.04	0.094	524.30	0.06	0.23	135	13.5	2.7
p3	127.24	0.00	0.07	183.88	0.01	0.092	524.37	0.09	0.23	130	13	2.6
p4	127.41	0.03	0.07	184.10	0.05	0.094	524.43	0.11	0.24	110	11	2.2
p5	127.13	-0.01	0.07	183.71	-0.02	0.090	524.20	0.01	0.22	90	9	1.8
p6	127.44	0.03	0.07	184.25	0.07	0.095	524.64	0.21	0.25	70	7	1.4
p7	127.72	0.07	0.07	184.15	0.06	0.094	524.75	0.26	0.26	50	5	1
p8	124.07	-0.42	0.06	181.35	-0.46	0.079	523.23	-0.43	0.19	30	3	0.6
p9	123.82	-0.46	0.06	181.00	-0.52	0.079	523.37	-0.36	0.20	10	1	0.2
p10	123.06	-0.56	0.06	180.50	-0.62	0.080	522.74	-0.65	0.20	5	0.5	0.1
p11	122.95	-0.57	0.06	180.63	-0.59	0.080	522.82	-0.61	0.19	0	0	0
reference	*119.75*			*178.42*			*521.95*					

This implies the possibility to have thinner hosts for softer inclusions such as coesite or quartz in garnet but, however, the possibility of fracturing during polishing is high (Enami et al., 2007).

5.5 Implications

These results show that Raman shift is homogeneous only in rounded inclusions while it can be non-homogeneous in faceted ones (Figure 5.2 a and b), in full agreement with numerical calculations (Mazzucchelli et al. 2018) and theory (Eshelby, 1957). Therefore, multiple Raman spectra collected on faceted inclusions should not be averaged if their differences are larger than the instrumental peak precision. Instead, to avoid the effects of grain shape on Raman peak positions, only Raman spectra measured at the center of the inclusions should be used because there it is possible to apply the geometrical correction developed by Mazzucchelli et al. (2018).

The results from polishing experiments confirm that the Raman shift of the inclusion decreases as the inclusion gets closer to the external surface (Rosenfeld and Chase, 1961; Zhang, 1998; Mazzucchelli et al., 2018). Therefore, only inclusions whose centers are distant more than 4 radii (Figure 5.3 b) from the section surface and internal surfaces of the host should be used. If the Raman peak positions vary from one inclusion to another, even when the inclusions are properly selected, this indicates that some other factor is responsible, such as chemical variation in the host or inclusions, or growth of the host and thus inclusion entrapment under different conditions, such as along a prograde subduction path. More importantly, our results, coupled with our FE numerical simulations, show how anisotropy (i.e. crystallographic orientation of the inclusion with respect to the external surface) and the contrast between the inclusion and host physical properties influences the strain release during polishing. Furthermore, even when an inclusion is exposed at the surface of the host

grain, it can still exhibit a variation in the peak position with respect to a free crystal, and thus residual strains and stresses (Figure 5.3 c). Therefore, partially entrapped grains as a strain-free standard should be avoided or chosen very carefully against which to measure the Raman shifts of unexposed inclusions.

Finally, as an example, if we calculate from our experimental Raman shift values the strain and then the mean stress in the inclusion after subsequent polishing steps, following the approach given by Murri et al. (2018), the zircon S3 has an initial residual pressure (P_{inc}) before polishing of 0.5 GPa. After 55 microns of polishing (1.5 of normalized distance in Figure 5.3 b), when the inclusion is still buried in its garnet host, the P_{inc} drops to 0.2 GPa. A value of 0.06 GPa is recorded when the inclusion is half exposed. For zircon S2 the initial P_{inc} was about 0.9 GPa and about 0.3 GPa when the inclusion was just touching the external surface of the host. In the supplementary material a table showing the evolution of the P_{inc} as function of the polishing for the two zircon inclusions is reported (Table 5.6). For coesite no reliable data are available to give the strain state of the inclusion from the Raman peak positions.

Table 5.6

RESIDUAL PRESSURES FOR THE ZIRCON S2

N. Distance	$\Delta\omega$ 975 (cm^{-1})	$\Delta\omega$ 1008 (cm^{-1})	e_1-e_2	e_3	P_{inc} (GPa)
4.5	4.96000	4.63000	-1.162525	-0.44395	0.923
3.5	5.00000	4.60000	-1.1895	-0.40035	0.92645
3.0	4.56000	4.38000	-1.027	-0.4618	0.8386
2.0	4.08000	4.07000	-0.8892	-0.5382	0.7722
1.0	2.13000	2.04000	-0.4888	-0.21595	0.39785

RESIDUAL PRESSURE FOR THE ZIRCON S3

N. Distance	$\Delta\omega$ 975 (cm^{-1})	$\Delta\omega$ 1008 (cm^{-1})	e_1-e_2	e_3	P_{inc} (GPa)
5.0	2.78000	2.94017	-0.56355	-0.46095	0.52935
4.2	2.78000	2.81077	-0.5928	-0.3588	0.5148
2.7	2.46000	2.58099	-0.4992	-0.38205	0.46015
2.2	1.81000	2.00278	-0.3562	-0.3754	0.3626
1.5	1.16000	1.14690	-0.2717	-0.16445	0.23595
1.0	1.52000	1.52951	-0.3211	-0.19435	0.27885
0.7	0.44000	0.51245	-0.06435	-0.0789	0.0692

Chapter 6

Establishing a protocol for the selection of zircon inclusions in garnet for Raman thermobarometry

This chapter reports the results and discussions from the published paper:

Campomenosi, N., Rubatto, D., Hermann, J., Mihailova, B., Scambelluri, M., Alvaro, M. (2020a) *Establishing a protocol for the selection of zircon inclusions in garnet for Raman thermobarometry.* American Mineralogist, **DOI: 10.2138/am-2020-7246**.

Original Abstract

The structural and chemical properties of zircon inclusions in garnet megablasts from the Dora Maira Massif (Western Alps, Italy) were characterised in detail using Charge Contrast imaging, Raman spectroscopy and Laser Ablation Inductively Coupled Plasma Mass Spectrometry. The aim of this work is to determine to what extent the degree of metamictization, metamorphic recrystallization, inherent structural heterogeneity, chemical composition and zoning, along with the elastic stress imposed by the host mineral, can influence the Raman peak position of the zircon inclusion and hence, the residual pressure estimated via Raman geo-barometry. We show and confirm that metamictization and inherent structural heterogeneity have a major influence in the Raman spectra of zircon in terms of peak position and peak width. We suggest that for a spectral resolution of 2 cm^{-1} the peak width of the B_{1g} mode near 1008 cm^{-1} of reliable grains must be smaller than 5 cm^{-1}. The method can be applied to both inherited igneous and newly formed Alpine metamorphic crystals. By coupling structural and chemical information, we demonstrate that there are no significant differences between the Raman spectra of zircon with oscillatory-zoned texture, formed during magmatic crystallization, and those formed by fluid-induced Alpine (re)crystallization. The discrimination between magmatic and metamorphic zircon based only on micro-textural constraints is therefore not robust. Finally, our results allow a protocol to be established for the selection of reliable buried zircon inclusions, relying only on Raman spectroscopic measurements, to use for elastic thermobarometry applications.

6.1 Introduction and motivation

Zircon is one of the most common accessory minerals in various igneous, sedimentary and metamorphic rocks. Furthermore, due to its large stability field and its physical robustness, zircon often hosts UHP metamorphic minerals such as coesite and diamond (Parkinson and Katayama, 1999; Ye et al., 2000b; Hermann et al., 2001; Katayama and Maruyama, 2009). In general, zircon can be used for a wide range of applications, including U-Pb geochronology, and potential use as a host phase for the disposal of excess weapons-grade Pu, because of its capacity to incorporate radioactive elements, (e.g. Ewing et al., 1995). Further, radiation-damaged zircon has been successfully applied as a model system to elucidate the behaviour of partially-ordered structures at high pressure and temperature conditions (e.g. Colombo et al., 1999; Binvignat et al. 2018).

A recent development in zircon petrology is its exploitation as a mineral inclusion in the frame of Raman elastic thermobarometry (Campomenosi et al., 2018; Zhong et al. 2019). The main idea is that the geochemical and isotopic information that can be obtained from zircon is complemented by elastic thermobarometry of zircon and its host in order to retrieve P-T-time-fluid-deformation paths of metamorphic and igneous rocks. For this new application, however, zircon composition and structural metamictization due to the decay of radioactive elements such as U and Th within its crystal structure has to be taken into account, because the radiation-induced structural changes can lead to large variations in the Raman spectrum as well as the elastic properties (Binvignat et al., 2018). Indeed, the Raman peaks of radiation-damaged crystals shift towards lower wavenumbers, while the peak width increases with respect to pristine crystals taken as reference (Rios et al. 2000; Colombo et al., 1999; Nasdala et al., 2001; Geisler and Pidgeon, 2002; Binvignat et al, 2018). In this regard, useful diagrams such as peak width (Γ), in terms of *full width at half maximum*, vs peak position of the major Raman peak near 1008 cm^{-1} (B_{1g} phonon mode related to

antisymmetric SiO_4 stretching) can be exploited to recognize the zircon crystals whose Raman spectra is unaffected by metamictization processes and that can be safely used for elastic thermobarometry purposes (e.g. Zhong et al. 2019). However, even though the degree of metamictization is the main factor affecting the Raman spectra of zircon, it is not the only one. Cathodoluminescence (CL) studies of zircon internal zoning (e.g. Rubatto and Gebauer, 2000, Corfu et al. 2003) reveal that single crystals of zircon, particularly in metamorphic rocks, commonly show a complex internal chemical and structural heterogeneity at the micrometer-scale. Furthermore, variations in the Raman peak positions can be caused also by chemical substitution: a typical example is Hf replacing Zr at the dodecahedral crystallographic site (e.g. Hoskin and Rodgers, 1996).

To investigate these potential problems we have chosen a particularly well-known sample suite from the Dora Maira UHP unit (Western Alps, Italy), where garnet megablasts host abundant zircon inclusions. This work reports micrometre-scale structural and chemical information of partially exposed zircon crystals studied by complementary Raman spectroscopy, charge contrast (CC) imaging, and Laser Ablation Inductively Coupled Plasma Mass Spectrometry (LA-ICP-MS). The purpose is (i) to determine quantitatively how the structural and chemical heterogeneities of zircons can affect their Raman spectrum and (ii) to propose a best-practice protocol for the selection of zircon inclusions suitable for elastic thermobarometric estimations.

6.2 Specific sample description

The investigated samples come from the two major outcrops of the Brossasco-Isasca Unit (e.g. Chopin, 1984): Vallone Gilba and Vallone Martiniana close to the Case Canova and Case Parigi localities, respectively. Previous results on these localities (Gebauer et al., 1997; Gautiez-Putallaz et al., 2016) suggested the existence of two main zircon generations that

can coexist within the same crystal in these rocks. The first one records the crystallization of the Permian protolith (~275 Ma), while the second domain is Eocene in age (35.1 ±0.8 Ma) and related to metamorphism during the Alpine subduction.

The selection of completely buried zircon inclusions follows the protocol given by Campomenosi et al. (2018) for elastic barometry applications (see Chapter 4 and Chapter 5). On the other hand, the selection of the exposed grains (about 60% of the total number of zircon inclusions present in the samples) was based on criteria such as variable size of the inclusion and of the surrounding intact host (the *effective* host), exposure degree of the inclusions (optically estimated in terms of the ratio between the exposed and buried inclusion surface) and presence of fractures or any other kind of discontinuity in both the host and the inclusion.

6.3 Results

Partially exposed zircon inclusions

Charge Contrast (CC) imaging

CC imaging of 64 inclusions from samples DM17-13 and DM17-49 (Martiniana locality) and 83 grains from samples DMG4-6 and DM17-35 (Gilba locality) showed a large variability in zircon internal texture. By combining the data on various crystals, it was possible to recognize at least 4 major domains (Figure 6.1): (i) a *dark* (i.e. low CC-emission) domain, commonly corresponding to the crystal cores, (ii) an *oscillatory-zoned* domain (medium-high CC emission), which usually corresponds to entire crystals or the core of elongated crystals and are further subdivided into *oscillatory-dark* and *oscillatory-bright* domains based on CC emission, (iii) a transition (or *undefined*) domain, whose appearance is between the darker and a brighter domains and without a defined internal texture, and (iv) a *bright* domain (i.e. high CC-emission), which usually belongs to the external rim of the

crystals. About 70% of zircon inclusions from the Gilba locality show a more elongated shape with a typical oscillatory-zoned core surrounded by 1 or 2 thin brighter rims. On the other hand, about 80% zircon inclusions from the Martiniana locality present more sub-idiomorphic shape and more homogeneous internal texture. Furthermore, as already reported by Gautiez-Putallaz et al. (2016) for zircon hosted in Si-undersaturated whiteschists, some of the analysed inclusions in Martiniana, where garnet is more abundant, display oscillatory dark domains.

Raman spectroscopy

According to previous studies (Williams and Knittel, 1993; Nasdala et al., 2001; Binvignat et al., 2018), both pressure and metamictization affect most strongly the B_{1g} mode near 1008 cm^{-1}, originating from anti-symmetrical SiO_4 stretching. For this reason, our discussion is mainly focused on this phonon mode. The Raman spectroscopic analysis is based on 250 spectra collected from 60 zircon inclusions in different CC domains. As an example, Figure 6.1 shows the variation of the internal SiO_4 antisymmetric stretching mode (B_{1g}) near to 1008 cm^{-1} of representative zircon inclusions exhibiting heterogeneous CC emission. Generally, dark CC domains correspond to Raman peak broadening and shift towards lower wavenumbers when compared to those collected across brighter or oscillatory-zoned domains. Transition CC domains show transitional average features also for the Raman spectra. A more quantitative evaluation of the structural state of zircon crystals can be achieved by plotting the relationship between the phonon wavenumber ω and the corresponding peak width Γ (Geisler and Pidgeon 2002; Zhong et al. 2019). The data measured on partially exposed zircon inclusions (Figure 6.2) show two different trends that correlate with the four different zircon domains (*bright, oscillatory-zoned, undefined* and *dark)* .

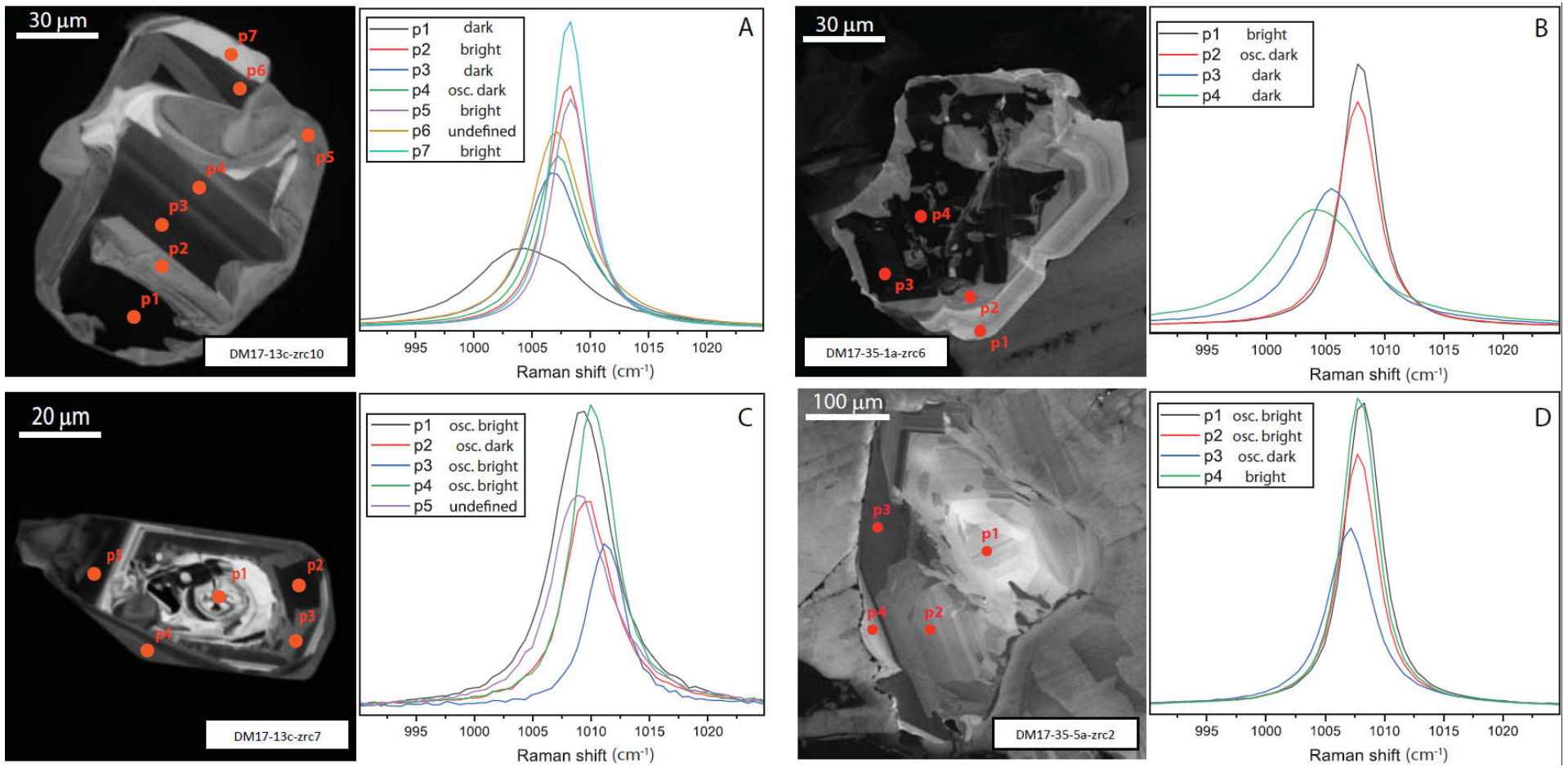

Figure 6.1. Relationship between the CC emission domain and the corresponding Raman spectra (B_{1g} mode near 1008 cm^{-1}) in partially exposed zircon inclusions. Samples DM17-35 are from Gilba locality while sample DM17-13 comes from the Martiniana locality (continue).

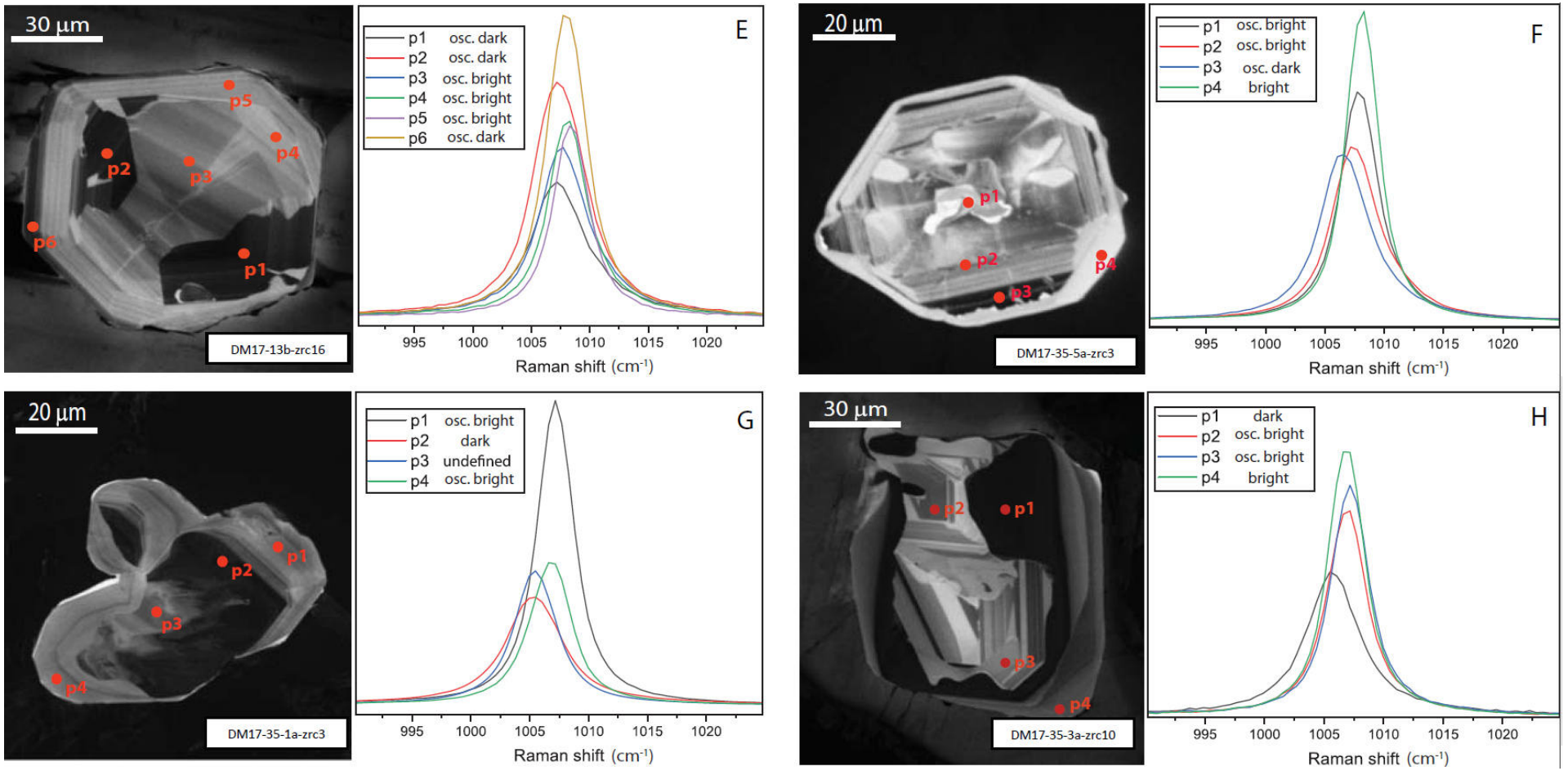

Figure 6.1. Relationship between the CC emission domain and the corresponding Raman spectra (B_{1g} mode near 1008 cm^{-1}) in partially exposed zircon inclusions. Samples DM17-35 are from Gilba locality while sample DM17-13 comes from the Martiniana locality.

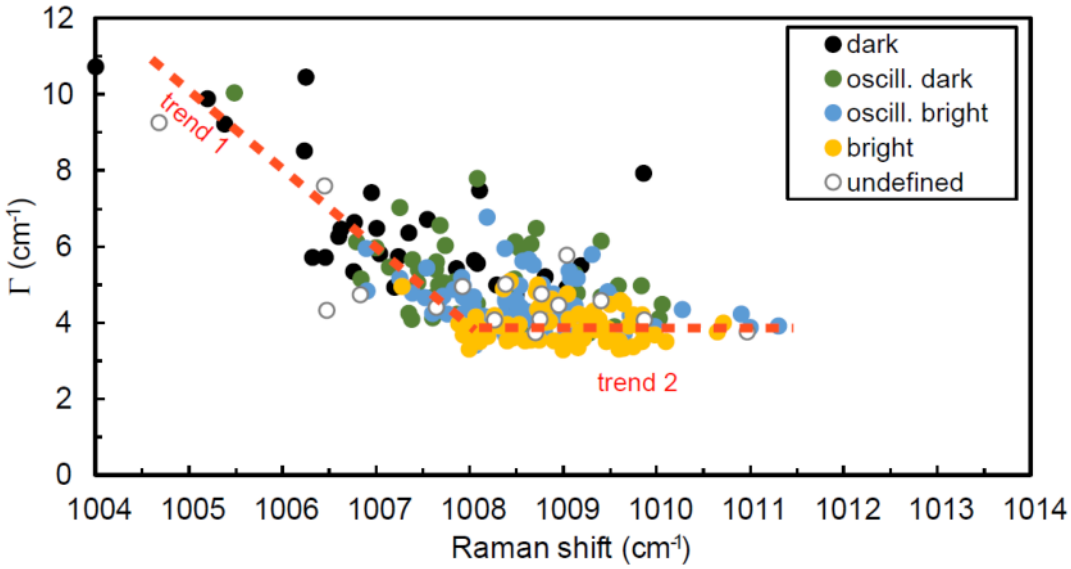

Figure 6.2. Γ vs Raman shift of the antisymmetric SiO_4 stretching B_{1g} mode near 1008 cm^{-1} of partially exposed crystals with highlighted CC-emission domains.

- The first trend is characterized by $\omega < 1008$ cm^{-1}, 4.5 $cm^{-1} \leq \Gamma < 12$ cm^{-1}, and $\omega(\Gamma)$ with a negative slope (inverse correlation). The data points on this trend are mostly from zircon domains with dark and oscillatory-dark CC emission.
- The second trend, at higher wavenumbers, is characterized by 1008 $cm^{-1} < \omega < 1011$ cm^{-1}, 3.5 $cm^{-1} < \Gamma < 5.5$ cm^{-1}, and $\omega(\Gamma) \approx$ constant. This trend is mostly defined by zircon domains with *bright* and *oscillatory(-brigh)* CC emission.

Note that, on average, *oscillatory-dark* domains display the largest Γ and lowest wavenumber with respect to *oscillatory-bright* domains. On the other hand, *undefined* domains are difficult to classify since they scatter over the entire field of the data.

LA-ICP-MS

The different types of zircon domains also show differences in trace element composition. Table 1a-b reports representative major, minor and trace elements composition of analysed zircon crystal inclusions as determined by LA-ICP-MS with the associated CC-emission domains. Hf concentration is usually around 11000 µg/g and only few analyses show higher values up to 14000 µg/g. U content varies significantly between oscillatory-bright zoned, oscillatory-dark and dark CC domains, with the last showing, usually, the highest concentration (see for example DM17-35-3a-zrc10-p1 and p2 or even DM17-35-3a-zrc14-p3 and p2 in Table 1a). U contents vary from a few hundred µg/g in the bright domains in crystal cores or rims to 5000 µg/g for the darker domains and generally show an inverse relationship with CC emission, indicating that U suppresses luminescence (e.g. Rubatto and Gebauer 2000).

In line with previous REE datasets (e.g. Gautiez-Putallaz et al. 2016), zircon cores with oscillatory or convolute zoning have a steep HREE-enriched pattern with a pronounced negative Eu anomaly (e.g. Figure 6.3-C p1). This REE pattern is characteristic of conditions where plagioclase was present and garnet was absent, i.e during the crystallization of the granitic protholith in Permian times (e.g. Gautiez-Putallaz et al. 2016).

Table 6.1a. Major, minor and trace elements (in µg/g) of zircon inclusions (spots refer to Figure 6.3).

sample name	CC domain	Ti	Y	Nb	Hf	Pb	Th	U	sample name	CC domain	Ti	Y	Nb	Hf	Pb	Th	U
DM17-35-3A-zrc8-p1	Osc. dark	2.28	1639	3.16	10300	154	158	1436	DM17-35-1a-zrc6-p2	Osc. dark	14.3	720	8.31	14570	65.8	41.1	3147
DM17-35-3A-zrc8-p2	Osc. bright	4.70	2651	8.73	7710	390	793	1241	DM17-35-1a-zrc6-p3	dark	20.2	826	7.62	12610	77.1	32.8	2949
DM17-35-3A-zrc10-p1	Osc. bright	35.3	492	34.2	10880	10.0	84.9	378	DM17-35-1a-zrc3-p1	Osc. bright	13.3	204	1.63	12930	19.7	9.89	452
DM17-35-3A-zrc10-p2	dark	5.03	197	5.98	13690	52.4	2.61	2122	DM17-35-1a-zrc3-p2	dark	9.90	103.3	2.98	11690	73.7	7.82	3154
DM17-35-3A-zrc10-p3	bright	7.90	183	4.01	10840	24.3	6.85	883	DM17-35-1a-zrc3-p3	Osc. bright	13.1	161.8	3.09	12280	80.7	12.1	3700
DM17-35-3A-zrc14-p1	Osc. bright	2.91	850	1.94	12450	138	40.7	730	DM17-35-1a-zrc9-p1	Osc. bright	6.38	179.3	2.47	12190	43.7	16.8	1640
DM17-35-3A-zrc14-p2	Osc. dark	6.90	3140	8.05	10300	326	696	1900	DM17-35-1a-zrc10-p1	Osc. bright	10.8	587	2.42	11220	9.10	10.7	249.8
DM17-35-3A-zrc14-p3	Osc.bright	4.90	1820	4.50	11660	237	158	1320	DM17-35-1a-zrc10-p2	Osc. bright	790	536	8.53	10980	8.71	13.0	261
DM17-35-3A-zrc14-p4	Osc. bright	2.67	1353	1.42	8680	66.1	73.4	333	DM17-13-b-zrc13-p1	Osc. bright	17.0	1479	21.6	11960	31.1	51.5	1307
DM17-35-3A-zrc18-p1	Osc. bright	6.85	1850	1.64	9100	308	179.6	474	DM17-13-b-zrc13-p2	Osc. bright	11.8	1209	11.5	10820	22.5	26.6	755
DM17-35-3A-zrc13-p2	Osc. bright	1.69	920	3.05	9570	130	89.0	673	DM17-13-b-zrc15-p2	Osc bright	6.30	649	4.80	10180	16.9	11.5	604
DM17-35-3A-zrc13-p1	Osc. bright	1.79	1051	2.80	10960	154	87.0	828	DM17-13-b-zrc15-p3	Osc. bright	6.10	589	5.86	10310	9.37	7.11	346
DM17-35-3A-zrc13-p3	bright	3.04	1150	4.26	7070	242	336	635	DM17-13-b-zrc16-p1	Osc. bright	16.8	1817	13.7	10840	34.7	35.2	1342
DM17-35-5A-zrc2-p1	Osc. bright	10.3	211	5.86	11770	9.65	22.4	367	DM17-13-b-zrc16-p2	Osc. bright	8.50	383	3.96	11030	16.8	14.9	562
DM17-35-5A-zrc2-p2	Osc. bright	8.81	83.3	9.95	11190	17.6	34.3	695	DM17-13-b-zrc16-p3	Osc. dark	20.9	1504	29.9	10550	43.3	56.8	1538
DM17-35-5A-zrc2-p3	Osc. dark	8.30	83.4	8.75	11270	31.4	34.9	1208	DM17-13-b-zrc16-p4	Osc. bright	5.66	227.8	4.54	11550	10.3	18.5	435.3
DM17-35-5A-zrc2-p4	Osc. dark	4.60	58.5	3.10	11030	32.3	11.3	1148	DM17-13-c-zrc7-p1	Osc. bright	16.5	2140	2.44	10600	125	149	719
DM17-35-5A-zrc2-p5	bright	5.10	198	2.85	11170	28.6	7.17	1092	DM17-13-c-zrc7-p2	Osci. dark	10.2	1790	7.65	11900	21.1	13.2	950
DM17-35-5A-zrc3-p1	Osc. bright	2.02	930	0.76	9950	51.5	44.1	253	DM17-13-c-zrc7-p3	undefined	10.1	1982	12.5	12280	25.4	17.8	1037
DM17-35-5A-zrc14-p1	Osc. bright	48.3	1682	26.8	9768	8.94	87.1	380	DM17-13-c-zrc4-p1	bright	27.0	3250	24.3	12380	32.4	35.2	1335
DM17-35-5A-zrc14-p2	dark	10.1	490	5.49	11520	16.4	15.7	530	DM17-13-c-zrc4-p2	undefined	11.8	2100	13.6	11850	56.1	39.8	931
DM17-35-5A-zrc14-p3	bright	10.8	430	6.06	10840	3.80	12.3	112	DM17-13-c-zrc10-p1	dark	20.9	2680	33.7	11080	102	33.0	5060
DM17-35-5A-zrc14-p4	bright	22.5	632	20.1	11400	8.96	32.7	370	DM17-13-c-zrc10-p2	bright	7.30	582	4.56	11860	28.0	7.63	1175
DM17-35-5A-zrc14-p5	Osc. dark	7.10	262	6.38	12790	10.5	8.84	407	DM17-13-c-zrc10-p3	Osc. dark	10.7	1540	8.24	11480	46.2	6.67	2004

*Precision plus accuracy of measurements is within 10%

Table 6.1b. REE composition (in µg/g) of zircon inclusions (spots refer to Figure 6.3)

sample name	CC domain	La	Ce	Pr	Nd	Sm	Eu	Gd	Tb	Dy	Ho	Er	Tm	Yb	Lu
DM17-35-3A-zrc8-p1	Osc. dark	0.04	5.90	0.21	2.65	5.07	0.15	28.9	10.5	143	54.9	273	60.7	553	112
DM17-35-3A-zrc8-p2	Osc. bright	0.46	18.7	0.40	6.43	12.1	0.26	65.8	21.8	267	91.0	411	79.6	653	128
DM17-35-3A-zrc10-p1	Osc. bright	b.d.l.	2.80	0.04	1.06	6.80	2.23	70.5	16.0	86.2	12.3	29.5	4.80	38.9	6.95
DM17-35-3A-zrc10-p2	dark	b.d.l.	0.59	b.d.l.	b.d.l.	0.51	0.11	4.78	2.01	20.1	4.93	15.8	2.73	22.2	3.98
DM17-35-3A-zrc10-p3	bright	b.d.l.	1.03	b.d.l.	0.14	0.54	0.14	4.54	1.83	19.6	4.77	17.0	2.67	19.3	2.80
DM17-35-3A-zrc14-p1	Osc. bright	b.d.l.	0.44	b.d.l.	0.17	1.06	0.19	10.05	4.41	63.0	26.4	143	35.7	351	73.0
DM17-35-3A-zrc14-p2	Osc. dark	12.0	37.0	3.10	14.6	11.5	0.55	61.0	22.7	291	104	497	101	839	156
DM17-35-3A-zrc14-p3	Osc.bright	0.49	3.40	0.21	1.19	3.14	0.19	22.0	9.90	142	57.1	305	71.7	670	135
DM17-35-3A-zrc14-p4	Osc. bright	0.04	1.54	0.04	1.13	3.51	0.15	20.8	8.45	115	44.7	219	46.1	408	79.5
DM17-35-3A-zrc18-p1	Osc. bright	1.12	5.21	0.85	8.20	10.7	0.97	51.6	16.9	192	62.1	269	53.6	454	84.8
DM17-35-3A-zrc13-p2	Osc. bright	b.d.l.	2.78	b.d.l.	0.29	1.49	0.12	9.77	4.76	73.3	30.2	161	37.3	350	71.9
DM17-35-3A-zrc13-p1	Osc. bright	b.d.l.	2.38	0.02	0.33	1.08	0.10	9.02	4.55	75.7	32.9	182	43.8	424	88.1
DM17-35-3A-zrc13-p3	bright	0.34	14.1	0.17	1.78	3.15	0.73	16.5	6.16	85.0	34.4	185	44.1	442	97.0
DM17-35-5A-zrc2-p1	Osc. bright	0.08	1.08	0.04	0.42	3.30	1.36	53.7	10.8	48.2	5.31	11.1	1.39	10.0	1.69
DM17-35-5A-zrc2-p2	Osc. bright	b.d.l.	0.75	b.d.l.	0.34	4.74	1.41	43.7	6.35	22.2	2.26	4.55	0.61	5.21	0.90
DM17-35-5A-zrc2-p3	Osc. dark	b.d.l.	0.99	b.d.l.	0.12	3.47	1.13	34.8	5.44	19.9	2.26	4.60	0.61	5.82	1.03
DM17-35-5A-zrc2-p4	Osc. dark	b.d.l.	0.57	b.d.l.	b.d.l.	0.91	0.37	13.3	2.64	12.1	1.45	3.48	0.61	4.62	0.88
DM17-35-5A-zrc2-p5	bright	b.d.l.	0.81	b.d.l.	b.d.l.	0.62	0.14	5.83	1.92	20.3	5.27	18.7	3.33	23.5	3.37
DM17-35-5A-zrc3-p1	Osc. bright	0.06	1.27	0.11	0.78	2.50	0.07	14.1	5.45	76.9	30.7	154	33.6	301	59.3
DM17-35-5A-zrc14-p1	Osc. bright	b.d.l.	3.06	0.02	1.10	10.1	3.72	164	46.6	288	47.8	117	16.7	118	19.3
DM17-35-5A-zrc14-p2	dark	0.40	2.11	0.19	1.35	2.51	0.86	31.0	9.74	70.3	12.9	32.5	4.76	31.7	5.42
DM17-35-5A-zrc14-p3	bright	b.d.l.	0.75	b.d.l.	0.27	2.44	0.65	31.7	9.81	68.9	11.6	30.1	4.66	34.8	6.21
DM17-35-5A-zrc14-p4	bright	b.d.l.	1.89	0.04	0.68	4.14	1.39	54.2	15.9	104	16.4	40.5	5.53	38.8	6.39
DM17-35-5A-zrc14-p5	Osc. dark	b.d.l.	0.72	b.d.l.	0.10	1.19	0.40	16.3	5.58	38.4	6.47	16.4	2.28	15.6	2.60

*Precision plus accuracy of measurements is within 10%

Table 6.1c. REE composition (in µg/g) of zircon inclusions (spots are referred to Figure 6.3)

sample name	CC domain	La	Ce	Pr	Nd	Sm	Eu	Gd	Tb	Dy	Ho	Er	Tm	Yb	Lu
DM17-35-1a-zrc6-p2	Osc. dark	b.d.l.	1.42	0.02	0.66	6.17	1.75	64.7	18.2	118	18.4	43.4	5.31	30.5	4.17
DM17-35-1a-zrc6-p3	dark	0.08	2.06	0.07	1.08	7.30	1.84	72.4	20.2	131	21.2	49.2	6.34	36.5	5.05
DM17-35-1a-zrc3-p1	Osc. bright	0.06	1.83	0.06	0.86	1.35	0.27	8.60	2.45	21.8	5.43	19.8	3.36	24.6	3.52
DM17-35-1a-zrc3-p2	dark	b.d.l.	0.45	b.d.l.	0.13	0.74	0.23	7.75	2.34	15.4	2.60	7.27	1.19	8.46	1.46
DM17-35-1a-zrc3-p3	Osc. bright	b.d.l.	0.95	0.02	0.26	1.50	0.44	14.4	4.10	25.8	4.42	12.0	2.04	14.0	2.42
DM17-35-1a-zrc9-p1	Osc. bright	b.d.l.	0.53	b.d.l.	0.19	1.40	0.46	16.1	4.63	27.3	4.51	12.9	2.03	14.5	2.48
DM17-35-1a-zrc10-p1	Osc. bright	b.d.l.	0.56	b.d.l.	0.23	3.06	0.93	38.1	11.7	89.1	18.0	51.8	7.30	47.6	7.10
DM17-35-1a-zrc10-p2	Osc. bright	0.05	0.70	b.d.l.	0.20	2.45	0.91	36.0	10.4	81.6	16.8	47.4	6.71	42.7	6.59
DM17-13-b-zrc13-p1	Osc. bright	b.d.l.	1.14	0.01	0.44	7.78	3.36	110	32.1	219	42.4	115	16.5	96.9	14.3
DM17-13-b-zrc13-p2	Osc. bright	b.d.l.	0.64	b.d.l.	0.40	5.57	2.46	86.6	25.6	177	35.2	95.6	14.4	85.9	12.7
DM17-13-b-zrc15-p2	Osc bright	b.d.l.	0.67	b.d.l.	0.12	2.26	1.08	39.2	11.2	90.3	18.9	58.5	9.16	62.8	10.9
DM17-13-b-zrc15-p3	Osc. bright	b.d.l.	0.44	b.d.l.	0.09	1.87	0.97	33.6	10.1	80.4	17.2	54.2	8.52	55.6	8.56
DM17-13-b-zrc16-p1	Osc. bright	b.d.l.	0.88	b.d.l.	0.58	9.34	4.24	147	40.6	288	54.3	149	21.4	133	19.4
DM17-13-b-zrc16-p2	Osc. bright	b.d.l.	0.41	b.d.l.	0.16	2.34	0.96	32.0	8.26	58.5	11.0	30.3	4.72	33.8	6.03
DM17-13-b-zrc16-p3	Osc. dark	b.d.l.	1.28	b.d.l.	0.34	7.11	3.05	116	33.2	233	44.0	116	16.2	99.6	13.2
DM17-13-b-zrc16-p4	Osc. bright	b.d.l.	0.35	b.d.l.	0.14	1.32	0.54	15.3	4.54	32.1	6.00	16.2	3.04	26.4	5.43
DM17-13-c-zrc7-p1	Osc. bright	0.84	3.40	0.31	2.32	5.24	0.18	31.2	13.0	175	69.7	334	71.6	647	122
DM17-13-c-zrc7-p2	Osci. dark	b.d.l.	0.57	b.d.l.	0.15	2.20	1.22	54.0	23.0	230	55.0	164	25.0	160	24.0
DM17-13-c-zrc7-p3	undefined	b.d.l.	0.73	b.d.l.	b.d.l.	3.23	1.36	54.2	24.5	250	63.5	197	30.1	210	32.9
DM17-13-c-zrc4-p1	bright	b.d.l.	1.64	b.d.l.	0.53	6.90	2.72	97.7	39.0	397	104	335	54.3	407	69.1
DM17-13-c-zrc4-p2	undefined	b.d.l.	1.21	b.d.l.	0.28	3.64	1.53	54.4	21.5	230	67.1	247	45.7	377	68.5
DM17-13-c-zrc10-p1	dark	b.d.l.	1.97	b.d.l.	0.47	6.10	2.69	90.3	33.8	310	84.0	326	64.0	536	94.8
DM17-13-c-zrc10-p2	bright	b.d.l.	0.35	b.d.l.	b.d.l.	0.95	0.44	18.9	7.34	69.3	19.0	74.4	14.6	126	23.0
DM17-13-c-zrc10-p3	Osc. dark	b.d.l.	0.62	b.d.l.	0.32	2.79	1.19	40.9	16.8	170	47.9	191	39.1	347	65.0

*Precision plus accuracy of measurements is within 10%

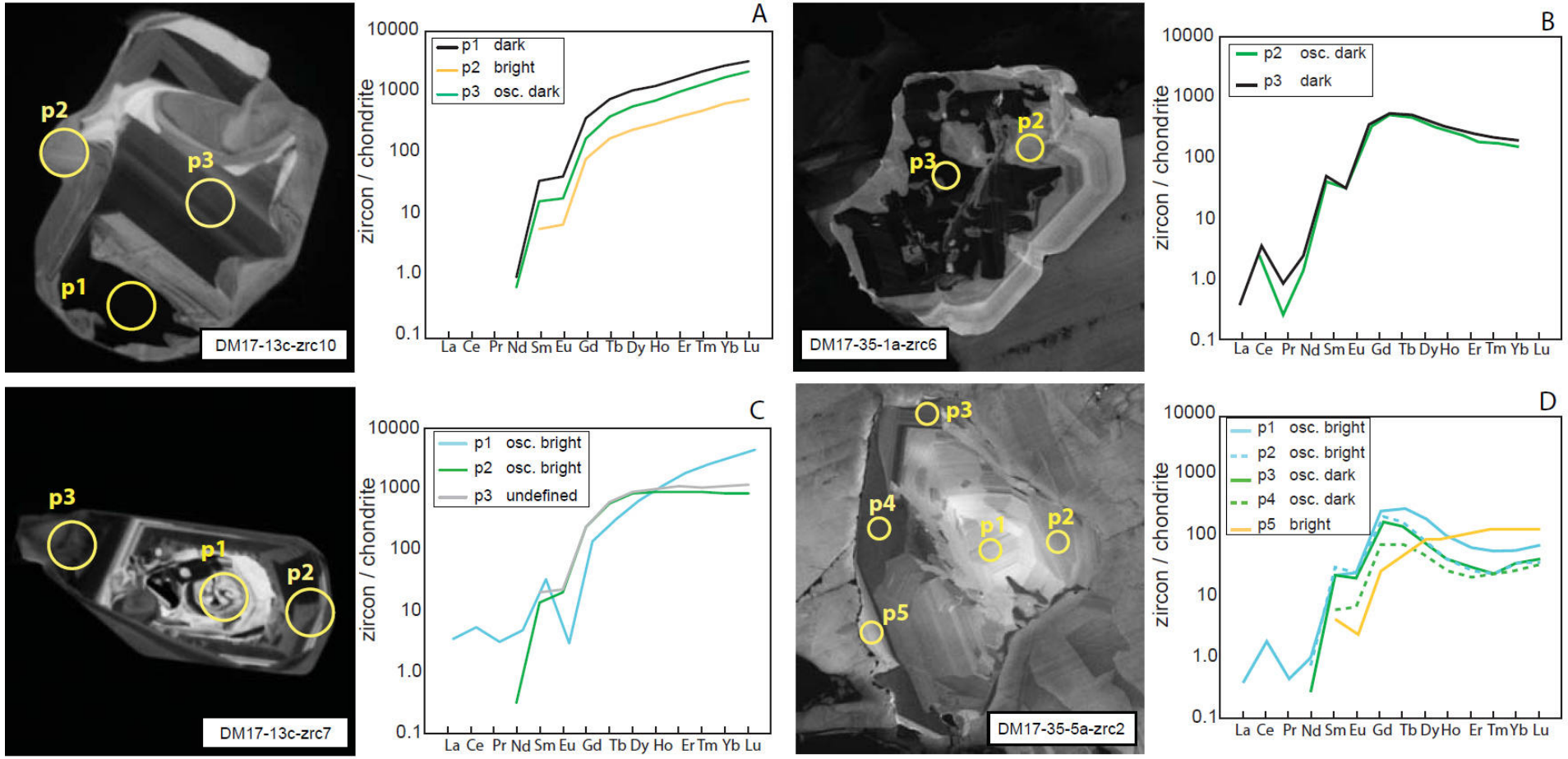

Figure 6.3. REE pattern in selected partially exposed zircon inclusions. Colour coding follows that in Figure 6.2: black = dark, green = oscillatory-dark, blue = oscillatory-bright, orange = bright, grey = undefined. Yellow circles are scaled with respect the figure and are 20 micron across (laser spot)

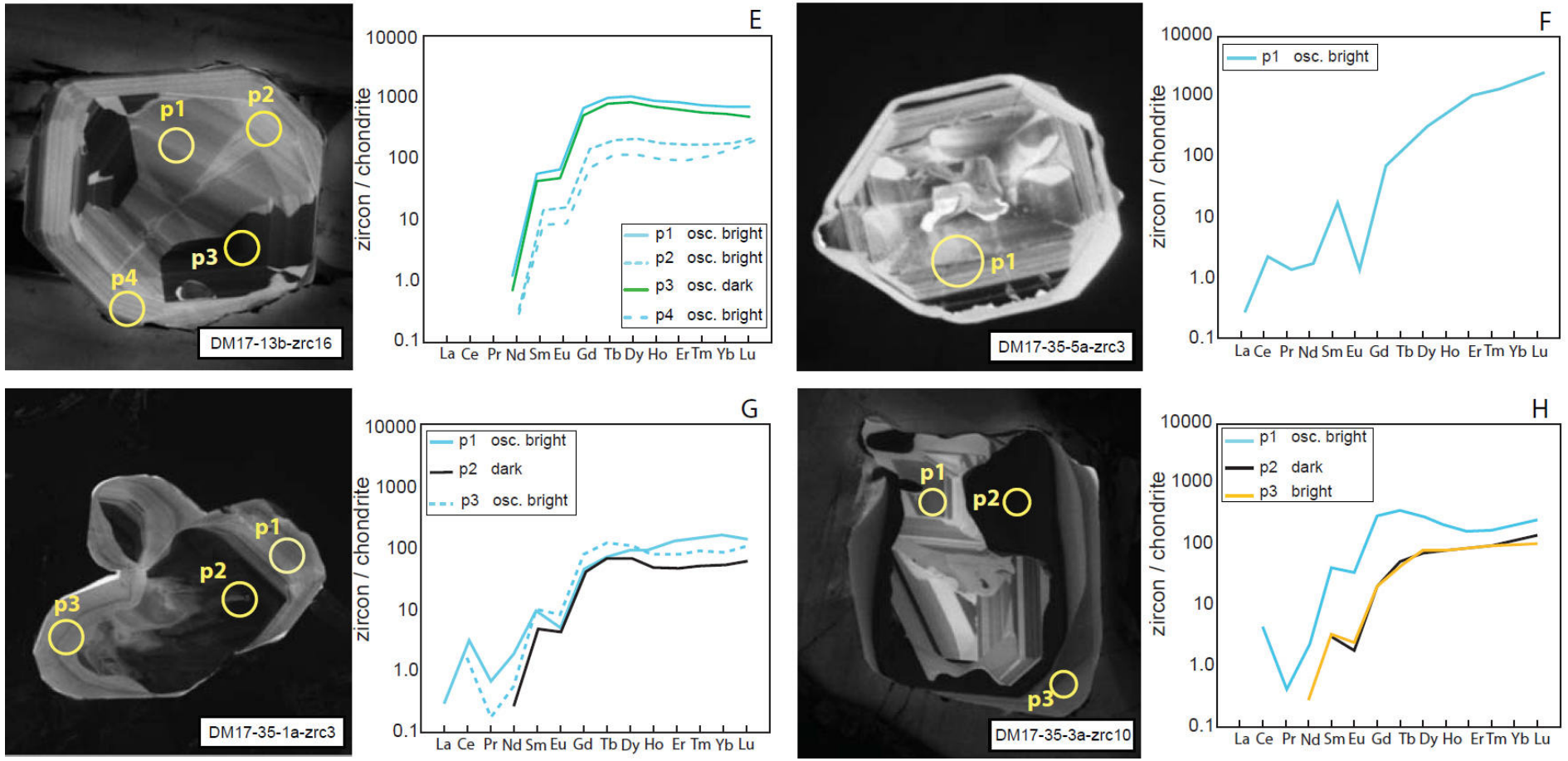

Figure 6.3. REE pattern in selected partially exposed zircon inclusions. Colour coding follows that in Figure 6.2: black = dark, green = oscillatory-dark, blue = oscillatory-bright, orange = bright, grey = undefined. Yellow circles are scaled with respect the figure and are 20 micron across (laser spot)

The rims and many crystals with oscillatory zoning have lower REE contents and a flat HREE pattern with no or weak Eu-anomaly (e.g. Figure 6.3). This REE pattern is diagnostic for zircons formed during prograde to peak metamorphism, where feldspar is no longer stable (e.g. Gautiez-Putallaz et al. 2016). The variable slope of the HREE patterns ranging from slightly positive to even negative (Figure 6.3-C) indicates zircon growth together with garnet, as both minerals compete for the HREE. Therefore a first distinction between pre-Alpine inherited igneous zircon and Alpine metamorphic zircon can be obtained from the trace element analysis. Notably, a number of large crystals that display a fine oscillatory to sector zoning, more or less surrounded by a dark or light rim, present a depletion in HREE and remain rather constant across the entire grain (e.g. Figure 6.3-D, 6.3-E). This demonstrates that oscillatory zoning occurs also in Alpine metamorphic zircon and is not restricted to inherited igneous zircon, and that *both* CC and trace element analyses are required for the correct classification of the zircons.

Previous analyses on zircons from the same locality demonstrated that inherited zircon cores are ca. 275 Ma old and metamorphic rims are 35.1 ± 0.8 Ma old (Gebauer et al., 1997, Gauthiez-Putallaz et al. 2016). In our case, a rough estimate of the age can also be obtained from the LA-ICP-MS data, even if proper age standardisation and correction for common Pb have not been performed. The $^{206}Pb/^{238}U$ values estimated in such a way are in general agreement with those obtained before on zircon from the same locality and correlate with the distinction made from the REE patterns (Gauthiez-Putallaz et al. 2016). This rough age estimate allows one to distinguish between Alpine domains (usually lower U content and bright or oscillatory-bright CC domains) and pre-Alpine domains (higher U content and dark or oscillatory-zoned CC domains at the zircon cores) especially in cases where REE patterns might be ambiguous (see Table 6.2). Notably the large crystals with oscillatory-sector zoning and low HREE content are of Alpine age.

Assuming an age of 275 Ma for the pre-Alpine and 35 Ma for the Alpine domains (Gebauer et al., 1997, Gauthiez-Putallaz et al. 2016) and using the measured U-Th composition of the zircon domains, their accumulation radiation doses D_a were calculated as follows (e.g. Nasdala et al., 2001):

$$D_\alpha = \frac{0.9928\, N_A c_U n_{238}}{10^6 m_{238}} \left(e^{\lambda_{238} t} - 1\right) + \frac{0.0072\, N_A c_U n_{235}}{10^6 m_{235}} \left(e^{\lambda_{235} t} - 1\right) + \frac{N_A c_{Th} n_{232}}{10^6 m_{232}} \left(e^{\lambda_{232} t} - 1\right)$$

(6.1)

where λ_n and m_n are, respectively, the nuclear decay constant and mass of the corresponding isotope (^{238}U, ^{235}U and ^{232}Th) (Steiger and Jaeger; 1977), the coefficient n represents the number of α decays per nucleus ($n_{238} = 8$, $n_{235} = 7$ and $n_{232} = 6$) and N_A is the Avogadro's number c_U and c_{Th} are the measured concentrations of U and Th respectively and t the time.

Table 6.2. Indicative age and dose of partially exposed zircon inclusions (spots are referred to Figure 6.3)

sample name	CC domain	Indicative $^{206}Pb/^{238}U$	Indicative Age	D_alfa * (g/events)	Raman shift (cm^{-1})	FWHM (cm^{-1})
DM17-35-3A-zrc8-p1	Osc. dark	0.04	Permian	8.3E+17	1007.6	5.6
DM17-35-3A-zrc8-p2	Osc. bright	0.08	Caledonian	2.2E+18	1008.0	3.4
DM17-35-3A-zrc10-p1	Osc. bright	0.01	Alpine	5.3E+16	1007.9	3.9
DM17-35-3A-zrc10-p2	dark	0.01	Alpine	2.6E+17	1006.7	5.3
DM17-35-3A-zrc10-p3	bright	0.01	Alpine	1.2E+17	1007.9	3.6
DM17-35-5A-zrc2-p1	Osc. bright	0.01	Alpine	4.9E+16	1009.1	3.6
DM17-35-5A-zrc2-p4	Osc. dark	0.01	Alpine	1.6E+17	1008.0	4.5
DM17-35-5A-zrc2-p5	bright	0.01	Alpine	1.4E+17	1008.9	3.5
DM17-35-1A-zrc6-p2	Osc. dark	0.01	Alpine	3.3E+17	1008.9	3.5
DM17-35-1A-zrc6-p3	dark	0.01	Alpine	3.9E+17	1006.6	6.2
DM17-35-1A-zrc3-p2	dark	0.01	Alpine	3.7E+17	1006.3	5.7
DM17-35-1A-zrc3-p3	Osc. bright	0.01	Alpine	4.1E+17	1007.7	4.2
DM17-13-b-zrc13-p1	Osc. bright	0.01	Alpine	1.5E+17	1007.9	4.6
DM17-13-b-zrc13-p2	Osc. bright	0.01	Alpine	1.1E+17	1007.7	4.7
DM17-13-b-zrc15-p2	Osc bright	0.01	Alpine	8.6E+16	1008.3	4.5
DM17-13-b-zrc15-p3	Osc. bright	0.01	Alpine	4.7E+16	1008.3	4.0
DM17-13-b-zrc16-p1	Osc. bright	0.01	Alpine	1.7E+17	1007.9	5.1
DM17-13-b-zrc16-p2	Osc. bright	0.01	Alpine	8.5E+16	1008.2	4.0
DM17-13-b-zrc16-p3	Osc. dark	0.01	Alpine	2.2E+17	1007.3	5.6
DM17-13-b-zrc16-p4	Osc. bright	0.01	Alpine	5.3E+16	1008.3	3.6
DM17-13-c-zrc7-p1	Osc. bright	0.04	Permian	6.6E+17	1009.3	5.8
DM17-13-c-zrc7-p2	Osci. dark	0.01	Alpine	1.1E+17	1011.3	3.9
DM17-13-c-zrc7-p3	undefined	0.01	Alpine	1.3E+17	1010.2	4.3
DM17-13-c-zrc10-p1	dark	0.01	Alpine	5.2E+17	1006.2	10.6
DM17-13-c-zrc10-p2	bright	0.01	Alpine	1.4E+17	1008.3	3.3
DM17-13-c-zrc10-p3	Osc. dark	0.01	Alpine	2.3E+17	1007.4	5.0

Note that Equation 1 presumes a U isotopic composition of 99,28% ^{238}U and 0.72% ^{235}U. The resulting D_a values are reported in Table 6.2.

Completely buried zircon inclusions

Raman spectra collected on the completely buried zircon crystals have higher wavenumbers (from 1010 cm^{-1} up to 1013.5 cm^{-1}) with respect to the partially exposed grains, with a Γ mostly between 3.5 and 5.5 cm^{-1}. Only a few analyses reach values up to 6.5 cm^{-1} (Figure 6.4). The overlap between the two sets of inclusions is limited to about 10% of the analyses.

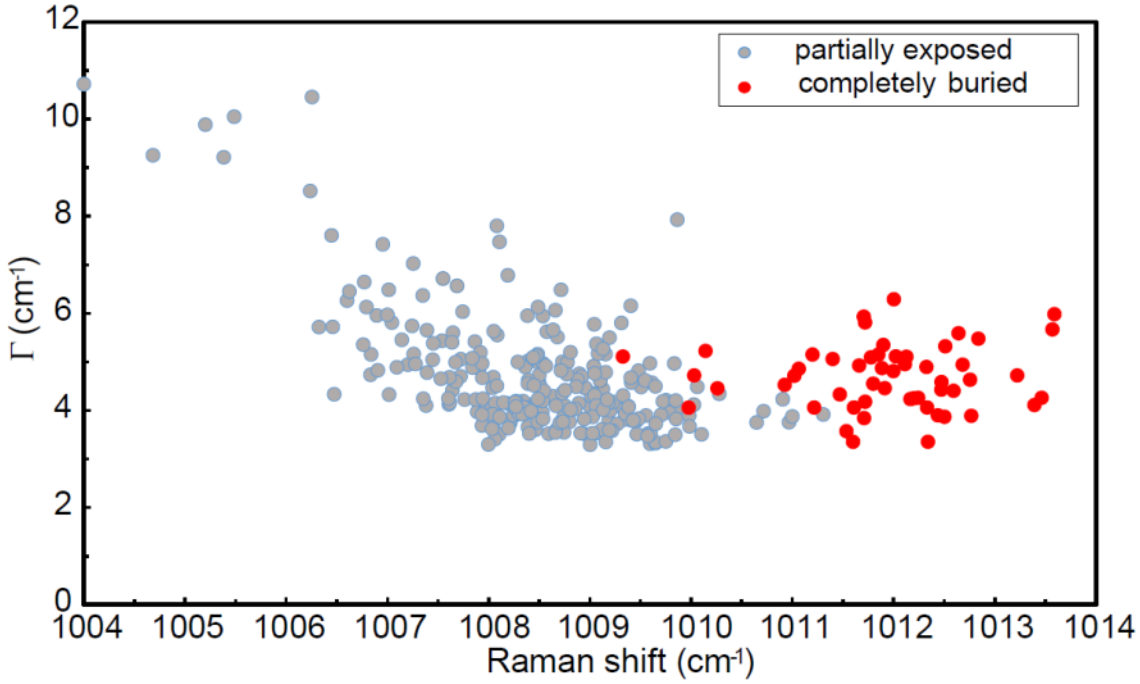

Figure 6.4. Γ and Raman shift of partially exposed vs completely buried zircon inclusions

The data from the exposed and fully enclosed zircon inclusions can also be analysed in terms of the wavenumber difference (Δω) between the B_{1g} mode near 1008 cm^{-1} and the A_{1g} mode near 440 cm^{-1} rather than the *absolute* wavenumber. In this way, since the data were collected along different sessions of measurements, we can avoid any possible effects due to instrumental drift. As shown previously by William and Knittel (1992), and more recently

by Binvignat et al. (2018), both phonon modes show an increase in the phonon wavenumber as the hydrostatic pressure increases. However, as reported from the same authors, the A_{1g} mode shows a weaker pressure dependence with respect to the B_{1g} mode and, therefore, to an increase of the pressure acting on the crystal should correspond an increase in the value of $\Delta\omega$ (Figure 6.5).

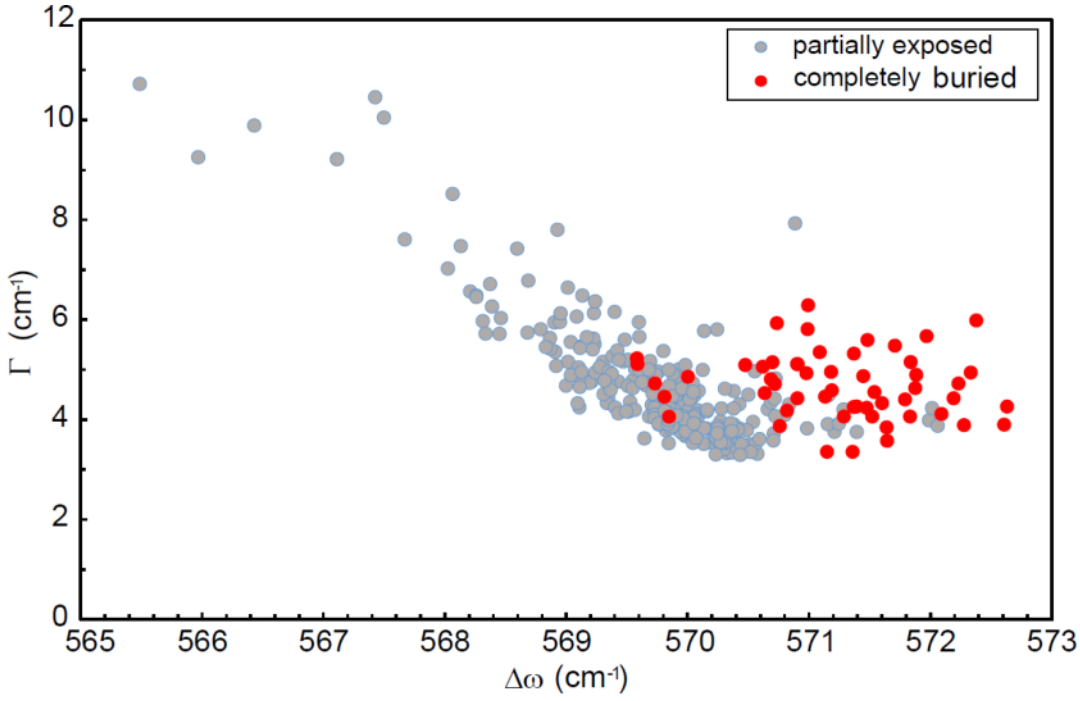

Figure 6.5. Variation of peak width Γ of the B_{1g} mode near 1008 cm^{-1} as a function of $\Delta\omega = \omega_{1008} - \omega_{440}$ of partially exposed and selected completely-buried zircon inclusions.

6.4 Discussion

Effect of minor and trace elements on zircon Raman shift

A large number of non-formula elements can be incorporated in the zircon crystal structure, however, most of them are usually far below 1 wt% (e.g. Hoskin and Schaltegger 2003), with the notable exception of Hf. Raman data measured on the isomorphic series $ZrSiO_4$ – $HfSiO_4$ suggest that even if as much as 25% of all Zr ions are replaced by Hf the frequency variation of the main peaks does not exceed 3 cm^{-1} (Hoskin and Rodgers, 1996).

Furthermore, Nasdala et al. (2002) suggested that positions and Γ of the main peaks in annealed, metamict gemstone-quality zircon, containing up to 6000 ppm of U and 16300 ppm of Hf, deviate less than 1 cm^{-1} from the data of pure well-crystalline $ZrSiO_4$. Therefore, since the exposed zircon inclusions considered in this study contain impurities and trace elements below these values (maximum U content is 5060 ppm and maximum Hf content is 14570 ppm, see Table 1), the effect of chemical variations on these Raman spectra is negligible for this set of samples.

Zircon variation in HREE composition (i.e. depletion in the Alpine domains) has been previously interpreted as the result of growth zoning during metamorphism in a fractionating bulk composition where REE are largely incorporated in garnet (e.g. Gautiez-Putallaz et al., 2016). Indeed, the garnet host shows a similar REE pattern along a core-to-rim line profile (e.g. Gautiez-Putallaz et al. 2016), indicating equilibrium conditions with the associated zircon grains. The qualitative $^{206}Pb/^{238}U$ measurements confirm that zircon crystals showing a flat HREE pattern throughout the entire grain are completely metamorphic in origin. In this regard, it is important to note that, although REE chemical zonation does not influence the main Raman scattering features, such as peak broadening and position, it can give rise to heterogeneous photoluminescence, and hence to different background levels of the Raman spectra collected from zones. Besides, depending on the excitation laser wavelength, additional photoluminescence peaks may be observed next to the fundamental Raman peaks of zircon.

Metamorphic vs inherited zircon domains

Charge contrast or cathodoluminesce imaging of metamorphic and inherited zircons usually show notable differences in terms of the corresponding internal texture (e.g. Rubatto and Gebauer 2000, Corfu et al. 2003). Oscillatory-zoned grains have been chemically interpreted

as the result of alternating depletion and enrichment in trace elements (i.e. U and Y) during crystal growth at the crystal-melt interface. On the other hand, bright domains at the rim of the crystals usually show higher and homogeneous CL-emission, presenting irregular shape that often overgrows the pre-existing crystals whose texture can sometimes be evident as a relic (Rubatto and Gebauer, 2000). Our results indicate that metamorphic zircon can also include dark, bright, oscillatory and undefined CC domains. This observation warns against using internal zircon zoning alone for distinguishing magmatic versus metamorphic zircon. As portrayed in Figure 6.2, bright and oscillatory-bright domains (yellow and blue spots, respectively), have the same Raman spectral features and define the "non-metamict" domain in the diagram (see details below). Therefore, whether or not they are magmatic or metamorphic in origin, from a structural point of view these two domains are effectively equivalent and there will be no difference in the calculated residual stress even if the two domains co-exist within the same crystal.

Finally, in a plot of Γ of the B_{1g} mode near 1008 cm^{-1} vs D_{α}, most of our data for the Alpine domains fall within the broad interpolation trend given by Nasdala et al. 2001 (Figure 6.6). Nasdala et al. (2001) interpreted the data falling outside of this band as the possible effects of thermal annealing in the crystal. Then, in this case, the few points outside the interpolation band are interpreted as the result of possible partial annealing of inherited zircon cores (Permian and Caledonian in age) during the Alpine metamorphism.

Effect of metamictization and annealing on Raman shift

Previous studies have established that partial metamictization can have a major influence on zircon Raman spectra (e.g. Zhang et al., 2000; Geisler et al., 2001; Nasdala et al., 2001; Binvignat et al. 2018). In general, depending on the degree of metamictization, zircon crystals can show a

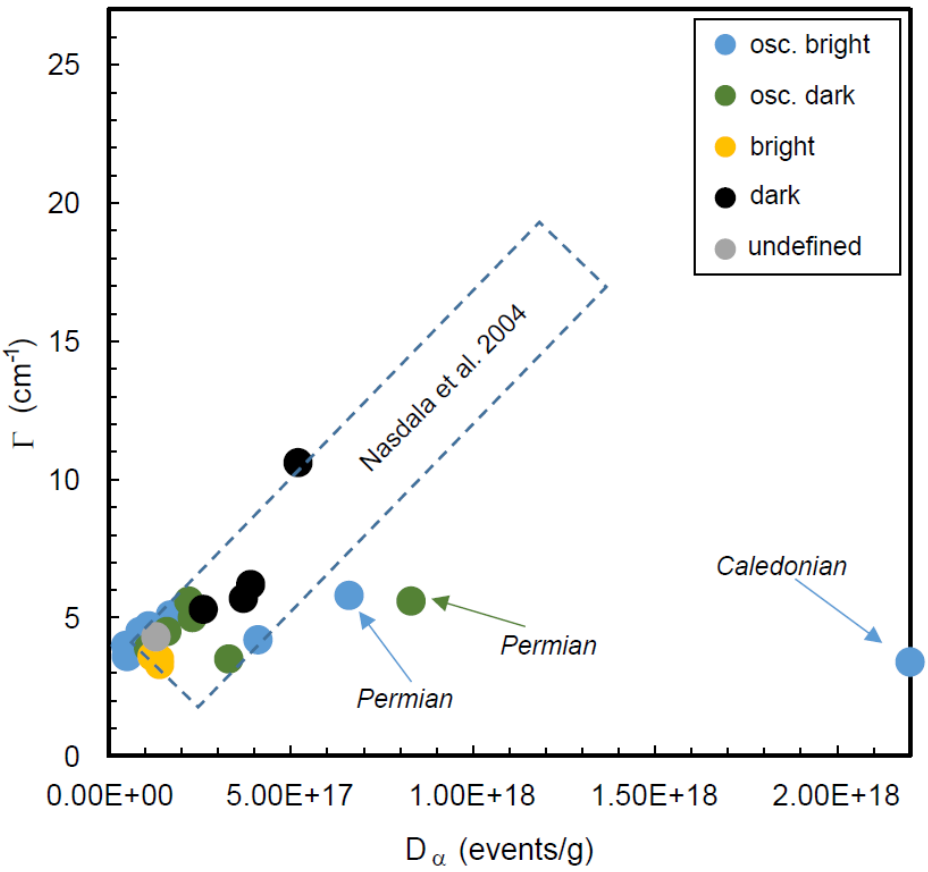

Figure 6.6. FWHM of the B_{1g} mode near 1008 cm^{-1} as function of the effect of increasing metamictization in terms of accumulated radiation dose.

significant Raman peak broadening and frequency shift toward lower wavenumbers with respect to pristine samples taken as reference. Furthermore, Geisler et al. (2001) pointed out the possible heterogeneous (*step-evolution*) effect that annealing could have on peak broadening and position.

Based on these considerations, the relationship between the peak width and the Raman shift (Figure 6.2) can be exploited as a discriminant between partially metamict/annealed crystals and pristine crystals, even when they are completely buried within their mineral host (see also Zhong et al. 2019). Indeed, differently to phonon wavenumber, variation in the Γ of a Raman peak is independent of the level of the minor amounts of stress (Binvignat et al., 2018) usually recorded in host-inclusion systems. It follows that, when considering zircon inclusions, a buried partially metamict crystal should present a peak width Γ comparable to

partially metamict crystals exposed at the surface, and the same is valid for well-crystalline zircon grains. Therefore, in this case, the measurements with Γ values greater than 5 cm^{-1} showing an inverse relationship with the Raman shift, represent partially metamict/annealed domains. On the other hand, lower Γ values (i.e. 3.5 – 5.0 cm^{-1}) with no correlation with the Raman shift are associated with non-metamict domains. In this regard, it is worth noting that Alpine zircons with high U contents fall into the metamict domain.

Geisler and Pidgeon (2002) pointed out that possible annealing processes may influence both the Raman shift and the peak width, as well as the relationship between them during secondary geological processes. However, from their results, it is evident that such effects are critical for zircon with moderate to heavy levels of radiation damage (i.e. $\omega < 1004$ cm^{-1} and $\Gamma >$ than 11-12 cm^{-1}). In this study, the zircon inclusions displaying a negative correlation betwen ω and Γ all have $\Gamma < 11$ cm^{-1} and $\omega > 1004$ cm^{-1}. This correlation can be tentatively interpreted as an indication that, as previously stated (e.g. Figure 6.6), annealing effects were negligible or absent in most of the samples over the relatively short geological evolution (280 or 35 Ma to present) and fast subduction metamorphism (Gebauer et al. 1997, Rubatto and Hermann 2001, Gauthiez Putallaz et al. 2016).

However, it is difficult to make a rigorous prediction of the effect of metamictization on the determination of the residual pressure of a buried inclusion. For zircon with Γ larger than 5 cm^{-1} there are at least two additional unknown variables:

- The reference wavenumber ω_0 of an equally metamict free crystal;
- The phonon mode compressibility $\beta = [1/\omega_0][d\omega/dP]$

Both variables are very sensitive to the accumulated radiation dose D_α (e.g. Binvignat et al., 2018). Unfortunately, the dispersion of the data in the established $\Gamma - D_\alpha$ trend is, in this case, too large to give a reliable value of D_α and consequently of ω_0 and β for the purposes of Raman thermobarometry.

Effect of zircon size on Raman shift for partially exposed inclusions

For completely unstressed pristine crystals, the phonon wavenumber usually is expected not to exceed the values of 1008.5 – 1009 cm^{-1} (see Binvignat et al., 2018; Geisler et al., 2001). Nevertheless, our partially exposed grains, even considering only the non-metamict domain in Figure 6.2, show a larger variation (up to 1011 cm^{-1}).

As reported by Campomenosi et al. (2018), partially exposed inclusions can still preserve a notable stress state in terms of Raman peak shift as function of the inclusion exposition degree and size. In order to better clarify this issue, Figure 6.7 shows a Γ vs Δω diagram of partially exposed inclusions discriminating between grains with different size (< and > 50 microns). Note that, in this case, we show only data from the exposed inclusions showing bright and or oscillatory-bright domains at CC because only for such domains we can safely exclude other effects described above. Data from inclusions of different size largely overlap. However, about 20% of the smaller inclusions have a higher Δω than the larger one (with one exclusion) and reach a Δω of 572 cm^{-1} that are never observed in the larger inclusions.

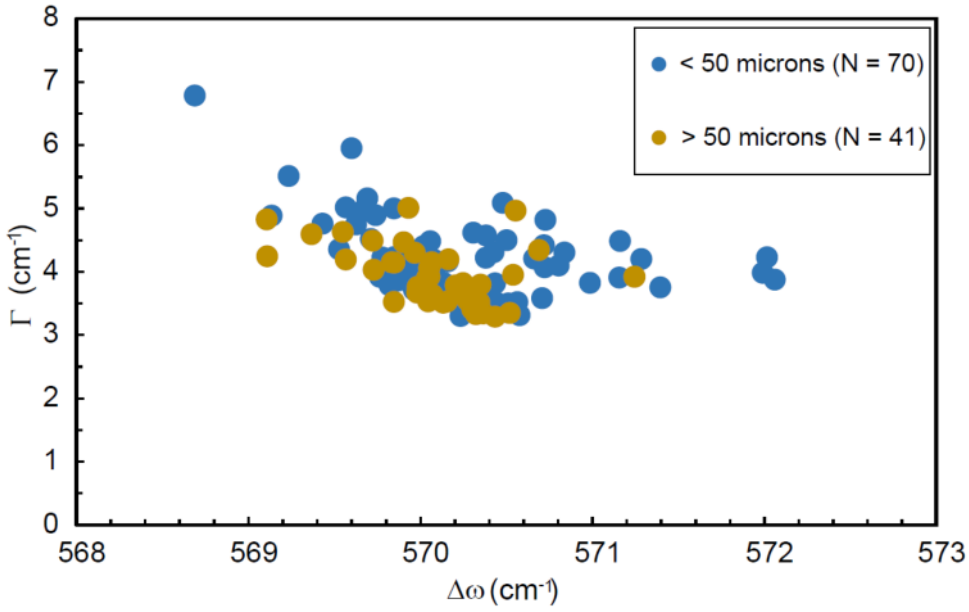

Figure 6.7. Γ of the B_{1g} mode near 1008 cm^{-1} vs $\Delta\omega = \omega_{1008} - \omega_{440}$ comparing small (< 50 microns) and large (> 50 microns) partially exposed zircon inclusions. The spots refer only to bright and oscillatory bright domains

This is in agreement with theoretical predictions (Mazzucchelli et al., 2018) for which, within the same host, small inclusions, when partially exposed, tend to retain more stress, due to the larger surface-to-volume ratio, i.e. larger impact of the host upon relatively larger surface of the inclusion. On the other hand, small inclusions should exhibit less dispersion of the degree of exposure. Hence, the quite large spread of our data is most probably due to the superposition of both effects related to the inclusion size: the surface-to-volume ratio and the degree of exposure.

A new protocol for the selection of zircon inclusions in garnet for elastic thermobarometry

Based on the above considerations, we propose a simple protocol for selecting zircon inclusions to get reliable residual pressure estimates for elastic barometry.

- Buried crystals must be isolated from other inclusions, section surfaces, host boundary, cracks and from any other kind of boundaries. This implies that thicker sections (i.e. 300 microns) are better (see also Campomenosi et al. 2018).
- At least 2-3 measurement spots for each crystal moving from core to rim should be performed: this enables detection of eventual structural heterogeneity within the crystal. For this pourpose, it is better to use a spectrometer with a confocal optical microscope in order to reach the best spatial resolution.
- An instrumental sepctral resolution equal or better than 2 cm^{-1} should be used and only those inclusions presenting a Γ of the B_{1g} mode near 1008 cm^{-1} smaller than 5 cm^{-1} should be considered. Note that this value represents the summation of the analytical uncertainty (i.e. instrumental spectral resolution) to the minimum value of about 3 cm^{-1} that has been measured on several grains by the two different spectrometers (see Figure 6.4).

- Only inclusions in which the phonon wave number and the Γ is constant across the entire crystal volume should be selected.
- If Γ is constant, but the phonon wavenumber changes across the crystal volume there could be effects due to the shape of the inclusion (Campomenosi et al. 2018). In this case it is recommended to consider the measurement collected at the centre of the crystal to calculate the residual pressure of the inclusion.
- Partially exposed crystals should not be used as reference to calculate residual stress in the buried inclusions: they can be still under a notable residual stress state. It is recommended using a completely free crystal or large exposed inclusions for which the residual stress state and the metamictization effects are negligible (see for example Figure 6.1-D).
- Whenever possible, a statistically significant amount of partially exposed inclusions should be selected in order to double check their textural complexity by CC or CL imaging and their chemistry. As an alternative, imaging and chemical checks should be performed on inclusions that have been exposed after the Raman measurements.
- Chemical and age measurements should be considered as important corollary information to reconstruct the petrogenesis of the zircon inclusions and the garnet host.

6.5 Implications

Zircon inclusions are difficult to manage correctly for elastic thermobarometry applications and a detailed characterization of the inclusions should be performed before extracting barometric data. In this systematic study the combination of structural and chemical information obtained by different analytical techniques on partially exposed zircon inclusions, allows the structural state of buried crystals for Raman spectroscopic

measurements to be determined reliably. These results provide a solid basis for the selection of reliable zircon inclusions to use for elastic thermobarometry applications. These methods, in combination with the already rich tool set that can be applied to zircon (e.g. Ti-in-zircon thermometry (Watson et al., 2006), U-Pb geochronology, oxygen isotopes) will provide an even more detailed characterization of P-T-t-fluid and deformation history of metamorphic rocks.

Chapter 7

Measuring strain and stress distribution in minerals showing optical anomalies: a new Raman spectroscopy approach

This chapter reports the results and discussions from the paper:

Campomenosi, N., Mazzucchelli, M. L., Mihailova, B., Angel, R. J., Alvaro, M. (2020) *Using polarized Raman spectroscopy to study the stress gradient in mineral systems with anomalous birefringence.* Contribution to Mineralogy and Petrology, **DOI :10.1007/s00410-019-1651-x**.

Original abstract

Polarized Raman spectroscopy was applied to garnet hosts which exhibit anomalous birefringence around inclusions of zircon and quartz, in order to elucidate the spatial distribution of the anisotropic strain fields in the vicinity of the host-inclusion boundary. We show that there is a direct relationship between the stress-induced birefringence and the Raman scattering generated by the fully symmetrical phonon modes (the A_{1g} modes in cubic crystals). Our experimental results coupled with selected finite element models show that the ratio between the measured Raman peak intensity collected in cross and parallel polarized scattering geometries of totally symmetrical modes, represents a useful tool to constrain the radial stress profile in the host around the inclusions. Further, we demonstrate how group-theoretical considerations and tensor analysis of the morphic effect (external-field-induced change of the symmetry) on the phonons and the optical properties of the host can help to derive useful information on the symmetry of the stress field. Finally, we show experimentally that, under the same amount of applied stress, this approach is more sensitive than the commonly-used approach of measuring differences in phonon frequencies and provides better opportunities to map the spatial variations of strain. This approach is an alternative technique to study structural phenomena associated with anomalous birefringence in host crystals surrounding stressed inclusions, and could be applied to other systems in which similar optical effects are observed.

7.1 Introduction and motivation

Anomalous birefringence in minerals is the result of strains imposed on crystals that break their symmetry. Such strains can be generated by intra-crystalline processes during crystal growth or mineral re-crystallization, and by inter-crystalline processes due to the constrained interaction between mineral grains with different physical properties (see Shtukenberg and Punin, 2007 for a comprehensive review of the subject). One simple example is host-inclusion systems, in which an excess stress is developed in a soft mineral trapped inside a stiff cubic garnet host, and this stress generates strains in the host that break its cubic symmetry. As a consequence, an optical birefringence halo in a cubic host can be observed in the vicinity of the host-inclusion boundary (e.g. Howell et al., 2010).

The study of the complex thermo-elastic interaction in host-inclusion systems is of increasing interest in the petrology because of its potential to retrieve the pressure-temperature (P-T) conditions in metamorphic rocks at the time of inclusion entrapment (Rosenfeld and Chase, 1961; van der Molen and van Roermound, 1986; Izraeli et al., 1999; Enami et al., 2007; Kohn, 2014; Angel et al., 2014; Zhukov and Korsakov, 2015; Anzolini et al., 2018; Murri et al., 2018). However, while controversial issues related to the application of elastic barometry to non-ideal cases have been addressed (e.g., Angel et al., 2015; Mazzucchelli et al., 2018; Murri et al., 2018), the strain state in the host mineral is still poorly understood. Howell et al. (2010) carried out a detailed description of the birefringence induced in cubic host minerals by inclusions. In their work, the analysis of the induced birefringence was treated in terms of a change in the shape and orientation of the optical indicatrix of the host as a function of the stress field arising from the adjacent pressurized inclusion. On the other hand, Izraeli et al. (1999) were the first to consider the change in the Raman peak positions in a diamond host surrounding stressed inclusions while Nasdala et al. (2003; 2005) applied 2D Raman mapping of the diamond peak position (near 1332 cm^{-1})

and peak width, in order to analyse the spatial distribution of the strain in the diamond host. Nevertheless, the use of the shift in the Raman peak position measured in the host as a proxy for the stress in the inclusion is still controversial. When an inclusion is under a residual stress, the stress in the host close to the inclusion is not isotropic but a radial stress and two tangential components are developed even for a spherical inclusion (see e.g. Zhang, 1998; Mazzucchelli et al. 2016). As a consequence, the stress calculated by measuring the Raman peak position in the host and applying a simple hydrostatic calibration cannot be equal to the average pressure in the inclusion. Indeed, from simple arguments of force balance, we should expect that only the radial components of the stress of the two minerals are equal to each other (e.g. Zhang, 1998, Angel et al., 2015). These considerations explain why, usually, different stress values were inferred between the host and the inclusion, when derived from the Raman peak positions (Izraeli et al., 1999).

This study introduces an alternative approach for strain analysis in host-inclusion systems that exploits the symmetry relationship between the optical indicatrix and the Raman polarizability tensor of the fully-symmetric phonon modes, in order to relate the stress-induced optical anomalies in host cubic crystals to changes in the intensities of the Raman bands. This will be shown by theory supported by preliminary experimental results on natural samples.

7.2 A bit of theory: the *morphic effect* in crystals and in their lattice dynamics

In general, the term ’morphic effect’ refers to a reduction of the point symmetry of a crystal caused by an applied external anisotropic force field (Nye, 1957). The Neumann-Curie principle defines the way in which this modification takes place: a crystal under an external force will exhibit only those point symmetry elements that are common to the unperturbed

crystal and the applied force field (e.g. Nye, 1957; Schtukenberg and Punin, 2007). If this perturbation extends over a discrete portion of a crystal, which exceeds the length scale of short and intermediate range order, i.e. at least 10 unit cells, it will modify the crystal's macroscopic physical properties. An example is the anomalous birefringence haloes observed under cross-polarized light in cubic crystals that surround pressurized inclusions (e.g. Figure 7.1). Indeed, when the inclusion is strained due to the confined space, it exerts a radial stress on the surrounding host that compresses the host in a radial direction, and at the same time the host is expanded in the tangential directions (e.g. Angel et al., 2015). To take a simple example, consider a point in a cubic host crystal adjacent to a soft over-pressured inclusion, where the ***c***-axis of the garnet is parallel to the radius. The compressive radial stress will shorten the c-axis of the garnet, and the a- and b-axes that are tangential to the inclusion wall will be expanded. Locally, the symmetry of the garnet at this point has been reduced to tetragonal, and it is therefore expected to exhibit optical birefringence. Thus the strains created by the inclusion lower the point symmetry of the host which in turn break its optical extinction rules (Howell et al., 2010; Howell, 2012). In this particular case, the anomalous birefringence represents the morphic effect (a symmetry reduction) due to the external stress field imposed on the host by the host-inclusion boundary.

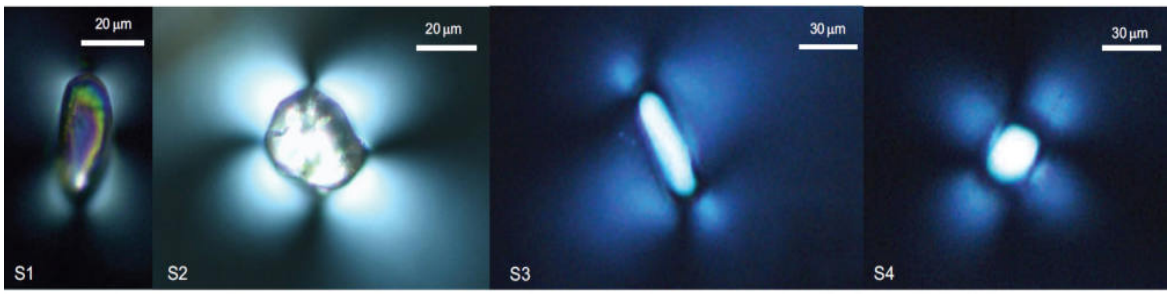

Figure 7.1. Zircon (S1 and S2) and quartz (S3 and S4) stressed inclusions in garnet host crystals under cross-polarized light. Note that the typical cross-shaped extinction pattern is given by the orientation of the microscope polarizers, and remains fixed in orientation upon rotation of the microscope stage.

In general, the occurrence of birefringence in a crystal is due to the difference between the refractive indices along different directions and it is related to the shape of the optical indicatrix.

In a tensorial form, this is represented by the symmetric 2nd-rank matter tensor of relative dielectric impermeability $\boldsymbol{B}$. Then, if we do not consider the contribution of the wavelength of the light, the intensity of the transmitted light at the optical microscope can be expressed as function of the polarization vectors of the incident and transmitted light, $\boldsymbol{e^{pol}}$ and $\boldsymbol{e^{an}}$ respectively, and of the dielectric impermeability tensor $\boldsymbol{B}$ as follows:

$$I \propto \left| e_i^{pol} \, B_{ij} \, e_j^{an} \right|^2 \quad (7.1)$$

Note the use of Einstein's summation convention in Eq. 1 and throughout this paper, which means a summation over all the index values when an index variable appears twice in a single term (see also Appendix). Under an external anisotropic force, such as an electric field, magnetic field or a stress field, the values of the components B_{ij} of the tensor will change according to the symmetry of the applied force, which are phenomena called the electro-optic, magneto-optic and piezo-optic effects respectively. In the case of piezo-optic effect, the components B_{ij} of the resulting tensor can be considered as composed of intrinsic and force-field induced constituents:

$$B_{ij} = B_{ij}^0 + \Delta B_{ij} = B_{ij}^0 + \left[\left(\frac{dB_{ij}}{d\sigma_{kl}} \right) \sigma_{kl} \right] = B_{ij}^0 + [\pi_{ijkl} \sigma_{kl}], \quad (7.2)$$

where $\pi_{ijkl} = \frac{dB_{ij}}{d\sigma_{kl}}$ is the piezo-optic 4th-rank tensor (Nye, 1957).

On the other hand, the Raman effect is due to inelastic scattering of light by optical phonons. Therefore, Raman activity is related to changes of the electrical polarizability of the crystal during the atomic vibrations and is described by the Raman polarizability tensor $\boldsymbol{\alpha}$. This, like the relative dielectric impermeability tensor $\boldsymbol{B}$, is a second-rank symmetric tensor and can be represented geometrically by an ellipsoid called the Raman polarizability ellipsoid. Each Raman-active phonon mode *m* in a crystal will have its own Raman polarizability

tensor $\boldsymbol{\alpha^m}$. Therefore, in the same way that the intensity of light transmitted through a crystal viewed between polarisers depends on the $\boldsymbol{B}$ tensor, the Raman intensity of any phonon mode depends on the polarisation directions of the incident and scattered light, described by the unit vectors $\boldsymbol{e}^i$ and $\boldsymbol{e}^s$, and the Raman polarizability tensor:

$$I^m \propto \left| e_k^i \alpha^m{}_{kl} e_l^s \right|^2 , \quad (7.3)$$

Thus the intensity of the Raman scattering peak from the mode depends on the orientation of the electric-field unit vectors e^i and e^s of both the incident and scattered light. Experimentally, the directions of the electric-field vectors of the incident and scattered light are defined by the polarisers placed in the incident and scattered beam paths, so e^i and e^s (in the crystal) depend on the orientation of the crystal with respect to the polarisers in the spectrometer system. Written out in the terms of the individual components of the tensors, equation (3) becomes:

$$I^m \propto \left(e_1^i \alpha^m{}_{11} e_1^s + e_1^i \alpha^m{}_{12} e_2^s + e_1^i \alpha^m{}_{13} e_3^s + e_2^i \alpha^m{}_{21} e_1^s + e_2^i \alpha^m{}_{22} e_2^s + e_2^i \alpha^m{}_{23} e_3^s + \right.$$

$$\left. e_3^i \alpha^m{}_{31} e_1^s + e_3^i \alpha^m{}_{32} e_2^s + e_3^i \alpha^m{}_{33} e_3^s \right)^2$$

with $\alpha^m{}_{kl} = \alpha^m{}_{lk}$ for first order Raman scattering.

Therefore, the experimentally-observed Raman intensity of a given mode depends on three factors (i) the intrinsic symmetry constraints on the Raman polarizability tensor $\boldsymbol{\alpha}^m$; (ii) the orientation of the crystal with respect to $\boldsymbol{e}^i$ and $\boldsymbol{e}^s$, and (iii) the mutual orientation of the polarisation of the incident and scattered light beams $\boldsymbol{e}^i$ and $\boldsymbol{e}^s$ which are experimentally determined by the polarisers. In parallel polarized spectra (denoted here as HH spectra) $\boldsymbol{e}^i \parallel \boldsymbol{e}^s$ and in cross polarized spectra (VH spectra) $\boldsymbol{e}^i \perp \boldsymbol{e}^s$.

As described above for the relative dielectric impermeability tensor, the Raman polarizability tensor $\boldsymbol{\alpha}^m$ will also change under anisotropic external forces. This change is usually referred to as the *morphic effect* on the lattice dynamics (Anastassakis, 1980; Gregora 2006) and generally, the force field can influence both the phonon mode energies

(i.e. peak positions) and the atomic vector displacements (i.e. symmetry of the vibrational mode). The latter is what determines the ${\alpha^m}_{ij}$ components, that is, the shape and orientation of the polarizability ellipsoid. Therefore, in the case of an applied stress field we have (Gregora, 2006):

$$\alpha^m{}_{ij} = {\alpha^{m_0}}_{ij} + \Delta\alpha_{ij} = \alpha_{ij}^{m_0} + \left[\left(\frac{d\alpha^m{}_{ij}}{d\sigma_{kl}}\right)\sigma_{kl}\right] = \alpha_{ij}^{m_0} + [\tau_{ijkl}\sigma_{kl}]\,, \qquad (7.4)$$

where $\tau_{ijkl}=\frac{d\alpha_{ij}}{d\sigma_{kl}}$ is a 4th-rank tensor and will be referred hereafter as the piezo-phonon tensor. Furthermore, in each crystal class the Raman polarizability tensor of the fully-symmetric modes obeys the same symmetry constraints as any 2nd-rank property tensor, including $\boldsymbol{B}$, because all point-symmetry elements in the crystal equilibrium structure are preserved during the atomic vibrations of a fully-symmetric mode. Consequently, $\boldsymbol{\tau}$ for the fully-symmetric phonons will be subjected to the same symmetry constraints as the piezo-optic tensor $\boldsymbol{\pi}$. Then, we should expect a one-to-one correspondence between the anomalous (symmetry-forbidden) cross-polarized (VH) Raman scattering of totally symmetric modes and the anomalous occurrence of birefringence: for any stress-induced distortion of the optical indicatrix a proportional stress-induced distortion of the Raman polarizability ellipsoid should be expected. This will modify the Raman selection rules of a given phonon mode resulting in Raman scattering, which appears anomalous with respect to the undistorted structure of the mineral. Thus, by measuring the stress-induced depolarization of the Raman signal one can go beyond a simple visual inspection and quantify the micrometre-scale gradients of elastic stress and strain in mineral systems such as host-inclusion systems or mineral grains exhibiting inhomogeneous birefringence (i.e. undulose extinction).

7.3 Specific methodology

The selection of suitable inclusions for this study was conducted by means of optical microscopy. The garnet host surrounding the selected inclusions presents clear birefringence haloes and is free of fracturing. The inclusions are entirely embedded in their host and located approximately at the middle of the thin polished section (Figure 7.1), in order to avoid any artificial effects from close proximity to the external surface of the host (Campomenosi et al., 2018). For this study we selected two zircon inclusions, one elongated (S1) and one rounded (S2) from coesite-bearing whiteschist rocks of the UHP Brossasco-Isasca unit of the Dora-Maira massif (e.g. Chopin, 1984; Hermann, 2003) as well as two quartz crystals S3 and S4, elongated and rounded respectively, from a diamond-grade eclogite xenolith of the Mir Kimberlite pipe (Korsakov et al., 2009). All of these inclusions are trapped in pyrope-rich garnet hosts. Peak metamorphic conditions for the whiteschist rocks in Dora-Maira Massif were constrained between 3 and 4 GPa and 730 °C (e.g. Chopin et al., 1991; Schertl et al., 1991; Hermann, 2003) while the estimated entrapment conditions for the Mir Kimberlite pipe were 3 GPa and 850 °C (Alvaro et al., 2019). The analysis of the Raman spectra from the zircon inclusions (e.g. Geisler et al., 2001; Nasdala et al., 2001; see also Chapter 6) showed that they are not affected by radiation damage that would strongly affect their physical properties (e.g. Binvignat et al., 2018) and thus the residual pressure acting on the host wall.

Micro-Raman measurements were collected and processed in the same way as described in Chapter 2. Point analyses have been conducted on the inclusions and the corresponding host crystals across the induced birefringence haloes in both parallel (HH) and cross (VH) polarized scattering geometries. As a strain-free standard of the host we simply selected a spectrum from a birefringence-free area of the host well away from any inclusions. In order

to determine the spatial distribution of the morphic effect around an inclusion, the point analyses of the host were performed along radial trails with different orientations with respect to both the inclusion and the polarization of the incident light, as shown in the scheme in Figure 7.2.

Motivated by the ideas in equation (2), to detect the presence of morphic effects by Raman spectroscopy, we have used the depolarization ratio of totally symmetric modes:

$$\rho = \frac{I_{\perp}}{I_{\parallel}}, \qquad (7.5)$$

where $I_{\perp}$ is the measured intensity of a Raman peak in cross-polarized geometry (VH) and $I_{\parallel}$ is the measured intensity of the same peak in parallel-polarized geometry (HH). In this way, we can obtain information on the change in the magnitudes of the non-diagonal (from the VH spectra) and diagonal components (from the HH spectra) of the Raman polarizability tensor and thus the phonon symmetry properties. Indeed, this is a simple technique commonly used to probe the symmetry of a phonon mode in a given crystal class (e.g. Nakamoto, 2009).

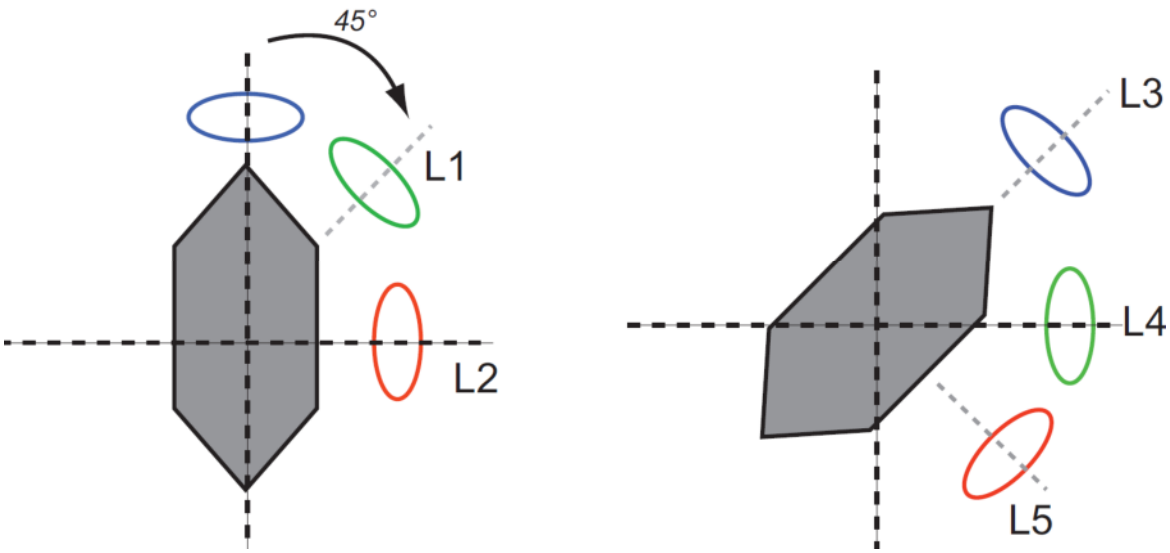

Figure 7.2. Direction of analysis transects across birefringent domains in garnet. The three ellipsoids correspond ideally to the three main possible strained domains of the host surrounding a stressed inclusion as function of its shape. The lines oriented to 45 degrees (i.e. L1, L3 and L5) with respect the polarizers were collected in both parallel (HH) and crossed (VH) scattering geometry while the horizontal ones (i.e. L2 and L4) only in parallel scattering geometry.

In our case, it can provide important information on how the phonon symmetry properties change as function of the morphic effect. Hence, the angular dependence of the depolarization ratio can be directly associated with the extinction angle of a crystal in cross-polarized light when using an optical microscope.

Finally, the experimental depolarization ratio has been compared to the radial component of the strain in the host computed with a Finite Elements (FE) analysis of a simplified 3D model of the inclusion S2. To compute the strain field around the inclusion we first measured the residual strain in our inclusion using the multiple-peak approach of Murri et al. (2018) (see the Results section and Table 7.1). We applied the concept of the relaxation tensor (Mazzucchelli et al., 2019) for the system zircon-in-pyrope to compute the unrelaxed strain in the inclusion, i.e. the eigenstrain in the equivalent inclusion problem of Eshelby (1957). In our FE model the geometry of the inclusion was reproduced as a 2:1:1 ellipsoid embedded in a practically infinite matrix (i.e. the distance between the inclusion and the boundary of the model is 100 times larger than the radius of the inclusion). The host-inclusion system was discretized with a finer mesh in the region of the host closer to the inclusion where high gradients in strain are expected. We assumed anisotropic elastic properties for both the zircon inclusion (Ozkan et al., 1974) and the pyrope host (Sinogeikin and Bass, 2002). A static finite element analysis was carried out starting from a prestress state applied to the inhomogeneity, corresponding to the unrelaxed strain of our inclusion, and a zero-stress state of the host. This is a non-equilibrium configuration since the tractions at the host-inclusion interface are not balanced. Suitable Dirichlet boundary conditions are applied to the host to prevent rigid body motions. From the FE analysis we obtained the final strain field in the system at equilibrium. The strain in the region of the host surrounding the inclusion was compared with the measured depolarization ratio. Because the strain and the experimental

depolarization ratio have different magnitudes, in order to compare their trends we normalised the experimental depolarization ratio by:

$$\rho_x^n = \frac{(\rho_x - \rho_0)}{C} \quad (7.6)$$

where ρ_x^n is the normalized depolarization ratio at distance x from the host-inclusion boundary, ρ_x is the measured depolarization ratio at the same position, ρ_0 is the measured depolarization ratio of an unperturbed crystal domain (i.e. the reference point) and C is a scale factor given by the ratio between the measured depolarization ratio and the value of the radial component of the strain computed at the host-inclusion boundary.

7.4 Results

All Raman spectra collected from zircon and quartz inclusions, surrounded by anomalous birefringent haloes of their host, show a shift in phonon wavenumbers toward higher values with respect to free crystals taken as reference, indicating the presence of compressive elastic strains in the inclusions. The residual strain of such inclusions can be estimated using the multiple-peak approach by Murri et al. (2018) and the software stRAinMAN (Angel et al., 2018). Table 7.1 reports the peaks used for both quartz and zircon inclusions, their wavenumbers and the resulting strain. Residual pressures (defined as the negative of the mean normal stress) for the zircon inclusions S1 and S2 are 0.5 and 0.6 GPa respectively while for the quartz inclusions S3 and S4 are 0.9 and 1.2 GPa, respectively.

Table 7.1. Strain components and inclusion pressure derived from the corresponding Raman peak position

zircon						
sample	**B_{1g} (cm^{-1})**	**A_{1g} (cm^{-1})**	**E_g (cm^{-1})**	**$\varepsilon_{11} + \varepsilon_{22}$**	**ε_{33}**	**P_{inc} (GPa)**
S1	1,011.39(03)	977.56(25)	359.13(02)	-0.00152(17)	-0.00070(16)	0.5(1)
S2	1,011.58(01)	978.39(02)	360.27(01)	-0.0026(4)	-0.0002(4)	0.6(2)
ref	*1,008.53(02)*	*974.85(05)*	*356.80(01)*			
quartz						
sample	**E (cm^{-1})**	**A_1 (cm^{-1})**	**E (cm^{-1})**	**$\varepsilon_{11} + \varepsilon_{22}$**	**ε_{33}**	**P_{inc} (GPa)**
S3	133.83(04)	473.59(43)	703.63(93)	-0.018(2)	-0.0065(14)	0.9(1)

S4	135.28(08)	475.68(05)	707.51(06)	-0.031(4)	-0.004(2)	1.3(2)
ref	*128.41(01)*	*465.18(01)*	*695.60(61)*			

Garnet are the surrounding host crystals for all of the measured inclusions. The garnet structure is cubic, having a space-group symmetry *Ia3̲d*. Site-symmetry group analysis of unstrained garnet shows that Raman-active modes at the Brillouin-zone centre belong to the following irreducible representations (e.g. Kroumova et al., 2003):

$$\Gamma_{Raman} = 3\,A_{1g} + 8\,E_g + 14\,T_{2g} \qquad (7.7)$$

The Raman polarizability tensors of these vibrational modes in a matrix representation in a conventional coordinate system are given in Table 7.2.

Table 7.2. A matrix representation of the Raman polarizability tensors of the Raman-active modes in garnet

$\begin{pmatrix} a & . & . \\ . & a & . \\ . & . & a \end{pmatrix}$	$\begin{pmatrix} b & . & . \\ . & b & . \\ . & . & -2b \end{pmatrix}$ $\begin{pmatrix} -\sqrt{3}b & . & . \\ . & \sqrt{3}b & . \\ . & . & . \end{pmatrix}$	$\begin{pmatrix} . & . & . \\ . & . & c \\ . & c & . \end{pmatrix}$ $\begin{pmatrix} . & . & c \\ . & . & . \\ c & . & . \end{pmatrix}$ $\begin{pmatrix} . & c & . \\ c & . & . \\ . & . & . \end{pmatrix}$
A_{1g}	E_g	T_{2g}

Which components of the Raman polarizability tensor are zero, and the constraints on the values of the non-zero components, are defined by the symmetry of the mode and of the crystal. As shown in Table 7.2, for the A_{1g} modes in cubic crystals with point symmetry $m\bar{3}m$, $\alpha^{A_{1g}}{}_{11} = \alpha^{A_{1g}}{}_{22} = \alpha^{A_{1g}}{}_{33}$, and $\alpha^{A_{1g}}{}_{12} = \alpha^{A_{1g}}{}_{13} = \alpha^{A_{1g}}{}_{23} = 0$, the same as the constraints on the ***B*** tensor for optical birefringence. This is the reason why the behaviour of the intensities of A_{1g} modes in cubic crystals under stress follows that of the optical birefringence. And the expression for the intensity for A_{1g} mode in cubic crystals becomes:

$$I^{A_{1g}} \propto \left(e_1^i \alpha^{A_{1g}}{}_{11} e_1^s + e_2^i \alpha^{A_{1g}}{}_{22} e_2^s + e_3^i \alpha^{A_{1g}}{}_{33} e_3^s\right)^2 = \left(\alpha_{11}^{A_{1g}}\right)^2 \left(e_1^i e_1^s + e_2^i e_2^s + e_3^i e_3^s\right)^2.$$

This equation shows that the symmetry of the Raman polarizability tensor of the A_{1g} modes in cubic crystals means that the intensity is independent of the direction of propagation of

light through the crystal, and depends only on the relative orientation of the two polarisers to one another. We can now choose any convenient coordinate system for these polarisers and the experiment. For this example, we choose the incident beam to be along the z-axis, and the polarisation direction to be along the x-axis. Thus e^i = [1 0 0]. If one makes measurements in HH polarisation, the polarisation of the scattered beam is parallel to the incident beam, so $e^i = e^s$, and equation above for the intensity becomes:

$I^m \propto \left(\alpha^m{}_{11} e_1^i e_1^s\right)^2 = (\alpha_{11}^m)^2$

By contrast, when the polarisations of the incident and scattered radiation are 'crossed', (i.e. mutually perpendicular and denoted VH), then e^s = [0 1 0] and the intensity will be zero. Thus, in cubic crystals, A_{1g} modes can be observed by polarised Raman spectroscopy with HH polarisation, but are not observed with VH polarisation.

Because the symmetry of the Raman tensor of the A_{1g} modes is the same as the $\boldsymbol{B}$ tensor, we only discuss them. The complication with the E_g and T_{2g} modes is that they are doubly and triply degenerate modes (i.e. effectively two and three phonon modes with the same frequency) in the cubic structure, but can split into 2 (or 3 for T_{2g}) modes when the cubic symmetry is broken. Therefore the analysis of the evolution of their peak positions and intensities in the strain halo around the inclusion is complex and is not expected to exactly follow the optical birefringence. We further focus on the A_{1g} mode near 928 cm^{-1} because it has the highest intensity and is well-resolved from other Raman peaks from both the garnet and the inclusion crystals.

Figure 7.3 shows the scattering behaviour of the A_{1g} mode near 928 cm^{-1}, for both parallel and cross-polarized scattering geometry, in representative points located at different distances from the inclusion and along transect with different orientation with respect to the polarizers (Figure 7.3a and b). For any orientation of the crystal, A_{1g} modes (totally symmetric modes in garnet) in cross-polarized scattering geometry (VH in Figure 7.3) should be Raman inactive due to the polarization selection rules (see Appendix). However, this is

true only for spectra collected well away from the areas exhibiting a birefringence halo (i.e. *unstrained* in Figure 7.3) while Raman spectra collected closer to the inclusion (e.g. *p1*, *p2* and *p3* in Figure 7.3-a), within the areas having a birefringence halo, show a tiny but well-resolved Raman activity in the cross polarized scattering geometry.

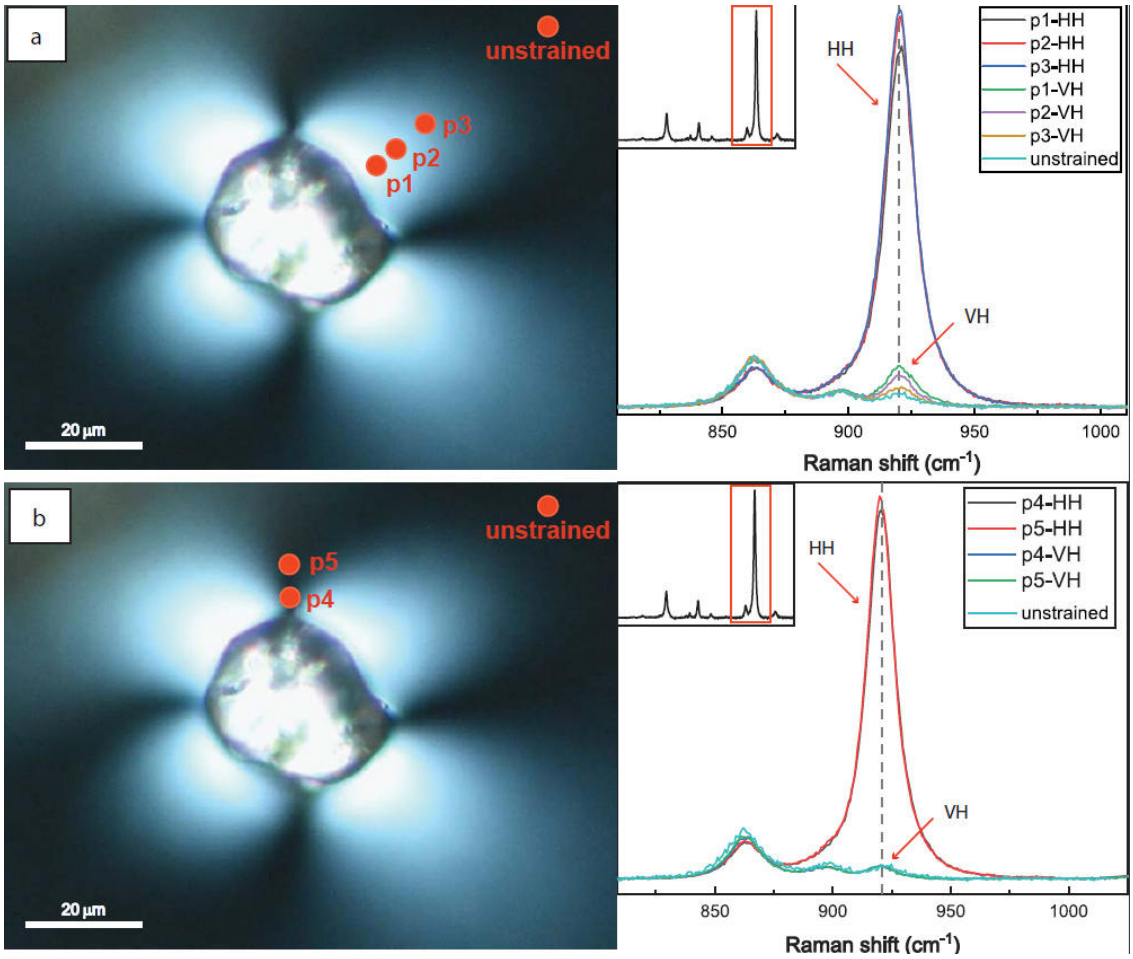

Figure 7.3 Anomalous Raman scattering of totally symmetric vibration A_{1g} near 928 cm^{-1}. VH and HH spectra correspond to cross and parallel-polarized scattering geometry respectively.

The depolarization ratio ρ of this A_{1g} mode calculated from these spectra shows a clear trend with a maximum close to the inclusion (up to 0.06) and it drops to ~0.005 (i.e. effectively zero allowing for experimental noise) outside the birefringence halo (Figure 7.4). Table 7.3-a b reports the depolarization ratio values for all of the measured transects radially distributed around both the zircon and quartz inclusions.

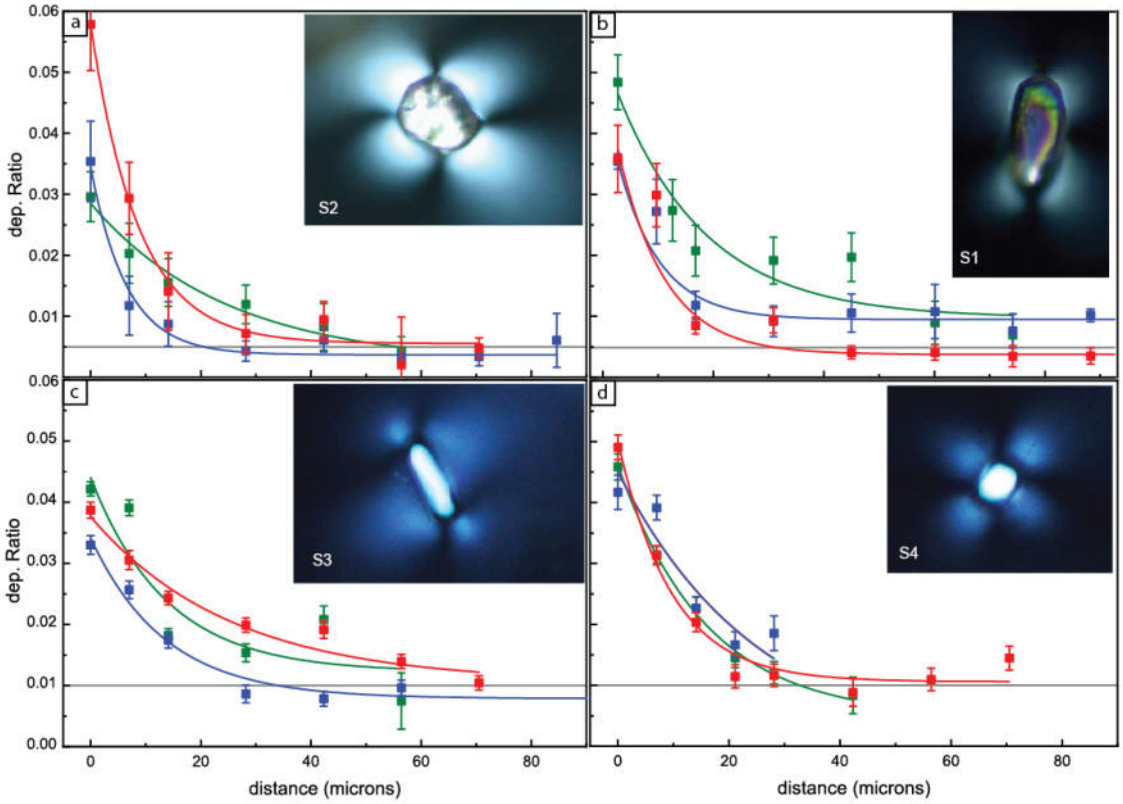

Figure 7.4. Depolarization ratio versus distance of totally symmetric mode near 928 cm^{-1} for garnet surrounding zircon and quartz inclusions. Experimental results with associated errors computed on fitted intensity are plotted as symbols, and the lines are the best fit of Equation 8. Colour coding represents different directions (Figure 7.2).

It is important to point out that the maximum of stress-induced cross-polarized Raman scattering is observed along transects oriented at 45 degrees with respect to the polarization of the incident light $\boldsymbol{e}^i$, (Figure 7.3) which corresponds exactly to the maximum interference colour in crossed-polarised optical imaging. On the other hand, the stress-induced cross-polarised Raman scattering is zero along transects that are parallel or perpendicular to $\boldsymbol{e}^i$ (which corresponds to a crystal grain in extinction in cross-polarised optical imaging). In this case the variation in HH spectra still can be recorded and analysed, which is an advantage over polarized-light optical microscopy. Note that all of the above observations are valid also for the other two A_{1g} modes of garnet, but because the one near to 928 cm^{-1} shows the strongest Raman intensity the effects are more evident.

Table 7.3-a Measured intensity (peak area) and calculated depolarization ratio of the A_{1g} mode near 928 cm^{-1}

zircon														
	S1							S2						
	Dis. (μm)	**$I^{(HH)}$** ($cts.cm^{-1}$)	**err.** ($cts.cm^{-1}$)	**$I^{(VH)}$** ($cts.cm^{-1}$)	**err.** ($cts.cm^{-1}$)	**dep. ratio**	**err.**	**Dis.** (μm)	**$I^{(HH)}$** ($cts.cm^{-1}$)	**err.** ($cts.cm^{-1}$)	**$I^{(VH)}$** ($cts.cm^{-1}$)	**err.** ($cts.cm^{-1}$)	**dep. ratio**	**err.**
L1	0	3724	11	180	17	0.048	0.004	0	6148	26	182	26	0.030	0.004
	10	3828	13	105	20	0.027	0.005	7	6297	24	128	32	0.020	0.005
	14	4282	13	89	18	0.021	0.004	14	6210	26	96	25	0.016	0.004
	28	4336	12	83	17	0.019	0.004	28	6245	27	75	20	0.012	0.003
	42	4305	12	85	17	0.020	0.004	42	6362	27	52	25	0.008	0.004
	57	4292	12	39	15	0.009	0.004	56	6076	26	27	14	0.004	0.002
	71	4303	13	30	15	0.007	0.003							
L3	0	4063	13	144	5	0.035	0.001	0	5815	24	206	39	0.035	0.007
	7	5105	17	139	28	0.027	0.005	7	6273	19	74	30	0.012	0.005
	14	5119	16	61	12	0.012	0.002	14	6222	20	54	23	0.009	0.004
	28	5131	15	47	13	0.009	0.003	28	6119	20	26	10	0.004	0.002
	42	5141	19	55	16	0.011	0.003	42	6086	19	37	12	0.006	0.002
	57	5272	16	57	23	0.011	0.004	56	6124	19	18	6	0.003	0.001
	71	5255	14	40	15	0.008	0.003	70	6032	20	20	9	0.003	0.002
	86	5190	16	53	6	0.010	0.001	85	6028	30	36	27	0.006	0.004
L5	0	5339	22	192	30	0.036	0.006	0	5234	20	252	34	0.048	0.006
	7	5686	22	170	30	0.030	0.005	7	5843	20	143	29	0.024	0.005
	14	5920	21	51	8	0.009	0.001	14	6030	21	71	32	0.012	0.005
	28	5895	23	56	12	0.009	0.002	28	6202	19	37	16	0.006	0.003
	42	5938	24	25	6	0.004	0.001	42	6183	20	48	15	0.008	0.002
	57	6212	33	26	8	0.004	0.001	56	6128	19	10	40	0.002	0.007
	71	5900	22	21	10	0.004	0.002	70	5990	22	24	8	0.004	0.001
	86	5875	22	21	8	0.004	0.001							

Table 7.3-b Measured intensity (peak area) and calculated depolarization ratio of the A_{1g} mode near 928 cm^{-1}

quartz														
	S3							S4						
	Dis. (μm)	**$I^{(HH)}$** ($cts.cm^{-1}$)	**err.** ($cts.cm^{-1}$)	**$I^{(VH)}$** ($cts.cm^{-1}$)	**err.** ($cts.cm^{-1}$)	**dep. ratio**	**err.**	**Dis.** (μm)	**$I^{(HH)}$** ($cts.cm^{-1}$)	**err.** ($cts.cm^{-1}$)	**$I^{(VH)}$** ($cts.cm^{-1}$)	**err.** ($cts.cm^{-1}$)	**dep. ratio**	**err.**
L1	0	7243	18	305	9	0.042	0.001	0	4158	14	191	10	0.046	0.002
	7	7345	16	287	10	0.039	0.001	7	4277	16	134	6	0.031	0.001
	14	7294	16	132	8	0.018	0.001	14	4190	15	95	8	0.023	0.002
	28	6708	17	103	10	0.015	0.001	21	4087	15	59	7	0.015	0.002
	42	5951	16	124	13	0.021	0.002	28	3865	13	46	7	0.012	0.002
	56	5325	24	40	25	0.007	0.005	42	3424	13	28	10	0.008	0.003
L3	0	6134	86	202	12	0.033	0.002	0	3841	15	160	11	0.042	0.003
	7	6490	21	166	10	0.026	0.001	7	3983	16	156	9	0.039	0.002
	14	6445	22	112	9	0.017	0.001	14	3883	15	88	8	0.023	0.002
	28	6443	23	55	9	0.009	0.001	21	3626	16	60	8	0.017	0.002
	42	6508	21	51	8	0.008	0.001	28	3379	13	63	10	0.019	0.003
	56	6564	21	63	9	0.010	0.001							
L5	0	6365	13	246	9	0.039	0.001	0	4019	15	197	9	0.049	0.002
	7	5924	14	181	10	0.031	0.002	7	4210	14	132	7	0.031	0.002
	14	6307	16	153	7	0.024	0.001	14	4296	15	87	7.	0.020	0.002
	28	6431	14	128	8	0.020	0.001	21	4264	15	49	8	0.011	0.002
	42	6441	15	123	10	0.019	0.001	28	4322	14	50	8	0.012	0.002
	56	6481	14	90	8	0.014	0.001	42	4251	16	37	10	0.009	0.002
	70	6630	14	69	8	0.010	0.001	56	4094	16	45	8	0.011	0.002
								70	4117	14	60	8	0.014	0.002

Each series of experimentally-determined depolarisation ratios along a radius away from an inclusion can be fitted with the following analytical function:

$\rho = a - bc^x$ (7.8)

where x represents the distance from the host-inclusion surface boundary. Table 7.4 reports the parameters of the fitting function and their uncertainties. Note that along some trails it was possible to conduct only a few point analyses because the Raman signal was interfered by a strong photoluminescence signal, which is most probably due to inhomogeneous distribution of trace elements within the garnet host.

Table 7.4. Fitting parameters of equation 8

sample S1	**L1**	**L3**	**L5**
a	0.010 ± 0.003	0.010 ± 0.001	0.004 ± 0.001
b	-0.040 ± 0.006	-0.026 ± 0.001	-0.034 ± 0.007
c	0.940 ± 0.024	0.875 ± 0.028	0.889 ± 0.024
Reduced Chi-Sqr	1.63529	0.74791	1.88509
R-Square	0.90047	0.98567	0.84175
Adj. R-Square	0.85071	0.9809	0.78899
sample S2	**L1**	**L3**	**L5**
a	0.000 ± 0.003	0.004 ± 0.001	0.005 ± 0.001
b	-0.026± 0.003	-0.032 ± 0.005	-0.044 ± 0.004
c	0.960 ± 0.011	0.858 ± 0.034	0.891 ± 0.019
Reduced Chi-Sqr	0.22892	0.56303	0.47295
R-Square	0.97996	0.90366	0.96933
Adj. R-Square	0.9666	0.86513	0.95399
sample S3	**L1**	**L3**	**L5**
a	0.012 ± 0.011	0.008 ± 0.001	0.011 ± 0.002
b	-0.032 ± 0.011	-0.026 ± 0.002	-0.027 ± 0.003
c	0.930 ± 0.056	0.929 ± 0.014	0.961 ± 0.011
Reduced Chi-Sqr	25.25981	2.10941	2.99045
R-Square	0.81279	0.97084	0.96625
Adj. R-Square	0.68799	0.95626	0.94938
sample S4	**L1**	**L3**	**L5**
a	0.005 ± 0.002	0.000 ± 0.047	0.016 ± 0.002
b	-0.041 ± 0.002	-0.046 ± 0.045	-0.040 ± 0.003
c	0.939 ± 0.007	0.961 ± 0.064	0.902 ± 0.015
Reduced Chi-Sqr	0.25818	6.85203	2.02424
R-Square	0.99667	0.86353	0.97119
Adj. R-Square	0.99445	0.72706	0.95967

A comparison of different transects around the inclusions measured under the same scattering geometry (at 45 degrees with respect to $\boldsymbol{e}^i$), shows no close relationship between the depolarization ratio decay and the shape of the inclusion or its amount of stress. Note also that, since the intensity decreases very quickly away from the inclusion, a few micrometres of uncertainty in the distance from the inclusion can lead to large changes in the depolarization ratio. However, the trend of decay of the depolarization ratio measured experimentally is in good agreement with the trend of decay of the radial component of the strain in the host calculated from FE simulations (Figure 7.5).

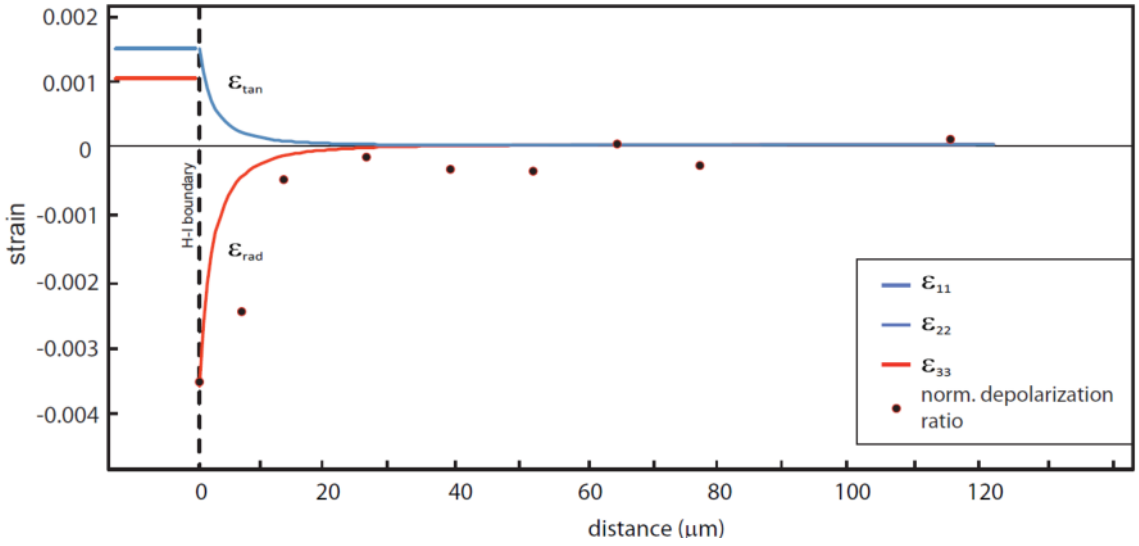

Figure 7.5. Decay of strain and normalized depolarization ratio (Equation 6) from the host-inclusion boundary. The reported radial strain (red solid line) is the direction L3 in Figure 7.2 that is parallel to the c axis (elongated axis in the crystal) of zircon inclusion S1.

7.5 Discussion

Preliminary experimental results from this study show an identical spatial distribution between the stress-induced birefringence and the intensity of the stress-induced cross-polarized Raman scattering of fully symmetric modes. Furthermore, the direct correlation between stress-induced birefringence and stress-induced Raman scattering found experimentally suggests a direct proportionality between the piezo-optic and the piezo-phonon tensors.

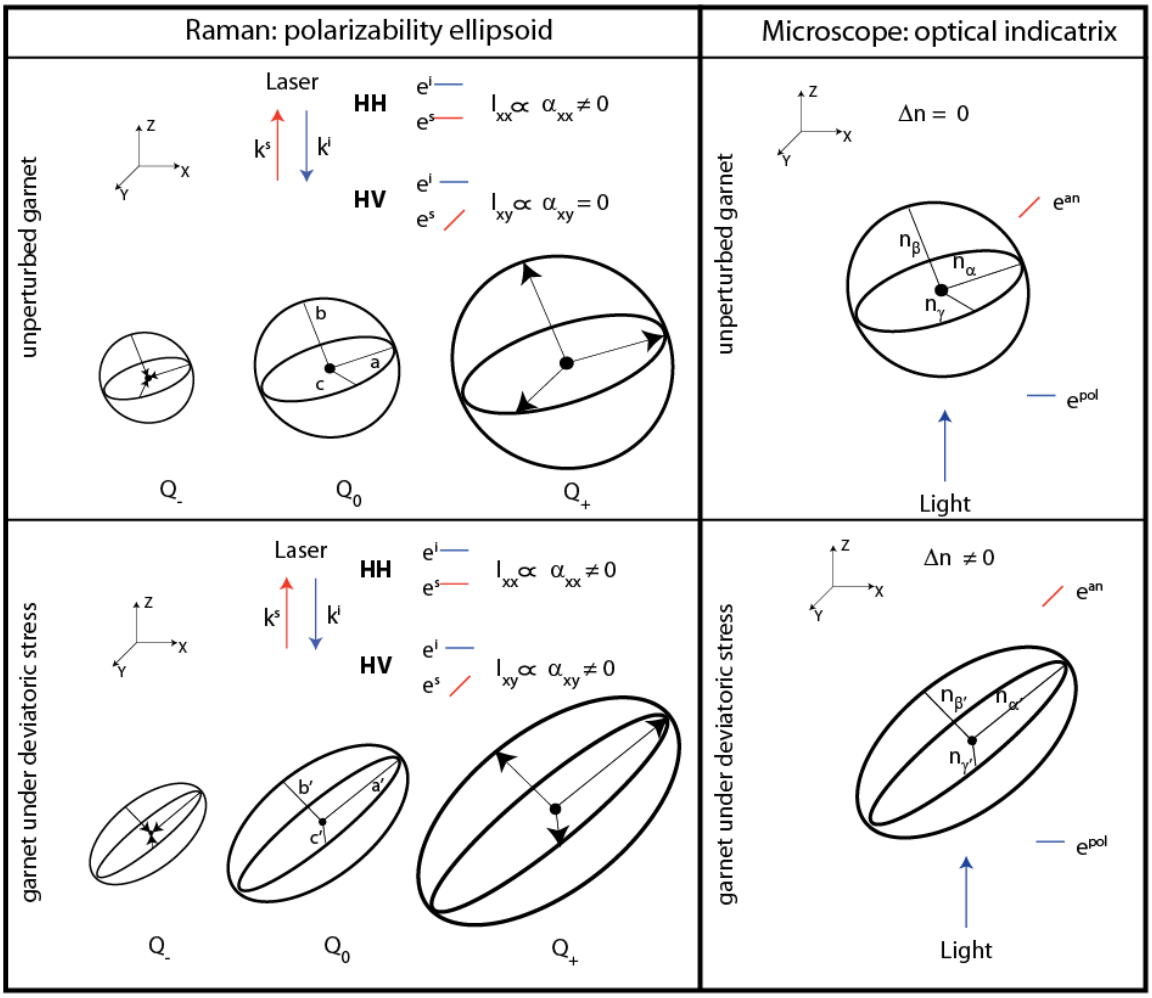

Figure 7.6. Schematic representation of polarization selection rules for totally symmetric modes (to the left) and optical birefringence in unstrained and cubic crystals under deviatoric stress. XYZ are the instrumental reference frame while a, b, c and a', b', and c' are the semi-axes of the polarizability ellipsoid for an unstrained and strained crystal respectively. The same scheme is adopted for the refractive indices n_α, n_β and n_γ in the optical indicatrix. Q_- and Q_+ represent the normal coordinate end-members from the equilibrium configuration Q_0 of the polarizability ellipsoid during vibration. Note that for fully symmetrical modes Raman activity is given by the change in volume of the polarizability ellipsoid during vibration (i.e. simultaneous and proportional change in the diagonal components of the Raman polarizability tensor $\boldsymbol{\alpha}$*). $\boldsymbol{e}^i$ and $\boldsymbol{e}^s$ represent the polarization direction of the incident and scattered light respectively, $\boldsymbol{e}^{an}$ and $\boldsymbol{e}^{pol}$ the direction of light polarization in the microscope. $\boldsymbol{k}^i$ and $\boldsymbol{k}^s$ represent the propagation direction of the incident and scattered light. See the text for the discussion.*

From equation 4 it is evident that a mode will be active as function of the applied stress if $\left(\frac{\alpha^m{}_{ij}}{\sigma_{kl}}\right)_{Q\to 0} \neq 0$ during the vibration where Q is the phonon normal coordinate (Figure 7.6).

For fully-symmetric modes this is equivalent to a stress-induced change in the point symmetry. Therefore, in the case of garnet, the shape of the polarizability ellipsoid will

change from spherical to truly ellipsoidal, and the geometry is a function only of the applied stress. Then the Raman polarization tensor will be modified according to the new symmetry and a non-zero phonon-induced dipole moment will be detectable also in cross polarized scattering geometry. This is exactly the same as the rules for the birefringence observed under an optical microscope (see Figure 7.6). Note that in general, for centrosymmetric crystals, strain/stress-induced Raman scattering is allowed only for even-parity modes (Anastassakis, 1980; Gregora, 2006). A general way to obtain the matrix form of the piezo-phonon tensor ($\boldsymbol{\tau}$) was reported by Anastassakis (1980) and can be applied to all of the symmetry modes. However, the symmetry constraints imposed by fully-symmetric modes can simplify the treatment.

Let us consider as an example the effect of a stress on the totally symmetric phonon (A_{1g}) modes imposed by an anisotropic inclusion along the [100] direction of the host cubic crystal. For cubic crystals, the symmetry constraints of the piezo-phonon tensor expressed in Voigt notation are (Nye, 1985):

$$\begin{bmatrix} \tau_{11} & \tau_{12} & \tau_{12} & \cdot & \cdot & \cdot \\ \tau_{12} & \tau_{11} & \tau_{12} & \cdot & \cdot & \cdot \\ \tau_{12} & \tau_{12} & \tau_{11} & \cdot & \cdot & \cdot \\ \cdot & \cdot & \cdot & \tau_{44} & \cdot & \cdot \\ \cdot & \cdot & \cdot & \cdot & \tau_{44} & \cdot \\ \cdot & \cdot & \cdot & \cdot & \cdot & \tau_{44} \end{bmatrix}$$

When the inclusion is uniaxial, such as for the case of quartz and zircon, and is elongated or flattened along the unique axis, the stress field in the surrounding host is anisotropic with normal components:

$$\begin{bmatrix} \sigma_1 \\ -\sigma_2 \\ -\sigma_3 \\ \vdots \\ \cdot \end{bmatrix}$$

Then equation 3 takes the form:

$$\Delta\alpha_i^{\sigma} = \begin{bmatrix} \tau_{11} & \tau_{12} & \tau_{12} & \cdot & \cdot & \cdot \\ \tau_{12} & \tau_{11} & \tau_{12} & \cdot & \cdot & \cdot \\ \tau_{12} & \tau_{12} & \tau_{11} & \cdot & \cdot & \cdot \\ \cdot & \cdot & \cdot & \tau_{44} & \cdot & \cdot \\ \cdot & \cdot & \cdot & \cdot & \tau_{44} & \cdot \\ \cdot & \cdot & \cdot & \cdot & \cdot & \tau_{44} \end{bmatrix} \cdot \begin{bmatrix} \sigma_1 \\ -\sigma_2 \\ -\sigma_3 \\ \vdots \\ \cdot \end{bmatrix} = \begin{bmatrix} \sigma_1\tau_{11} - (\sigma_2 + \sigma_3)\tau_{12} \\ -\sigma_2\tau_{11} + (\sigma_1 - \sigma_3)\tau_{12} \\ -\sigma_3\tau_{11} + (\sigma_1 - \sigma_2)\tau_{12} \\ \vdots \\ \cdot \end{bmatrix} =$$

$$\begin{bmatrix} \Delta\alpha_1{}^{\sigma} \\ \Delta\alpha_2{}^{\sigma} \\ \Delta\alpha_3{}^{\sigma} \\ \vdots \\ \cdot \end{bmatrix} \quad (7.9)$$

It is evident that the tensor $\Delta\boldsymbol{\alpha}^{\sigma}$ in the host will also have three different normal components. Note that such a symmetry would correspond to the *intrinsic* Raman scattering of the totally symmetric phonon of an orthorhombic crystal. In general, if the stress is applied along an arbitrary direction of a cubic host crystal, the corresponding tensor $\Delta\boldsymbol{\alpha}^{\sigma}$ would correspond to a biaxial crystal (orthorhombic, monoclinic or triclinic).

Then, once $\Delta\boldsymbol{\alpha}^{\sigma}$ is obtained in this way, the total contribution in the electronic polarizability becomes:

$$\alpha_{ij}^{m_{tot}} = \begin{bmatrix} \alpha_{11}^0 & \cdot & \cdot \\ \cdot & \alpha_{11}^0 & \cdot \\ \cdot & \cdot & \alpha_{11}^0 \end{bmatrix} + \begin{bmatrix} \Delta\alpha_{11}^{\sigma} & \cdot & \cdot \\ \cdot & \Delta\alpha_{22}^{\sigma} & \cdot \\ \cdot & \cdot & \Delta\alpha_{33}^{\sigma} \end{bmatrix} \quad (7.10)$$

where the two superscripts i and σ represent the contribution of *intrinsic* and stress-induced Raman effects respectively. However, it is important to point out that since the piezo-phonon tensor is of fourth-rank, the resulting morphic effect will depend on the crystallographic orientation of the cubic crystal with respect to the applied stress. This means that, for a correct interpretation of the experimental results, we need to know the mutual crystallographic orientation of the host-inclusion pair because the orientation of the inclusion determines the orientation of the stress field. Furthermore, the entire system must be oriented with respect to the observation plane (i.e. the thin section surface) and then with respect to the polarizers. Then, combining equations (2) and (9), the intensity of the stress-induced Raman scattering is:

$$I^m \propto \left|e_k^i(\alpha^{m_0}{}_{kl} + \Delta\alpha^{\sigma}{}_{kl})e_l^s\right|^2 = \left|e_k^i(\alpha^{m_0}{}_{kl} + \tau_{kmnl}\sigma_{mn})e_l^s\right|^2 \quad (7.11)$$

Hence, the observed Raman intensity is just proportional to the stress of the crystal and, through Hooke Laws, to the strain, as shown in Figure 7.5.

One of the major advantages of this method is that the Raman peak intensity is more sensitive to the applied stress than the vibrational frequency, as shown in Figure 7.3 where the peak position (i.e. vibrational frequency) remains unchanged across the birefringence halo while the difference in the intensity is well-defined. A stress-induced change in the phonon wavenumber was only detected when using confocal optics and an objective 100×; the measured wavenumber shift was already quite small (~2 cm^{-1}) very close to the host-inclusion boundary and decayed away very quickly with increasing distance from the boundary, making it impossible to use this to follow quantitatively the radial stress gradient. To explain this, it is necessary to recall the nature of the two phenomena. Indeed, as seen in equation (3) and (11), the peak intensity depends on the electrical polarizability of a crystal and how it changes as function of the vibration, that is, the stress-induced Raman intensities are related to the redistribution of the electron density of states, similar to the stress-induced changes in the optical properties. On the other hand, the vibrational frequency of a Raman peak depends on the atomic motions around their equilibrium positions in the crystal structure. Since the electrons are much lighter than the atomic nuclei they are affected more than the atomic nuclei by the same stress field.

In particular, the phonon frequency variation in a stressed crystal is directly related to its strain state by the 2nd rank phonon-mode Grueneisen tensor $\boldsymbol{\gamma^m}$ (e.g. Ziman, 1960) which obeys the same symmetry constraints as any 2nd rank property tensor. In a cubic mineral, for example, changes in the wavenumber should only be related to a volume change of the crystal in the probed area (e.g. Angel et al., 2018). However, as demonstrated above, the host crystal is no longer cubic close to the inclusion. Then, the Grueneisen tensor will be modified, as is the polarizability tensor, by the stress field acting on the crystal which will

reduce its symmetry from cubic to a lower symmetry. For a spherical elastically-isotropic inclusion the resulting symmetry is approximately uniaxial, otherwise for lower-symmetry inclusions the resulting symmetry in the host is, as noted above, effectively biaxial. This is what is seen in the observed stress-induced birefringence. As a consequence, changes in the wavenumbers of Raman peaks are not solely a function of the volume but also of the anisotropic strain. However, for the reasons given above, if the amount of stress is small, the perturbation of the initial Grueneisen tensor components, which depends on the redistribution of the heavy nuclei, will be very small and then the change in the Raman peak position will be very small and difficult to detect.

Another advantage is that, with respect to the observations performed at the optical microscope, in which the observed birefringence is the result of an integration of the signal coming from the entire thickness of the thin section, with confocal Raman spectroscopy it is possible to reduce the volume of the probed area down to a few cubic micrometres. Even in a non-confocal configuration, assuming a refractive index of pure pyrope of about 1.7, using the correction given by Everall (2000), for an inclusion sitting at about 80 μm below the sample surface (i.e. our cases) an objective N.A. of 0.5, the resulting (predicted) axial resolution is approximately 14 μm over the 260 μm of sample thickness.

Currently, we cannot provide a way to directly measure the strain and stress because the absolute values of the piezo-phonon coefficients are unknown. They can in general be derived from DFT calculations at 0 K but this would help only in the case of spherical inclusions because the inclusion shape is quite important in determining the exact stress tensor induced by the host-inclusion boundary. Nevertheless, the method gives the opportunity to quantify the spatial distribution of the stress propagating in the host, that is, the stress field acting in host-inclusion systems, directly from the depolarization ratio of the cubic fully-symmetric modes.

Finally, it is interesting to note that, with such an approach, it would be possible to discriminate between compressive and tensile stress conditions acting on the host crystal by anomalous Raman scattering. Indeed, coupling the above considerations with the proportionality between the scattered intensity of a mode and its polarizability, the total contribution in the measured intensity under parallel polarized scattering geometry (HH), can be written as:

$$I^{||} \propto \left\{ \begin{bmatrix} \alpha_{11}^0 & . & . \\ . & \alpha_{11}^0 & . \\ . & . & \alpha_{11}^0 \end{bmatrix} + \begin{bmatrix} \Delta\alpha_{11}^\sigma & . & . \\ . & \Delta\alpha_{22}^\sigma & . \\ . & . & \Delta\alpha_{33}^\sigma \end{bmatrix} \right\}^2 \quad (7.12)$$

Then, from equation (12), it is evident that the sign of the stress-induced polarizability tensor components, which depend on the sign of the acting stress, can give an increase or a decrease in the total intensity of parallel polarized spectra when compared to those acquired in the unperturbed reference domain which corresponds to just the first term in brackets. Finally, from equation (12) it is also evident that we can potentially use mapping of peak intensity to visualize strain gradients in the host surrounding stressed inclusions as shown in Figure 7.7.

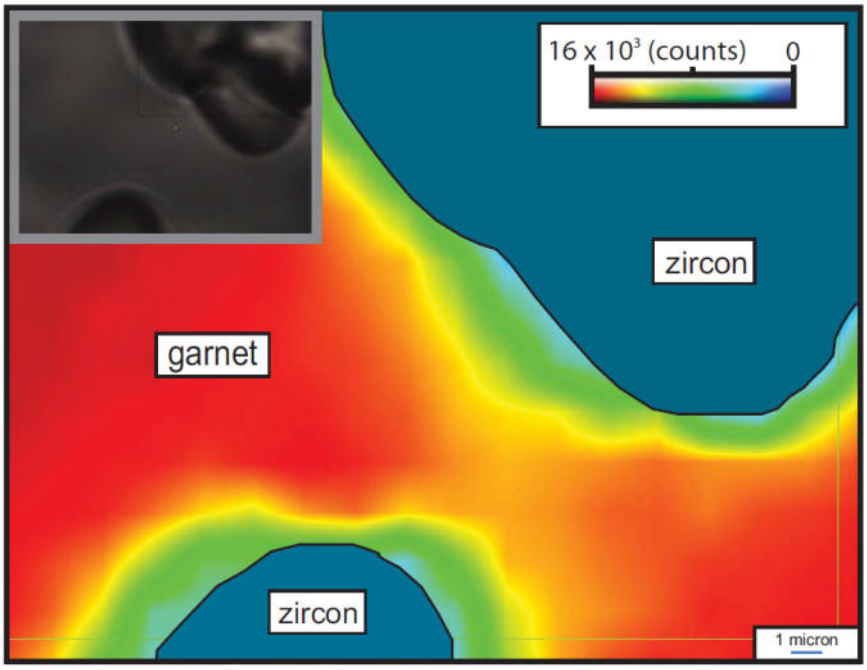

Figure 7.7. Intensity map of A_{1g} mode near 928 cm^{-1} in garnet under parallel polarized scattering geometry (HH). The intensity variation (plotted here in terms of peak area) represents the changes in the shape of the polarizability ellipsoid (i.e. changes in the polarizability tensor coefficients) as result of the stress field acting on the garnet.

7.6 Implications

In this Chapter, an alternative method to study the strain state acting on host crystals surrounding pressurized inclusions has been presented. In particular, we pointed out the anomalous scattering behaviour of totally symmetric phonons as a bridge between the stress-induced Raman scattering and the observed stress-induced birefringence of a crystal. Indeed both processes obey the same symmetry constraints and are directly proportional to each other. Furthermore, because they depend upon the redistribution of the electron density of states, they are much more sensitive to the stresses and strains than changes in phonon frequencies or splitting of degenerate modes. Then, the depolarization ratio and intensity maps of totally symmetric phonons represent a powerful tool to visualize strain gradients in crystals. Finally, even if an absolute description of the strain state of the host is not yet available because we still do not know the absolute value of the piezo-phonon coefficients, theoretical considerations can be exploited to determine the stress-induced symmetry of the crystal and an evaluation of the sense of the applied stress could be performed.

This new and complementary methodology sheds further light on the possibility in analysing and quantifying stress gradients in optically anomalous crystals with an experimentally-friendly technique such as Raman spectroscopy. For instance, its application to host-inclusion systems is just one of many potential cases for study. One example, which is of increasing interest in the petrological literature, is the analysis and quantification of stress heterogeneity and distribution in reacting mineral parageneses (e.g. Tajcmanova et al., 2014). At the moment, such quantifications are mainly performed by means of numerical models. Our new technique could provide an opportunity for experimental validation when optical anomalies due to symmetry breaking are present. Further, it is well known that the study of anomalous optical birefringence in grossular-andradite garnet solid solutions provides information on their origin and crystal growth (see Shtuckenberg and Punin, 2007;

Cesare et al. 2019). And this technique can also provide, similarly to optical birefringence, valuable and complementary information in studying high-pressure / temperature phase transitions in minerals if, for example, the depolarization ratio is used as a Landau order parameter. Finally, with hyper- spatial resolution spectrometers, another possible application could be the study of strain fields due to coherency developed in exsolution processes around exsolution lamellae, which, in turn, gives information on the enthalpy of mixing in solid solutions (e.g. Putnis, 1992).

Chapter 8

Application of the elastic thermobarometric method to a natural case of study: the UHP Brossasco-Isasca unit (Dora-Maira Massif, Western Alps)

8.1 Introduction and motivation

In the previous Chapters a correct methodological approach to the elastic thermobarometry of anisotropic mineral inclusions has been defined by establishing the working procedures, by selecting zircon inclusions possibly unaffected by metamictization. Therefore, the main goal of the former Chapters was to provide the necessary analytical protocols to achieve reliable *P-T* results from anisotropic zircon inclusions in garnet.

To the purpose of elastic thermobarometry, zircon is a common accessory mineral phase having a large *P-T* stability field and frequently occurring as inclusion in metamorphic garnet-bearing rocks. Besides, zircon can also provide age constraints on inclusion entrapment and/or metamorphic recrystallization.

In this Chapter, zircon inclusions in three different garnet megablasts from the ultrahigh-pressure (UHP) Brossasco-Isasca unit (Dora-Maira Massif, Western Alps) are analysed by means of the elastic approach to retrieve their entrapment *P-T* conditions and, if possible, to gain information on the ambient stress conditions during zircon entrapment inside the growing garnet host. The choice of the UHP Brossasco-Isasca unit mostly arises from the historical relevance of the Dora-Maira Massif in the petrological community and in the development of modern petro-tectonic models on subduction and exhumation of high- and ultrahigh-pressure rocks. As described in Chapter 3, Dora-Maira is the place where Chopin

(1984) showed for the first time continental subduction to depths greater than 90 km. Today, while the presence of coesite inclusions is the indisputable record of the attainment of ultrahigh pressures during metamorphism, the true depths of rock recrystallization are strongly debated.

In the whole Dora-Maira Massif, the UHP continental rocks are confined to a small tectonic sliver (Brossasco-Isasca is about 15 km wide and less than 2 km thick) recording peak conditions up to 4.3 GPa and 730 °C (Hermann, 2003). The Brossasco-Isasca unit is surrounded by other units recording much lower metamorphic conditions (1.5 GPa - 550 °C; see Chapter 3 and reference therein). Moreover, it is interesting to note that subduction and exhumation of the UHP Dora-Maira rocks probably went very fast and took place at plate velocities of approximately 5 cm/yr (Rubatto and Hermann, 2001). To explain this evidence, the following subduction and exhumation models have been proposed: (1) continuous return flow in a subduction channel during syn-convergent exhumation (Butler et al., 2014); (2) lithospheric-scale extension caused by slab roll-back (Beltrando et al., 2010); (3) upwards flow of crustal rock at the rear of the accretionary wedge (Yamato et al., 2008). However, other authors pointed out that such mechanisms are inconsistent with the geological data. Malusà et al. (2015) suggested that the volume of rocks eroded after syn-convergent exhumation should be at least one order of magnitude larger than the volume estimated from geological records. Schmalholz et al. (2014), to explain the tectonic evolution of the Western Alps, proposed an orogenic thrust model considering tectonic overpressures, viscous shearing and shear heating as the major driving forces for UHP metamorphism.

In this Chapter, the Brossasco-Isasca garnet-bearing whiteschists are analysed by means of the elastic thermobarometric method. It is worth mentioning that this approach not only enables defining the inclusion entrapment conditions, but also to test the presence of deviatoric stresses during entrapment (Alvaro et al., 2020). By integrating petrography with experimental measurements and numerical models, here I show that the analysis of the

residual strains of pressurised inclusions can shed light on the mechanisms of inclusion entrapment and subsequent exhumation. A possible hypothesis arising from this study is that deviatoric stresses might have been continuously active on the Dora-Maira UHP rocks during garnet growth and inclusion entrapment.

8.2 Specific methodology and approach

Inclusion selection

The petrographic description provided in Chapter 4 suggests that zircon inclusions are the best ones for the application of the elastic thermobarometry to the Brossasco-Isasca whiteschists. The index mineral coesite, though present, in most cases is partially to fully back-reacted to quartz, kyanite is too large with respect to the host garnet and usually crowded of solid and fluid inclusions, while the rutile inclusions do not display residual pressures at room conditions (Zaffiro et al. 2019). The last point has been also shown experimentally by comparing the Raman spectra of completely buried rutile inclusions to a free crystal taken as reference.

The selection of suitable zircon inclusions obeyed the following requirements:

1) Ideal crystals have to be chemically homogeneous across their volume and among different grains. Eventual heterogeneities have to be negligible in terms of position of the Raman peaks. This cannot be really detected by means of Raman spectroscopy of buried inclusions, however, compositional analysis of several partially exposed grains revealed a very limited compositional variability.
2) The crystals have to be unaffected by metamictization.
3) The crystals have to be isolated by at least 3 times their radius or major axis from any kind of discontinuity (host surfaces, fractures) and from other inclusions.

Chapters 5 and 6 provide the guidelines able to address the above issues.

Measuring residual pressure using the hydrostatic model

Translating the Raman shifts into residual pressures by means of the hydrostatic calibration is an easy task vastly applied so far to all host-inclusion systems. The only limitation to this approach is the availability of the calibration (i.e. peak position as function of P) for a given crystal. Indeed, once the dependence of a Raman phonon mode from P and the difference between the peak position of a buried crystal and a free reference crystal are known, the calculation is straightforward. However, strictly speaking, such calibrations should be valid only for host-inclusion pairs sharing are both pseudoisotropic in terms of elastic properties. Indeed, if the zircon inclusion's symmetry is lower than cubic and, even though the surrounding host is isotropic, the stress field involved between the host and the inclusion cannot be hydrostatic because the anisotropic inclusion, by definition, can be compressed in different amounts along different crystallographic directions. Perfect hydrostatic conditions should be only attained if a continuous fluid film surrounds the inclusions.

A way to check if the hydrostatic calibration can be used to determine residual pressure in solid inclusions is plotting the resulting P_{inc} (i.e. residual pressure) obtained from different Raman peaks. If the P_{inc} is the same for different peaks, then the hydrostatic calibration is a good assumption. In this study, the comparison has been carried out cross-checking information from four different phonon modes namely: the B_{1g} mode near 1008 cm^{-1}, the A_{1g} mode near 975 cm^{-1}, the E_g mode near to 357 cm^{-1} and the A_{1g} mode near to 440 cm^{-1}.

Measuring residual pressure using the anisotropic model

Murri et al. (2018) and Angel et al. (2018) introduced a more rigorous approach to calculate residual pressure (P_{inc}) of inclusions buried inside the host using Raman spectroscopy. This has been referred as the *multi-phonon approach* or as *the phonon-mode Grueneisen tensor approach.* In this approach, as envisaged from the first name, to determine the residual

pressure of anisotropic inclusions, more than one phonon mode must be used. The approach exploits a relatively simple relation between the fractional change in the wavenumber ω of a given phonon mode m and the strain tensor $\boldsymbol{\varepsilon}$ that was first defined by the famous physicist Grueneisen:

$$\frac{-\Delta\omega^m}{\omega_0^m} = \boldsymbol{\gamma}^m : \boldsymbol{\varepsilon} \tag{8.1}$$

in which the symbol "**:**" indicates a double scalar product between the two tensors and $\boldsymbol{\gamma}^m$ is the Grueneisen tensor. Considering that both the strain and the Grueneisen tensors are of the second rank and symmetric (i.e. $\varepsilon_{ij} = \varepsilon_{ji}$ and ${\gamma^m}_{ij} = {\gamma^m}_{ji}$ respectively) it is possible to expand out eq. (8.1) as follows:

$$\frac{-\Delta\omega^m}{\omega_0^m} = \gamma_{11}^m\varepsilon_{11} + \gamma_{22}^m\varepsilon_{22} + \gamma_{33}^m\varepsilon_{33} + 2\gamma_{23}^m\varepsilon_{23} + 2\gamma_{13}^m\varepsilon_{13} + 2\gamma_{12}^m\varepsilon_{12}$$

(8.2)

In the simplified Voigt notation this assumes the form:

$$\frac{-\Delta\omega^m}{\omega_0^m} = \gamma_1^m\varepsilon_1 + \gamma_2^m\varepsilon_2 + \gamma_3^m\varepsilon_3 + \gamma_4^m\varepsilon_4 + \gamma_5^m\varepsilon_5 + \gamma_6^m\varepsilon_6$$

(8.3)

Note that the introduction of a factor of ½ into the strain vector components and not into the Grueneisen ones avoids factors of 2 appearing for the terms with subscripts i = 4, 5 and 6 in equation (8.3). The value of $\boldsymbol{\gamma}^m$ is different for different Raman peaks (i.e. phonon modes). Since both the Grueneisen and strain properties are second rank tensors, they obey the same symmetry constraints. This is an important point since it defines which strain components can be determined using the change in the Raman shift. Table 8.1 reports the symmetry constraints for the Grueneisen tensor (see Angel et al. 2019 for major details).

Table 8.1 Grueneisen tensor symmetry constraints

Crystal system	Independent values	Symmetry constraints
Triclinic	All components	None
Monoclinic b-unique	$\gamma_1^m, \gamma_2^m, \gamma_3^m, \gamma_5^m$	$\gamma_4^m = \gamma_6^m = 0$
Monoclinic c-unique	$\gamma_1^m, \gamma_2^m, \gamma_3^m, \gamma_6^m$	$\gamma_4^m = \gamma_5^m = 0$
Orthorhombic	$\gamma_1^m, \gamma_2^m, \gamma_3^m$	$\gamma_4^m = \gamma_5^m = \gamma_6^m = 0$
Tetragonal/trigonal/hexagonal	γ_1^m, γ_3^m	$\gamma_4^m = \gamma_5^m = \gamma_6^m = 0$ $\gamma_1^m = \gamma_2^m$
Cubic	γ_1^m	$\gamma_4^m = \gamma_5^m = \gamma_6^m = 0$ $\gamma_1^m = \gamma_2^m = \gamma_3^m$

Assuming no symmetry breaking, from Table 8.1 it is evident that for uniaxial minerals, such as zircon, the strain independent components that can be determined are two: ε_1 and ε_3 with $\varepsilon_2 = \varepsilon_1$. Now, in order to obtain the strain components, it is necessary to use the fractional change of the Raman wavenumber from at least two different phonon modes. For this purpose, however, the two phonon modes (i.e. Raman peaks) should have different $\boldsymbol{\gamma}^m$ values one more sensitive to ε_1 and the other more sensitive to ε_3. Graphically, for uniaxial crystals, the Grueneisen tensor (computed from ab-initio methods) represents the slope of the lines indicating the equal values of Raman shift as function of the two independent strain components ε_1 and ε_3 (Figure 8.1). It turns out that, to define a point within such a diagram (i.e. define the strain state of the mineral), two Raman peaks with different slope (i.e. different Grueneisen coefficients) in the iso-shift lines are needed. Figure 8.1 reports the *iso-shift lines* plots for some of the phonon-modes in zircon as function of the two independent strain components ε_1 and ε_3 (Stangarone et al. 2018).

The Raman peaks used for calculating the residual pressure with the Grueneisen tensor approach are the same used for the hydrostatic approach. Note that phonon modes such as those near 224 cm^{-1} and to 201 cm^{-1} have not been considered here because of their low

sensitivity to strain fields and because of their small scattering intensity that, in some cases, was difficult to detect.

Once the strain values have been obtained, it is possible to calculate the stress components using the elastic constants at room conditions following the relation:

$$\sigma_{ij} = C_{ijkl}\varepsilon_{kl} \qquad (8.4)$$

Where C_{ijkl} and σ_{ij} are the stiffness and the stress tensors respectively. Note that since no variance-covariance matrix is available for the stiffness tensor of zircon, the uncertainties on the stress tensor coefficients $\delta\sigma_{ij}$ have been estimated assuming an error on all the C_{ijkl} components of 0.01. Then the uncertainty on the stress has been propagated in Voigt notation using the following formalism (see Mazzucchelli 2019, PhD Thesis):

$$\delta(\sigma_i^{rel}) = \sum_{j=1}^{6}\left\{\left[\left(\frac{\delta(C_{ij})}{C_{ij}}\right)^2 + \left(\frac{\delta(\varepsilon_j^{rel})}{\varepsilon_j^{rel}}\right)^2\right]^{0.5} \left|C_{ij}\varepsilon_j^{rel}\right|\right\} \qquad (8.5)$$

Finally, the residual pressure can be calculated simply as the negative of the mean normal stress.

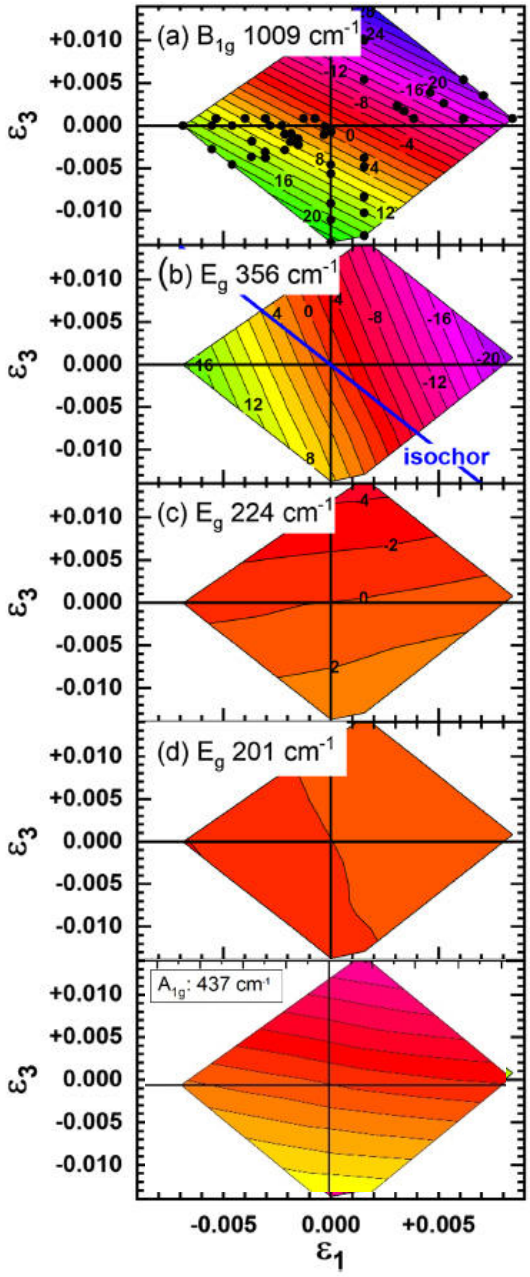

Figure 8.1 Contour maps of the calculated change of the wavenumbers of selected phonon modes of zircon with non-symmetry-breaking strains ε_1 and ε_3. Contours were interpolated on the calculated mode wavenumbers without any model. They are drawn with the same interval of 2 cm^{-1} in each map, and are labelled in cm^{-1}. The same colour scale is used for all plots. The black dots in part (a) indicate the strain conditions at which DFT simulations were performed. The blue line in part (b) is the isochor of the volume of the reference structure. Note that the wavenumber of this mode changes significantly along an isochor (From Stangarone et al., 2019). The A_{1g} mode near 975 cm^{-1}, not reported here, presents similar behaviour of the B_{1g} mode near 1008 cm^{-1}

Chemical thermodynamics vs elasticity

Once the residual pressure is obtained, the resulting entrapment conditions, computed by means of the elastic models, can be compared with previous petrological results and with selected *P-T* pseudosections. Since the pyrope-zircon pair is the only host-inclusion system available for the Dora-Maira whiteschist, an independent constraint on *P* and/or on *T* is necessary to get a unique point in the *P-T* space. Consequently, in this case, the combination with traditional thermobarometric calibrations is necessary to define a unique point in the *P-T* space. This has been carried out by applying the Zr-in-rutile thermometer to the rutile inclusions in garnet and by using garnet chemical zoning. Pseudosection modelling has been carried out by means of Gibbs free energy minimization approach using the software Perple_X (Connolly, 2005) with the thermodynamic database of Holland and Powell (2002). Bulk chemistry of Si-poor whiteschists has been taken from Gautiez-Putallaz et al. (2016).

Using numerical models to predict inclusion behaviour after entrapment

Another check is the analysis of the independent strain components of the inclusions at room conditions. Numerical models predicting the anisotropic behaviour of a crystal as function of *T* and *P* can provide important indications on the obtained experimental results (Mazzucchelli et al., 2019). The validity and reliability of such models has been already pointed out in the previous Chapters (see Chapters 5 and 7). Figure 8.2 shows the change in the expected residual deviatoric strain (i.e. $\varepsilon_3 - \varepsilon_1$) of zircon inclusions as function of different *P-T* conditions of entrapment. For example, a zircon inclusion entrapped in garnet at 800 °C and about 2.7 GPa should exhibit at room conditions a residual deviatoric strain of 0.002.

This contour-map diagram is based on the assumptions that (1) the host-inclusion system behaves elastically during the entire *P-T* history and (2) that during inclusion entrapment the *P* was hydrostatic and (3) the shape of the inclusion is spherical. It is important to note that residual deviatoric strains computed this way are the result of the intrinsic anisotropy of the inclusions.

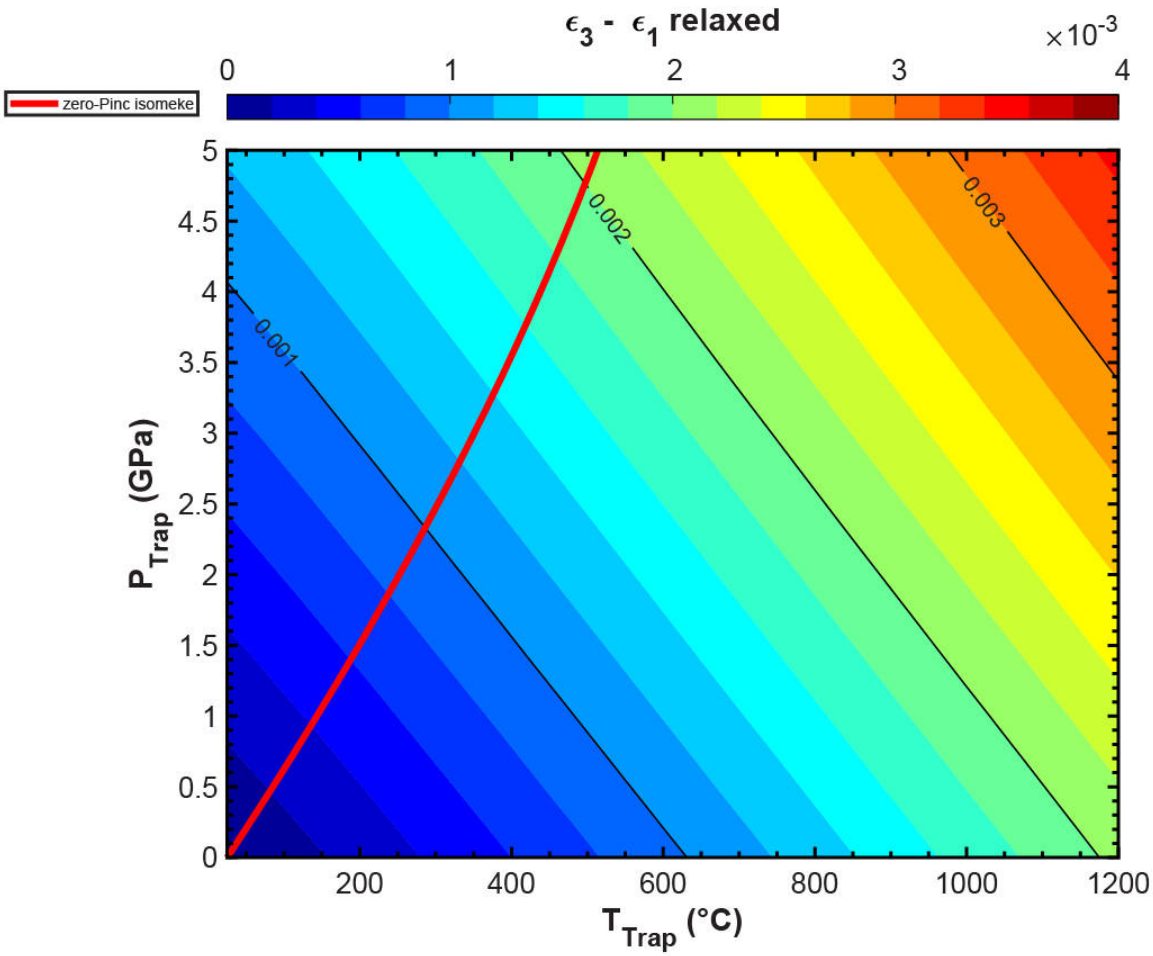

Figure 8.2 Room condition deviatoric strain calculated for a zircon inclusion entrapped within a garnet host as function of different P-T conditions. The developed deviatoric strain is the results of the intrinsic anisotropy of zircon (from Mazzucchelli et al. 2019).

8.3 Results and Discussion

Raman shift in buried zircon inclusions

Zircon inclusions entrapped from core to rim of three different garnet megablasts (samples DM17-35 and DMG4-5 from Gilba and sample DM17-13 from Martiniana) have been analysed by means of Raman spectroscopy. Figure 8.3 shows a polished slice of a garnet megablast and reports a core to rim profile where numerous inclusions have been measured in order to cover the entire range of garnet growth. Following the zircon selection protocol presented in Chapter 6 (i.e. FWHM $\leq$ 5 cm^{-1}), it is possible to rely on 34 zircon inclusions (Figure 8.4). Figure 8.5 shows the experimental results in terms of Raman shift as function of the garnet growth-zone. This has been defined as the shortest distance from the garnet core to the visible rim (in mm).

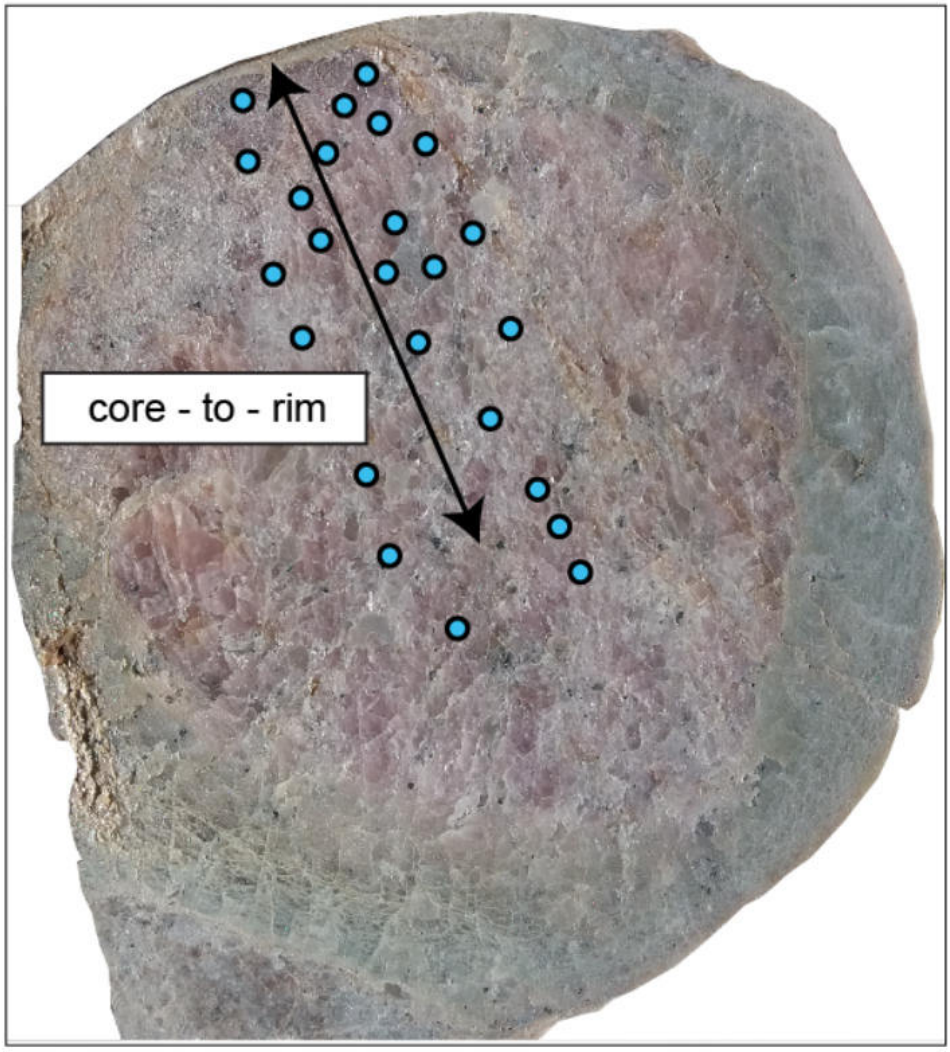

Figure 8.3 Selection scheme of completely buried zircon inclusion in garnet.

On average, there is a systematic decrease in the Raman shift wavenumber from core to rim (Figure 8.5). In particular, this is more evident for the internal phonon modes which are the Si-O symmetric (A_{1g}) and antisymmetric (B_{1g}) stretching modes. On the other hand, for the external mode near to 357 cm^{-1} (E_g symmetry) the trends are less evident.

Furthermore, the inclusions in the garnet megablasts from Martiniana (DM17-13) show the highest shift values (up to 1013.5 cm^{-1} for the B_{1g} mode): their core-to-rim bell-shaped trends in Raman shifts seem to be inconsistent with the linear trends recorded by the zircon inclusions from Gilba.

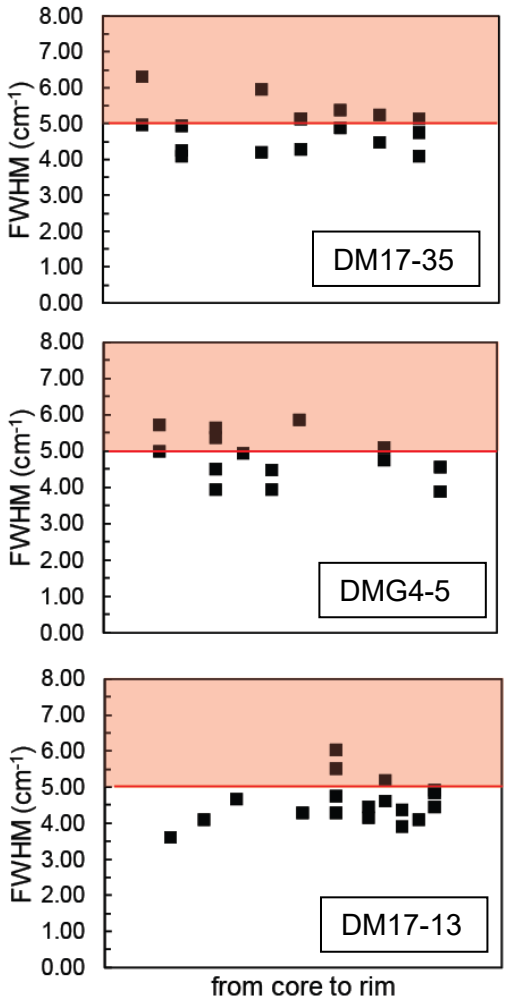

Figure 8.4 peak width (FWHM) of the B_{1g} mode near 1008 cm^{-1} as function of the garnet growth zone

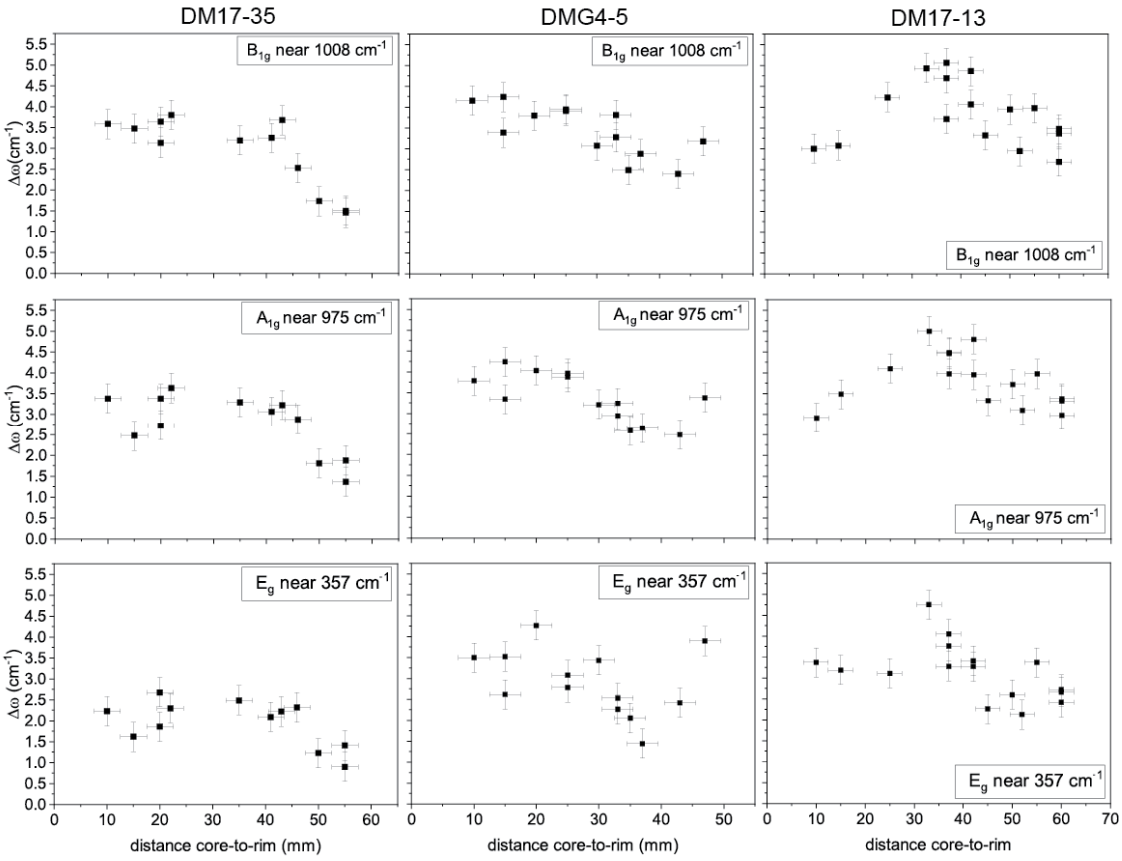

Figure 8.5 Raman shifts of selected zircon inclusions as function of the garnet growth zone. Error bars referred to $\Delta\omega$ corresponds to the instrumental uncertainty in determining the peak position (0.35 cm^{-1}). Error bars referred to the distance from core to rim of the inclusion is of 2.5 mm.

From Raman shift to residual pressure: the hydrostatic approach

As described above, a way to test if the hydrostatic calibration is applicable to inclusions is to cross-check, for the same inclusion, the resulting hydrostatic residual pressure recorded by different phonon modes (Figure 8.6). The $\Delta\omega/\Delta P$ relationships of zircon adopted for this purpose are from Binvignat et al. (2018). The results suggest that the majority of inclusions apparently records hydrostatic stress conditions (black dashed lines in Figure 8.6). However, this is not always true if the A_{1g} mode near 440 cm^{-1} is considered due to the effect of the low P sensitivity of this phonon mode. Indeed, for the peaks at 357 and 975 cm^{-1}, more sensitive to P, the data are more consistent. Table 8.2 reports the resulting residual pressure and associated uncertainties for the zircon inclusions within the three different garnet

megablasts. The estimated uncertainties on residual pressure values has been defined using the standard error propagation formalism from the uncertainty in the peak position and in the $\Delta\omega/\Delta P$.

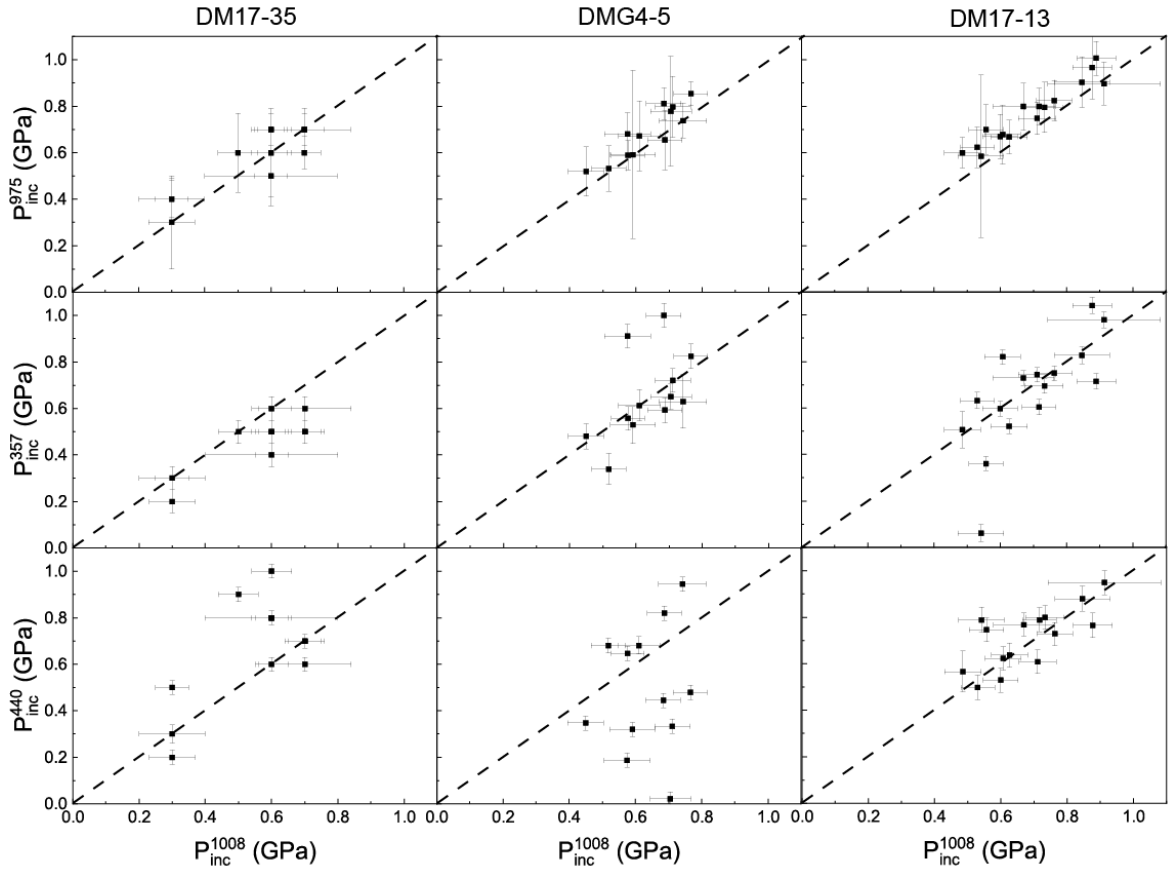

Figure 8.6 Residual pressure (P_{inc}) of zircon inclusions calculated by means of the hydrostatic calibration of peak position as function of pressure.

From Raman shift to residual pressure: the anisotropic approach

For the anisotropic approach, the strain acting on zircon inclusions has been calculated with the dedicated software StRAinMAN (Angel et al., 2019) using the same Raman peaks reported above: B_{1g} mode near 1008 cm^{-1}, the A_{1g} mode near 975 cm^{-1}, the E_g mode near 356 cm^{-1} and the A_{1g} mode near 440 cm^{-1}.

Table 8.3 reports the obtained results. Note that stress values have been derived from the strains using equation 8.4. It is apparent that within the data uncertainty, residual pressures obtained by means of the two different methods are equal to each other.

Table 8.2.a Estimated inclusion residual pressure (Pinc) using the hydrostatic calibration

Megablast Gilba DM17-35									
	Raman shift								
S.	near 1008 (cm^{-1})	er. Fit (cm^{-1})	near 975 (cm^{-1})	er. Fit (cm^{-1})	near 440 (cm^{-1})	er. Fit (cm^{-1})	near 357 (cm^{-1})	er. Fit (cm^{-1})	position core-to-rim (mm)
s45	1.73	0.01	1.81	0.07	0.65	0.01	1.23	0.01	50
s47	1.50	0.09	1.88	0.06	0.5	0.02	1.41	0.02	55
s49	1.45	0.05	1.37	0.19	0.33	0.02	0.90	0.02	55
s52	3.19	0.03	3.29	0.05	1.10	0.01	2.49	0.00	35
s54	3.25	0.03	3.06	0.10	1.50	0.01	2.09	0.01	41
s57	3.67	0.02	3.22	0.05	1.03	0.01	2.22	0.01	43
s58	2.53	0.02	2.88	0.17	1.26	0.01	2.32	0.01	46
s60	3.80	0.03	3.63	0.07	1.01	0.01	2.30	0.01	22
s63	3.58	0.02	3.38	0.07	1.13	0.01	2.23	0.01	10
s65	3.47	0.19	2.47	0.12	1.21	0.01	1.62	0.01	15
s66	3.13	0.01	2.72	0.07	0.88	0.01	1.86	0.01	20
s67	3.64	0.13	3.37	0.05	0.89	0.01	2.68	0.01	20
	Hydrostatic calibration from Binvignat et al. (2018)								
	$\Delta\omega$/dP (cm^{-1}/GPa)	esd (cm^{-1}/GPa)	$\Delta\omega$/dP (cm^{-1}/GPa)	esd (cm^{-1}/GPa)	$\Delta\omega$/dP (cm^{-1}/GPa)	esd (cm^{-1}/GPa)	$\Delta\omega$/dP (cm^{-1}/GPa)	esd (cm^{-1}/GPa)	
	5.54	0.05	4.97	0.05	1.44	0.03	4.27	0.05	
	Calculated residual pressure								
S.	P_{inc} (GPa)	esd (GPa)	P_{inc} (GPa)	esd (GPa)	P_{inc} (GPa)	esd (GPa)	P_{inc} (GPa)	esd (GPa)	position core-to-rim (mm)
s45	0.31	0.05	0.36	0.09	0.45	0.03	0.29	0.05	50
s47	0.27	0.10	0.38	0.08	0.35	0.04	0.33	0.05	55
s49	0.26	0.07	0.28	0.20	0.23	0.03	0.21	0.05	55
s52	0.58	0.06	0.66	0.07	0.76	0.03	0.58	0.05	35
s54	0.59	0.06	0.62	0.11	1.04	0.03	0.49	0.05	41
s57	0.66	0.05	0.65	0.07	0.72	0.03	0.52	0.05	43
s58	0.46	0.06	0.58	0.17	0.87	0.03	0.54	0.05	46
s60	0.69	0.06	0.73	0.09	0.70	0.03	0.54	0.05	22
s63	0.65	0.05	0.68	0.09	0.78	0.03	0.52	0.05	10
s65	0.63	0.20	0.50	0.13	0.84	0.03	0.38	0.05	15
s66	0.56	0.05	0.55	0.09	0.61	0.03	0.44	0.05	20
s67	0.66	0.14	0.68	0.07	0.62	0.03	0.63	0.05	20

Table 8.2.b Estimated inclusion residual pressure (P_{inc}) using the hydrostatic calibration

Megablast Gilba DMG4-5

S.	Raman shift: near 1008 (cm^{-1})	er. Fit (cm^{-1})	near 975 (cm^{-1})	er. Fit (cm^{-1})	near 440 (cm^{-1})	er. Fit (cm^{-1})	near 357 (cm^{-1})	er. Fit (cm^{-1})	position core-to-rim (mm)
s18	3.19	0.007	2.93	0.039	0.93	0.011	2.38	0.004	33
s19	3.94	0.018	3.96	0.121	0.48	0.008	3.08	0.008	33
s20	3.91	0.036	3.87	0.231	0.03	0.005	2.78	0.022	30
s1	4.11	0.052	3.67	0.057	1.36	0.007	2.69	0.104	25
s2	4.24	0.008	4.24	0.009	0.69	0.009	3.52	0.017	25
s3	3.38	0.040	3.34	0.143	0.98	0.022	2.62	0.043	15
s7	3.79	0.017	4.03	0.047	0.64	0.005	4.27	0.012	15
s8	3.18	0.049	3.38	0.077	0.27	0.010	3.89	0.012	10
s10	2.87	0.016	2.64	0.084	0.98	0.010	1.45	0.044	20
s12	2.49	0.022	2.58	0.094	0.5	0.008	2.05	0.018	47
s13	3.27	0.046	2.94	0.358	0.46	0.007	2.26	0.062	43
s14	3.81	0.015	3.25	0.118	1.18	0.008	2.53	0.020	37
s17	2.67	0.016	2.35	0.068	0.7	0.008	0.80	0.004	35
	Hydrostatic calibration from Binvignat et al. (2018)								
	$\Delta\omega/dP$ (cm^{-1}/GPa)	esd (cm^{-1}/GPa)	$\Delta\omega/dP$ (cm^{-1}/GPa)	esd (cm^{-1}/GPa)	$\Delta\omega/dP$ (cm^{-1}/GPa)	esd (cm^{-1}/GPa)	$\Delta\omega/dP$ (cm^{-1}/GPa)	esd (cm^{-1}/GPa)	
	5.54	0.05	4.97	0.05	1.44	0.03	4.27	0.05	
	Calculated residual pressure								
S.	P_{inc} (GPa)	esd (GPa)	P_{inc} (GPa)	esd (GPa)	P_{inc} (GPa)	esd (GPa)	P_{inc} (GPa)	esd (GPa)	position core-to-rim (mm)
s18	0.58	0.050	0.59	0.064	0.65	0.032	0.56	0.050	33
s19	0.71	0.053	0.80	0.131	0.33	0.031	0.72	0.051	33
s20	0.71	0.062	0.78	0.237	0.02	0.030	0.65	0.055	30
s1	0.74	0.072	0.74	0.076	0.94	0.031	0.63	0.115	25
s2	0.77	0.051	0.85	0.051	0.48	0.031	0.82	0.053	25
s3	0.61	0.064	0.67	0.151	0.68	0.037	0.61	0.066	15
s7	0.68	0.053	0.81	0.069	0.44	0.030	1.00	0.051	15
s8	0.57	0.070	0.68	0.092	0.19	0.032	0.91	0.051	10
s10	0.52	0.053	0.53	0.098	0.68	0.032	0.34	0.067	20
s12	0.45	0.054	0.52	0.106	0.35	0.031	0.48	0.053	47
s13	0.59	0.068	0.59	0.361	0.32	0.031	0.53	0.080	43
s14	0.69	0.052	0.65	0.128	0.82	0.031	0.59	0.054	37
s17	0.48	0.052	0.47	0.085	0.49	0.031	0.19	0.050	35

Table 8.2.c Estimated inclusion residual pressure (P_{inc}) using the hydrostatic calibration

Megablast Martiniana DM17-13

S.	Raman shift: near 1008 (cm^{-1})	er. Fit (cm^{-1})	near 975 (cm^{-1})	er. Fit (cm^{-1})	near 440 (cm^{-1})	er. Fit (cm^{-1})	near 357 (cm^{-1})	er. Fit (cm^{-1})	position core-to-rim (mm)
s6	3.08	0.01	3.48	0.10	3.19	0.01	0.52	0.01	15
s7	3	0.05	2.91	0.35	3.37	0.02	0.09	0.02	10
s11	4.23	0.02	4.1	0.07	3.11	0.01	1.08	0.01	37
s21	4.69	0.07	4.49	0.10	3.76	0.02	1.19	0.02	37
s25	3.71	0.08	3.97	0.09	3.28	0.01	1.05	0.01	37
s23	4.93	0.03	5	0.05	4.75	0.01	1.03	0.01	33
s28	4.06	0.03	3.95	0.10	3.41	0.01	1	0.01	42
s29	4.86	0.03	4.8	0.13	3.27	0.02	1.5	0.02	42
s34	3.32	0.02	3.33	0.08	2.26	0.01	0.86	0.01	45
s35	3.94	0.03	3.72	0.05	2.6	0.01	1.07	0.01	50
s36	2.94	0.01	3.1	0.07	2.13	0.02	0.91	0.02	52
s37	3.97	0.01	3.97	0.06	3.37	0.02	0.87	0.02	55
s39	2.69	0.02	2.98	0.04	2.42	0.07	0.73	0.07	60
s40	3.47	0.02	3.32	0.05	2.72	0.01	0.75	0.01	60
s44	3.36	0.02	3.37	0.12	2.66	0.01	1.18	0.01	60
	Hydrostatic calibration from Binvignat et al. (2018)								
	$\Delta\omega/dP$ (cm^{-1}/GPa)	esd (cm^{-1}/GPa)	$\Delta\omega/dP$ (cm^{-1}/GPa)	esd (cm^{-1}/GPa)	$\Delta\omega/dP$ (cm^{-1}/GPa)	esd (cm^{-1}/GPa)	$\Delta\omega/dP$ (cm^{-1}/GPa)	esd (cm^{-1}/GPa)	
	5.54	0.05	4.97	0.05	4.27	0.05	1.44	0.03	
	Calculated residual pressure								
S.	P_{inc} (GPa)	esd (GPa)	P_{inc} (GPa)	esd (GPa)	P_{inc} (GPa)	esd (GPa)	P_{inc} (GPa)	esd (GPa)	position core-to-rim (mm)
s6	0.56	0.05	0.70	0.11	0.75	0.05	0.36	0.03	15
s7	0.54	0.07	0.59	0.35	0.79	0.05	0.06	0.04	10
s11	0.76	0.05	0.82	0.09	0.73	0.05	0.75	0.03	37
s21	0.85	0.08	0.90	0.11	0.88	0.05	0.83	0.04	37
s25	0.67	0.09	0.80	0.10	0.77	0.05	0.73	0.03	37
s23	0.89	0.06	1.01	0.07	1.11	0.05	0.72	0.03	33
s28	0.73	0.06	0.79	0.11	0.80	0.05	0.69	0.03	42
s29	0.88	0.06	0.97	0.14	0.77	0.05	1.04	0.03	42
s34	0.60	0.05	0.67	0.10	0.53	0.05	0.60	0.03	45
s35	0.71	0.06	0.75	0.07	0.61	0.05	0.74	0.03	50
s36	0.53	0.05	0.62	0.09	0.50	0.05	0.63	0.03	52
s37	0.72	0.05	0.80	0.08	0.79	0.05	0.60	0.03	55
s39	0.49	0.05	0.60	0.07	0.57	0.09	0.51	0.08	60
s40	0.63	0.06	0.67	0.07	0.64	0.05	0.52	0.03	60
s44	0.61	0.05	0.68	0.13	0.62	0.05	0.82	0.03	60

Table 8.3 Strain, stress and inclusion residual pressure computed using the anisotropic approach

Megablast Gilba DM17-35												
Sample	ε_3	Err.	$\varepsilon_1=\varepsilon_2$	Err.	Cov.	σ_3 (GPa)	Err. (GPa)	$\sigma_1=\sigma_2$ (GPa)	Err. (GPa)	P_{inc} (GPa)	Err. (GPa)	position core-to-rim (mm)
s45	-0.00054	0.00005	-0.00036	0.00003	-1.82E-09	-0.39	0.03	-0.27	0.02	0.31	0.02	50
s47	-0.00045	0.00011	-0.00045	0.00004	-5.66E-09	-0.37	0.07	-0.30	0.04	0.32	0.05	55
s49	-0.00047	0.00008	-0.00026	0.00003	-2.89E-09	-0.32	0.05	-0.20	0.02	0.24	0.03	55
s52	n.d.	n.d	n.d.	n.d.	n.d.	n.d.	n.d.	n.d.	n.d.	n.d.	n.d	35
s54	-0.00127	0.00017	-0.00055	0.00005	-1.288E-08	-0.81	0.10	-0.48	0.05	0.59	0.07	41
s57	-0.00128	0.00012	-0.00061	0.00005	-8.56E-09	-0.83	0.07	-0.51	0.04	0.61	0.05	43
s58	-0.00049	0.00015	-0.00077	0.00005	-1.157E-08	-0.49	0.09	-0.47	0.05	0.47	0.06	46
s60	-0.00125	0.00019	-0.00064	0.00006	-1.713E-08	-0.83	0.11	-0.52	0.06	0.62	0.08	22
s63	-0.00126	0.00008	-0.00061	0.00003	-3.51E-09	-0.83	0.05	-0.51	0.03	0.61	0.03	10
s65	-0.00138	0.00005	-0.00036	0.00001	-1.04E-09	-0.81	0.03	-0.40	0.01	0.54	0.02	15
s66	-0.00115	0.00008	-0.00050	0.00004	-4.84E-09	-0.73	0.05	-0.43	0.03	0.53	0.04	20
s67	-0.00086	0.00016	-0.00085	0.00004	-9.56E-09	-0.70	0.09	-0.57	0.04	0.61	0.06	20

Table 8.3 Strain, stress and inclusion residual pressure computed using the anisotropic approach

Megablast Gilba DMG4-5												
Sample	ε_3	Err.	$\varepsilon_1=\varepsilon_2$	Err.	Cov.	σ_3 (GPa)	Err. (GPa)	$\sigma_1=\sigma_2$ (GPa)	Err. (GPa)	P_{inc} (GPa)	Err. (GPa)	position core-to-rim (mm)
s18	n.d.	n.d.	n.d.	n.d.	n.d.	n.d.	n.d.	n.d	n.d	n.d	n.d.	33
s19	-0.00095	0.00018	-0.00098	0.00007	-1.783E-08	-0.79	0.11	-0.65	0.06	0.66	0.08	33
s20	-0.00056	0.00057	-0.00098	0.00022	-1.8274E-07	-0.59	0.35	-0.58	0.19	0.58	0.24	30
s1	-0.00136	0.00017	-0.00082	0.00011	-3.288E-08	-0.94	0.12	-0.63	0.08	0.72	0.09	25
s2	-0.00076	0.00039	-0.00135	0.00025	-1.7812E-07	-0.81	0.26	-0.80	0.18	0.75	0.21	25
s3	-0.00090	0.00008	-0.00082	0.00004	-5.32E-09	-0.71	0.05	-0.56	0.03	0.60	0.04	15
s7	-0.00017	0.00005	-0.00156	0.00002	-1.29E-09	-0.58	n.d.	-0.82	n.d	0.73	n.d	15
s8	0.00019	0.00008	-0.00148	0.00002	-2.72E-09	-0.38	0.05	-0.72	0.02	0.62	0.00	10
s10	-0.00118	0.00011	-0.00036	0.00008	-1.457E-08	-0.71	0.08	-0.37	0.05	0.5	0.06	20
s12	-0.00054	0.00009	-0.00068	0.00005	-6.94E-09	-0.49	0.06	-0.43	0.04	0.44	0.05	47
s13	-0.00074	0.00030	-0.00079	0.00018	-8.852E-08	-0.62	0.20	-0.52	0.13	0.49	0.16	43
s14	-0.00126	0.00002	-0.00072	0.00001	-4.4E-10	-0.86	0.02	-0.57	0.01	0.72	0.01	37
s17	n.d.	n.d.	n.d.	n.d.	n.d.	n.d.	n.d.	n.d	n.d	n.d	n.d.	35

Table 8.3 Strain, stress and inclusion residual pressure computed using the anisotropic approach

Megablast Martiniana DM17-13												
Sample	ε_3	Err.	$\varepsilon_1=\varepsilon_2$	Err.	Cov.	σ_3 (GPa)	Err. (GPa)	$\sigma_1=\sigma_2$ (GPa)	Err. (GPa)	P_{inc} (GPa)	Err. (GPa)	position core-to-rim (mm)
s6	-0.00030	0.00004	-0.00113	0.00002	-1.28E-09	-0.51	0.03	-0.62	0.02	0.58	0.02	15
s7	-0.00012	0.00004	-0.00123	0.00001	-7.4E-10	-0.45	0.02	-0.64	0.01	0.57	0.02	10
s11	-0.00119	0.00010	-0.00095	0.00004	-5.84E-09	-0.90	0.06	-0.67	0.03	0.74	0.04	37
s21	-0.00107	0.00012	-0.00121	0.00004	-6.25E-09	-0.92	0.07	-0.78	0.04	0.83	0.05	37
s25	-0.00088	0.00014	-0.00107	0.00003	-7.2E-09	-0.78	0.08	-0.68	0.04	0.71	0.05	37
s23	-0.00065	0.00008	-0.00166	0.00004	-3.6E-09	-0.85	0.05	-0.94	0.03	0.91	0.04	33
s28	-0.00088	0.00006	-0.00111	0.00002	-1.78E-09	-0.80	0.04	-0.70	0.02	0.73	0.03	42
s29	-0.00158	0.00010	-0.00094	0.00005	-6.71E-09	-1.09	0.06	-0.73	0.04	0.84	0.05	42
s34	-0.00104	0.00011	-0.00066	0.00004	-5.97E-09	-0.73	0.06	-0.50	0.03	0.57	0.04	45
s35	-0.00123	0.00017	-0.00076	0.00006	-1.342E-08	-0.86	0.10	-0.58	0.05	0.67	0.07	50
s36	-0.00086	0.00008	-0.00065	0.00006	-7.97E-09	-0.64	0.06	-0.46	0.04	0.52	0.04	52
s37	-0.00080	0.00010	-0.00114	0.00007	-1.311E-08	-0.76	0.07	-0.70	0.05	0.72	0.06	55
s39	-0.00054	0.00015	-0.00083	0.00013	-3.37E-08	-0.53	0.11	-0.50	0.09	0.51	0.10	60
s40	-0.00082	0.00013	-0.00088	0.00005	-8.78E-09	-0.69	0.08	-0.57	0.04	0.61	0.05	60
s44	-0.00088	0.00007	-0.00083	0.00003	-2.66E-09	-0.71	0.04	-0.56	0.02	0.61	0.03	60

Zircon residual pressure distribution within garnet

Figure 8.7 shows the distribution of the residual pressures of zircon inclusions from different garnet growth zones with estimated error bars.

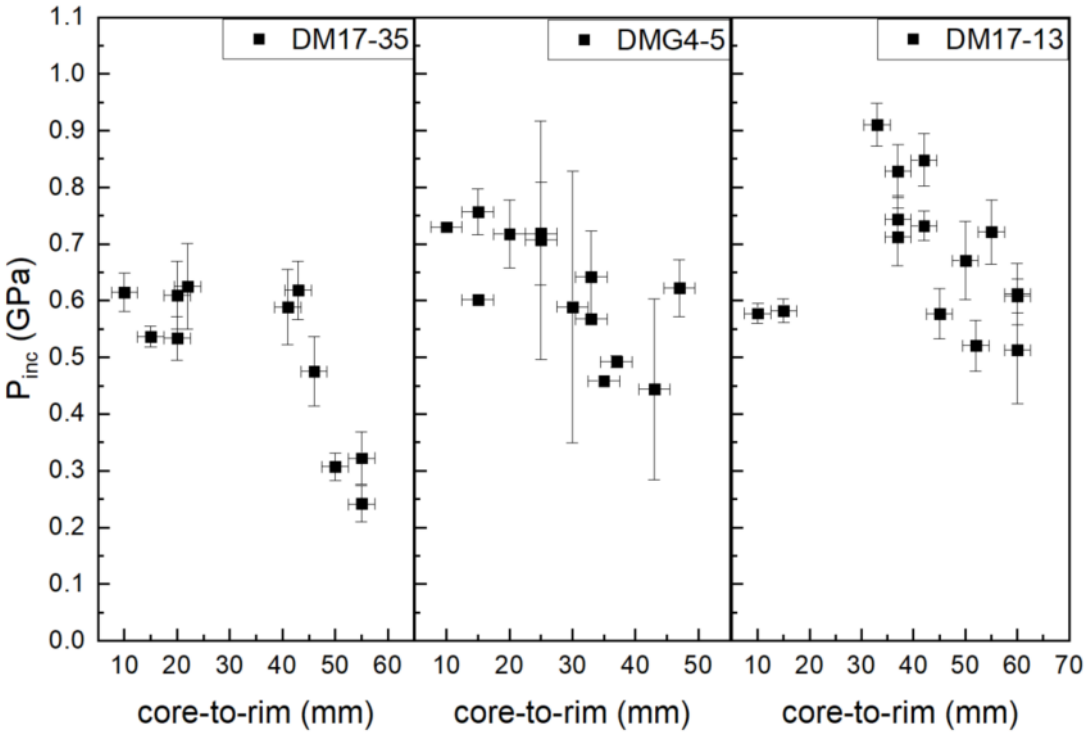

Figure 8.7 Residual pressure distribution of zircon inclusions as function of the garnet growth zone computed using the anisotropic approach.

The trends in the residual pressures follow exactly those reported in Figure 8.5 for the change in the Raman wavenumbers. The data point out that higher residual pressures pertain to the inclusions in the garnet core, whereas lower residual pressures pertain to the inclusions entrapped at the garnet rim. In particular, the trend in measured pressures is in better agreement with the trend recorded for the Raman shift of the B_{1g} mode near 1008 cm^{-1}.

Zircon inclusions entrapped within the garnet megablasts DM17-35 and DMG4-5 from Gilba show maximum residual pressures of 0.6 and 0.8 GPa respectively which gradually decrease to about 0.2 and 0.4 GPa respectively.

On the other hand, the zircon inclusions from the Martiniana garnet megablast DM17-13 show, on average, higher residual pressure values with a maximum of about 0.9 GPa. Furthermore, in agreement with the trends in the Raman shift, this maximum value pertains to the inclusions entrapped at garnet mantle (Figure 8.7).

Translating residual pressure in entrapment pressure: are chemistry and elasticity best friends?

Detailed chemical analysis of the garnet megablasts together with trace elements of rutile inclusions have been combined to better understand the conditions of garnet formation and then zircon inclusion entrapment. This way, it is possible to compare the results from mineral chemistry with those achieved from the residual pressures obtained from the zircon inclusions. Figure 8.8 shows the change in the almandine mole fraction for the three analysed garnet megablasts.

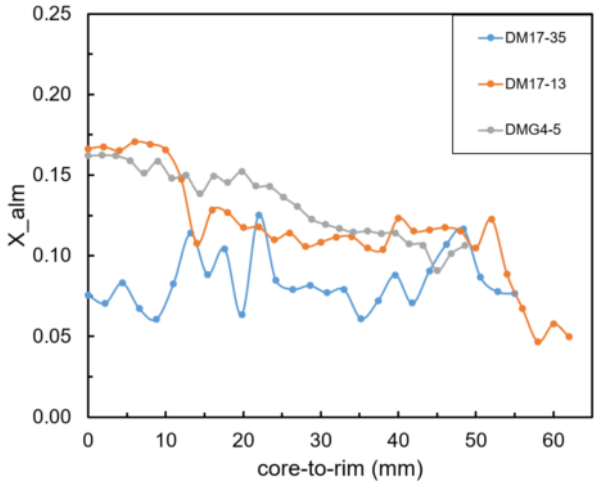

Figure 8.8. Almandine mole fraction of the three garnet megablasts (DM17-35 and DMG4-5 are from the Gilba locality while sample DM17-13 is from the Martiniana locality)

In general, the three crystals display pyrope-rich compositions. The samples DM17-13 and DMG4-5 are characterized by slight but well resolved zonation with higher Fe content at the

garnet core that decreases towards the rim. On the other hand, the sample DM17-35 does not show a clear zonation and, in average, it has the lowest Fe content (around 0.08).

The analysis of the Zr content of rutile inclusions has been performed in order to cover the entire range of garnet growth and to achieve temperature constraints (Zack, 2004; Watson et al., 2006; Tomkins et al., 2007). In this case of study, the Zr content of more than 20 inclusions per garnet megablast remains constant across the entire garnet volume (Table 8.4). The two Gilba garnet megablasts DM17-35 and DMG4 have comparable average Zr concentration (220 and 216 ppm, respectively) while the rutile inclusions of the Martiniana garnet megablast display lower Zr average concentration of 144 ppm.

Table 8.4 Zr-in-rutile inclusion within garnet megablasts.

Sample	DM17-35	DMG4-5	DM17-13
average Zr conc. (ppm)	220	216	144
min - max values (ppm)	169-275	134-288	125-174
e.st.dev. (ppm)	35	58	9
n. of measurements	*53*	*33*	*38*

Figure 8.9a shows a calculated pseudosection for Si-poor whiteschists in which the chemical composition of garnet (in terms of almandine mole-fraction), as computed from the pseudosection, and the Zr-in-rutile isopleths are reported. The black dashed arrow in the diagrams of Figure 8.9 indicates the prograde P-T path of these rocks proposed by Hermann (2003). The Zr-in-rutile isopleths follow the thermometer calibration given by Tomkins et al. (2007). Cross-checking the garnet compositional data with the Zr-in-rutile concentration, it is evident that the core to rim depletion in the almandine component corresponds to an increase in the P-T conditions during crystallization, that is in good agreement with the previous published results on these rocks (see Chapter 3 and reference therein). In particular,

the garnet isopleths and the Zr-in-rutile composition suggest that the garnet starts to grow at the limit of the quartz stability field at about 2.8 GPa and 680 °C with a metamorphic peak condition (i.e. garnet rim) at about 3.8 GPa and 720 °C with lower T values for the Martiniana garnet megablast.

On the other hand, Figure 8.9b shows an alternative approach for constructing *P-T* path of the studied rocks. In this case, rather than using garnet isopleths (difficult to constrain in terms of absolute values), the zircon-in-garnet isomekes, resulting from residual pressures measured in zircon inclusions, have been used together with the Zr-in-rutile isopleths. In this regard, it is important to emphasize that zircon and rutile inclusions are very common in metamorphic rocks and the presence of both phases validate, at the same time, the possibility to use the Zr-in-rutile thermometer (e.g. Tomkins et al. 2007). The slopes of the zircon-in-garnet isomekes are different from those of the Zr-in-rutile isopleths, which make possible their use to constrain a *P-T* path (see Figure 8.9b). Assuming a residual pressure uncertainty of 0.05 GPa, the expected residual pressure of completely buried zircon inclusions should range, for a Zr-in-rutile concentration of about 200-220 ppm, between 0.5-0.6 and 0.2-0.3 GPa from core to rim respectively. Note that such an uncertainty represents an average uncertainty in the entrapment pressure of about 0.5 GPa. Therefore, by combining residual pressure of zircon inclusions in garnet megablasts with Zr-in-rutile isopleths, it becomes clear that the trend of decreasing residual pressure recorded by core-to-rim zircon inclusions in the garnet megablasts is in good agreement with the core to rim increase of pressure during garnet growth documented by the pseudo-sections and by the literature works (Chopin, 1984; Hermann 2003).

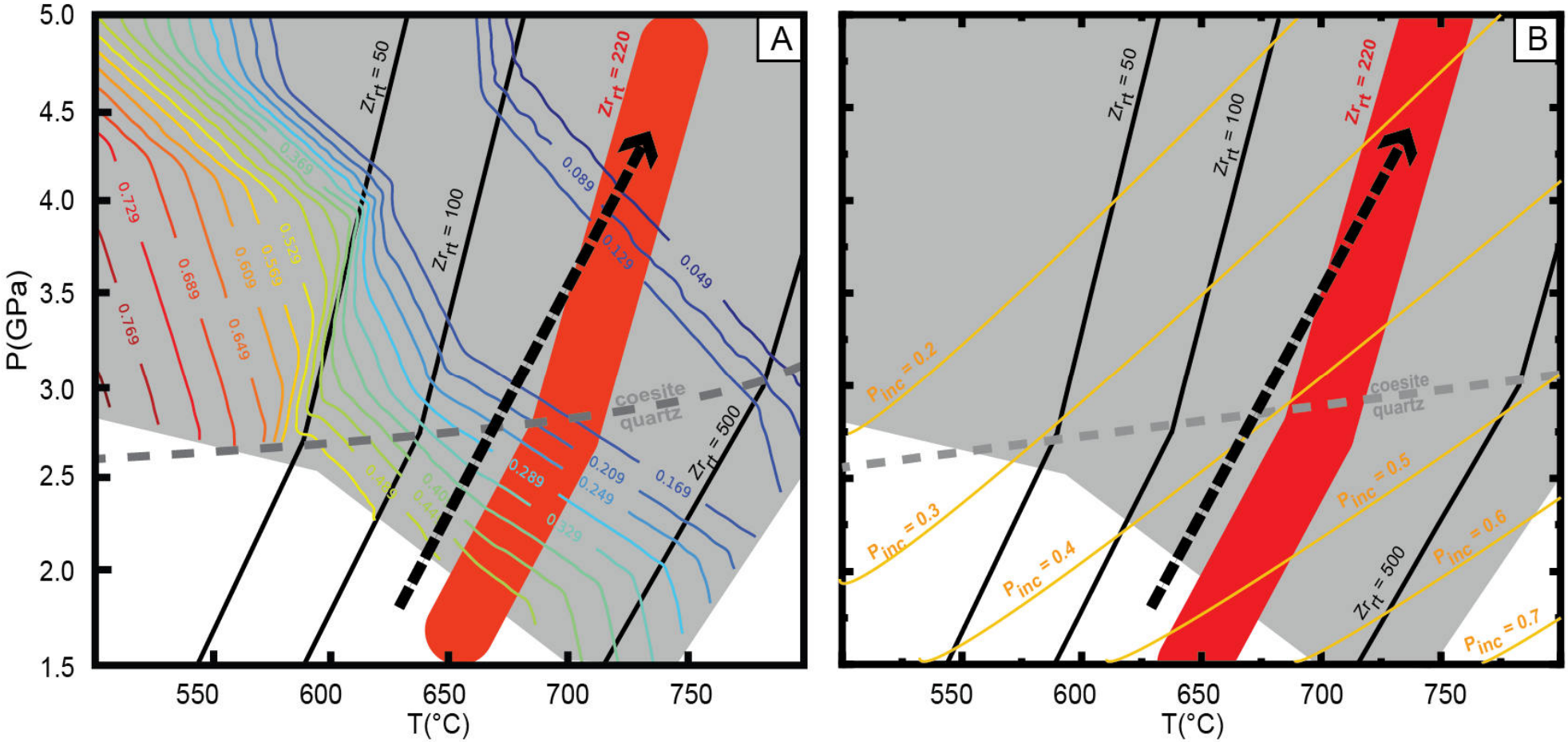

Figure 8.9 A) Pseudosection modelling of garnet stability field in Si-poor whiteschists and Zr-in-rutile (inclusions) isopleths. Rainbow-coloured lines represents the garnet isopleths in terms of almandine concentration. B) Entrapment zircon-in-garnet isomekes and Zr-in-rutile (inclusions) isopleths as function of P and T. The grey area represents the garnet stability field as computed from the pseudosection (A).

Furthermore, considering the absolute values of zircon residual pressures, there is also a very good agreement between the data obtained from the garnet rim of the sample DM17-35 and the theoretical prediction on the absolute P and T values of possible zircon entrapment conditions. In Figure 8.9, the Zr-in-rutile isopleth of 220 ppm is high-lighted in red. Combining this line with the measured residual pressures (ranging from 0.3 and 0.2 GPa for this sample) it is possible to constrain the formation of garnet rims at about 720 °C and 4-4.5 GPa (within the coesite stability field) which is consistent with the P-T conditions given by Hermann (2003).

Nevertheless, the absolute values of residual pressure measured for the zircon inclusions entrapped at the core of sample DM17-35 and most of the inclusions entrapped in the other two garnet megablasts, (i.e. especially DM17-13) are too high and do not agree with the numerical simulations. For instance, according to Figure 8.9b, residual pressures of 0.7 GPa (lower right corner of the *P-T* plot) correspond to pressures and temperatures outside the stability field of garnet if the known P-T path is considered. Consequently, residual pressures larger than 0.7, like those documented in zircon inclusions from the garnets DMG4-5 and DM17-13, cannot be explained in these terms. In the following section, therefore, a detailed analysis of possible factors that might have determined such high residual pressure values is provided.

Factors influencing the entrapment pressure estimates for zircon inclusions

Zircon chemistry

As described in chapter 6 deviations in the peak position of zircon Raman spectra can be due to the incorporation of other elements such as Hf, U and Th replacing Zr in the dodecahedral site of the zircon crystal structure. In the case of Hf substitution the B_{1g} mode near 1008 cm^{-1} and the A_{1g} mode near 975 cm^{-1} shift toward higher wavenumbers while the E_g mode near 357 cm^{-1} goes toward lower wavenumbers. On the other hand, due to their mass, elements such as U and Th shift all the peak positions towards lower wavenumbers (see Nasdala et al., 2003 for a comprehensive review). As reported in detail in chapter 6, however, these changes in the peak positions can be only appreciated for relatively large amount of chemical impurities (e.g. 16000 ppm for Hf and 6000 ppm for U) that have never been found in any exposed zircon inclusion analysed by laser ablation from the same rocks (see Chapter 6).

Instrumental artefacts

Changes of ± 1°C in the room temperature of the spectrometer lab can create changes in the Raman peak position of about 0.2 cm^{-1}. In this regard, air conditioning of the lab kept the T constant for all the entire duration of the Raman measurement sessions. Furthermore, the internal standard of a free zircon taken as reference has been analysed every 4 hours. However, given the validity of the hydrostatic calibration of zircon residual pressure (see above), there is a graphical way to point out eventual instrumental artefacts. As shown in Table 8.2, the change in the Raman peak position that is more sensitive to pressure is the B_{1g} mode near 1008 cm^{-1} ($\Delta\omega/\Delta P$ = 5.54(5) cm^{-1}/GPa). On the other hand, the A_{1g} mode near to 440 cm^{-1} is much less sensitive to pressure ($\Delta\omega/\Delta P$ = 1.44(3) cm^{-1}/GPa). In both cases however, the change in their phonon wavenumber is positive with respect to an increase in

the applied pressure. Consequently, for hydrostatic stress conditions in the inclusions, which is the case reported here (see Table 8.2), an increase in the residual pressure of the inclusion would correspond to an increase in the difference between the wavenumbers (i.e. $\Delta\omega_{1008\text{-}440}$) of these two phonon modes. Therefore, plotting this difference as function of the garnet growth zone, the trend in the residual pressure of the inclusions reported above should be completely reflected. Figure 8.10 shows that this is exactly the case.

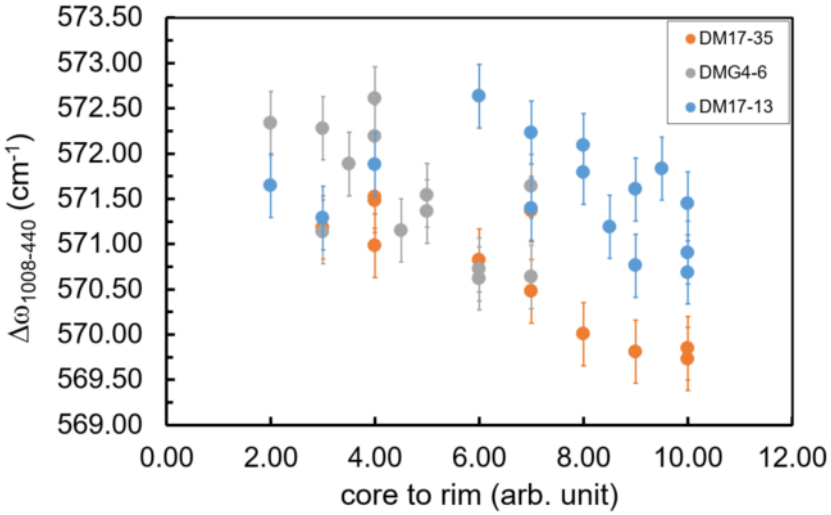

Figure 8.10 $\Delta\omega_{1008\text{-}440}$ as function of garnet growth zone. Error bars refer to the instrumental uncertainty in defining peak position (i.e. 0.35 cm^{-1})

Indeed the largest $\Delta\omega_{1008\text{-}440}$ values corresponds to those inclusions showing the largest value in the residual pressure. Furthermore, it is also evident that the inclusions entrapped within the Martiniana megablast (namely DM17-13) show systematically higher $\Delta\omega_{1008\text{-}440}$ with respect to the inclusions entrapped in the other two garnet megablasts with the same anomalous trend shown for the residual pressures. Therefore, instrumental artefacts can be neglected in this case.

Presence of fluids at the host-inclusion boundary

The presence of water at the host-inclusion boundary has been already pointed out in other rocks (Nimis et al. 2016). Unpublished results from Angel (2019) suggest that the presence of a free fluid phase (e.g. water) in the host-inclusion system can have a notable influence on the resulting residual pressure of the inclusions mainly due to the change in the isomeke slope in the P-T space. In such a case, the inclusion is composite and the resulting bulk modulus is a mix between the one of water and the one of the inclusion. However, FTIR mapping of the host-inclusion boundary has not revealed any evidence of free fluid.

Zircon metamictization: effects on the Equation of State

While metamictization effects on zircon Raman spectra are discussed in detail in Chapter 6, the effect on the EoS parameters has not been taken into account yet. Zircon is a stiff mineral and, therefore, it is difficult to determine the parameters of its equation of state (Zaffiro, 2019 PhD Thesis). Calculations of the entrapment isomekes show that the main parameter affecting the inclusion residual pressure (i.e. P_{inc}) is the bulk modulus.

In general, radiation damage processes lower the density of zircon crystals and significantly decreases their bulk modulus (e.g. Binvignat et al., 2018). Figure 8.11 shows calculations of entrapment isomekes for zircon in garnet host-inclusion systems. The plotted residual pressure of 0.2, 0.5 and 0.8 GPa are compared for different values of the bulk modulus K^0 (250, 230, 188 and 175 GPa).

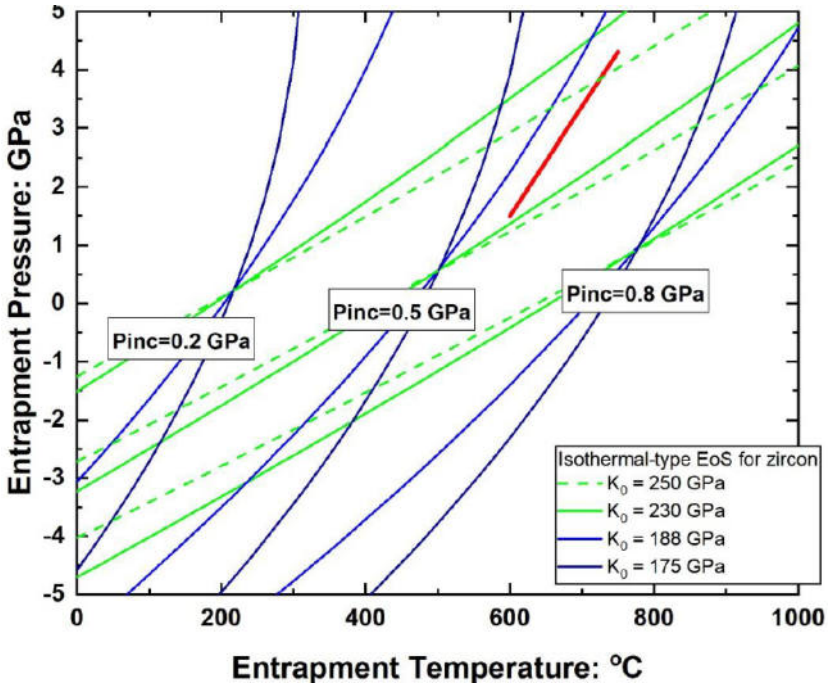

Figure 8.11. Calculated entrapment isomekes for zircon in pyrope, with different values of K^0 for zircon. The red line represents the approximate prograde path of the Dora-Maira rocks and the range over which garnet might grow

For the expected peak metamorphic conditions of whiteschists (top end of the red line in Figure 8.11) and a zircon bulk modulus of 230 GPa, the entrapment isomekes lie between residual pressure values of 0.2 and 0.5 GPa. This is consistent with inclusion residual pressure of 0.2-0.3 GPa measured at the garnet rim for the sample DM17-35. With decreasing bulk modulus, the trend of the isomekes rotate anti-clockwise increasing their slope. For a bulk modulus of 188 GPa, for example, the isomeke slope is parallel to the P-T path followed by the garnet megablast during their growth. If this would be the case, then, no trend in the inclusion residual pressure should be detected from core to rim of the garnet. On the other hand, for a bulk modulus of 175 GPa, which is representative of a quite large radiation dose in a zircon crystal (Binvignat et al., 2018), the trend in the inclusion residual pressure is inverted: the residual pressures should increase from core to rim. Increasing the bulk modulus to 250 GPa, the entrapment isomekes are flatter resulting in a general decrease

in the residual pressure. The same conclusions apply also to any other process that modifies the bulk modulus of the inclusion (i.e. incorporation of OH in the crystal structure of zircon).

Therefore, it becomes evident that only small degree of radiation damage could explain the anomalous values of residual pressure. Preliminary calculations, (Angel, 2019 unpublished results) suggest that an increase in the zircon volume, due to radiation damage, of just 0.2% can be sufficient to change the residual pressure from 0.5 to 0.8 GPa. Since tiny radiation damages in zircon are hard to detect even with high magnification techniques, and since no strong constraints on the EoS of zircon are available, any consideration in such terms could be risky and speculative and dealing with this type of features requires further years of detailed and dedicated research. For instance, zircon inclusions have been already successfully applied to other localities (e.g. Zhong et al., 2019) suggesting that small (undetectable) volume changes would have, on the other hand, a negligible effect.

Zircon annealing

Let us consider a partially metamict crystal entrapped during the garnet growth. As stated above, garnet grows along a prograde path. Consequently, the high T of metamorphic peak conditions (around 750 °C) would potentially result in a recrystallization process of the zircon inclusion. In a free crystal, this would result in a volume decrease. In an inclusion, where the volume is constrained by the garnet host, this would result in a drop in the residual pressure that was built up prior to the annealing process. Therefore, annealing of radiation damaged crystals can generate lower residual pressures with respect to crystalline zircon inclusion: therefore, this process cannot explain the residual pressure anomalies reported in this study. Note that the same considerations are valid for annealing process acting during the exhumation.

Plastic flow in the inclusion and/or in the garnet host

Plastic flow has a strong influence on the elastic thermo-barometric approach (Angel et al. 2015). Plasticity has the effect of completely resetting the system and transforms the entrapment conditions to those for which the system returns within the P-T field where the elastic behaviour is dominant.

In this regard, theory and numerical models (e.g. Mazzucchelli et al., 2019) suggest that due to the intrinsic anisotropy of uniaxial mineral inclusions, like zircon, a certain degree of deviatoric strain is expected at room conditions if the behaviour of the entire host-inclusion system has been elastic. The computed contour map reported in Figure 8.2, for example, suggests that for the conditions of possible entrapment (i.e. garnet growth) the zircon inclusions should display, from core to rim of their garnet host, a deviatoric strain (i.e. $\varepsilon_3 - \varepsilon_1$) ranging from 0.0012 to 0.0024 respectively (indicated by the black line in Figure 8.12).

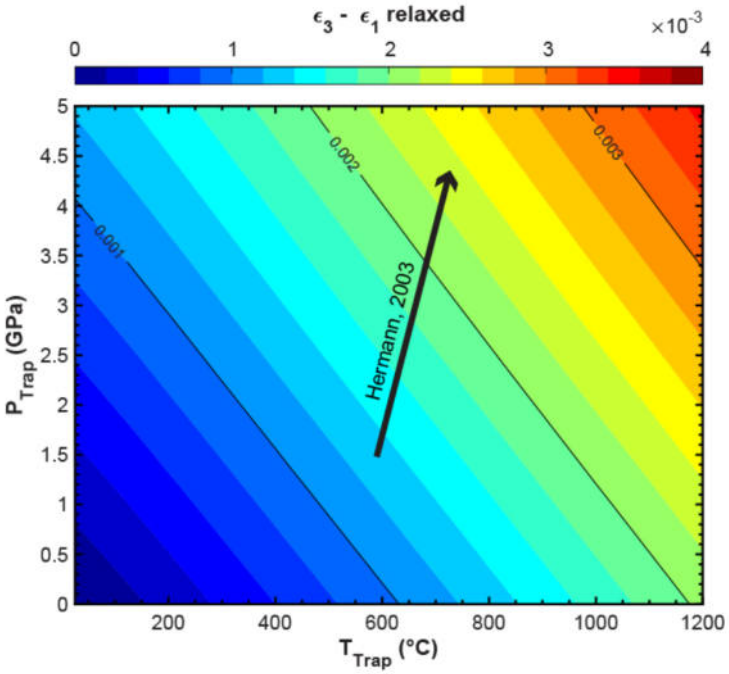

Figure 8.12 Computed contour map of residual deviatoric strain at room conditions for zircon inclusions with different entrapment conditions

The Grueneisen tensor approach, used to calculate the *residual strain*, provides information on the strain independent components (i.e. ε_3 and ε_1 in zircon). Figure 8.13 shows the independent strain components of the measured zircon inclusions as computed via the Grueneisen tensor approach. In this case the data have been plotted in terms of the two independent strain coefficients ε_3 against ε_1 which makes possible the direct comparison of our experimental data with the numerical prediction of Mazzucchelli et al. (2019). The thick solid black line represents the theoretically expected deviatoric strains as extrapolated from Figure 8.12 for the known P-T path of the Dora-Maira massif. The blue and the green lines represents the isotropic strain and the hydrostatic stress conditions of zircon inclusion respectively while diagonal black dashed lines represent equal volume strain (isochores). The inclusion residual pressure corresponding to each isochor is given as a reference in GPa.

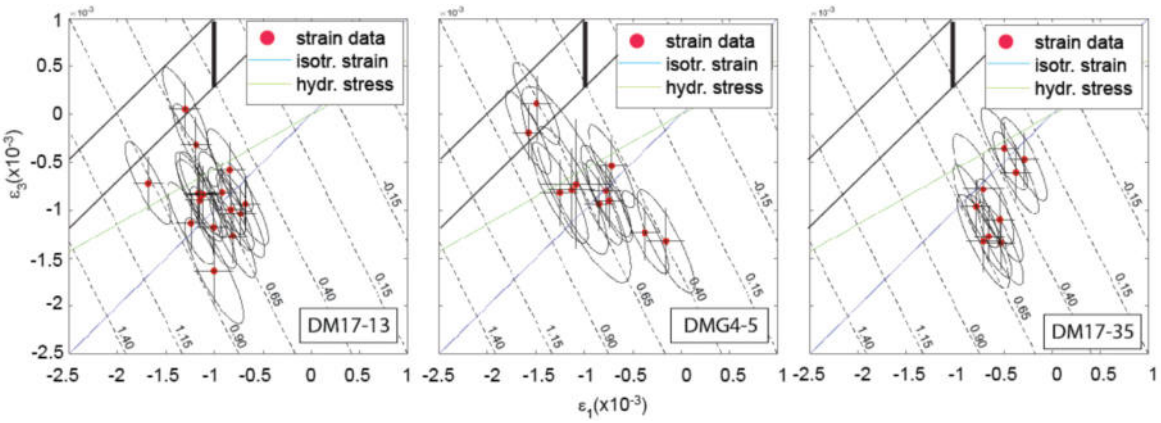

Figure 8.13. Experimentally determined deviatoric strains (in terms of $\varepsilon_3 - \varepsilon_1$) in zircon inclusions compared with the prediction from numerical models reported in Figure 8.12 (indicated by the yellow area).

The experimentally determined deviatoric strains, of selected zircon inclusions, actually show large differences with respect to the theoretical predictions and, in general, tends to be closer to the black line representing isotropic strain. This disagreement between the experimental and predicted data could be due, in principle, to the effect of plastic flow in the

inclusion that would reset eventual deviatoric strain components by means of local dislocation in the crystal structure. In this regard, multiple Raman measurements along one grain showed, in some cases, spatial variations in the relative intensity of the Raman peaks arising from the B_{1g} modes with respect those generated by A_{1g} modes (Figure 8.14). This indicates a slight mismatch of the c axis orientation in different grain zones, due to different degrees of point and extended defects, disturbing the periodicity on the level of several unit cells. Therefore, Raman data in Figure 8.14 suggest more likely faults in translational symmetry in the grain bulk (e.g. point p3) than in the periphery (point p4), which could be caused by plastic deformation within a single crystal.

However, complementary EBSD analyses (Figure 8.15) on this zircon inclusion displays no crystallographic distortion of the zircon structure, which reveals that the slight misorientation of the zircon ternary axis of symmetry occurs within spatial nano-regions insufficiently large to be detected by Bragg diffraction. Nevertheless, to avoid any uncertainties related to bulk-modulus reduction caused by periodic faults, buried inclusions showing such anomalous variations in the relative intensities have been discarded when calculating the residual pressure.

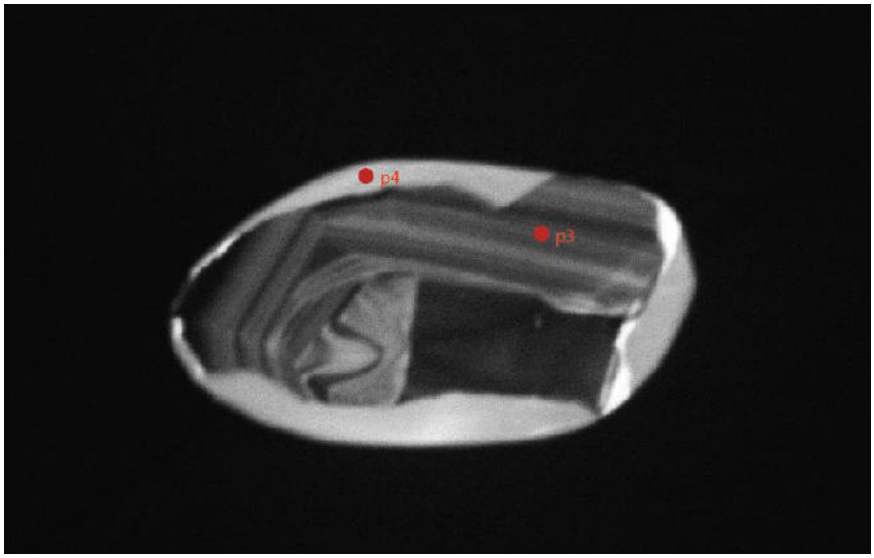

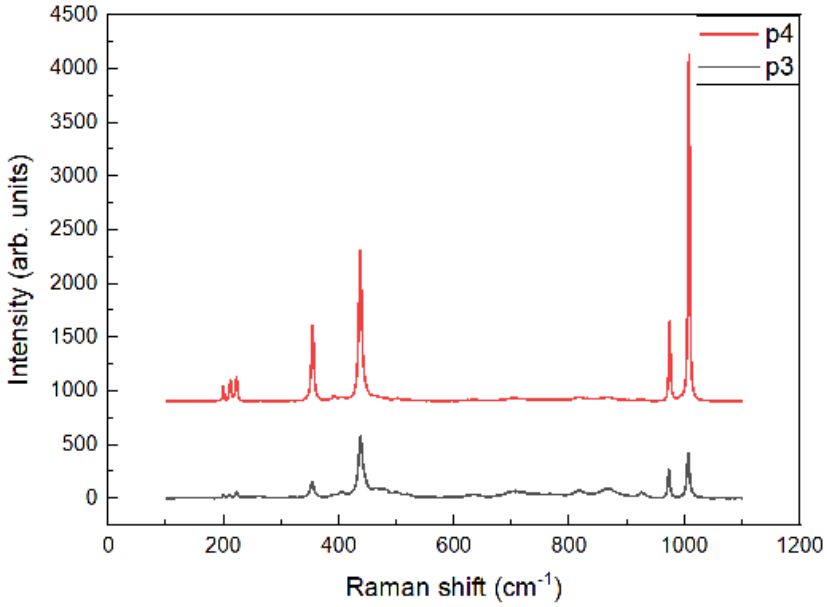

Figure 8.14 Change in the relative scattering intensity of Raman peaks within a single crystal of zircon.

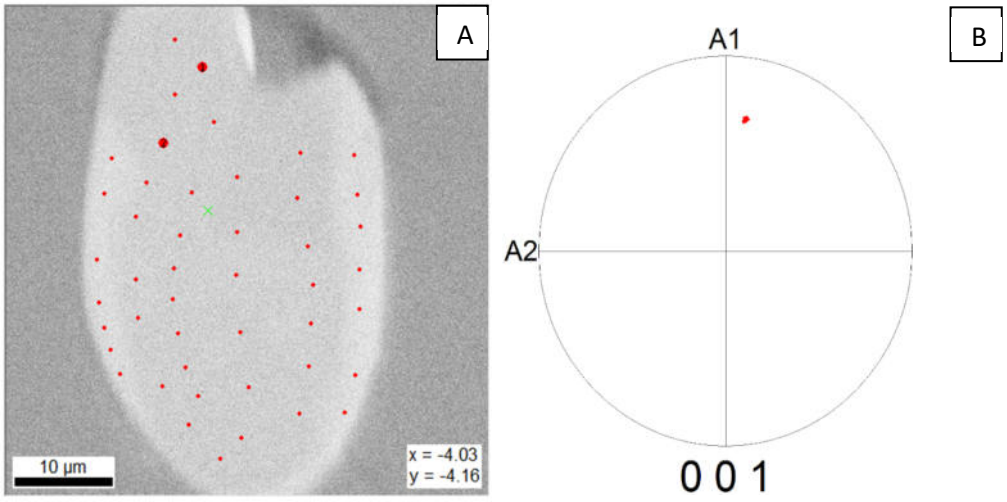

Figure 8.15. EBSD measurements on the zircon inclusions reported in Figure 8.14 revealing no crystallographic misorientation between different zircon domains. (A) scheme of EBSD point analysis; (B) stereographic plot of the c-axis (001) of zircon.

On the other hand, plastic relaxation could also occur in the garnet host. However, the advantage of considering cubic crystals has mineral host is the possibility to detect local crystal deformation by observation of its optical extinction properties under polarized light. Finally, it is important to point out that if any plastic deformation occurred it would have

resected the inclusion residual pressure of all the crystals to a unique value corresponding to the conditions of transition from the plastic to the elastic behaviour of the system. From the features described above this does not appear to be the case.

Deviatoric stress during the entrapment

Another important assumption behind the contour map of 8.12 is that entrapment conditions occurred under hydrostatic stress. Consequently, the divergence of measured strain values from the predicted values of deviatoric strain (Figure 8.13) beyond estimated uncertainties can be related, in principle, to small-scale local deviations from hydrostatic stress field around the inclusions active while the entrapment is occurring along the prograde garnet growth.

Moreover, as described in Chapter 4, garnet-forming reactions are always dehydration reactions where, according to Gautiez-Putallaz et al. (2016) up to 10 modal % of water can be produced during garnet growth. Because fluid cannot support deviatoric stresses, if the available fluid would be able to create a continuous film around the inclusion, then this would inhibit the development of deviatoric stresses. Nevertheless, in this scenario, for the complex process of nucleation and growth of host-inclusion systems traces of trapped fluid would be expected (e.g. Nimis et al. 2016). But, as stated previously, no fluid has been found at the host-inclusion boundary in our samples. Fluid inclusions have been found in garnet and kyanite only as retrograde product in the form of secondary trails. Therefore, in the absence of a continuous film of fluid surrounding the inclusion, if no post-entrapment process occurred (e.g. plastic/brittle deformation, radiation damage etc.) the level of deviatoric strain (far smaller than those predicted) could be developed because of local deviations in the hydrostatic stress field active right before inclusion isolation from the

external environment. In this regard, it is interesting to note that Henry et al. (1993) described the presence of internal S-shaped foliation within some garnet megablasts that, indeed, would potentially suggest a crystal growth in the presence of a local stress field. However, it appears to be difficult that, under a local deviatoric stress field, all the inclusion residual strains cluster along the isotropic conditions.

8.4 Implications

- This work represents the first application of the elastic thermobarometric method to the UHP unit of Dora-Maira Massif
- Measured zircon inclusions in three different garnet megablasts from the whiteschists of the UHP Brossasco-Isasca unit show a decrease in the residual pressure moving from core to rim of their garnet hosts.
- This evidence confirms the hypothesis of garnet growth during the prograde path of the studied whiteschists, as extensively documented by previous published results and thermodynamic modelling.
- Our thermodynamic modelling, together with the experimental results suggest that zircon-in-garnet isomekes coupled with Zr-in-rutile isopleths (calculated from the rutile inclusions within the same garnet), can be used to constrain the P-T conditions of metamorphic crystallization of these rocks. Indeed, this approach works quite well for a set of selected inclusions within a single garnet megablasts (sample DM17-35).
- An interesting result is represented by the fact that the absolute residual pressure values of numerous inclusions from the other garnet megablasts are too high with respect the theoretical estimates.

- The detailed analysis of processes that might have influenced the mismatch between the residual pressures measured experimentally and those predicted from modelling indicates that:
    1) Very low degrees of metamictization (undetectable with current instrumentations having spectral resolution of 2 cm^{-1}) could increase the residual pressure of zircon inclusions.
    2) The high residual pressure of zircon inclusions might be attributed to local scale deviatoric stresses during the entrapment conditions. However, this is still difficult to prove since there is not yet smocking gun evidence of this process for which further development of the elastic thermobarometric approach is needed in the years to come.

Chapter 9

General conclusions and perspectives

The main goal of this PhD Thesis has been the experimental development and the application of elastic thermobarometry to natural case studies. The work is focused on two main aspects of this new technique: setting up a methodological approach devoted to quantify the residual strains and pressures developed by elastically anisotropic mineral inclusions, and apply this approach to natural host-inclusion mineral systems from ultrahigh pressure (UHP) metamorphic rocks.

The famous UHP witheschists from the Dora-Maira Massif have been taken as favourite playground to apply this new approach for a couple of reasons. First, this rock unit is a milestone in the development of the modern petrological concept of continental subduction to depths in excess of 90-100 km (Chopin, 2003). Second, a preliminary petrographic check of these rocks has shown the presence of zircon inclusions encased in garnet showing a birefrigent halo around them (Figure 9.1).

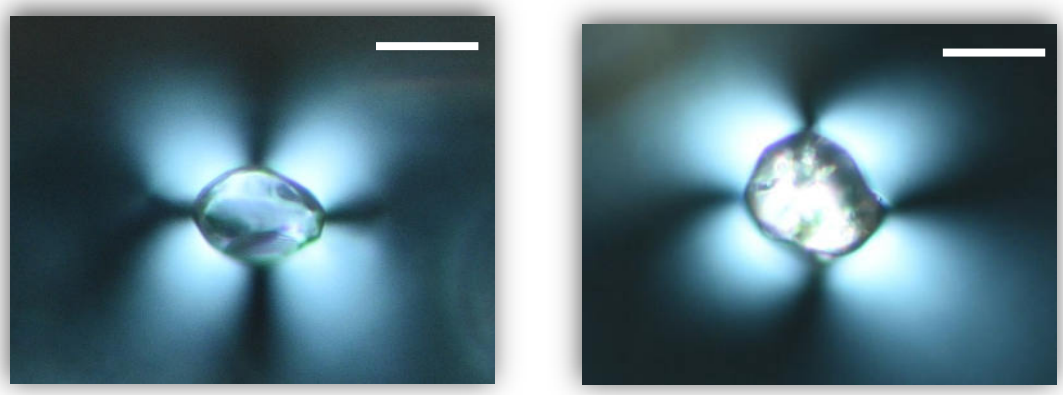

Figure 9.1. Zircon (to the left) and coesite (to the right) inclusions showing anomalous stress-induced birefringent haloes in the surrounding garnet host (scale bar of 20 μm).

The same has been shown to occur in diamonds hosting mineral inclusions as the result of elastic deformation of the diamond around inclusions that experienced an increase in volume and the built up of residual pressures during uplift (Howell et al., 2010; Howell, 2012).
This has been the starting evidence convincing me to investigate the zircon and garnet pairs from Dora-Maira for elastic thermobarometry. Backbone of this work has been the analysis of zircon inclusions within garnet. Zircon is a common accessory mineral in many metamorphic rock types: it is important because it is stable under a large range of P-T conditions and because it can be used for dating metamorphic processes. Therefore, zircon inclusions potentially are very good candidates for the elastic thermobarometry method.
The first part of my PhD has been mainly dedicated to the re-evaluation of the Raman spectroscopy method to determine, experimentally, the strain field still acting on the inclusions at room conditions: the so-called residual pressure.

Part of the PhD Thesis has been developed to understand the experimental effects that the intrinsic anisotropy and the geometry of crystals can have on the measured Raman peak positions: this represents the starting point for determining the residual pressure in stressed inclusions (Chapter 5). A major result of this analysis is that shape, corners and edges of an idiomorphic crystal act as stress concentrators developing heterogeneous stress field in (and around) the inclusions. Consequently, the peak position can change if measured in different microdomains of the same crystal, yielding to different residual pressure values (Campomenosi et al., 2018). Step-by-step polishing experiments demonstrated not only that the residual pressure is released while the inclusion is approaching the external surface but that such a stress release is a function of the crystallographic orientation of the inclusion (i.e. intrinsic anisotropy of the inclusion). Furthermore, this showed that the common method of using partially exposed inclusions as reference strain-free crystals, to determine the residual pressure of buried inclusions, is dangerous since partially exposed inclusions can partially

preserve notable amount of residual stress (Chapter 5). Overall, the results of this initial methodological study are published on an international journal (Campomenosi et al., 2018).

Another important topic addressed during this PhD Thesis regards the proper selection of zircon inclusions suitable for the application of the elastic thermobarometry. The great advantage of zircon, behaving as a geochronometer as the result of its radioactive decay, can also represent a strong limitation in using it for the elastic method. Radiation damage, due to the alpha decay of radioactive elements (metamictization), produces significant changes in the crystal physical properties that in turn affect the elastic properties of zircon and the residual pressure estimates retrieved from this mineral. In order to address this problem, a detailed study on partially exposed zircon inclusions by means of different techniques has been carried out. Charge Contrast (CC) imaging coupled with Raman spectroscopy and laser ablation ICP-MS revealed the presence of zircon crystals with notable inherited structural heterogeneity. Our study demonstrates that, for an instrumental spectral resolution of about 2 cm^{-1}, zircon crystals with peak width (in terms of full width at half maximum, FWHM) larger than 5 cm^{-1} can retain trace of partial metamictization. It is important to note, however, that this threshold value is function of the instrumental setup, and represents the analytical limitation in detecting metamictization degree that would change the peak width for values lower than 2 cm^{-1}. The results of this study are presented in a publication now available online (Campomenosi et al., 2020a).

Another part of this PhD Thesis focused on the strain state of the garnet host crystal. Cubic garnet can display characteristic anomalous birefringent haloes around stressed inclusions. A first quantitative attempt in determining the strain state of the host, by means of Raman spectroscopy, was performed using the change in the wavenumber of the Raman peaks of the host crystal close to the host-inclusion boundary. Subsequently, the quantitative analysis moved in exploiting the optical anomaly by means of the well known piezo-optic tensor (see

Chapter 7 and reference therein). In this Thesis, I present a new and alternative method to determine the stress state of the host crystal showing optical anomalies; this method exploits a similar approach of the piezo-optic tensor but translated for the Raman scattering effect. Rather than using the changes in the phonon wavenumber, this methodology exploits the changes in the Raman peak intensity and the depolarization ratio of fully symmetric phonon modes. Indeed, the relationships between an applied stress and the change in the Raman scattering are dictated by another property, called here the piezo-phonon tensor, which obeys the same symmetry constraints of the piezo-optic tensor for these modes of vibrations. The advantage of using this approach is that it is more sensitive with respect to the peak position and even if the technique is semi-quantitative, since the absolute values of the piezo-phonon tensor are still unknown, the theory developed to explain the qualitative observations opens the avenue of more detailed stress analysis of crystals by means of Raman spectroscopy that can go beyond the simple image analysis. The results of this study are now in press in an international journal (Campomenosi et al., 2020b)

Finally, the last part of my PhD Thesis has been devoted to the first application of the elastic thermobarometric method to the famous Brossasco-Isasca UHP unit in the Dora-Maira Massif (Western Alps). In this study, the above mentioned for the methodological approach, together with other methods developed by my colleagues in companion studies have been applied. In particular, zircon inclusions have been selected in order to cover the entire range of crystal growth of a garnet megablast host using the protocol developed in Chapters 5 and 6. Then, I compared and analysed the different methods in determining the residual pressure in crystals (i.e. anisotropic and hydrostatic approaches). The measured trend of residual pressure measured in zircon inclusions entrapped from core to rim of several Dora-Maira pyrope megablasts are in agreement with a prograde (increasing P and T) path during garnet crystallization, as stated in literature. However, the absolute values of residual pressures tend

to be too high with respect to the theoretical expectations and, consequently, the entrapment conditions are inconsistent with previous results. The detailed analysis of the possible processes that might have affected the residual pressure estimates and hence the recalculated entrapment conditions suggests two principal factors. The first one suggests that very low degrees of zircon metamictization, although undetectable with a spectral resolution of 2 cm^{-1}, may be enough to modify the zircon bulk modulus to a sufficient amount to notably increase the residual pressure (± 0.3 GPa). On the other hand, a second intriguing possibility is that the zircon inclusions grew and/or were trapped under non hydrostatic stress conditions. This last point is quite interesting since it would be in agreement with previous results obtained from numerical models on the Western Alps (see Chapter 8 and reference therein) claiming the presence of certain amounts of tectonic overpressure during metamorphic and deformation processes. In conclusion, even if further work would be required to shed light on this great debate, this work represents the first attempt suggesting the presence of deviatoric stresses during metamorphism based on experimental strain and stress measurements on natural samples at UHP conditions.

References

Alvaro, M., Mazzucchelli, M. L., Angel, R. J., Murri, M., Campomenosi, N., Scambelluri, M., Nestola, F., Korsakov, A., Tomilenko, A. A., Marone, F., & Morana, M. (2020). Fossil subduction recorded by quartz from the coesite stability field. Geology, 48(1), 24-28.

Anastassakis, E. M. (1980). Morphic effects in lattice dynamics. In Dynamical properties of solids, Horton G. K. & Maradudin A. A. (Eds.), 4, 159-375. Amsterdam, New York, Oxford, North-Holland

Angel R. J., Murri M., Mihailova B. D., & Alvaro M., (2018). Stress, strain and Raman shifts. Zeitschrift für Kristallographie. doi.org/10.1515/zkri-2018-2112

Angel, R. J., Mazzucchelli, M. L., Alvaro, M., Nimis, P. & Nestola, F., (2014). Geobarometry from host-inclusion systems: the role of elastic relaxation. American Mineralogist, 99, 2146-2149.

Angel, R. J., Nimis, P., Mazzucchelli, M. L., Alvaro, M., & Nestola, F. (2015). How large are departures from lithostatic pressure? Constraints from host–inclusion elasticity. Journal of Metamorphic Geology, 33(8), 801-813.

Anzolini, C., Prencipe, M., Alvaro, M., Romano, C., Vona, A., Lorenzon, S., Smith, E. M., Brenker, F. E., & Nestola, F., 2018, Depth of formation of super-deep diamonds: Raman barometry of CaSiO3-walstromite inclusions. American Mineralogist, 103(1): 69-74

Avigad, D., Chopin, C., & Le Bayon, R. (2003). Thrusting and extension in the southern Dora-Maira ultra-high-pressure massif (Western Alps): view from below the coesite-bearing unit. The Journal of Geology, 111(1), 57-70.

Avigad, D., Chopin, C., Goffe, B., & Michard, A. 1993. Tectonic model for the evolution of the western Alps. Geology 21, 659–662

Bakun-Czubarow, N. (1991). On the possibility of occurence of quartz pseudomorph after coesite in the eclogite-granulite rock series of the Zlote Mountains in the Sudetes (SW Poland). Archiwum Mineralogiczne, 47(1), 5-16.

Beltrando, M., Compagnoni, R., & Lombardo, B. (2010). (Ultra-) High-pressure metamorphism and orogenesis: an Alpine perspective. Gondwana Research, 18(1), 147-166.

Binvignat, F. A. P., Malcherek, T., Angel, R. J., Paulmann, C., Schlüter, J., & Mihailova, B. (2018). Radiation-damaged zircon under high pressures. Physics and Chemistry of Minerals, 45(10), 981-993.

Brodie, K. H., & Rutter, E. H. (1985). On the relationship between deformation and metamorphism, with special reference to the behavior of basic rocks. In Metamorphic reactions (pp. 138-179). Springer, New York, NY.

Caby, R. (1994). Precambrian coesite from northern Mali: first record and implications for plate tectonics in the trans-Saharan segment of the Pan-African belt. European Journal of Mineralogy, 6, 235-244.

Campomenosi, N., Mazzucchelli, M. L., Mihailova, B., Angel, R. J., & Alvaro, M. (2020b). Contribution to Mineralogy and Petrology, DOI :10.1007/s00410-019-1651-x

Campomenosi, N., Mazzucchelli, M. L., Mihailova, B., Scambelluri, M., Angel, R. J., Nestola, F., Reali, A., & Alvaro, M. (2018) How geometry and anisotropy affect residual strain in host-inclusion system: coupling experimental and numerical approaches. American Mineralogist, 103, 2032-2035

Campomenosi, N., Rubatto, D., Hermann, J., Mihailova, B., Scambelluri, M., Alvaro, M. (2020a) Establishing a protocol for the selection of zircon inclusions in garnet for Raman thermobarometry. American Mineralogist, DOI: 10.2138/am-2020-7246

Carpenter, M. A., & Putnis, A. (1985). Cation order and disorder during crystal growth: some implications for natural mineral assemblages. In Metamorphic Reactions (pp. 1-26). Springer, New York, NY.

Carswell, D. A., Compagnoni, R., & Rolfo, F. (Eds.). (2003). Ultrahigh pressure metamorphism (Vol. 5). EMU Notes in Mineralogy.

Castelli, D., Compagnoni, R., Lombardo, B., Angiboust, S., Balestro, G., Ferrando, S., Groppo, C., Rolfo. F., & Hirajima, T. (2010) GFT–Geological Field Trips.

Castelli, D., Rolfo, F., Groppo, C., & Compagnoni, R. (2007). Impure marbles from the UHP Brossasco-Isasca Unit (Dora-Maira Massif, western Alps): evidence for Alpine equilibration in the diamond stability field and evaluation of the X (CO_2) fluid evolution. Journal of Metamorphic Geology, 25(6), 587-603.

Cesare, B., Nestola, F., Johnson, T., Mugnaioli, E., Della Ventura, G., Peruzzo, L., Bartoli, O., Viti, C., & Erickson, T. (2019) Garnet, the archetypal cubic mineral, grows tetragonal. Scientific Reports 9, 14672

Chesnokov, B. V., & Popov, V. A. (1965). Increase in the volume of quartz grains in South Urals eclogite. In Dokl Akad Nauk SSSR (Vol. 162, pp. 176-178).

Chopin, C. (1984). Coesite and pure pyrope in high-grade blueschists of the Western Alps: a first record and some consequences. Contributions to Mineralogy and Petrology, 86(2), 107-118.

Chopin, C. (1987). Very-high-pressure metamorphism in the western Alps: implications for subduction of continental crust. Philosophical Transactions of the Royal Society of London. Series A, Mathematical and Physical Sciences, 321(1557), 183-197.

Chopin, C. (2003). Ultrahigh-pressure metamorphism: tracing continental crust into the mantle. Earth and Planetary Science Letters, 212(1-2), 1-14.

Chopin, C., & Schertl, H. P. (1999). The UHP unit in the Dora-Maira massif, western Alps. International Geology Review, 41(9), 765-780.

Chopin, C., Henry, C., & Michard, A. (1991). Geology and petrology of the coesite-bearing terrain, Dora Maira massif, Western Alps. European Journal of Mineralogy, 3(2), 263-291.

Coe, R. S., & Paterson, M. S. (1969). The α–β inversion in quartz: a coherent phase transition under nonhydrostatic stress. Journal of Geophysical Research, 74(20), 4921-4948.

Colombo, M., Chrosch, J., & Salje, E. K. (1999) Annealing Metamict Zircon: A Powder X-ray Diffraction Study of a Highly Defective Phase. Journal of the American Ceramic Society, 82(10), 2711-2716

Compagnoni, R., & Hirajima, T. (2001). Superzoned garnets in the coesite-bearing Brossasco-Isasca Unit, Dora-Maira massif, Western Alps, and the origin of the whiteschists. Lithos, 57(4), 219-236.

Compagnoni, R., Hirajima, T., & Chopin, C. (1995). Ultra-high-pressure metamorphic rocks in the Western Alps. In Ultrahigh pressure metamorphism, Coleman, R. G., & Wang, X. (Eds.). Cambridge University Press. 206-243.

Compagnoni, R., Hirajima, T., Turello, R., & Castelli, D. (1994, September). The Brossasco-Isasca Unit. In High pressure metamorphism in the Western Alps. Guide-book to the field

excursion B1 16th General Meeting of the International Mineralogical Association, Pisa (pp. 10-15).

Compagnoni, R., Rolfo, F., Groppo, C., Hirajima, T., & Turello, R. (2012). Geological map of the ultra-high pressure Brossasco-Isasca unit (Western Alps, Italy). Journal of Maps, 8(4), 465-472.

Connolly, J. A. (2005). Computation of phase equilibria by linear programming: a tool for geodynamic modeling and its application to subduction zone decarbonation. Earth and Planetary Science Letters, 236(1-2), 524-541.

Corfu, F., Hanchar, J. M., Hoskin, P. W. O., and Kinny, P. (2003) Atlas of zircon textures. Reviews in Mineralogy and Geochemistry 53:469-500

Dobrzhinetskaya, L. F., Eide, E. A., Larsen, R. B., Sturt, B. A., Trønnes, R. G., Smith, D. C., Taylor, W. R., & Posukhova, T. V. (1995). Microdiamond in high-grade metamorphic rocks of the Western Gneiss region, Norway. Geology, 23(7), 597-600.

Duchêne, S., Blichert-Toft, J., Luais, B., Télouk, P., Lardeaux, J. M., & Albarede, F. (1997). The Lu–Hf dating of garnets and the ages of the Alpine high-pressure metamorphism. Nature, 387(6633), 586-589.

Enami, M., Nishiyama, T., & Mouri, T., 2007, Laser Raman microspectrometry of metamorphic quartz: A simple method for comparison of metamorphic pressures. American Mineralogist, 92, 1303–1315.

Eshelby, J. D., 1957, The determination of the elastic field of an ellipsoidal inclusion and related problems. Proceedings of the Physical Society of London, Series A, 241, 376-396.

Ewing, R. C., Lutze, W., and Weber, W. J. (1995) Zircon: A host-phase for the disposal of weapons plutonium. Journal of Materials Research, 10(2), 243-246

Ferrando, S., Frezzotti, M. L., Petrelli, M., & Compagnoni, R. (2009). Metasomatism of continental crust during subduction: the UHP whiteschists from the Southern Dora-Maira Massif (Italian Western Alps). Journal of Metamorphic Geology, 27(9), 739-756.

Ferraris, C., Chopin, C., & Wessicken, R. (2000). Nano-to micro-scale decompression products in ultrahigh-pressure phengite: HRTEM and AEM study, and some petrological implications. American Mineralogist, 85(9), 1195-1201.

Ferraris, C., Castelli, D., & Lombardo, B. (2005). SEM/TEM-AEM characterization of micro-and nano-scale zonation in phengite from a UHP Dora-Maira marble: petrologic significance of armoured Si-rich domains. European Journal of Mineralogy, 17(3), 453-464.

Frezzotti, M. L., Selverstone, J., Sharp, Z. D., & Compagnoni, R. (2011). Carbonate dissolution during subduction revealed by diamond-bearing rocks from the Alps. Nature Geoscience, 4(10), 703-706.

Gauthiez-Putallaz, L., Rubatto, D., & Hermann, J. (2016). Dating prograde fluid pulses during subduction by in situ U–Pb and oxygen isotope analysis. Contributions to Mineralogy and Petrology, 171(2), 15.

Gebauer, D., Schertl, H. P., Brix, M., & Schreyer, W. (1997). 35 Ma old ultrahigh-pressure metamorphism and evidence for very rapid exhumation in the Dora Maira Massif, Western Alps. Lithos, 41(1-3), 5-24.

Geisler, T., & Pidgeon, R. T. (2002) Raman scattering from metamict zircon: comments on" Metamictisation of natural zircon: accumulation versus thermal annealing of radioactivity-induced damage" by Nasdala et al. 2001 (Contribution to Mineralogy and Petrology 141: 125-144). Contributions to Mineralogy and Petrology, 143(6), 750-755

Geisler, T., Pidgeon, R. T., van Bronswijk, W., & Pleysier, R. (2001) Kinetics of thermal recovery and recrystallization of partially metamict zircon: a Raman spectroscopic study. European Journal of Mineralogy, 13(6), 1163-1176

Ghiribelli, B., Frezzotti, M. L., & Palmeri, R. (2002). Coesite in eclogites of the Lanterman Range (Antarctica) Evidence from textural and Raman studies. European Journal of Mineralogy, 14(2), 355-360.

Gibbs, J. W. (1906). On the equilibrium of heterogeneous substances. The Scientific Papers of JW Gibbs (Vol. 1, pp. 55-354). Longmans, Green and Company, London, New York and Bombay.

Gillet, P., Fiquet, G., Malezieux, J. M., & Geiger, C. A. (1992). High-pressure and high-temperature Raman spectroscopy of end-member garnets; pyrope, grossular and andradite. European Journal of Mineralogy, 4(4), 651-664.

Gilotti, J. A., & Ravna, E. J. K. (2002). First evidence for ultrahigh-pressure metamorphism in the North-East Greenland Caledonides. Geology, 30(6), 551-554.

Gregora I. (2006). Raman Scattering. In International Tables for Crystallography. D-2.3, 314-328

Griffin, B. J. (2000). Charge contrast imaging of material growth and defects in environmental scanning electron miscroscopy—linking electron emission and cathodoluminescence. Scanning 22(4):234-242.

Groppo, C., Lombardo, B., Castelli, D., & Compagnoni, R. (2007). Exhumation history of the UHPM Brossasco-Isasca Unit, Dora-Maira Massif, as inferred from a phengite-amphibole eclogite. International Geology Review, 49(2), 142-168.

Groppo, C., Ferrando, S., Gilio, M., Botta, S., Nosenzo, F., Balestro, G., ... & Rolfo, F. (2019). What's in the sandwich? New P–T constraints for the (U) HP nappe stack of southern Dora-Maira Massif (Western Alps). European Journal of Mineralogy, 31(4), 665-683.

Henry, C., Michard, A., & Chopin, C. (1993). Geometry and structural evolution of ultra-high-pressure and high-pressure rocks from the Dora-Maira massif, Western Alps, Italy. Journal of Structural Geology, 15, 965-965.

Hermann, J. (2003). Experimental evidence for diamond-facies metamorphism in the Dora-Maira massif. Lithos, 70(3-4), 163-182.

Hermann, J., Rubatto, D., Korsakov, A., and Shatsky, V. S. (2001) Multiple zircon growth during fast exhumation of diamondiferous, deeply subducted continental crust (Kokchetav massif, Kazakhstan). Contribution to Mineralogy and Petrology 141:66-82

Hobbs, B., & Ord, A. (2015). Dramatic effects of stress on metamorphic reactions: COMMENT. Geology, 43(11), e372-e372.

Holland, T. J. B., & Powell, R. (2011). An improved and extended internally consistent thermodynamic dataset for phases of petrological interest, involving a new equation of state for solids. Journal of Metamorphic Geology, 29(3), 333-383.

Hoskin, P. W. O., & Rodgers, K. A. (1996) Raman spectral shift in the isomorphous series (Zr1-xHfx)SiO4. European Journal of Solid State Inorganic Chemistry 33, 1111-1121

Hoskin, P. W., & Schaltegger, U. (2003) The composition of zircon and igneous and metamorphic petrogenesis. In J. M. Hanchar and P. W. O. Hoskin, Eds., Zircon, 53, p. 427 467. Review in Mineralogy and Geochemistry, Mineralogical Society of America, Chantilly, Virginia

Howell, D. (2012) Strain-Induced Birefringence in Natural Diamonds. European Journal of Mineralogy, 24, 575-585

Howell, D., Wood, I. G., Dobson, D. P., Jones, A. P., Nasdala, L., & Harris, J. W. (2010). Quantifying strain birefringence halos around inclusions in diamond. Contributions to Mineralogy and Petrology, 160(5), 705-717.

Izraeli, E. S., Harris, J. W., & Navon, O. (1999). Raman barometry of diamond formation. Earth and Planetary Science Letters, 173(3), 351-360.

Katayama I., and Maruyama S. (2009) Inclusion study in zircon from ultrahigh-pressure metamorphic rocks in the Kokchetav massif: an excellent tracer of metamorphic history. Journal of the Geological Society 166:783-796

Knittle, E., & Williams, Q. (1993) High-pressure Raman spectroscopy of ZrSiO4: Observation of the zircon to scheelite transition at 300 K. American Mineralogist, 78(3-4), 245-252

Kohn, M. J. (2014). "Thermoba-Raman-try": Calibration of spectroscopic barometers and thermometers for mineral inclusions. Earth and Planetary Science Letters, 388, 187-196.

Korsakov, A.V., Perraki, M., Zhukov, V.P., De Gussem, K., Vandenabeele, P., and Tomilenko, A.A., 2009 Is quartz a potential indicator of ultrahigh pressure metamorphism? Laser Raman spectroscopy of quartz inclusions in ultrahigh-pressure garnets: European Journal of Mineralogy, 21, 1313–1323

Krohe, A., & Mposkos, E. (2001). Structural evolution and exhumation history of the Rhodope UHP-HP metamorphic province (Northern Greece). Bulletin of the Geological Society of Greece, 34(1), 75-82.

Kroumova, E., Aroyo, M. I., Perez-Mato, J. M., Kirov, A., Capillas, C., Ivantchev S., & Wondratschek, H. (2010) Bilbao Crystallographic Server : Useful Databases and Tools for Phase-Transition Studies. Phase Transitions, 76:1-2, 155-170

Kuzmany, H. (2009). Solid-state spectroscopy: an introduction. Springer Science & Business Media.

Lan, T., Tang, X., & Fultz, B. (2012). Phonon anharmonicity of rutile TiO_2 studied by Raman spectrometry and molecular dynamics simulations. Physical Review B, 85(9), 094305.

Lanari, P., & Engi, M. (2017). Local bulk composition effects on metamorphic mineral assemblages. Reviews in Mineralogy and Geochemistry, 83(1), 55-102.

Leech, M., & Ernst, W. G. (1998). Graphite pseudomorphs after diamond? A carbon isotope and spectroscopic study of graphite cuboids from the Maksyutov Complex, south Ural Mountains, Russia. Geochimica et Cosmochimica Acta, 62(12), 2143-2154.

Liu, L., Chen, D. L., Sun, Y., Zhang, A. D., & Luo, J. H. (2003, June). Discovery of relic majoritic garnet in felsic metamorphic rocks of Qinling complex, north Qinling orogenic belt, China. In Alice Wain Memorial Western Norway Eclogite Field Symposium. Selje, Western Noway, Abstract (Vol. 82).

Liu, L., Sun, Y., Wang, Y., Chen, D. L., Luo, J. H., & Zhang, A. D. (2003). Ultrahigh-P evidence for the country rocks of garnet-bearing lherzolite in Altyn Tagh-exsolution of clinopyroxene in the garnet of retrograde eclogite. In Alice Wain Memorial Western Norway eclogite field symp., Selje, Western Norway, Abstr Vol (Vol. 81).

Malusà, M. G., Faccenna, C., Baldwin, S. L., Fitzgerald, P. G., Rossetti, F., Balestrieri, M. L., Danisik, M., Ellero, A., Ottria, G., & Piromallo, C. (2015). Contrasting styles of (U) HP

rock exhumation along the Cenozoic Adria-Europe plate boundary (Western Alps, Calabria, Corsica). Geochemistry, Geophysics, Geosystems, 16(6), 1786-1824.

Mancktelow, N. S. (2009). Fracture and flow in natural rock deformation. Trabajos de geología, 29(29).

Matsumoto, N., & Hirajima, T. (2000). Garnet in pelitic schists from a quartz-eclogite unit of the southern Dora-Maira massif, Western Alps. Schweizerische mineralogische und petrographische Mitteilungen, 80(1), 53-62.

Mazzucchelli M. L., Burnley P., Angel R. J., Domeneghetti M. C., Nestola F., Alvaro M. (2016) Elastic geobarometry: uncertainties arising from the shape of the inclusion. In: 12nd European mineralogical conference, Rimini, Italy, September, 2016. Book of Abstracts, p 232

Mazzucchelli M. L., Reali, A., Morganti, S., Angel, R. J., Alvaro, M. (2019) Elastic geobarometry for anisotropic inclusions in cubic hosts. Lithos, 105218

Mazzucchelli, M. L., Burnley, P., Angel, R. J., Morganti, S., Domeneghetti, M. C., Nestola, F., & Alvaro, M. (2018). Elastic geothermobarometry: Corrections for the geometry of the host-inclusion system. Geology, 46(3), 231-234.

Milani, S., Nestola, F., Alvaro, M., Pasqual, D., Mazzucchelli, M. L., Domeneghetti, M. C., & Geiger, C. A. (2015). Diamond–garnet geobarometry: The role of garnet compressibility and expansivity. Lithos, 227, 140-147.

Monie, P., & Chopin, C. (1991). 40Ar/39Ar dating in coesite-bearing and associated units of the Dora Maira massif, Western Alps. European Journal of Mineralogy, 239-262.

Murri, M., Mazzucchelli, M. L., Campomenosi, N., Korsakov, A. V., Prencipe, M., Mihailova, B. D., Scambelluri, M., Angel, R. J., & Alvaro, M. (2018). Raman elastic

geobarometry for anisotropic mineral inclusions. American Mineralogist, 103(11), 1869-1872.

Nakamoto K. (2009), Infrared and Raman Spectra of Inorganic and Coordination Compounds Part A: Theory and Applications in Inorganic Chemistry. Wiley, U.S.A

Nasdala, L., & Massonne, H. J. (2000). Microdiamonds from the Saxonian Erzgebirge, Germany: in situ micro-Raman characterisation. European Journal of Mineralogy, 12(2), 495-498.

Nasdala, L., Brenker, F. E., Glinnemann, J., Hofmeister, W., Gasparik, T., Harris, J. W. Stachel, T., & Reese, I. (2003). Spectroscopic 2D-tomography: Residual pressure and strain around mineral inclusions in diamonds. European Journal of Mineralogy, 15(6), 931-935.

Nasdala, L., Hofmeister, W., Harris, J. W., Glinnemann, J. (2005): Growth zoning and strain patterns inside diamond crystals as revealed by Raman maps. American Mineralogist, 90, 745-748

Nasdala, L., Lengauer, C. L., Hanchar, J. M., Kronz, A., Wirth, R., Blanc, P., & Seydoux-Guillaume, A. M. (2002) Annealing radiation damage and the recovery of cathodoluminescence. Chemical Geology, 191(1-3), 121-140

Nasdala, L., Pidgeon, R.T., Wolf, D., & Irmer, G., 1998, Metamictization and U-Pb isotopic discordance in single zircons: a combined Raman microprobe and SHRIMP ion probe study. Mineralogy and Petrology, 62, 1–27

Nasdala, L., Wenzel, M., Vavra, G., Irmer, G., Wenzel, T., & Kober, B. (2001). Metamictisation of natural zircon: accumulation versus thermal annealing of radioactivity-induced damage. Contributions to Mineralogy and Petrology, 141(2), 125-144.

Nimis, P., Alvaro, M., Nestola, F., Angel, R. J., Marquardt, K., Rustioni, G., Harris, J. W., & Marone, F. (2016). First evidence of hydrous silicic fluid films around solid inclusions in gem-quality diamonds. Lithos, 260, 384-389.

Nye, J. F. (1985). Physical properties of crystals: their representation by tensors and matrices. Oxford university press.

O'Brien, P. J., Zotov, N., Law, R., Khan, M. A., & Jan, M. Q. (2001). Coesite in Himalayan eclogite and implications for models of India-Asia collision. Geology, 29(5), 435-438.

Özkan, H., Cartz, L., and Jamieson, J.C. (1974) Elastic constants of nonmetamict zirconium silicate. Journal of Applied Physics, 45, 556–562

Palmeri, R., Ghiribelli, B., Talarico, F., & Ricci, C. A. (2003). Ultra-high-pressure metamorphism in felsic rocks: the garnet-phengite gneisses and quarzites from the Lanterman Range, Antarctica. European Journal of Mineralogy, 15(3), 513-525.

Parkinson, C. D., & Katayama, I. (1999). Present-day ultrahigh-pressure conditions of coesite inclusions in zircon and garnet: Evidence from laser Raman microspectroscopy. Geology, 27(11), 979-982.

Parkinson, C. D., Miyazaki, K., Wakita, K., Barber, A. J., & Carswell, D. A. (1998). An overview and tectonic synthesis of the pre-Tertiary very-high-pressure metamorphic and associated rocks of Java, Sulawesi and Kalimantan, Indonesia. Island Arc, 7(1-2), 184-200.

Parkinson, C. D., Motoki, A., Onishi, C. T., & Maruyama, S. (2001). Ultrahigh-pressure pyrope-kyanite granulites and associated eclogites in Neoproterozoic nappes of southeast Brazil. In UHPM Workshop (pp. 87-90). Waseda University.

Paton, C., Hellstrom, J., Paul, B., Woodhead, J., and Hergt, J. (2011) Iolite: freeware for the visualisation and processing of mass spectrometric data. Journal of Analytical Atomic Spectrometry. 26:2508–2518

Putnis, A. (1992) Introduction to mineral science. Cambridge University Press, New York, pp. 457.

Reinecke, T. (1991). Very-high-pressure metamorphism and uplift of coesite-bearing metasediments from the Zermatt-Saas zone, Western Alps. European Journal of Mineralogy, 7-18.

Ríos, S., Salje, E. K., Zhang, M., & Ewing, R. C. (2000) Amorphization in zircon: evidence for direct impact damage. Journal of Physics: Condensed Matter, 12(11), 2401

Roermund, van, H.L. (1998). Ultra-high pressure (P> 6 GPa) garnet peridotites in Western Norway: exhumation of mantle rocks from> 185 km depth. Terra Nova, 10(6), 295-301.

Rosenfeld, J. L., & Chase, A. B. (1961). Pressure and temperature of crystallization from elastic effects around solid inclusions in minerals?. American Journal of Science, 259(7), 519-541.

Rubatto, D., & Gebauer, D. (2000) Use of cathodoluminescence for U-Pb zircon dating by ion microprobe: some examples from the Western Alps. In: Pagel M, Barbin V, Blanc P, Ohnenstetter D (eds) Cathodoluminescence in geosciences, vol. Springer, Berlin Heidelberg New York, pp 373-400.

Rubatto, D., & Hermann, J. (2001). Exhumation as fast as subduction?. Geology, 29(1), 3-6.

Rubatto, D., & Hermann, J. (2007) Zircon behaviour in deeply subducted rocks. Elements, 2007, 3.1: 31-35

Săbău, G. (2000). A possible UHP-eclogite in the Leaota Mts.(South Carpathians) and its history from high-pressure melting to retrograde inclusion in a subduction melange. Lithos, 52(1-4), 253-276.

Sachan, H.K. & Mukherjee, B.R. (2003): Metamorphic and fluid evolution of ultra-high metamorphosed (UHP) crust of Tso-Morari region, Ladakh, Himalaya, (India): constraints from mineral chemistry and fluid inclusions. In Alice Wain Memorial Western Norway Eclogite Field Symp., Selje, Western Norway, Abstr. Vol., 124–125.

Sandrone, R., & Borghi, A. (1992). Zoned garnets in the northern Dora-Maira Massif and their contribution to a reconstruction of the regional metamorphic evolution. European journal of mineralogy, 465-474.

Scambelluri, M., Van Roermund, H. L., & Pettke, T. (2008). Mantle wedge peridotites: fossil reservoirs of deep subduction zone processes: inferences from high and ultrahigh-pressure rocks from Bardane (Western Norway) and Ulten (Italian Alps). Lithos, 120(1-2), 186-201.

Schertl, H. P., & Schreyer, W. (2008). Geochemistry of coesite-bearing “pyrope quartzite” and related rocks from the Dora-Maira Massif, Western Alps. European Journal of Mineralogy, 20(5), 791-809.

Schertl, H. P., Schreyer, W., & Chopin, C. (1991). The pyrope-coesite rocks and their country rocks at Parigi, Dora Maira Massif, Western Alps: detailed petrography, mineral chemistry and PT-path. Contributions to Mineralogy and Petrology, 108(1-2), 1-21.

Schmalholz, S. M., Duretz, T., Schenker, F. L., & Podladchikov, Y. Y. (2014). Kinematics and dynamics of tectonic nappes: 2-D numerical modelling and implications for high and ultra-high pressure tectonism in the Western Alps. Tectonophysics, 631, 160-175.

Schreyer, W., Massonne, H.-J. & Chopin, C. (1987) Continental crust subducted to mantle depths near 100 km: implications for magma and fluid genesis in collision zones. In Mysen, O. (ed.): Magmatic processes: physicochemical principles. Geochemical Society, 155–163

Sharp, Z. D., Essene, E. J., & Hunziker, J. C. (1993). Stable isotope geochemistry and phase equilibria of coesite-bearing whiteschists, Dora Maira Massif, western Alps. Contributions to Mineralogy and Petrology, 114(1), 1-12.

Shtukenberg, A., Punin, Y., (2007). Optically Anomalous Crystals. Springer, Netherlands

Sinogeikin, S. V., & Bass, J.D., 2002, Elasticity of pyrope and majorite-pyrope solid solutions to high temperatures. Earth and Planetary Science Letters, 203, 549-555

Smith, D. C. (1984). Coesite in clinopyroxene in the Caledonides and its implications for geodynamics. Nature, 310(5979), 641-644.

Sobolev, N. V., & Shatsky, V. S. (1990). Diamond inclusions in garnets from metamorphic rocks: a new environment for diamond formation. Nature, 343(6260), 742-746.

Song, S. G., Yang, J. S., Xu, Z. Q., Liou, J. G., & Shi, R. D. (2003). Metamorphic evolution of the coesite-bearing ultrahigh-pressure terrane in the North Qaidam, Northern Tibet, NW China. Journal of metamorphic Geology, 21(6), 631-644.

Stangarone, C., Angel, R. J., Prencipe, M., Campomenosi, N., Mihailova, B., & Alvaro, M. (2019). Measurement of strains in zircon inclusions by Raman spectroscopy. European Journal of Mineralogy, 31 (4): 685–694.

Tagiri, M., Yano, T., Bakirov, A., Nakajima, T., & Uchiumi, S. (1995). Mineral parageneses and metamorphic P-T paths of ultrahigh-pressure eclogites from Kyrghyzstan Tien-Shan. Island Arc, 4(4), 280-292.

Tajčmanová, L., Vrijmoed, J., & Moulas, E. (2015). Grain-scale pressure variations in metamorphic rocks: implications for the interpretation of petrographic observations. Lithos, 216, 338-351.

Tilton, G. R., Schreyer, W., & Schertl, H. P. (1989). Pb-Sr-Nd isotopic behavior of deeply subducted crustal rocks from the Dora Maira Massif, Western Alps, Italy. Geochimica et Cosmochimica Acta, 53(6), 1391-1400.

Tomkins, H. S., Powell, R., & Ellis, D. J. (2007). The pressure dependence of the zirconium-in-rutile thermometer. Journal of metamorphic Geology, 25(6), 703-713.

Treloar, P. J., O'Brien, P. J., Parrish, R. R., & Khan, M. A. (2003). Exhumation of early Tertiary, coesite-bearing eclogites from the Pakistan Himalaya. *Journal of the Geological Society*, *160*(3), 367-376.

Van der Klauw, S. N. G. C., Reinecke, T., & Stöckhert, B. (1997). Exhumation of ultrahigh-pressure metamorphic oceanic crust from Lago di Cignana, Piemontese zone, western Alps: the structural record in metabasites. Lithos, 41(1-3), 79-102.

van der Molen I. and van Roermund H. L. M., (1986) The pressure path of solid inclusions in minerals: the retention of coesite inclusions during uplift. Lithos, 19, 317-324

Vialon, P. (1966). Etude géologique du massif cristallin Dora-Maira: Alpes cottiennes internes: Italie (Doctoral dissertation, Université de Grenoble).

Wang, X., Liou, J. G., & Mao, H. K. (1989). Coesite-bearing eclogite from the Dabie Mountains in central China. Geology, 17(12), 1085-1088.

Watson, E. B., Wark, D. A., & Thomas, J. B. (2006) Crystallization thermometers for zircon and rutile. Contribution to Mineralogy and Petrology 151, 413-433

Watt, G. R., Kinny, P. D., and Griffin, B. J. (2000) Charge contrast imaging of geological materials in the environmental scanning electron microscope. American Mineralogist 85(11-12):1784-1794

Wheeler, J. (2014). Dramatic effects of stress on metamorphic reactions. Geology, 42(8), 647-650.

Woodhead, J. D., Hellstrom, J., Hergt, J. M., Greig, A., and Maas R. (2007) Isotopic and elemental imaging of geological materials by laser ablation inductively coupled plasma-mass spectrometry. Geostand Geoanal Res 31:331–343

Yamato, P., Burov, E., Agard, P., Le Pourhiet, L., & Jolivet, L. (2008). HP-UHP exhumation during slow continental subduction: Self-consistent thermodynamically and thermomechanically coupled model with application to the Western Alps. Earth and Planetary Science Letters, 271(1-4), 63-74.

Yang, J., Xu, Z., Zhang, J., Song, S., Wu, C., Shi, R., Li, H. & Brunel, M. (2002): Early Palaeozoic North Qaidam UHP metamorphic belt on the north-eastern Tibetan plateau and a paired subduction zone. Terra Nova, 14:397–404.

Ye K., Yao Y. P., Katayama I., Cong B. L., Wang Q. C., and Maruyama S. (2000) Large areal extent of ultrahigh-pressure metamorphism in the Sulu ultrahigh-pressure terrane of East China: New implications from coesite and omphacite inclusions in zircon of granitic gneiss. Lithos 52: 157–164.

Zack, T., Moraes, R. D., & Kronz, A. (2004). Temperature dependence of Zr in rutile: empirical calibration of a rutile thermometer. Contributions to Mineralogy and Petrology, 148(4), 471-488.

Zhang, L., Ellis, D. J., Williams, S., & Jiang, W. (2002). Ultra-high pressure metamorphism in western Tianshan, China: Part II. Evidence from magnesite in eclogite. American Mineralogist, 87(7), 861-866.

Zhang, M., Salje, E. K., Capitani, G. C., Leroux, H., Clark, A. M., Schlüter, J., & Ewing, R. C. (2000) Annealing of alphadecay damage in zircon: a Raman spectroscopic study. Journal of Physics: Condensed Matter, 12(13), 3131

Zhang, R. Y. & Liou, J. G. (1998). Ultrahigh-pressure metamorphism of the Sulu terrane, eastern China: A prospective view. Continental Dynamics, 3, 32-53.

Zhang, R. Y., Hirajima, T., Banno, S., Cong, B., & Liou, J. G. (1995). Petrology of ultrahigh-pressure rocks from the southern Su-Lu region, eastern China. Journal of Metamorphic Geology, 13(6), 659-675.

Zhang, Y. (1998). Mechanical and phase equilibria in inclusion–host systems. Earth and Planetary Science Letters, 157(3-4), 209-222.

Zhong, X., Andersen, N. H., Dabrowski, M., & Jamtveit, B. (2019). Zircon and quartz inclusions in garnet used for complementary Raman thermobarometry: application to the Holsnøy eclogite, Bergen Arcs, Western Norway. Contributions to Mineralogy and Petrology, 174(6), 50.

Zhukov, V. P., & Korsakov, A. V. (2015). Evolution of host-inclusion systems: a visco-elastic model. Journal of Metamorphic Geology, 33(8), 815-828.

Ziman J. M., (1960) Electrons and Phonons: the Theory of Transport Phenomena in Solids. Oxford University Press, Oxford, pp. 469

APPENDIX A1

MICROPROBE ANALYSIS

GARNETS

Table A.1.1: Compositional (in wt%) transect in garnet neoblast DM17-29-1 (part 1)

S.	Line 1 DM17291-L1	Line 2 DM17291-L1	Line 3 DM17291-L1	Line 4 DM17291-L1	Line 5 DM17291-L1	Line 6 DM17291-L1	Line 7 DM17291-L1	Line 8 DM17291-L1	Line 9 DM17291-L1	Line 10 DM17291-L1	Line 11 DM17291-L1	Line 12 DM17291-L1	Line 13 DM17291-L1	Line 14 DM17291-L1	Line 16 DM17291-L1	Line 17 DM17291-L1	Line 18 DM17291-L1	Line 19 DM17291-L1
Na2O	b.d.l.	b.d.l.	b.d.l.	b.d.l.	b.d.l.	b.d.l.	b.d.l.	b.d.l.	b.d.l.	b.d.l.	b.d.l.	b.d.l.	b.d.l.	b.d.l.	b.d.l.	b.d.l.	b.d.l.	b.d.l.
MgO	26.45	27.98	27.18	27.43	27.30	26.72	26.74	26.89	26.72	26.73	26.80	26.77	26.66	27.09	26.71	26.86	27.28	27.76
Al2O3	24.85	25.28	25.03	25.58	24.93	25.10	24.90	24.82	24.84	25.14	24.86	24.96	25.21	24.92	25.04	25.00	25.11	25.07
SiO2	43.16	43.17	43.15	42.50	42.85	43.50	43.37	43.33	43.19	43.52	43.26	43.93	43.41	42.99	42.64	43.16	44.15	43.77
K2O	b.d.l.	b.d.l.	b.d.l.	b.d.l.	b.d.l.	b.d.l.	b.d.l.	b.d.l.	b.d.l.	b.d.l.	b.d.l.	b.d.l.	b.d.l.	b.d.l.	b.d.l.	b.d.l.	b.d.l.	b.d.l.
CaO	0.27	0.31	0.30	0.28	0.29	0.31	0.28	0.29	0.29	0.31	0.27	0.26	0.29	0.24	0.28	0.25	0.26	0.24
TiO2	0.02	0.02	0.03	0.09	b.d.l.	b.d.l.	b.d.l.	0.02	b.d.l.	0.05	0.04	0.05	b.d.l.	b.d.l.	0.07	0.05	0.06	0.06
Cr2O3	0.02	b.d.l.	b.d.l.	b.d.l.	0.04	b.d.l.	b.d.l.	0.01	b.d.l.	b.d.l.	b.d.l.	0.04	0.02	0.03	0.02	b.d.l.	b.d.l.	b.d.l.
Mno	b.d.l.	0.02	0.02	0.03	0.05	0.01	0.03	0.05	0.04	0.05	0.08	0.02	0.01	0.07	0.02	0.01	0.02	0.05
FeO	3.46	2.38	3.18	3.35	3.28	3.36	3.37	3.47	3.29	3.38	3.57	3.61	3.53	3.52	3.84	3.70	3.21	2.21
Sum	98.23	99.16	98.88	99.27	98.74	99.00	98.69	98.89	98.37	99.17	98.88	99.64	99.13	98.86	98.61	99.04	100.09	99.16
Si	3.00	2.96	2.97	2.92	2.96	2.99	3.00	2.99	2.99	2.99	2.99	3.01	2.99	2.97	2.96	2.98	3.00	2.99
Ti	b.d.l.	b.d.l.	b.d.l.	b.d.l.	b.d.l.	b.d.l.	b.d.l.	b.d.l.	b.d.l.	b.d.l.	b.d.l.	b.d.l.	b.d.l.	b.d.l.	b.d.l.	b.d.l.	b.d.l.	b.d.l.
Al	2.03	2.04	2.03	2.07	2.03	2.04	2.03	2.02	2.03	2.04	2.02	2.01	2.04	2.03	2.05	2.03	2.01	2.02
Cr	b.d.l.	b.d.l.	b.d.l.	b.d.l.	b.d.l.	b.d.l.	b.d.l.	b.d.l.	b.d.l.	b.d.l.	b.d.l.	b.d.l.	b.d.l.	b.d.l.	b.d.l.	b.d.l.	b.d.l.	b.d.l.
Fe2+	0.20	0.14	0.18	0.19	0.19	0.19	0.19	0.20	0.19	0.19	0.21	0.21	0.20	0.20	0.22	0.21	0.18	0.13
Fe3+	b.d.l.	b.d.l.	b.d.l.	b.d.l.	b.d.l.	b.d.l.	b.d.l.	b.d.l.	b.d.l.	b.d.l.	b.d.l.	b.d.l.	b.d.l.	b.d.l.	b.d.l.	b.d.l.	b.d.l.	b.d.l.
Mn	b.d.l.	b.d.l.	b.d.l.	b.d.l.	b.d.l.	b.d.l.	b.d.l.	b.d.l.	b.d.l.	b.d.l.	b.d.l.	b.d.l.	b.d.l.	b.d.l.	b.d.l.	b.d.l.	b.d.l.	b.d.l.
Mn3+	b.d.l.	b.d.l.	b.d.l.	b.d.l.	b.d.l.	b.d.l.	b.d.l.	b.d.l.	b.d.l.	b.d.l.	b.d.l.	b.d.l.	b.d.l.	b.d.l.	b.d.l.	b.d.l.	b.d.l.	b.d.l.
Mg	2.74	2.86	2.79	2.81	2.81	2.74	2.75	2.77	2.76	2.74	2.76	2.73	2.73	2.79	2.76	2.76	2.77	2.83
Ca	0.02	0.02	0.02	0.02	0.02	0.02	0.02	0.02	0.02	0.02	0.02	0.02	0.02	0.02	0.02	0.02	0.02	0.02
Na	b.d.l.	b.d.l.	b.d.l.	b.d.l.	b.d.l.	b.d.l.	b.d.l.	b.d.l.	b.d.l.	b.d.l.	b.d.l.	b.d.l.	b.d.l.	b.d.l.	b.d.l.	b.d.l.	b.d.l.	b.d.l.
Sum	7.99	8.02	8.01	8.03	8.02	7.99	7.99	8.00	7.99	7.99	8.00	7.98	7.99	8.01	8.02	8.01	7.99	7.99

Table A.1.2: Compositional (in wt%) transect in garnet neoblast DM17-29-1 (part 2)

S.	Line 1 DM172 91-L2	Line 2 DM172 91-L2	Line 3 DM172 91-L2	Line 4 DM172 91-L2	Line 5 DM172 91-L2	Line 6 DM172 91-L2	Line 7 DM172 91-L2	Line 8 DM172 91-L2	Line 9 DM172 91-L2	Line 10 DM172 91-L2	Line 11 DM172 91-L2	Line 12 DM172 91-L2	Line 13 DM172 91-L2	Line 14 DM172 91-L2	Line 15 DM172 91-L2	Line 16 DM172 91-L2	Line 17 DM172 91-L2	Line 18 DM172 91-L2	Line 19 DM172 91-L2
Na2O	b.d.l.	b.d.l.	b.d.l.	b.d.l.	b.d.l.	b.d.l.	b.d.l.	b.d.l.	b.d.l.	b.d.l.	b.d.l.	b.d.l.	b.d.l.	b.d.l.	b.d.l.	b.d.l.	b.d.l.	b.d.l.	b.d.l.
MgO	28.98	27.98	27.23	27.16	27.04	26.92	26.42	26.35	26.91	26.95	26.57	26.21	26.41	26.93	27.11	26.77	26.70	26.99	27.28
Al2O3	25.73	25.16	25.01	25.57	25.18	25.27	24.96	25.15	25.04	25.22	25.20	25.05	24.95	25.45	25.04	25.28	24.87	25.07	25.15
SiO2	43.55	44.16	43.67	43.78	43.60	43.69	43.49	43.50	43.69	43.38	43.77	43.96	43.22	43.76	43.70	43.49	43.64	43.39	43.62
K2O	b.d.l.	b.d.l.	b.d.l.	b.d.l.	b.d.l.	b.d.l.	b.d.l.	b.d.l.	b.d.l.	b.d.l.	b.d.l.	b.d.l.	b.d.l.	b.d.l.	b.d.l.	b.d.l.	b.d.l.	b.d.l.	b.d.l.
CaO	0.31	0.10	0.35	0.33	0.38	0.41	0.41	0.42	0.39	0.40	0.36	0.35	0.36	0.33	0.33	0.33	0.31	0.30	0.25
TiO2	0.02	b.d.l.	0.02	0.09	b.d.l.	0.06	0.01	b.d.l.	0.02	b.d.l.	0.06	b.d.l.	0.02	0.05	0.01	b.d.l.	b.d.l.	0.06	b.d.l.
Cr2O3	b.d.l.	b.d.l.	b.d.l.	b.d.l.	b.d.l.	0.02	0.02	b.d.l.	b.d.l.	b.d.l.	b.d.l.	b.d.l.	0.01	b.d.l.	0.02	b.d.l.	b.d.l.	b.d.l.	b.d.l.
Mno	0.05	b.d.l.	b.d.l.	0.04	0.04	0.06	0.02	0.03	0.01	0.03	0.09	0.02	0.03	0.01	b.d.l.	0.07	0.04	0.02	0.04
FeO	2.51	2.12	2.90	3.19	3.27	3.60	3.88	3.77	3.89	3.93	3.79	4.06	3.99	3.78	3.64	3.62	3.32	3.45	2.98
Sum	101.15	99.52	99.18	100.16	99.51	100.04	99.20	99.22	99.95	99.91	99.83	99.65	98.99	100.31	99.85	99.56	98.88	99.28	99.32
Si	2.93	3.00	2.99	2.98	2.99	2.98	3.00	2.99	2.99	2.97	2.99	3.01	2.99	2.98	2.99	2.98	3.01	2.98	2.99
Ti	b.d.l.	b.d.l.	b.d.l.	b.d.l.	b.d.l.	b.d.l.	b.d.l.	b.d.l.	b.d.l.	b.d.l.	b.d.l.	b.d.l.	b.d.l.	b.d.l.	b.d.l.	b.d.l.	b.d.l.	b.d.l.	b.d.l.
Al	2.04	2.02	2.02	2.05	2.03	2.03	2.03	2.04	2.02	2.04	2.03	2.02	2.03	2.04	2.02	2.04	2.02	2.03	2.03
Cr	b.d.l.	b.d.l.	b.d.l.	b.d.l.	b.d.l.	b.d.l.	b.d.l.	b.d.l.	b.d.l.	b.d.l.	b.d.l.	b.d.l.	b.d.l.	b.d.l.	b.d.l.	b.d.l.	b.d.l.	b.d.l.	b.d.l.
Fe2+	0.14	0.12	0.17	0.18	0.19	0.21	0.22	0.22	0.22	0.23	0.22	0.23	0.23	0.22	0.21	0.21	0.19	0.20	0.17
Fe3+	b.d.l.	b.d.l.	b.d.l.	b.d.l.	b.d.l.	b.d.l.	b.d.l.	b.d.l.	b.d.l.	b.d.l.	b.d.l.	b.d.l.	b.d.l.	b.d.l.	b.d.l.	b.d.l.	b.d.l.	b.d.l.	b.d.l.
Mn	b.d.l.	b.d.l.	b.d.l.	b.d.l.	b.d.l.	b.d.l.	b.d.l.	b.d.l.	b.d.l.	b.d.l.	b.d.l.	b.d.l.	b.d.l.	b.d.l.	b.d.l.	b.d.l.	b.d.l.	b.d.l.	b.d.l.
Mn3+	b.d.l.	b.d.l.	b.d.l.	b.d.l.	b.d.l.	b.d.l.	b.d.l.	b.d.l.	b.d.l.	b.d.l.	b.d.l.	b.d.l.	b.d.l.	b.d.l.	b.d.l.	b.d.l.	b.d.l.	b.d.l.	b.d.l.
Mg	2.91	2.84	2.78	2.75	2.76	2.74	2.71	2.70	2.74	2.75	2.71	2.68	2.72	2.73	2.76	2.74	2.74	2.76	2.79
Ca	0.02	0.01	0.03	0.02	0.03	0.03	0.03	0.03	0.03	0.03	0.03	0.03	0.03	0.02	0.02	0.02	0.02	0.02	0.02
Na	b.d.l.	b.d.l.	b.d.l.	b.d.l.	b.d.l.	b.d.l.	b.d.l.	b.d.l.	b.d.l.	b.d.l.	b.d.l.	b.d.l.	b.d.l.	b.d.l.	b.d.l.	b.d.l.	b.d.l.	b.d.l.	b.d.l.
Sum	8.05	7.99	7.99	7.99	8.00	8.00	7.99	7.99	8.00	8.01	7.99	7.97	8.00	8.00	8.00	8.00	7.98	8.00	8.00

Table A.1.3: Compositional (in wt%) transect in garnet neoblast DM17-8A-2 (part 1)

S.	Line 1 DM178 A2-L1	Line 2 DM178A 2-L1	Line 3 DM178A 2-L1	Line 4 DM178A 2-L1	Line 5 DM178A 2-L1	Line 6 DM178A 2-L1	Line 7 DM178A 2-L1	Line 8 DM178A 2-L1	Line 9 DM178A 2-L1	Line 10 DM178A 2-L1	Line 11 DM178A 2-L1	Line 12 DM178A 2-L1	Line 13 DM178A 2-L1	Line 14 DM178A 2-L1	Line 15 DM178A 2-L1	Line 16 DM178A 2-L1
Na2O	b.d.l.	b.d.l.	b.d.l.	b.d.l.	b.d.l.	b.d.l.	b.d.l.	b.d.l.	b.d.l.	b.d.l.	b.d.l.	b.d.l.	b.d.l.	b.d.l.	b.d.l.	b.d.l.
MgO	28.63	28.20	27.58	27.62	27.07	27.37	27.60	27.47	27.27	27.19	26.85	27.10	27.26	26.88	27.39	27.26
Al2O3	25.97	25.47	25.63	25.55	25.45	25.44	25.40	25.37	25.45	25.51	25.20	25.32	25.24	25.41	25.39	25.29
SiO2	44.20	44.27	44.06	43.87	44.60	44.05	44.04	44.14	44.03	43.59	43.88	44.22	44.08	43.96	43.86	43.67
K2O	b.d.l.	b.d.l.	b.d.l.	b.d.l.	b.d.l.	b.d.l.	b.d.l.	b.d.l.	b.d.l.	b.d.l.	b.d.l.	b.d.l.	b.d.l.	b.d.l.	b.d.l.	b.d.l.
CaO	0.05	0.10	0.78	0.75	0.75	0.83	0.71	0.77	0.61	0.45	0.33	0.25	0.20	0.20	0.19	0.17
TiO2	0.03	b.d.l.	b.d.l.	b.d.l.	0.03	b.d.l.	b.d.l.	b.d.l.	b.d.l.	0.01	b.d.l.	b.d.l.	b.d.l.	b.d.l.	0.07	b.d.l.
Cr2O3	0.04	b.d.l.	b.d.l.	b.d.l.	b.d.l.	0.02	0.01	b.d.l.	0.01	b.d.l.	b.d.l.	b.d.l.	b.d.l.	0.08	b.d.l.	b.d.l.
Mno	0.01	b.d.l.	b.d.l.	0.02	b.d.l.	0.04	b.d.l.	0.03	b.d.l.	b.d.l.	b.d.l.	b.d.l.	0.01	b.d.l.	b.d.l.	b.d.l.
FeO	1.06	1.33	1.88	1.78	2.07	2.36	1.81	2.02	2.37	2.79	3.34	3.31	3.21	3.22	3.32	3.23
Sum	99.99	99.37	99.93	99.59	99.97	100.11	99.57	99.80	99.74	99.55	99.60	100.20	10b.d.l.	99.75	100.22	99.63
Si	2.98	3.00	2.99	2.98	3.02	2.99	3.00	3.00	3.00	2.98	3.00	3.00	3.00	3.00	2.98	2.98
Ti	b.d.l.	b.d.l.	b.d.l.	b.d.l.	b.d.l.	b.d.l.	b.d.l.	b.d.l.	b.d.l.	b.d.l.	b.d.l.	b.d.l.	b.d.l.	b.d.l.	b.d.l.	b.d.l.
Al	2.06	2.04	2.05	2.05	2.03	2.04	2.04	2.03	2.04	2.05	2.03	2.03	2.02	2.04	2.03	2.04
Cr	b.d.l.	b.d.l.	b.d.l.	b.d.l.	b.d.l.	b.d.l.	b.d.l.	b.d.l.	b.d.l.	b.d.l.	b.d.l.	b.d.l.	b.d.l.	b.d.l.	b.d.l.	b.d.l.
Fe2+	0.06	0.08	0.11	0.10	0.12	0.13	0.10	0.11	0.13	0.16	0.19	0.19	0.18	0.18	0.19	0.18
Fe3+	b.d.l.	b.d.l.	b.d.l.	b.d.l.	b.d.l.	b.d.l.	b.d.l.	b.d.l.	b.d.l.	b.d.l.	b.d.l.	b.d.l.	b.d.l.	b.d.l.	b.d.l.	b.d.l.
Mn	b.d.l.	b.d.l.	b.d.l.	b.d.l.	b.d.l.	b.d.l.	b.d.l.	b.d.l.	b.d.l.	b.d.l.	b.d.l.	b.d.l.	b.d.l.	b.d.l.	b.d.l.	b.d.l.
Mn3+	b.d.l.	b.d.l.	b.d.l.	b.d.l.	b.d.l.	b.d.l.	b.d.l.	b.d.l.	b.d.l.	b.d.l.	b.d.l.	b.d.l.	b.d.l.	b.d.l.	b.d.l.	b.d.l.
Mg	2.88	2.85	2.79	2.80	2.73	2.77	2.80	2.78	2.77	2.77	2.74	2.74	2.77	2.73	2.78	2.78
Ca	b.d.l.	0.01	0.06	0.05	0.05	0.06	0.05	0.06	0.04	0.03	0.02	0.02	0.01	0.01	0.01	0.01
Na	b.d.l.	b.d.l.	b.d.l.	b.d.l.	b.d.l.	b.d.l.	b.d.l.	b.d.l.	b.d.l.	b.d.l.	b.d.l.	b.d.l.	b.d.l.	b.d.l.	b.d.l.	b.d.l.
Sum	7.99	7.98	7.99	7.99	7.96	7.99	7.99	7.99	7.98	7.99	7.98	7.98	7.99	7.98	8.00	8.00

Table A.1.4: Compositional (in wt%) transect in garnet neoblast DM17-8A-2 (part 2)

S.	Line 17 DM178A 2-L1	Line 18 DM178 A2-L1	Line 19 DM178 A2-L1	Line 1 DM178 A2-L2	Line 2 DM178 A2-L2	Line 3 DM178 A2-L2	Line 4 DM178 A2-L2	Line 5 DM178 A2-L2	Line 6 DM178 A2-L2	Line 7 DM178 A2-L2	Line 8 DM178 A2-L2	Line 9 DM178 A2-L2	Line 10 DM178 A2-L2	Line 11 DM178 A2-L2	Line 12 DM178 A2-L2	Line 13 DM178 A2-L2	Line 14 DM178 A2-L2
Na2O	b.d.l.	b.d.l.	b.d.l.	b.d.l.	b.d.l.	b.d.l.	b.d.l.	b.d.l.	b.d.l.	b.d.l.	b.d.l.	b.d.l.	b.d.l.	b.d.l.	b.d.l.	b.d.l.	b.d.l.
MgO	27.26	27.36	28.04	28.85	27.40	26.88	26.58	26.10	26.56	27.07	27.38	27.82	27.60	27.29	26.80	27.01	26.80
Al2O 3	25.29	25.36	25.43	25.43	25.32	25.49	25.16	25.18	25.50	25.45	25.59	25.60	25.77	25.54	25.69	25.32	25.33
SiO2	43.67	43.96	44.30	44.81	43.70	43.75	44.22	43.62	43.61	44.38	44.04	44.05	43.95	44.56	43.62	43.52	43.65
K2O	b.d.l.	b.d.l.	b.d.l.	b.d.l.	b.d.l.	b.d.l.	b.d.l.	b.d.l.	b.d.l.	b.d.l.	b.d.l.	b.d.l.	b.d.l.	b.d.l.	b.d.l.	b.d.l.	b.d.l.
CaO	0.17	0.13	0.08	0.05	0.17	0.43	0.56	0.56	0.59	0.67	0.57	0.40	0.70	0.51	0.64	0.53	0.40
TiO2	b.d.l.	b.d.l.	0.01	b.d.l.	b.d.l.	0.04	b.d.l.	0.03	b.d.l.	0.02	0.02	0.03	0.02	b.d.l.	0.08	0.05	0.03
Cr2O 3	b.d.l.	b.d.l.	b.d.l.	0.04	0.06	b.d.l.	b.d.l.	0.01	0.01	b.d.l.	0.03	0.04	0.01	b.d.l.	0.01	b.d.l.	b.d.l.
Mno	b.d.l.	b.d.l.	0.02	0.03	0.01	b.d.l.	0.02	0.05	0.06	b.d.l.	0.04	b.d.l.	0.02	b.d.l.	b.d.l.	b.d.l.	0.01
FeO	3.23	2.69	1.74	0.90	3.20	3.51	3.62	4.35	3.35	2.47	2.35	1.93	2.04	2.10	2.60	3.13	3.28
Sum	99.63	99.50	99.62	100.10	99.85	100.11	100.16	99.88	99.69	100.06	100.03	99.87	100.10	100.00	99.44	99.56	99.51
Si	2.98	3.00	3.00	3.01	2.98	2.98	3.01	2.99	2.98	3.01	2.99	2.99	2.98	3.02	2.98	2.98	2.99
Ti	b.d.l.	b.d.l.	b.d.l.	b.d.l.	b.d.l.	b.d.l.	b.d.l.	b.d.l.	b.d.l.	b.d.l.	b.d.l.	b.d.l.	b.d.l.	b.d.l.	b.d.l.	b.d.l.	b.d.l.
Al	2.04	2.04	2.03	2.02	2.04	2.05	2.02	2.04	2.06	2.03	2.05	2.05	2.06	2.04	2.07	2.04	2.04
Cr	b.d.l.	b.d.l.	b.d.l.	b.d.l.	b.d.l.	b.d.l.	b.d.l.	b.d.l.	b.d.l.	b.d.l.	b.d.l.	b.d.l.	b.d.l.	b.d.l.	b.d.l.	b.d.l.	b.d.l.
Fe2+	0.18	0.15	0.10	0.05	0.18	0.20	0.21	0.25	0.19	0.14	0.13	0.11	0.12	0.12	0.15	0.18	0.19
Fe3+	b.d.l.	b.d.l.	b.d.l.	b.d.l.	b.d.l.	b.d.l.	b.d.l.	b.d.l.	b.d.l.	b.d.l.	b.d.l.	b.d.l.	b.d.l.	b.d.l.	b.d.l.	b.d.l.	b.d.l.
Mn	b.d.l.	b.d.l.	b.d.l.	b.d.l.	b.d.l.	b.d.l.	b.d.l.	b.d.l.	b.d.l.	b.d.l.	b.d.l.	b.d.l.	b.d.l.	b.d.l.	b.d.l.	b.d.l.	b.d.l.
Mn3 +	b.d.l.	b.d.l.	b.d.l.	b.d.l.	b.d.l.	b.d.l.	b.d.l.	b.d.l.	b.d.l.	b.d.l.	b.d.l.	b.d.l.	b.d.l.	b.d.l.	b.d.l.	b.d.l.	b.d.l.
Mg	2.78	2.78	2.83	2.89	2.79	2.73	2.70	2.67	2.71	2.74	2.77	2.81	2.79	2.75	2.73	2.76	2.74
Ca	0.01	0.01	0.01	b.d.l.	0.01	0.03	0.04	0.04	0.04	0.05	0.04	0.03	0.05	0.04	0.05	0.04	0.03
Na	b.d.l.	b.d.l.	b.d.l.	b.d.l.	b.d.l.	b.d.l.	b.d.l.	b.d.l.	b.d.l.	b.d.l.	b.d.l.	b.d.l.	b.d.l.	b.d.l.	b.d.l.	b.d.l.	b.d.l.
Sum	8.00	7.98	7.98	7.98	8.00	7.99	7.98	7.99	7.99	7.97	7.99	7.99	7.99	7.96	7.98	8.00	7.99

Table A.1.5: Compositional (in wt%) transect in garnet neoblast DM17-8A-2 (part 3)

S.	Line 16 DM178A2-L2	Line 17 DM178A2-L2	Line 18 DM178A2-L2	Line 19 DM178A2-L2	Line 20 DM178A2-L2	DM178A2-1	DM178A2-2	DM178A2-3	DM178A2-4	DM178A2-5
Na2O	b.d.l.	b.d.l.	b.d.l.	b.d.l.	b.d.l.	b.d.l.	b.d.l.	b.d.l.	b.d.l.	b.d.l.
MgO	27.21	27.18	27.63	28.16	28.78	28.58	28.40	28.38	28.25	28.48
Al2O3	25.53	25.47	25.53	25.29	25.71	25.76	25.36	25.80	25.62	25.24
SiO2	43.87	43.73	43.60	43.83	44.31	44.47	44.50	43.90	44.53	44.50
K2O	b.d.l.	b.d.l.	b.d.l.	b.d.l.	b.d.l.	b.d.l.	b.d.l.	b.d.l.	b.d.l.	b.d.l.
CaO	0.17	0.17	0.12	0.08	0.06	0.06	0.08	0.10	0.08	0.05
TiO2	b.d.l.	0.04	0.04	b.d.l.	b.d.l.	0.03	b.d.l.	b.d.l.	b.d.l.	0.04
Cr2O3	0.02	0.04	0.03	b.d.l.	b.d.l.	0.01	b.d.l.	b.d.l.	0.03	b.d.l.
Mno	b.d.l.	0.02	0.04	0.01	0.05	b.d.l.	b.d.l.	b.d.l.	b.d.l.	b.d.l.
FeO	2.48	2.97	2.75	1.54	0.96	0.74	0.98	1.28	1.18	0.61
Sum	99.28	99.62	99.73	98.91	99.87	99.65	99.32	99.47	99.70	98.92
Si	3.00	2.99	2.97	2.99	2.99	3.00	3.02	2.98	3.01	3.02
Ti	b.d.l.	b.d.l.	b.d.l.	b.d.l.	b.d.l.	b.d.l.	b.d.l.	b.d.l.	b.d.l.	b.d.l.
Al	2.05	2.05	2.05	2.04	2.04	2.05	2.03	2.06	2.04	2.02
Cr	b.d.l.	b.d.l.	b.d.l.	b.d.l.	b.d.l.	b.d.l.	b.d.l.	b.d.l.	b.d.l.	b.d.l.
Fe2+	0.14	0.17	0.16	0.09	0.05	0.04	0.06	0.07	0.07	0.03
Fe3+	b.d.l.	b.d.l.	b.d.l.	b.d.l.	b.d.l.	b.d.l.	b.d.l.	b.d.l.	b.d.l.	b.d.l.
Mn	b.d.l.	b.d.l.	b.d.l.	b.d.l.	b.d.l.	b.d.l.	b.d.l.	b.d.l.	b.d.l.	b.d.l.
Mn3+	b.d.l.	b.d.l.	b.d.l.	b.d.l.	b.d.l.	b.d.l.	b.d.l.	b.d.l.	b.d.l.	b.d.l.
Mg	2.77	2.77	2.81	2.87	2.89	2.88	2.87	2.87	2.85	2.88
Ca	0.01	0.01	0.01	0.01	b.d.l.	b.d.l.	0.01	0.01	0.01	b.d.l.
Na	b.d.l.	b.d.l.	b.d.l.	b.d.l.	b.d.l.	b.d.l.	b.d.l.	b.d.l.	b.d.l.	b.d.l.
Sum	7.98	7.99	8.00	7.99	7.99	7.97	7.97	7.99	7.97	7.97

Table A.1.6: Compositional (in wt%) transect in garnet neoblast DM17-27 (part 1)

S.	Line 1 DM1727-L1	Line 2 DM1727-L1	Line 3 DM1727-L1	Line 4 DM1727-L1	Line 5 DM1727-L1	Line 6 DM1727-L1	Line 7 DM1727-L1	Line 8 DM1727-L1	Line 9 DM1727-L1	Line 10 DM1727-L1	Line 11 DM1727-L1	Line 12 DM1727-L1	Line 13 DM1727-L1	Line 14 DM1727-L1	Line 15 DM1727-L1	Line 16 DM1727-L1	Line 17 DM1727-L1	Line 18 DM1727-L1
Na2O	b.d.l.	b.d.l.	b.d.l.	b.d.l.	b.d.l.	b.d.l.	b.d.l.	b.d.l.	b.d.l.	b.d.l.	b.d.l.	b.d.l.	b.d.l.	b.d.l.	b.d.l.	b.d.l.	b.d.l.	b.d.l.
MgO	27.95	27.85	27.73	28.32	28.30	28.55	28.48	29.48	28.21	28.05	28.00	28.02	27.84	27.89	28.26	28.28	27.99	27.95
Al2O3	25.45	25.54	25.41	25.41	25.36	25.74	25.76	26.71	25.49	25.46	25.41	25.42	25.68	25.65	25.76	25.63	25.65	25.40
SiO2	43.68	44.03	44.39	43.78	44.47	44.19	43.88	46.88	44.24	44.25	44.15	44.36	43.98	44.15	43.87	44.12	44.47	43.92
K2O	b.d.l.	b.d.l.	b.d.l.	b.d.l.	b.d.l.	b.d.l.	b.d.l.	b.d.l.	b.d.l.	b.d.l.	b.d.l.	b.d.l.	b.d.l.	b.d.l.	b.d.l.	b.d.l.	b.d.l.	b.d.l.
CaO	0.28	0.24	0.08	0.07	0.04	0.10	0.08	0.11	0.14	0.13	0.17	0.18	0.49	0.23	0.16	0.07	0.12	0.16
TiO2	0.02	0.01	0.01	0.02	0.04	b.d.l.	0.07	0.06	b.d.l.	b.d.l.	0.07	0.02	b.d.l.	0.05	0.03	b.d.l.	0.03	b.d.l.
Cr2O3	b.d.l.	b.d.l.	0.02	b.d.l.	b.d.l.	b.d.l.	b.d.l.	0.02	b.d.l.	0.03	0.03	0.08	b.d.l.	b.d.l.	0.01	0.06	0.03	b.d.l.
Mno	0.04	b.d.l.	b.d.l.	0.02	b.d.l.	b.d.l.	b.d.l.	0.03	b.d.l.	b.d.l.	b.d.l.	b.d.l.	b.d.l.	b.d.l.	0.05	0.01	0.02	b.d.l.
FeO	1.79	1.66	2.00	1.88	1.12	1.21	1.14	1.19	1.21	1.39	1.52	1.94	1.86	2.03	1.86	1.85	1.81	1.79
Sum	99.21	99.33	99.64	99.50	99.32	99.79	99.42	104.47	99.28	99.32	99.35	100.01	99.85	100.00	100.00	100.01	100.11	99.22
Si	2.98	3.00	3.01	2.98	3.02	2.99	2.98	3.02	3.00	3.01	3.00	3.00	2.98	2.99	2.97	2.98	3.00	2.99
Ti	b.d.l.	b.d.l.	b.d.l.	b.d.l.	b.d.l.	b.d.l.	b.d.l.	b.d.l.	b.d.l.	b.d.l.	b.d.l.	b.d.l.	b.d.l.	b.d.l.	b.d.l.	b.d.l.	b.d.l.	b.d.l.
Al	2.05	2.05	2.03	2.04	2.03	2.05	2.06	2.03	2.04	2.04	2.04	2.03	2.05	2.05	2.06	2.04	2.04	2.04
Cr	b.d.l.	b.d.l.	b.d.l.	b.d.l.	b.d.l.	b.d.l.	b.d.l.	b.d.l.	b.d.l.	b.d.l.	b.d.l.	b.d.l.	b.d.l.	b.d.l.	b.d.l.	b.d.l.	b.d.l.	b.d.l.
Fe2+	0.10	0.09	0.11	0.11	0.06	0.07	0.06	0.06	0.07	0.08	0.09	0.11	0.11	0.11	0.11	0.10	0.10	0.10
Fe3+	b.d.l.	b.d.l.	b.d.l.	b.d.l.	b.d.l.	b.d.l.	b.d.l.	b.d.l.	b.d.l.	b.d.l.	b.d.l.	b.d.l.	b.d.l.	b.d.l.	b.d.l.	b.d.l.	b.d.l.	b.d.l.
Mn	b.d.l.	b.d.l.	b.d.l.	b.d.l.	b.d.l.	b.d.l.	b.d.l.	b.d.l.	b.d.l.	b.d.l.	b.d.l.	b.d.l.	b.d.l.	b.d.l.	b.d.l.	b.d.l.	b.d.l.	b.d.l.
Mn3+	b.d.l.	b.d.l.	b.d.l.	b.d.l.	b.d.l.	b.d.l.	b.d.l.	b.d.l.	b.d.l.	b.d.l.	b.d.l.	b.d.l.	b.d.l.	b.d.l.	b.d.l.	b.d.l.	b.d.l.	b.d.l.
Mg	2.84	2.82	2.81	2.87	2.86	2.88	2.88	2.83	2.86	2.84	2.84	2.83	2.81	2.81	2.85	2.85	2.82	2.84
Ca	0.02	0.02	0.01	0.01	b.d.l.	0.01	0.01	0.01	0.01	0.01	0.01	0.01	0.04	0.02	0.01	b.d.l.	0.01	0.01
Na	b.d.l.	b.d.l.	b.d.l.	b.d.l.	b.d.l.	b.d.l.	b.d.l.	b.d.l.	b.d.l.	b.d.l.	b.d.l.	b.d.l.	b.d.l.	b.d.l.	b.d.l.	b.d.l.	b.d.l.	b.d.l.
Sum	8.00	7.98	7.97	8.00	7.97	7.99	7.99	7.96	7.98	7.97	7.98	7.98	7.99	7.98	8.00	7.99	7.97	7.99

Table A.1.7: Compositional (in wt%) transect in garnet neoblast DM17-27 (part 2)

S.	Line 1 DM1727-L2	Line 2 DM1727-L2	Line 3 DM1727-L2	Line 4 DM1727-L2	Line 5 DM1727-L2	Line 6 DM1727-L2	Line 7 DM1727-L2	Line 8 DM1727-L2	Line 9 DM1727-L2	Line 10 DM1727-L2	Line 11 DM1727-L2	Line 12 DM1727-L2	Line 13 DM1727-L2	Line 14 DM1727-L2	Line 15 DM1727-L2	Line 16 DM1727-L2	Line 17 DM1727-L2	Line 18 DM1727-L2
Na2O	b.d.l.	b.d.l.	b.d.l.	b.d.l.	b.d.l.	b.d.l.	b.d.l.	b.d.l.	b.d.l.	b.d.l.	b.d.l.	b.d.l.	b.d.l.	b.d.l.	b.d.l.	b.d.l.	b.d.l.	b.d.l.
MgO	25.83	27.76	27.89	27.96	28.46	28.08	28.26	28.37	27.86	28.34	27.86	28.00	28.00	28.43	28.21	28.14	28.27	28.59
Al2O3	24.90	25.42	25.27	25.46	25.56	25.69	26.00	25.86	25.23	25.68	25.73	25.37	25.35	25.54	25.40	25.48	25.85	25.75
SiO2	43.59	43.81	44.20	44.38	44.01	44.32	43.71	43.66	44.30	44.18	44.39	44.40	44.13	44.19	44.30	44.13	43.94	43.71
K2O	b.d.l.	b.d.l.	b.d.l.	b.d.l.	b.d.l.	b.d.l.	b.d.l.	b.d.l.	b.d.l.	b.d.l.	b.d.l.	b.d.l.	b.d.l.	b.d.l.	b.d.l.	b.d.l.	b.d.l.	b.d.l.
CaO	0.19	0.42	0.10	0.10	0.20	0.22	0.22	0.16	0.16	0.14	0.27	0.13	0.04	0.07	0.12	0.09	0.09	0.21
TiO2	b.d.l.	b.d.l.	b.d.l.	0.03	0.03	0.05	b.d.l.	0.01	0.03	b.d.l.	b.d.l.	0.02	0.03	b.d.l.	0.04	0.05	0.02	b.d.l.
Cr2O3	0.02	0.08	0.02	0.01	0.03	0.03	b.d.l.	b.d.l.	b.d.l.	0.01	0.01	0.08	b.d.l.	0.02	0.02	0.02	b.d.l.	b.d.l.
Mno	b.d.l.	b.d.l.	b.d.l.	b.d.l.	b.d.l.	0.03	b.d.l.	0.01	0.01	0.01	0.04	b.d.l.	0.02	0.02	b.d.l.	b.d.l.	0.01	0.03
FeO	5.08	2.04	1.95	1.85	1.86	1.82	1.83	1.93	1.79	1.96	2.01	2.01	1.85	1.73	1.76	1.74	1.82	1.91
Sum	99.61	99.53	99.43	99.79	100.15	100.25	100.03	100.00	99.38	100.32	100.30	100.00	99.41	100.00	99.84	99.64	100.00	100.20
Si	3.00	2.98	3.01	3.01	2.98	2.99	2.96	2.96	3.01	2.98	3.00	3.00	3.00	2.99	3.00	2.99	2.97	2.96
Ti	b.d.l.	b.d.l.	b.d.l.	b.d.l.	b.d.l.	b.d.l.	b.d.l.	b.d.l.	b.d.l.	b.d.l.	b.d.l.	b.d.l.	b.d.l.	b.d.l.	b.d.l.	b.d.l.	b.d.l.	b.d.l.
Al	2.02	2.04	2.03	2.03	2.04	2.04	2.07	2.06	2.02	2.04	2.05	2.02	2.03	2.04	2.03	2.04	2.06	2.05
Cr	b.d.l.	b.d.l.	b.d.l.	b.d.l.	b.d.l.	b.d.l.	b.d.l.	b.d.l.	b.d.l.	b.d.l.	b.d.l.	b.d.l.	b.d.l.	b.d.l.	b.d.l.	b.d.l.	b.d.l.	b.d.l.
Fe2+	0.29	0.12	0.11	0.10	0.11	0.10	0.10	0.11	0.10	0.11	0.11	0.11	0.11	0.10	0.10	0.10	0.10	0.11
Fe3+	b.d.l.	b.d.l.	b.d.l.	b.d.l.	b.d.l.	b.d.l.	b.d.l.	b.d.l.	b.d.l.	b.d.l.	b.d.l.	b.d.l.	b.d.l.	b.d.l.	b.d.l.	b.d.l.	b.d.l.	b.d.l.
Mn	b.d.l.	b.d.l.	b.d.l.	b.d.l.	b.d.l.	b.d.l.	b.d.l.	b.d.l.	b.d.l.	b.d.l.	b.d.l.	b.d.l.	b.d.l.	b.d.l.	b.d.l.	b.d.l.	b.d.l.	b.d.l.
Mn3+	b.d.l.	b.d.l.	b.d.l.	b.d.l.	b.d.l.	b.d.l.	b.d.l.	b.d.l.	b.d.l.	b.d.l.	b.d.l.	b.d.l.	b.d.l.	b.d.l.	b.d.l.	b.d.l.	b.d.l.	b.d.l.
Mg	2.65	2.82	2.83	2.82	2.87	2.82	2.85	2.87	2.82	2.85	2.80	2.82	2.84	2.87	2.85	2.85	2.85	2.88
Ca	0.01	0.03	0.01	0.01	0.01	0.02	0.02	0.01	0.01	0.01	0.02	0.01	b.d.l.	0.01	0.01	0.01	0.01	0.02
Na	b.d.l.	b.d.l.	b.d.l.	b.d.l.	b.d.l.	b.d.l.	b.d.l.	b.d.l.	b.d.l.	b.d.l.	b.d.l.	b.d.l.	b.d.l.	b.d.l.	b.d.l.	b.d.l.	b.d.l.	b.d.l.
Sum	7.99	7.99	7.98	7.98	8.00	7.98	8.00	8.01	7.97	8.00	7.98	7.98	7.98	7.99	7.98	7.98	8.00	8.02

Table A.1.8: Compositional (in wt%) transect in garnet neoblast DM17-27 (part 3)

S.	Line 1 DM1727-L3	Line 2 DM1727-L3	Line 3 DM1727-L3	Line 4 DM1727-L3	Line 5 DM1727-L3	Line 6 DM1727-L3	Line 7 DM1727-L3	Line 8 DM1727-L3	Line 9 DM1727-L3	Line 10 DM1727-L3	Line 11 DM1727-L3	Line 12 DM1727-L3	Line 13 DM1727-L3	Line 14 DM1727-L3	Line 15 DM1727-L3	Line 16 DM1727-L3	Line 17 DM1727-L3	Line 18 DM1727-L3
Na2O	b.d.l.	b.d.l.	b.d.l.	b.d.l.	b.d.l.	b.d.l.	b.d.l.	b.d.l.	b.d.l.	b.d.l.	b.d.l.	b.d.l.	b.d.l.	b.d.l.	b.d.l.	b.d.l.	b.d.l.	b.d.l.
MgO	27.72	27.79	27.59	27.83	27.90	27.60	27.42	27.67	27.60	27.63	27.81	27.75	27.98	27.35	28.38	27.76	28.22	27.88
Al2O3	25.72	25.46	25.40	25.47	25.57	25.38	25.30	25.45	25.59	25.51	25.46	25.56	25.62	25.03	25.37	25.20	25.39	25.76
SiO2	43.74	43.92	44.32	43.95	43.84	43.84	43.85	43.95	44.10	44.01	44.24	44.25	44.24	44.07	43.93	44.04	43.97	44.13
K2O	b.d.l.	b.d.l.	b.d.l.	b.d.l.	b.d.l.	b.d.l.	b.d.l.	b.d.l.	b.d.l.	b.d.l.	b.d.l.	b.d.l.	b.d.l.	b.d.l.	b.d.l.	b.d.l.	b.d.l.	b.d.l.
CaO	0.44	0.18	0.13	0.09	0.05	0.04	0.05	0.06	0.05	0.04	0.03	0.19	0.03	0.12	0.05	0.04	0.03	0.05
TiO2	b.d.l.	0.01	0.02	b.d.l.	b.d.l.	0.04	b.d.l.	0.03	0.01	0.01	b.d.l.	b.d.l.	0.08	0.01	0.02	0.05	0.04	0.05
Cr2O3	b.d.l.	b.d.l.	0.02	b.d.l.	0.02	0.03	b.d.l.	b.d.l.	b.d.l.	b.d.l.	b.d.l.	b.d.l.	0.02	b.d.l.	b.d.l.	b.d.l.	b.d.l.	b.d.l.
Mno	0.02	b.d.l.	0.02	0.01	0.07	0.02	b.d.l.	b.d.l.	0.01	b.d.l.	b.d.l.	0.02	b.d.l.	0.01	b.d.l.	b.d.l.	b.d.l.	b.d.l.
FeO	2.50	2.07	2.13	2.40	2.60	2.52	2.68	2.62	2.56	2.49	2.55	2.41	2.33	2.19	2.25	2.13	2.02	2.13
Sum	100.13	99.43	99.62	99.75	100.05	99.47	99.31	99.78	99.93	99.69	100.09	100.18	100.30	98.77	99.99	99.22	99.67	99.99
Si	2.97	2.99	3.01	2.99	2.98	2.99	3.00	2.99	2.99	2.99	3.00	3.00	2.99	3.02	2.98	3.00	2.99	2.99
Ti	b.d.l.	b.d.l.	b.d.l.	b.d.l.	b.d.l.	b.d.l.	b.d.l.	b.d.l.	b.d.l.	b.d.l.	b.d.l.	b.d.l.	b.d.l.	b.d.l.	b.d.l.	b.d.l.	b.d.l.	b.d.l.
Al	2.06	2.04	2.03	2.04	2.05	2.04	2.04	2.04	2.05	2.04	2.03	2.04	2.04	2.02	2.03	2.03	2.03	2.06
Cr	b.d.l.	b.d.l.	b.d.l.	b.d.l.	b.d.l.	b.d.l.	b.d.l.	b.d.l.	b.d.l.	b.d.l.	b.d.l.	b.d.l.	b.d.l.	b.d.l.	b.d.l.	b.d.l.	b.d.l.	b.d.l.
Fe2+	0.14	0.12	0.12	0.14	0.15	0.14	0.15	0.15	0.15	0.14	0.14	0.14	0.13	0.13	0.13	0.12	0.11	0.12
Fe3+	b.d.l.	b.d.l.	b.d.l.	b.d.l.	b.d.l.	b.d.l.	b.d.l.	b.d.l.	b.d.l.	b.d.l.	b.d.l.	b.d.l.	b.d.l.	b.d.l.	b.d.l.	b.d.l.	b.d.l.	b.d.l.
Mn	b.d.l.	b.d.l.	b.d.l.	b.d.l.	b.d.l.	b.d.l.	b.d.l.	b.d.l.	b.d.l.	b.d.l.	b.d.l.	b.d.l.	b.d.l.	b.d.l.	b.d.l.	b.d.l.	b.d.l.	b.d.l.
Mn3+	b.d.l.	b.d.l.	b.d.l.	b.d.l.	b.d.l.	b.d.l.	b.d.l.	b.d.l.	b.d.l.	b.d.l.	b.d.l.	b.d.l.	b.d.l.	b.d.l.	b.d.l.	b.d.l.	b.d.l.	b.d.l.
Mg	2.80	2.82	2.79	2.82	2.82	2.81	2.79	2.81	2.79	2.80	2.81	2.80	2.82	2.79	2.87	2.82	2.86	2.81
Ca	0.03	0.01	0.01	0.01	b.d.l.	b.d.l.	b.d.l.	b.d.l.	b.d.l.	b.d.l.	b.d.l.	0.01	b.d.l.	0.01	b.d.l.	b.d.l.	b.d.l.	b.d.l.
Na	b.d.l.	b.d.l.	b.d.l.	b.d.l.	b.d.l.	b.d.l.	b.d.l.	b.d.l.	b.d.l.	b.d.l.	b.d.l.	b.d.l.	b.d.l.	b.d.l.	b.d.l.	b.d.l.	b.d.l.	b.d.l.
Sum	8.00	7.99	7.97	7.99	8.00	7.99	7.98	7.99	7.98	7.98	7.99	7.99	7.99	7.97	8.01	7.98	8.00	7.98

Table A.1.9: Compositional (in wt%) transect in garnet neoblast DM17-27 (part 4)

S.	DM1727-1	DM1727-2	DM1727-3	DM1727-4	DM1727-5	DM1727-6	DM1727-7	DM1727-8	DM1727-9	DM1727-10
Na2O	b.d.l.	b.d.l.	b.d.l.	b.d.l.	b.d.l.	b.d.l.	b.d.l.	b.d.l.	b.d.l.	b.d.l.
MgO	27.70	28.06	27.83	27.87	27.91	27.97	27.82	27.78	27.83	26.88
Al2O3	25.42	25.77	25.22	25.30	25.54	25.35	25.36	25.53	25.38	25.22
SiO2	43.92	44.07	43.91	43.88	44.08	44.19	44.05	44.25	44.05	44.27
K2O	b.d.l.	b.d.l.	b.d.l.	b.d.l.	b.d.l.	b.d.l.	b.d.l.	b.d.l.	b.d.l.	b.d.l.
CaO	0.38	0.25	0.15	0.07	0.06	0.05	0.03	0.05	0.06	0.42
TiO2	0.05	b.d.l.	0.03	0.01	0.04	0.01	b.d.l.	0.02	b.d.l.	0.02
Cr2O3	b.d.l.	0.05	0.01	0.08	0.01	b.d.l.	b.d.l.	b.d.l.	b.d.l.	b.d.l.
Mno	b.d.l.	0.02	b.d.l.	0.03	b.d.l.	b.d.l.	0.05	b.d.l.	b.d.l.	0.03
FeO	1.98	2.12	2.73	2.43	2.46	2.28	2.40	2.32	2.29	3.16
Sum	99.45	100.34	99.89	99.68	100.10	99.86	99.71	99.95	99.61	10b.d.l.
Si	2.99	2.98	2.99	2.99	2.99	3.00	3.00	3.00	3.00	3.01
Ti	b.d.l.	b.d.l.	b.d.l.	b.d.l.	b.d.l.	b.d.l.	b.d.l.	b.d.l.	b.d.l.	b.d.l.
Al	2.04	2.05	2.02	2.03	2.04	2.03	2.03	2.04	2.03	2.02
Cr	b.d.l.	b.d.l.	b.d.l.	b.d.l.	b.d.l.	b.d.l.	b.d.l.	b.d.l.	b.d.l.	b.d.l.
Fe2+	0.11	0.12	0.16	0.14	0.14	0.13	0.14	0.13	0.13	0.18
Fe3+	b.d.l.	b.d.l.	b.d.l.	b.d.l.	b.d.l.	b.d.l.	b.d.l.	b.d.l.	b.d.l.	b.d.l.
Mn	b.d.l.	b.d.l.	b.d.l.	b.d.l.	b.d.l.	b.d.l.	b.d.l.	b.d.l.	b.d.l.	b.d.l.
Mn3+	b.d.l.	b.d.l.	b.d.l.	b.d.l.	b.d.l.	b.d.l.	b.d.l.	b.d.l.	b.d.l.	b.d.l.
Mg	2.81	2.83	2.82	2.83	2.82	2.83	2.82	2.81	2.82	2.73
Ca	0.03	0.02	0.01	0.01	b.d.l.	b.d.l.	b.d.l.	b.d.l.	b.d.l.	0.03
Na	b.d.l.	b.d.l.	b.d.l.	b.d.l.	b.d.l.	b.d.l.	b.d.l.	b.d.l.	b.d.l.	b.d.l.
Sum	7.99	8.00	8.00	8.00	7.99	7.99	7.99	7.98	7.99	7.98

Table A.1.10: Compositional (in wt%) transect in garnet neoblast DM17-8A-1 (part 1)

S.	Line 1 DM17 8A1-L1	Line 2 DM17 8A1-L1	Line 3 DM17 8A1-L1	Line 4 DM17 8A1-L1	Line 5 DM17 8A1-L1	Line 6 DM17 8A1-L1	Line 7 DM17 8A1-L1	Line 8 DM17 8A1-L1	Line 9 DM17 8A1-L1	Line 10 DM17 8A1-L1	Line 11 DM17 8A1-L1	Line 12 DM17 8A1-L1	Line 13 DM17 8A1-L1	Line 14 DM17 8A1-L1	Line 15 DM17 8A1-L1	Line 16 DM17 8A1-L1	Line 17 DM17 8A1-L1
Na2O	b.d.l.	b.d.l.	b.d.l.	b.d.l.	b.d.l.	b.d.l.	b.d.l.	b.d.l.	b.d.l.	b.d.l.	b.d.l.	b.d.l.	b.d.l.	b.d.l.	b.d.l.	b.d.l.	b.d.l.
MgO	28.86	28.70	28.45	28.12	27.77	27.61	27.22	27.06	27.14	27.66	27.70	27.24	27.28	27.66	27.23	27.51	27.72
Al2O3	25.76	25.18	25.55	25.43	25.45	25.46	25.59	25.04	25.03	25.50	25.26	25.10	25.13	25.17	25.32	25.28	25.34
SiO2	44.07	44.55	44.37	43.90	44.27	43.94	43.64	43.93	44.00	44.04	44.23	43.80	44.20	44.15	44.06	44.11	43.90
K2O	b.d.l.	b.d.l.	b.d.l.	b.d.l.	b.d.l.	b.d.l.	b.d.l.	b.d.l.	b.d.l.	b.d.l.	b.d.l.	b.d.l.	b.d.l.	b.d.l.	b.d.l.	b.d.l.	b.d.l.
CaO	0.06	0.03	0.07	0.08	0.14	0.15	0.25	0.24	0.21	0.24	0.23	0.20	0.15	0.15	0.14	0.12	0.13
TiO2	0.05	b.d.l.	b.d.l.	0.01	b.d.l.	0.01	b.d.l.	0.02	0.02	0.01	b.d.l.	0.02	b.d.l.	0.01	b.d.l.	0.03	0.01
Cr2O3	b.d.l.	b.d.l.	0.04	b.d.l.	b.d.l.	0.04	0.02	b.d.l.	b.d.l.	b.d.l.	b.d.l.	0.04	b.d.l.	b.d.l.	b.d.l.	b.d.l.	b.d.l.
Mno	0.01	0.02	b.d.l.	0.03	b.d.l.	0.05	0.01	b.d.l.	0.04	0.03	0.04	0.02	b.d.l.	0.01	0.01	0.04	b.d.l.
FeO	1.58	0.83	1.16	1.82	2.04	2.38	2.66	3.14	2.81	2.25	2.02	2.62	3.09	2.80	2.56	2.07	1.99
Sum	100.39	99.32	99.64	99.39	99.67	99.65	99.39	99.44	99.25	99.73	99.48	99.04	99.85	99.94	99.33	99.15	99.08
Si	2.97	3.02	3.00	2.99	3.01	2.99	2.98	3.01	3.01	2.99	3.01	3.00	3.01	3.00	3.01	3.01	3.00
Ti	b.d.l.	b.d.l.	b.d.l.	b.d.l.	b.d.l.	b.d.l.	b.d.l.	b.d.l.	b.d.l.	b.d.l.	b.d.l.	b.d.l.	b.d.l.	b.d.l.	b.d.l.	b.d.l.	b.d.l.
Al	2.04	2.01	2.04	2.04	2.04	2.04	2.06	2.02	2.02	2.04	2.03	2.03	2.02	2.02	2.04	2.03	2.04
Cr	b.d.l.	b.d.l.	b.d.l.	b.d.l.	b.d.l.	b.d.l.	b.d.l.	b.d.l.	b.d.l.	b.d.l.	b.d.l.	b.d.l.	b.d.l.	b.d.l.	b.d.l.	b.d.l.	b.d.l.
Fe2+	0.09	0.05	0.07	0.10	0.12	0.14	0.15	0.18	0.16	0.13	0.11	0.15	0.18	0.16	0.15	0.12	0.11
Fe3+	b.d.l.	b.d.l.	b.d.l.	b.d.l.	b.d.l.	b.d.l.	b.d.l.	b.d.l.	b.d.l.	b.d.l.	b.d.l.	b.d.l.	b.d.l.	b.d.l.	b.d.l.	b.d.l.	b.d.l.
Mn	b.d.l.	b.d.l.	b.d.l.	b.d.l.	b.d.l.	b.d.l.	b.d.l.	b.d.l.	b.d.l.	b.d.l.	b.d.l.	b.d.l.	b.d.l.	b.d.l.	b.d.l.	b.d.l.	b.d.l.
Mn3+	b.d.l.	b.d.l.	b.d.l.	b.d.l.	b.d.l.	b.d.l.	b.d.l.	b.d.l.	b.d.l.	b.d.l.	b.d.l.	b.d.l.	b.d.l.	b.d.l.	b.d.l.	b.d.l.	b.d.l.
Mg	2.90	2.90	2.87	2.85	2.81	2.80	2.77	2.76	2.77	2.80	2.81	2.78	2.77	2.80	2.77	2.80	2.82
Ca	b.d.l.	b.d.l.	0.01	0.01	0.01	0.01	0.02	0.02	0.02	0.02	0.02	0.01	0.01	0.01	0.01	0.01	0.01
Na	b.d.l.	b.d.l.	b.d.l.	b.d.l.	b.d.l.	b.d.l.	b.d.l.	b.d.l.	b.d.l.	b.d.l.	b.d.l.	b.d.l.	b.d.l.	b.d.l.	b.d.l.	b.d.l.	b.d.l.
Sum	8.01	7.98	7.98	7.99	7.98	7.99	7.99	7.98	7.98	7.99	7.98	7.98	7.98	7.99	7.97	7.97	7.98

Table A.1.11: Compositional (in wt%) transect in garnet neoblast DM17-8A-1 (part 2)

S.	DM17 8A1-1	DM17 8A1-2	DM17 8A1-3	DM17 8A1-4	DM17 8A1-5	DM17 8A1-6	DM17 8A1-7	DM17 8A1-8	DM17 8A1-9	DM17 8A1-10	DM17 8A1-11	DM17 8A1-12	DM17 8A1-13	DM17 8A1-14	DM17 8A1-15
Na2O	b.d.l.	b.d.l.	b.d.l.	b.d.l.	b.d.l.	b.d.l.	b.d.l.	b.d.l.	b.d.l.	b.d.l.	b.d.l.	b.d.l.	b.d.l.	b.d.l.	b.d.l.
MgO	28.21	27.87	26.81	27.39	29.23	29.18	28.38	27.81	28.22	28.82	28.93	28.69	28.12	28.44	27.89
Al2O3	25.26	25.10	25.15	25.39	26.17	25.55	25.41	25.12	25.29	24.80	25.42	25.21	25.28	25.32	24.74
SiO2	44.15	44.33	43.55	43.58	43.90	44.07	44.23	44.18	44.52	44.98	43.77	44.08	44.25	44.05	44.79
K2O	b.d.l.	b.d.l.	b.d.l.	b.d.l.	b.d.l.	b.d.l.	b.d.l.	b.d.l.	b.d.l.	b.d.l.	b.d.l.	b.d.l.	b.d.l.	b.d.l.	b.d.l.
CaO	0.15	0.11	0.20	0.25	0.04	0.07	0.07	0.14	0.10	0.04	0.07	0.06	0.08	0.08	0.06
TiO2	b.d.l.	0.03	0.06	0.02	0.08	b.d.l.	0.05	0.01	b.d.l.	b.d.l.	0.02	b.d.l.	b.d.l.	b.d.l.	0.03
Cr2O3	b.d.l.	b.d.l.	b.d.l.	0.04	0.03	0.01	b.d.l.	0.06	0.02	0.05	0.03	b.d.l.	b.d.l.	b.d.l.	b.d.l.
Mno	b.d.l.	0.03	0.01	b.d.l.	0.03	b.d.l.	b.d.l.	0.01	b.d.l.	0.01	b.d.l.	0.01	b.d.l.	b.d.l.	b.d.l.
FeO	1.35	1.81	3.56	2.58	0.71	0.43	1.23	2.04	0.99	0.59	1.05	1.04	1.19	1.01	1.07
Sum	99.13	99.28	99.34	99.25	100.19	99.30	99.37	99.38	99.14	99.29	99.30	99.09	98.92	98.89	98.57
Si	3.00	3.02	2.99	2.98	2.95	2.98	3.00	3.01	3.02	3.04	2.97	3.00	3.01	3.00	3.06
Ti	b.d.l.	b.d.l.	b.d.l.	b.d.l.	b.d.l.	b.d.l.	b.d.l.	b.d.l.	b.d.l.	b.d.l.	b.d.l.	b.d.l.	b.d.l.	b.d.l.	b.d.l.
Al	2.03	2.01	2.03	2.05	2.07	2.04	2.03	2.02	2.02	1.98	2.04	2.02	2.03	2.03	1.99
Cr	b.d.l.	b.d.l.	b.d.l.	b.d.l.	b.d.l.	b.d.l.	b.d.l.	b.d.l.	b.d.l.	b.d.l.	b.d.l.	b.d.l.	b.d.l.	b.d.l.	b.d.l.
Fe2+	0.08	0.10	0.20	0.15	0.04	0.02	0.07	0.12	0.06	0.03	0.06	0.06	0.07	0.06	0.06
Fe3+	b.d.l.	b.d.l.	b.d.l.	b.d.l.	b.d.l.	b.d.l.	b.d.l.	b.d.l.	b.d.l.	b.d.l.	b.d.l.	b.d.l.	b.d.l.	b.d.l.	b.d.l.
Mn	b.d.l.	b.d.l.	b.d.l.	b.d.l.	b.d.l.	b.d.l.	b.d.l.	b.d.l.	b.d.l.	b.d.l.	b.d.l.	b.d.l.	b.d.l.	b.d.l.	b.d.l.
Mn3+	b.d.l.	b.d.l.	b.d.l.	b.d.l.	b.d.l.	b.d.l.	b.d.l.	b.d.l.	b.d.l.	b.d.l.	b.d.l.	b.d.l.	b.d.l.	b.d.l.	b.d.l.
Mg	2.86	2.83	2.74	2.79	2.93	2.95	2.87	2.82	2.86	2.91	2.93	2.91	2.86	2.89	2.84
Ca	0.01	0.01	0.01	0.02	b.d.l.	b.d.l.	0.01	0.01	0.01	b.d.l.	0.01	b.d.l.	0.01	0.01	b.d.l.
Na	b.d.l.	b.d.l.	b.d.l.	b.d.l.	b.d.l.	b.d.l.	b.d.l.	b.d.l.	b.d.l.	b.d.l.	b.d.l.	b.d.l.	b.d.l.	b.d.l.	b.d.l.
Sum	7.98	7.97	7.99	7.99	8.01	8.00	7.98	7.98	7.97	7.97	8.01	7.99	7.97	7.98	7.95

Table A1.12: compositional (in wt%) transect in garnet megablast DM17-49-4A (part 1)

S.	Line 1 DM174 9-4° -LO	Line 2 DM174 9-4° -LO	Line 3 DM174 9-4° -LO	Line 4 DM174 9-4° -LO	Line 5 DM174 9-4° -LO	Line 6 DM174 9-4° -LO	Line 7 DM174 9-4A -LO	Line 8 DM174 9-4A -LO	Line 9 DM174 9-4A -LO	Line 1 DM174 9-4A -LV	Line 2 DM174 9-4A -LV	Line 3 DM174 9-4A -LV	Line 4 DM174 9-4A -LV	Line 5 DM174 9-4A -LV	Line 6 DM174 9-4A -LV	Line 7 DM174 9-4A -LV	Line 8 DM174 9-4A -LV	Line 9 DM174 9-4A -LV
Na2O	0.07	0.07	0.04	0.04	0.03	0.04	0.08	0.05	0.03	0.04	0.07	0.06	0.05	0.10	0.06	0.04	0.04	0.04
MgO	26.44	26.97	26.75	26.38	26.56	26.13	25.93	26.65	26.54	26.65	26.39	26.25	26.16	26.01	26.29	26.63	26.55	27.07
Al2O3	25.20	25.64	25.10	25.40	25.39	25.05	25.17	25.19	25.16	25.32	25.34	25.30	25.25	25.33	25.29	25.25	25.40	25.44
SiO2	43.49	42.94	43.43	43.36	43.18	43.30	43.09	43.49	43.53	42.55	42.74	42.74	42.55	42.33	42.82	43.06	42.79	42.42
K2O	b.d.l.	b.d.l.	b.d.l.	0.01	b.d.l.	0.01	0.01	0.02	b.d.l.	b.d.l.	b.d.l.	0.01	b.d.l.	0.01	b.d.l.	b.d.l.	b.d.l.	0.01
CaO	0.94	0.89	0.75	0.88	0.74	0.78	0.89	0.84	0.76	0.66	0.73	1.13	1.03	1.00	0.84	0.61	0.68	0.60
TiO2	0.04	0.02	0.02	0.02	0.03	0.04	b.d.l.	0.03	0.05	0.06	b.d.l.	0.07	0.05	0.06	0.02	0.02	0.03	b.d.l.
Cr2O3	b.d.l.	b.d.l.	b.d.l.	b.d.l.	0.01	b.d.l.	b.d.l.	b.d.l.	0.05	0.10	0.03	0.03	0.03	b.d.l.	b.d.l.	b.d.l.	0.02	b.d.l.
Mno	0.04	b.d.l.	0.02	0.05	0.03	b.d.l.	0.01	0.05	0.01	0.03	0.02	b.d.l.	b.d.l.	0.05	b.d.l.	0.05	0.03	0.02
FeO	3.81	2.91	3.01	4.06	4.03	4.19	3.82	3.39	3.40	4.06	3.64	3.69	4.00	4.09	3.97	3.08	3.28	3.32
Sum	100.03	99.43	99.13	100.20	99.99	99.54	99.01	99.70	99.52	99.47	98.96	99.28	99.12	98.98	99.29	98.74	98.82	98.92
Si	2.98	2.95	2.99	2.97	2.96	2.98	2.98	2.98	2.99	2.94	2.96	2.95	2.95	2.94	2.96	2.97	2.96	2.93
Ti	b.d.l.	b.d.l.	b.d.l.	b.d.l.	b.d.l.	b.d.l.	b.d.l.	b.d.l.	b.d.l.	b.d.l.	b.d.l.	b.d.l.	b.d.l.	b.d.l.	b.d.l.	b.d.l.	b.d.l.	b.d.l.
Al	2.03	2.07	2.03	2.05	2.05	2.03	2.05	2.03	2.03	2.06	2.06	2.06	2.06	2.07	2.06	2.05	2.07	2.07
Cr	b.d.l.	b.d.l.	b.d.l.	b.d.l.	b.d.l.	b.d.l.	b.d.l.	b.d.l.	b.d.l.	0.01	b.d.l.	b.d.l.	b.d.l.	b.d.l.	b.d.l.	b.d.l.	b.d.l.	b.d.l.
Fe2+	0.22	0.17	0.17	0.23	0.23	0.24	0.22	0.19	0.20	0.23	0.21	0.21	0.23	0.24	0.23	0.18	0.19	0.19
Fe3+	b.d.l.	b.d.l.	b.d.l.	b.d.l.	b.d.l.	b.d.l.	b.d.l.	b.d.l.	b.d.l.	b.d.l.	b.d.l.	b.d.l.	b.d.l.	b.d.l.	b.d.l.	b.d.l.	b.d.l.	b.d.l.
Mn	b.d.l.	b.d.l.	b.d.l.	b.d.l.	b.d.l.	b.d.l.	b.d.l.	b.d.l.	b.d.l.	b.d.l.	b.d.l.	b.d.l.	b.d.l.	b.d.l.	b.d.l.	b.d.l.	b.d.l.	b.d.l.
Mn3+	b.d.l.	b.d.l.	b.d.l.	b.d.l.	b.d.l.	b.d.l.	b.d.l.	b.d.l.	b.d.l.	b.d.l.	b.d.l.	b.d.l.	b.d.l.	b.d.l.	b.d.l.	b.d.l.	b.d.l.	b.d.l.
Mg	2.70	2.76	2.74	2.69	2.71	2.68	2.67	2.72	2.71	2.74	2.72	2.70	2.70	2.69	2.71	2.74	2.73	2.79
Ca	0.07	0.07	0.06	0.06	0.05	0.06	0.07	0.06	0.06	0.05	0.05	0.08	0.08	0.07	0.06	0.04	0.05	0.04
Na	0.01	0.01	0.01	b.d.l.	b.d.l.	b.d.l.	0.01	0.01	b.d.l.	0.01	0.01	0.01	0.01	0.01	0.01	0.01	0.01	0.01
K	b.d.l.	b.d.l.	b.d.l.	b.d.l.	b.d.l.	b.d.l.	b.d.l.	b.d.l.	b.d.l.	b.d.l.	b.d.l.	b.d.l.	b.d.l.	b.d.l.	b.d.l.	b.d.l.	b.d.l.	b.d.l.
Sum	8.01	8.02	8.00	8.01	8.02	8.00	8.00	8.00	7.99	8.03	8.02	8.02	8.02	8.03	8.02	8.00	8.01	8.04

Table A.1.13: compositional (in wt%) transect in garnet megablast DM17-49-4A (part 2)

S.	Line 10 DM174 9-4A-LV	Line 1 DM174 9-1A-LO	Line 2 DM174 9-1A-LO	Line 3 DM174 9-1A-LO	Line 4 DM174 9-1A-LO	Line 5 DM174 9-1A-LO	Line 6 DM174 9-1A-LO	Line 7 DM174 9-1A-LO	Line 8 DM174 9-1A-LO	Line 1 DM174 9-1A-LV	Line 2 DM174 9-1A-LV	Line 3 DM174 9-1A-LV	Line 4 DM174 9-1A-LV	Line 5 DM174 9-1A-LV	Line 6 DM174 9-1A-LV	Line 7 DM174 9-1A-LV	Line 8 DM174 9-1A-LV	Line 9 DM174 9-1A-LV	Line 10 DM174 9-1A-LV
Na2O	0.08	0.02	0.07	0.08	0.06	0.10	0.04	0.06	0.03	0.05	0.08	0.02	0.06	0.08	0.07	0.11	0.11	0.10	0.08
MgO	26.83	27.19	27.11	27.37	26.84	26.77	26.72	26.88	26.53	27.39	27.14	27.17	27.17	27.33	27.14	27.26	27.17	27.43	27.29
Al2O3	25.13	25.37	25.47	25.38	25.52	25.66	25.45	25.41	25.25	25.45	25.37	24.77	25.53	25.51	24.93	25.29	25.22	25.11	25.68
SiO2	43.19	43.50	43.45	42.91	42.79	42.74	42.98	42.80	42.39	43.28	42.73	43.84	43.31	43.22	43.42	43.21	43.18	43.12	43.63
K2O	b.d.l.	0.02	b.d.l.	b.d.l.	b.d.l.	b.d.l.	0.01	0.01	b.d.l.	b.d.l.	b.d.l.	b.d.l.	0.01	b.d.l.	b.d.l.	0.01	0.01	0.01	b.d.l.
CaO	0.87	0.27	0.35	0.39	0.38	0.75	0.56	0.59	0.90	0.30	0.27	0.27	0.36	0.38	0.44	0.46	0.49	0.40	0.31
TiO2	0.01	b.d.l.	b.d.l.	b.d.l.	b.d.l.	0.05	0.04	b.d.l.	0.02	b.d.l.	b.d.l.	b.d.l.	b.d.l.	0.05	0.04	b.d.l.	b.d.l.	0.07	0.01
Cr2O3	0.01	0.03	b.d.l.	b.d.l.	b.d.l.	0.01	0.05	b.d.l.	0.02	0.05	0.04	b.d.l.	b.d.l.	b.d.l.	b.d.l.	b.d.l.	0.01	0.02	b.d.l.
Mno	0.03	b.d.l.	0.01	b.d.l.	0.04	0.02	0.04	0.04	b.d.l.	0.03	b.d.l.	0.03	0.02	0.10	0.04	0.01	0.01	0.05	0.02
FeO	3.24	3.13	2.93	2.97	3.19	3.28	3.27	3.26	3.51	2.54	2.93	3.14	2.63	3.18	3.18	3.27	3.14	2.85	2.89
Sum	99.40	99.54	99.38	99.10	98.82	99.38	99.15	99.05	98.65	99.08	98.56	99.24	99.09	99.85	99.25	99.62	99.33	99.15	99.91
Si	2.97	2.98	2.98	2.95	2.95	2.94	2.96	2.95	2.94	2.97	2.95	3.01	2.97	2.95	2.98	2.96	2.97	2.96	2.97
Ti	b.d.l.	b.d.l.	b.d.l.	b.d.l.	b.d.l.	b.d.l.	b.d.l.	b.d.l.	b.d.l.	b.d.l.	b.d.l.	b.d.l.	b.d.l.	b.d.l.	b.d.l.	b.d.l.	b.d.l.	b.d.l.	b.d.l.
Al	2.04	2.05	2.06	2.06	2.08	2.08	2.06	2.06	2.06	2.06	2.07	2.00	2.06	2.05	2.02	2.04	2.04	2.03	2.06
Cr	b.d.l.	b.d.l.	b.d.l.	b.d.l.	b.d.l.	b.d.l.	b.d.l.	b.d.l.	b.d.l.	b.d.l.	b.d.l.	b.d.l.	b.d.l.	b.d.l.	b.d.l.	b.d.l.	b.d.l.	b.d.l.	b.d.l.
Fe2+	0.19	0.18	0.17	0.17	0.18	0.19	0.19	0.19	0.20	0.15	0.17	0.18	0.15	0.18	0.18	0.19	0.18	0.16	0.16
Fe3+	b.d.l.	b.d.l.	b.d.l.	b.d.l.	b.d.l.	b.d.l.	b.d.l.	b.d.l.	b.d.l.	b.d.l.	b.d.l.	b.d.l.	b.d.l.	b.d.l.	b.d.l.	b.d.l.	b.d.l.	b.d.l.	b.d.l.
Mn	b.d.l.	b.d.l.	b.d.l.	b.d.l.	b.d.l.	b.d.l.	b.d.l.	b.d.l.	b.d.l.	b.d.l.	b.d.l.	b.d.l.	b.d.l.	0.01	b.d.l.	b.d.l.	b.d.l.	b.d.l.	b.d.l.
Mn3+	b.d.l.	b.d.l.	b.d.l.	b.d.l.	b.d.l.	b.d.l.	b.d.l.	b.d.l.	b.d.l.	b.d.l.	b.d.l.	b.d.l.	b.d.l.	b.d.l.	b.d.l.	b.d.l.	b.d.l.	b.d.l.	b.d.l.
Mg	2.75	2.77	2.77	2.81	2.76	2.74	2.74	2.76	2.74	2.80	2.80	2.78	2.78	2.78	2.78	2.78	2.78	2.81	2.77
Ca	0.06	0.02	0.03	0.03	0.03	0.05	0.04	0.04	0.07	0.02	0.02	0.02	0.03	0.03	0.03	0.03	0.04	0.03	0.02
Na	0.01	b.d.l.	0.01	0.01	0.01	0.01	0.01	0.01	b.d.l.	0.01	0.01	b.d.l.	0.01	0.01	0.01	0.01	0.01	0.01	0.01
K	b.d.l.	b.d.l.	b.d.l.	b.d.l.	b.d.l.	b.d.l.	b.d.l.	b.d.l.	b.d.l.	b.d.l.	b.d.l.	b.d.l.	b.d.l.	b.d.l.	b.d.l.	b.d.l.	b.d.l.	b.d.l.	b.d.l.
Sum	8.02	8.00	8.00	8.02	8.01	8.02	8.01	8.02	8.03	8.00	8.02	7.99	8.00	8.02	8.01	8.03	8.02	8.02	8.00

Table A.1.14: compositional (in wt%) transect in garnet megablast DM17-35-5A

S.	Line 2 DM173 5-5A-LO	Line 3 DM173 5-5A-LO	Line 4 DM173 5-5A-LO	Line 6 DM173 5-5A-LO	Line 7 DM173 5-5A-LO	Line 8 DM173 5-5A-LO	Line 9 DM173 5-5A-LO	Line 10 DM173 5-5A-LO	Line 1 DM173 5-5A-LV	Line 2 DM173 5-5A-LV	Line 3 DM173 5-5A-LV	Line 4 DM173 5-5A-LV	Line 5 DM173 5-5A-LV	Line 6 DM173 5-5A-LV	Line 7 DM173 5-5A-LV	Line 8 DM173 5-5A-LV	Line 9 DM173 5-5A-LV	Line 10 DM173 5-5A-LV
Na2O	0.07	0.04	0.05	0.04	0.07	0.11	0.06	0.07	0.08	0.04	0.06	0.07	0.07	0.09	0.06	0.11	0.06	0.03
MgO	27.72	27.94	27.83	27.02	27.56	27.93	27.99	27.81	27.93	27.02	27.64	27.52	27.59	27.90	27.80	27.88	27.79	27.63
Al2O3	25.46	25.42	25.55	25.53	25.53	25.60	25.33	25.30	25.33	25.24	25.42	25.18	25.42	25.53	25.38	25.50	25.38	25.31
SiO2	43.77	43.82	43.79	42.94	43.45	43.83	43.58	43.82	44.41	43.66	43.30	43.72	43.71	43.74	44.13	44.00	43.56	43.86
K2O	b.d.l.	b.d.l.	0.01	b.d.l.	0.01	b.d.l.	0.01	0.01	b.d.l.	0.02	0.01	b.d.l.	b.d.l.	0.01	b.d.l.	b.d.l.	b.d.l.	0.01
CaO	0.54	0.46	0.51	0.52	0.50	0.60	0.57	0.58	0.60	0.57	0.49	0.51	0.52	0.58	0.56	0.56	0.53	0.56
TiO2	0.01	b.d.l.	0.01	0.03	b.d.l.	b.d.l.	b.d.l.	0.02	0.01	0.02	0.05	0.02	b.d.l.	b.d.l.	b.d.l.	0.02	0.05	0.04
Cr2O3	b.d.l.	0.02	b.d.l.	0.03	b.d.l.	b.d.l.	0.06	0.01	b.d.l.	0.01	b.d.l.	0.03	b.d.l.	b.d.l.	0.04	b.d.l.	b.d.l.	b.d.l.
Mno	0.04	0.05	0.04	b.d.l.	b.d.l.	0.03	b.d.l.	0.02	0.04	b.d.l.	0.01	0.04	b.d.l.	b.d.l.	0.02	0.04	0.03	b.d.l.
FeO	2.11	1.96	1.91	2.53	2.17	1.89	1.67	1.83	1.61	2.84	2.12	2.46	2.06	2.13	1.79	1.64	1.65	2.10
Sum	99.72	99.71	99.70	98.65	99.28	99.99	99.28	99.48	100.01	99.42	99.10	99.55	99.37	99.98	99.78	99.75	99.04	99.53
Si	2.98	2.98	2.98	2.96	2.97	2.97	2.97	2.99	3.00	2.99	2.97	2.99	2.98	2.97	3.00	2.99	2.98	2.99
Ti	b.d.l.	b.d.l.	b.d.l.	b.d.l.	b.d.l.	b.d.l.	b.d.l.	b.d.l.	b.d.l.	b.d.l.	b.d.l.	b.d.l.	b.d.l.	b.d.l.	b.d.l.	b.d.l.	b.d.l.	b.d.l.
Al	2.04	2.04	2.05	2.07	2.06	2.05	2.04	2.03	2.02	2.04	2.05	2.03	2.04	2.04	2.03	2.04	2.05	2.03
Cr	b.d.l.	b.d.l.	b.d.l.	b.d.l.	b.d.l.	b.d.l.	b.d.l.	b.d.l.	b.d.l.	b.d.l.	b.d.l.	b.d.l.	b.d.l.	b.d.l.	b.d.l.	b.d.l.	b.d.l.	b.d.l.
Fe2+	0.12	0.11	0.11	0.15	0.12	0.11	0.10	0.10	0.09	0.16	0.12	0.14	0.12	0.12	0.10	0.09	0.09	0.12
Fe3+	b.d.l.	b.d.l.	b.d.l.	b.d.l.	b.d.l.	b.d.l.	b.d.l.	b.d.l.	b.d.l.	b.d.l.	b.d.l.	b.d.l.	b.d.l.	b.d.l.	b.d.l.	b.d.l.	b.d.l.	b.d.l.
Mn	b.d.l.	b.d.l.	b.d.l.	b.d.l.	b.d.l.	b.d.l.	b.d.l.	b.d.l.	b.d.l.	b.d.l.	b.d.l.	b.d.l.	b.d.l.	b.d.l.	b.d.l.	b.d.l.	b.d.l.	b.d.l.
Mn3+	b.d.l.	b.d.l.	b.d.l.	b.d.l.	b.d.l.	b.d.l.	b.d.l.	b.d.l.	b.d.l.	b.d.l.	b.d.l.	b.d.l.	b.d.l.	b.d.l.	b.d.l.	b.d.l.	b.d.l.	b.d.l.
Mg	2.81	2.83	2.82	2.78	2.81	2.82	2.85	2.82	2.82	2.76	2.82	2.80	2.81	2.82	2.81	2.82	2.83	2.81
Ca	0.04	0.03	0.04	0.04	0.04	0.04	0.04	0.04	0.04	0.04	0.04	0.04	0.04	0.04	0.04	0.04	0.04	0.04
Na	0.01	0.01	0.01	0.01	0.01	0.01	0.01	0.01	0.01	0.01	0.01	0.01	0.01	0.01	0.01	0.01	0.01	b.d.l.
K	b.d.l.	b.d.l.	b.d.l.	b.d.l.	b.d.l.	b.d.l.	b.d.l.	b.d.l.	b.d.l.	b.d.l.	b.d.l.	b.d.l.	b.d.l.	b.d.l.	b.d.l.	b.d.l.	b.d.l.	b.d.l.
Sum	8.00	8.00	8.00	8.00	8.01	8.01	8.01	8.00	7.99	8.00	8.01	8.00	8.00	8.01	7.99	8.00	8.00	7.99

Table A.1.15: compositional (in wt%) transect in garnet megablast DM17-35-1A

S.	Line 1 DM173 5-1A-LO	Line 2 DM173 5-1A-LO	Line 3 DM173 5-1A-LO	Line 4 DM173 5-1A-LO	Line 5 DM173 5-1A-LO	Line 6 DM173 5-1A-LO	Line 7 DM173 5-1A-LO	Line 8 DM173 5-1A-LO	Line 9 DM173 5-1A-LO	Line 10 DM173 5-1A-LO	Line 1 DM173 5-1A-LV	Line 2 DM173 5-1A-LV	Line 4 DM173 5-1A-LV	Line 5 DM173 5-1A-LV	Line 7 DM173 5-1A-LV	Line 8 DM173 5-1A-LV	Line 9 DM173 5-1A-LV	Line 10 DM173 5-1A-LV
Na2O	0.07	0.04	0.08	0.02	0.09	0.03	0.06	0.07	0.02	0.08	0.02	0.07	0.07	0.07	0.06	0.01	0.05	0.02
MgO	27.57	27.60	28.15	28.24	27.80	27.70	28.00	27.17	27.38	26.80	27.56	28.23	27.63	27.70	27.07	26.82	27.07	27.28
Al2O3	25.51	25.28	25.37	25.26	25.56	25.44	25.59	25.36	25.25	25.77	25.44	25.40	25.42	25.43	25.41	25.12	25.22	25.14
SiO2	43.93	43.52	43.93	43.86	42.94	43.62	43.78	43.59	43.19	43.17	43.74	43.77	43.65	44.43	43.77	43.36	43.77	43.74
K2O	b.d.l.	0.01	b.d.l.	b.d.l.	0.01	b.d.l.	b.d.l.	0.01	0.01	b.d.l.	b.d.l.	b.d.l.	0.01	b.d.l.	b.d.l.	b.d.l.	b.d.l.	0.01
CaO	0.52	0.56	0.49	0.47	0.48	0.37	0.42	0.54	0.51	0.50	0.48	0.57	0.48	0.39	0.43	0.46	0.53	0.48
TiO2	0.08	b.d.l.	0.06	b.d.l.	0.01	0.04	b.d.l.	0.05	b.d.l.	0.03	b.d.l.	b.d.l.	0.02	0.02	b.d.l.	0.04	0.02	0.01
Cr2O3	0.04	b.d.l.	b.d.l.	b.d.l.	b.d.l.	b.d.l.	b.d.l.	0.01	b.d.l.	b.d.l.	b.d.l.	b.d.l.	b.d.l.	0.08	0.01	0.01	0.08	b.d.l.
Mno	b.d.l.	0.02	b.d.l.	b.d.l.	b.d.l.	0.01	0.02	b.d.l.	0.04	0.03	0.04	0.03	0.02	b.d.l.	b.d.l.	0.08	0.03	b.d.l.
FeO	2.43	2.33	1.56	1.68	1.83	2.40	1.72	2.43	2.29	3.34	1.92	1.64	1.58	1.66	2.58	3.36	2.89	2.78
Sum	100.14	99.36	99.64	99.53	98.72	99.62	99.58	99.23	98.69	99.72	99.19	99.71	98.87	99.78	99.33	99.25	99.66	99.46
Si	2.98	2.98	2.98	2.98	2.95	2.97	2.98	2.98	2.97	2.95	2.99	2.97	2.99	3.01	2.99	2.98	2.99	2.99
Ti	b.d.l.	b.d.l.	b.d.l.	b.d.l.	b.d.l.	b.d.l.	b.d.l.	b.d.l.	b.d.l.	b.d.l.	b.d.l.	b.d.l.	b.d.l.	b.d.l.	b.d.l.	b.d.l.	b.d.l.	b.d.l.
Al	2.04	2.04	2.03	2.03	2.07	2.04	2.05	2.05	2.05	2.08	2.05	2.03	2.05	2.03	2.05	2.04	2.03	2.03
Cr	b.d.l.	b.d.l.	b.d.l.	b.d.l.	b.d.l.	b.d.l.	b.d.l.	b.d.l.	b.d.l.	b.d.l.	b.d.l.	b.d.l.	b.d.l.	b.d.l.	b.d.l.	b.d.l.	b.d.l.	b.d.l.
Fe2+	0.14	0.13	0.09	0.10	0.11	0.14	0.10	0.14	0.13	0.19	0.11	0.09	0.09	0.09	0.15	0.19	0.17	0.16
Fe3+	b.d.l.	b.d.l.	b.d.l.	b.d.l.	b.d.l.	b.d.l.	b.d.l.	b.d.l.	b.d.l.	b.d.l.	b.d.l.	b.d.l.	b.d.l.	b.d.l.	b.d.l.	b.d.l.	b.d.l.	b.d.l.
Mn	b.d.l.	b.d.l.	b.d.l.	b.d.l.	b.d.l.	b.d.l.	b.d.l.	b.d.l.	b.d.l.	b.d.l.	b.d.l.	b.d.l.	b.d.l.	b.d.l.	b.d.l.	b.d.l.	b.d.l.	b.d.l.
Mn3+	b.d.l.	b.d.l.	b.d.l.	b.d.l.	b.d.l.	b.d.l.	b.d.l.	b.d.l.	b.d.l.	b.d.l.	b.d.l.	b.d.l.	b.d.l.	b.d.l.	b.d.l.	b.d.l.	b.d.l.	b.d.l.
Mg	2.79	2.81	2.85	2.86	2.85	2.82	2.84	2.77	2.81	2.73	2.81	2.86	2.82	2.80	2.76	2.75	2.76	2.78
Ca	0.04	0.04	0.04	0.03	0.04	0.03	0.03	0.04	0.04	0.04	0.04	0.04	0.03	0.03	0.03	0.03	0.04	0.04
Na	0.01	0.01	0.01	b.d.l.	0.01	b.d.l.	0.01	0.01	b.d.l.	0.01	b.d.l.	0.01	0.01	0.01	0.01	b.d.l.	0.01	b.d.l.
K	b.d.l.	b.d.l.	b.d.l.	b.d.l.	b.d.l.	b.d.l.	b.d.l.	b.d.l.	b.d.l.	b.d.l.	b.d.l.	b.d.l.	b.d.l.	b.d.l.	b.d.l.	b.d.l.	b.d.l.	b.d.l.
Sum	8.00	8.01	8.00	8.00	8.02	8.00	8.00	8.00	8.01	8.01	7.99	8.01	7.99	7.98	7.99	8.00	8.00	8.00

Table A.1.16: compositional (in wt%) transect in garnet megablast DMG4-6 (part 1)

S.	DMG4-6A L01	DMG4-6A L02	DMG4-6A L03	DMG4-6A L04	DMG4-6A L05	DMG4-6A L06	DMG4-6A L07	DMG4-6A L08	DMG4-6A L09	DMG4-6A L10	DMG4-6A L11	DMG4-6A L12	DMG4-6A L13	DMG4-6A L14	DMG4-6A L15	DMG4-6A L16	DMG4-6A L17	DMG4-6A L18
Na2O	b.d.l.	b.d.l.	b.d.l.	b.d.l.	b.d.l.	b.d.l.	b.d.l.	b.d.l.	b.d.l.	b.d.l.	b.d.l.	b.d.l.	b.d.l.	b.d.l.	b.d.l.	b.d.l.	b.d.l.	b.d.l.
MgO	26.32	26.54	25.81	25.72	25.51	25.46	25.57	25.65	25.50	25.32	25.40	25.61	25.48	25.67	25.89	26.11	26.62	25.88
Al2O3	25.30	25.26	25.16	25.29	25.48	25.14	25.24	25.27	25.01	24.87	25.10	25.05	25.14	25.09	25.07	25.07	25.38	25.07
SiO2	43.71	43.60	43.29	43.67	43.06	43.13	43.30	43.29	43.49	43.86	43.50	43.44	43.57	43.53	43.40	43.72	43.77	43.56
K2O	b.d.l.	b.d.l.	b.d.l.	b.d.l.	b.d.l.	b.d.l.	b.d.l.	b.d.l.	b.d.l.	b.d.l.	b.d.l.	b.d.l.	b.d.l.	b.d.l.	b.d.l.	b.d.l.	b.d.l.	b.d.l.
CaO	0.87	0.76	0.90	0.82	0.93	0.92	1.09	0.96	0.91	1.00	0.97	1.07	1.06	0.86	0.96	0.76	0.82	1.07
TiO2	b.d.l.	0.03	0.01	b.d.l.	b.d.l.	0.07	0.01	0.01	b.d.l.	b.d.l.	0.02	0.03	b.d.l.	b.d.l.	0.04	b.d.l.	b.d.l.	b.d.l.
Cr2O3	b.d.l.	0.01	b.d.l.	b.d.l.	b.d.l.	b.d.l.	b.d.l.	b.d.l.	b.d.l.	0.05	b.d.l.	b.d.l.	0.05	b.d.l.	0.01	b.d.l.	0.03	b.d.l.
Mno	0.08	0.06	0.01	0.02	0.05	b.d.l.	0.06	0.02	b.d.l.	0.04	0.01	0.03	0.02	b.d.l.	0.03	0.01	b.d.l.	b.d.l.
FeO	4.00	4.12	4.38	4.71	4.91	5.02	4.98	4.74	4.77	4.84	4.76	4.77	4.68	4.85	4.27	3.78	3.75	3.67
Sum	100.27	100.38	99.57	100.23	99.94	99.74	100.25	99.94	99.68	99.98	99.76	100.00	100.00	100.00	99.67	99.44	100.37	99.25
Si	2.98	2.98	2.98	2.99	2.96	2.98	2.97	2.98	3.00	3.01	2.99	2.99	2.99	2.99	2.99	3.00	2.98	3.00
Ti	b.d.l.	b.d.l.	b.d.l.	b.d.l.	b.d.l.	b.d.l.	b.d.l.	b.d.l.	b.d.l.	b.d.l.	b.d.l.	b.d.l.	b.d.l.	b.d.l.	b.d.l.	b.d.l.	b.d.l.	b.d.l.
Al	2.04	2.03	2.04	2.04	2.07	2.04	2.04	2.05	2.03	2.01	2.04	2.03	2.04	2.03	2.03	2.03	2.04	2.03
Cr	b.d.l.	b.d.l.	b.d.l.	b.d.l.	b.d.l.	b.d.l.	b.d.l.	b.d.l.	b.d.l.	b.d.l.	b.d.l.	b.d.l.	b.d.l.	b.d.l.	b.d.l.	b.d.l.	b.d.l.	b.d.l.
Fe2+	0.23	0.24	0.25	0.27	0.28	0.29	0.29	0.27	0.27	0.28	0.27	0.27	0.27	0.28	0.25	0.22	0.21	0.21
Fe3+	b.d.l.	b.d.l.	b.d.l.	b.d.l.	b.d.l.	b.d.l.	b.d.l.	b.d.l.	b.d.l.	b.d.l.	b.d.l.	b.d.l.	b.d.l.	b.d.l.	b.d.l.	b.d.l.	b.d.l.	b.d.l.
Mn	b.d.l.	b.d.l.	b.d.l.	b.d.l.	b.d.l.	b.d.l.	b.d.l.	b.d.l.	b.d.l.	b.d.l.	b.d.l.	b.d.l.	b.d.l.	b.d.l.	b.d.l.	b.d.l.	b.d.l.	b.d.l.
Mn3+	b.d.l.	b.d.l.	b.d.l.	b.d.l.	b.d.l.	b.d.l.	b.d.l.	b.d.l.	b.d.l.	b.d.l.	b.d.l.	b.d.l.	b.d.l.	b.d.l.	b.d.l.	b.d.l.	b.d.l.	b.d.l.
Mg	2.68	2.70	2.65	2.63	2.62	2.62	2.62	2.63	2.62	2.59	2.61	2.62	2.61	2.63	2.66	2.67	2.70	2.66
Ca	0.06	0.06	0.07	0.06	0.07	0.07	0.08	0.07	0.07	0.07	0.07	0.08	0.08	0.06	0.07	0.06	0.06	0.08
Na	b.d.l.	b.d.l.	b.d.l.	b.d.l.	b.d.l.	b.d.l.	b.d.l.	b.d.l.	b.d.l.	b.d.l.	b.d.l.	b.d.l.	b.d.l.	b.d.l.	b.d.l.	b.d.l.	b.d.l.	b.d.l.
K	b.d.l.	b.d.l.	b.d.l.	b.d.l.	b.d.l.	b.d.l.	b.d.l.	b.d.l.	b.d.l.	b.d.l.	b.d.l.	b.d.l.	b.d.l.	b.d.l.	b.d.l.	b.d.l.	b.d.l.	b.d.l.
Sum	8.00	8.01	8.00	7.99	8.00	8.00	8.00	8.00	7.99	7.98	7.99	8.00	7.99	7.99	8.00	7.98	8.00	7.98

Table A.1.17: compositional (in wt%) transect in garnet megablast DMG4-6 (part 2)

S.	DMG4-6A L20	DMG4-6A L21	DMG4-6A L22	DMG4-6A L23	DMG4-6A L24	DMG4-6A L25	DMG4-6B L01	DMG4-6B L02	DMG4-6B L03	DMG4-6B L04	DMG4-6B L05	DMG4-6B L06	DMG4-6B L07	DMG4-6B L08	DMG4-6B L09	DMG4-6B L10	DMG4-6B L11	DMG4-6B L12	DMG4-6B L13
Na2O	b.d.l.	b.d.l.	b.d.l.	b.d.l.	b.d.l.	b.d.l.	b.d.l.	b.d.l.	b.d.l.	b.d.l.	b.d.l.	b.d.l.	b.d.l.	b.d.l.	b.d.l.	b.d.l.	b.d.l.	b.d.l.	b.d.l.
MgO	26.19	25.79	25.49	25.18	25.64	25.90	26.73	26.99	26.52	27.10	26.70	26.89	26.97	26.91	26.71	26.70	26.47	26.76	26.73
Al2O3	25.29	24.85	25.09	24.74	24.94	25.05	25.24	25.39	25.12	25.39	25.54	25.42	25.29	25.13	25.29	24.96	25.54	25.54	25.19
SiO2	43.34	43.12	43.40	43.73	43.52	43.68	43.75	43.80	43.72	43.86	43.70	43.92	44.08	44.19	43.45	44.31	43.96	44.25	44.12
K2O	b.d.l.	b.d.l.	b.d.l.	b.d.l.	b.d.l.	b.d.l.	b.d.l.	b.d.l.	b.d.l.	b.d.l.	b.d.l.	b.d.l.	b.d.l.	b.d.l.	b.d.l.	b.d.l.	b.d.l.	b.d.l.	b.d.l.
CaO	0.92	0.97	0.88	1.05	1.07	0.91	0.76	0.58	0.78	0.80	0.80	0.78	0.69	0.84	0.86	0.69	0.87	0.82	0.79
TiO2	0.03	0.01	0.06	0.02	0.06	b.d.l.	0.05	0.02	b.d.l.	0.01	0.04	0.04	0.01	0.03	0.01	0.04	b.d.l.	b.d.l.	0.06
Cr2O3	0.05	b.d.l.	b.d.l.	0.01	0.04	b.d.l.	b.d.l.	b.d.l.	0.04	0.04	0.01	0.04	0.01	0.05	b.d.l.	b.d.l.	0.03	0.05	0.01
Mno	0.07	0.02	0.02	b.d.l.	b.d.l.	b.d.l.	0.02	0.06	0.04	0.02	0.03	0.03	b.d.l.	0.02	b.d.l.	0.02	b.d.l.	0.08	0.03
FeO	3.81	3.94	4.46	4.40	4.52	4.69	3.19	3.24	3.11	3.13	3.28	3.21	3.29	3.30	3.33	3.38	3.37	3.37	3.53
Sum	99.71	98.70	99.40	99.12	99.79	100.23	99.74	100.09	99.32	100.34	100.10	100.33	100.34	100.46	99.65	100.10	100.24	100.87	100.46
Si	2.98	2.99	2.99	3.02	2.99	2.99	2.99	2.98	3.00	2.98	2.98	2.99	3.00	3.00	2.98	3.02	2.99	2.99	3.00
Ti	b.d.l.	b.d.l.	b.d.l.	b.d.l.	b.d.l.	b.d.l.	b.d.l.	b.d.l.	b.d.l.	b.d.l.	b.d.l.	b.d.l.	b.d.l.	b.d.l.	b.d.l.	b.d.l.	b.d.l.	b.d.l.	b.d.l.
Al	2.05	2.03	2.04	2.02	2.02	2.02	2.03	2.04	2.03	2.03	2.05	2.04	2.03	2.01	2.04	2.00	2.05	2.04	2.02
Cr	b.d.l.	b.d.l.	b.d.l.	b.d.l.	b.d.l.	b.d.l.	b.d.l.	b.d.l.	b.d.l.	b.d.l.	b.d.l.	b.d.l.	b.d.l.	b.d.l.	b.d.l.	b.d.l.	b.d.l.	b.d.l.	b.d.l.
Fe2+	0.22	0.23	0.26	0.25	0.26	0.27	0.18	0.18	0.18	0.18	0.19	0.18	0.19	0.19	0.19	0.19	0.19	0.19	0.20
Fe3+	b.d.l.	b.d.l.	b.d.l.	b.d.l.	b.d.l.	b.d.l.	b.d.l.	b.d.l.	b.d.l.	b.d.l.	b.d.l.	b.d.l.	b.d.l.	b.d.l.	b.d.l.	b.d.l.	b.d.l.	b.d.l.	b.d.l.
Mn	b.d.l.	b.d.l.	b.d.l.	b.d.l.	b.d.l.	b.d.l.	b.d.l.	b.d.l.	b.d.l.	b.d.l.	b.d.l.	b.d.l.	b.d.l.	b.d.l.	b.d.l.	b.d.l.	b.d.l.	b.d.l.	b.d.l.
Mn3+	b.d.l.	b.d.l.	b.d.l.	b.d.l.	b.d.l.	b.d.l.	b.d.l.	b.d.l.	b.d.l.	b.d.l.	b.d.l.	b.d.l.	b.d.l.	b.d.l.	b.d.l.	b.d.l.	b.d.l.	b.d.l.	b.d.l.
Mg	2.68	2.67	2.62	2.60	2.63	2.65	2.72	2.74	2.71	2.75	2.71	2.73	2.73	2.72	2.73	2.71	2.69	2.70	2.71
Ca	0.07	0.07	0.06	0.08	0.08	0.07	0.06	0.04	0.06	0.06	0.06	0.06	0.05	0.06	0.06	0.05	0.06	0.06	0.06
Na	b.d.l.	b.d.l.	b.d.l.	b.d.l.	b.d.l.	b.d.l.	b.d.l.	b.d.l.	b.d.l.	b.d.l.	b.d.l.	b.d.l.	b.d.l.	b.d.l.	b.d.l.	b.d.l.	b.d.l.	b.d.l.	b.d.l.
K	b.d.l.	b.d.l.	b.d.l.	b.d.l.	b.d.l.	b.d.l.	b.d.l.	b.d.l.	b.d.l.	b.d.l.	b.d.l.	b.d.l.	b.d.l.	b.d.l.	b.d.l.	b.d.l.	b.d.l.	b.d.l.	b.d.l.
Sum	8.00	7.99	7.98	7.97	7.99	8.00	7.99	8.00	7.98	8.00	7.99	7.99	7.99	7.99	8.00	7.98	7.98	7.99	7.99

Table A.1.18: compositional (in wt%) transect in garnet megablast DMG4-6 (part 3)

S.	DMG4-6B L14	DMG4-6B L15	DMG4-6B L16	DMG4-6B L17	DMG4-6B L18	DMG4-6B L19	DMG4-6B L20	DMG4-6B L21	DMG4-6B L22	DMG4-6B L23	DMG4-6B L24	DMG4-6B L25
Na2O	b.d.l.	b.d.l.	b.d.l.	b.d.l.	b.d.l.	b.d.l.	b.d.l.	b.d.l.	b.d.l.	b.d.l.	b.d.l.	b.d.l.
MgO	26.74	26.65	26.88	26.51	26.21	25.98	26.83	26.51	26.65	26.56	26.23	26.15
Al2O3	25.26	25.30	25.14	25.23	25.15	24.27	25.13	25.20	25.30	25.58	25.15	25.24
SiO2	44.01	44.11	44.20	43.97	43.92	44.31	44.14	43.75	44.07	43.55	43.69	43.63
K2O	b.d.l.	b.d.l.	b.d.l.	b.d.l.	b.d.l.	b.d.l.	b.d.l.	b.d.l.	b.d.l.	b.d.l.	b.d.l.	b.d.l.
CaO	0.80	0.87	0.87	0.89	0.88	0.74	0.90	0.92	0.72	0.84	0.98	0.85
TiO2	0.05	0.07	0.05	b.d.l.	0.01	0.01	0.03	b.d.l.	0.07	0.04	b.d.l.	b.d.l.
Cr2O3	b.d.l.	0.02	0.06	0.01	b.d.l.	b.d.l.	b.d.l.	b.d.l.	b.d.l.	0.02	0.01	b.d.l.
Mno	0.02	0.09	b.d.l.	0.01	0.04	0.01	b.d.l.	b.d.l.	0.03	0.06	0.01	0.04
FeO	3.35	3.46	3.41	3.61	3.83	4.15	3.88	3.84	3.94	4.04	3.92	3.89
Sum	100.22	100.57	100.61	100.24	100.04	99.47	100.91	100.23	100.78	100.69	99.99	99.80
Si	3.00	3.00	3.00	3.00	3.00	3.05	2.99	2.99	2.99	2.96	2.99	2.99
Ti	b.d.l.	b.d.l.	b.d.l.	b.d.l.	b.d.l.	b.d.l.	b.d.l.	b.d.l.	b.d.l.	b.d.l.	b.d.l.	b.d.l.
Al	2.03	2.02	2.01	2.03	2.03	1.97	2.01	2.03	2.02	2.05	2.03	2.04
Cr	b.d.l.	b.d.l.	b.d.l.	b.d.l.	b.d.l.	b.d.l.	b.d.l.	b.d.l.	b.d.l.	b.d.l.	b.d.l.	b.d.l.
Fe2+	0.19	0.20	0.19	0.21	0.22	0.24	0.22	0.22	0.22	0.23	0.22	0.22
Fe3+	b.d.l.	b.d.l.	b.d.l.	b.d.l.	b.d.l.	b.d.l.	b.d.l.	b.d.l.	b.d.l.	b.d.l.	b.d.l.	b.d.l.
Mn	b.d.l.	0.01	b.d.l.	b.d.l.	b.d.l.	b.d.l.	b.d.l.	b.d.l.	b.d.l.	b.d.l.	b.d.l.	b.d.l.
Mn3+	b.d.l.	b.d.l.	b.d.l.	b.d.l.	b.d.l.	b.d.l.	b.d.l.	b.d.l.	b.d.l.	b.d.l.	b.d.l.	b.d.l.
Mg	2.71	2.70	2.72	2.69	2.67	2.66	2.71	2.70	2.70	2.69	2.68	2.67
Ca	0.06	0.06	0.06	0.07	0.06	0.05	0.07	0.07	0.05	0.06	0.07	0.06
Na	b.d.l.	b.d.l.	b.d.l.	b.d.l.	b.d.l.	b.d.l.	b.d.l.	b.d.l.	b.d.l.	b.d.l.	b.d.l.	b.d.l.
K	b.d.l.	b.d.l.	b.d.l.	b.d.l.	b.d.l.	b.d.l.	b.d.l.	b.d.l.	b.d.l.	b.d.l.	b.d.l.	b.d.l.
Sum	7.99	7.99	7.99	7.99	7.98	7.97	8.00	8.00	7.99	8.01	7.99	7.99

Table A.1.19: compositional (in wt%) transect in garnet megablast DM17-13 (part 1)

S.	DM171 3-1A L01	DM171 3-1A L02	DM171 3-1A L03	DM171 3-1A L04	DM171 3-1A L05	DM171 3-1A L06	DM171 3-1A L07	DM171 3-1A L08	DM171 3-1A L09	DM171 3-1A L10	DM171 3-1A L11	DM171 3-1A L12	DM171 3-1A L13	DM171 3-1A L14	DM171 3-1A L15	DM171 3-1A L16	DM171 3-1A L17	DM171 3-1A L18
Na2O	b.d.l.	b.d.l.	b.d.l.	b.d.l.	b.d.l.	b.d.l.	b.d.l.	b.d.l.	b.d.l.	b.d.l.	b.d.l.	b.d.l.	b.d.l.	b.d.l.	b.d.l.	b.d.l.	b.d.l.	b.d.l.
MgO	26.47	26.18	26.80	26.65	26.07	26.56	26.69	25.89	25.59	25.82	25.95	25.74	25.80	27.55	25.90	26.27	25.87	25.26
Al2O3	25.02	25.24	25.50	25.04	25.19	25.42	24.96	24.98	25.04	25.15	24.74	25.06	25.00	25.69	24.91	25.07	25.12	24.90
SiO2	44.28	44.03	43.78	44.32	43.88	43.96	44.06	43.81	43.98	43.94	43.86	43.70	43.68	43.77	43.59	43.75	43.49	43.39
K2O	b.d.l.	b.d.l.	b.d.l.	b.d.l.	b.d.l.	b.d.l.	b.d.l.	b.d.l.	b.d.l.	b.d.l.	b.d.l.	b.d.l.	b.d.l.	b.d.l.	b.d.l.	b.d.l.	b.d.l.	b.d.l.
CaO	0.77	0.74	0.72	0.72	0.74	0.75	0.69	0.77	0.83	0.87	0.71	0.87	0.85	0.07	0.92	0.83	0.66	0.77
TiO2	0.05	0.01	0.02	b.d.l.	0.01	0.02	0.04	0.09	0.05	0.05	b.d.l.	0.05	b.d.l.	0.02	0.03	b.d.l.	0.01	0.02
Cr2O3	b.d.l.	b.d.l.	b.d.l.	b.d.l.	b.d.l.	0.01	0.03	b.d.l.	0.01	b.d.l.	0.02	b.d.l.	b.d.l.	b.d.l.	0.01	0.03	0.02	0.05
Mno	0.01	b.d.l.	0.09	0.04	0.02	0.04	b.d.l.	0.02	0.04	0.01	0.03	0.02	0.06	0.02	0.04	0.01	0.05	0.06
FeO	3.19	3.79	3.09	3.54	3.68	3.19	3.23	4.15	4.58	4.15	4.61	4.54	3.70	3.12	3.83	3.46	4.62	5.02
Sum	99.79	99.98	99.99	100.32	99.59	99.95	99.69	99.71	100.13	99.98	99.93	99.98	99.09	100.25	99.24	99.43	99.85	99.47
Si	3.02	3.01	2.98	3.01	3.01	3.00	3.01	3.01	3.01	3.01	3.01	3.00	3.01	2.97	3.00	3.00	2.99	3.00
Ti	b.d.l.	b.d.l.	b.d.l.	b.d.l.	b.d.l.	b.d.l.	b.d.l.	b.d.l.	b.d.l.	b.d.l.	b.d.l.	b.d.l.	b.d.l.	b.d.l.	b.d.l.	b.d.l.	b.d.l.	b.d.l.
Al	2.01	2.03	2.05	2.01	2.04	2.04	2.01	2.02	2.02	2.03	2.00	2.03	2.03	2.06	2.02	2.03	2.03	2.03
Cr	b.d.l.	b.d.l.	b.d.l.	b.d.l.	b.d.l.	b.d.l.	b.d.l.	b.d.l.	b.d.l.	b.d.l.	b.d.l.	b.d.l.	b.d.l.	b.d.l.	b.d.l.	b.d.l.	b.d.l.	b.d.l.
Fe2+	0.18	0.22	0.18	0.20	0.21	0.18	0.18	0.24	0.26	0.24	0.26	0.26	0.21	0.18	0.22	0.20	0.27	0.29
Fe3+	b.d.l.	b.d.l.	b.d.l.	b.d.l.	b.d.l.	b.d.l.	b.d.l.	b.d.l.	b.d.l.	b.d.l.	b.d.l.	b.d.l.	b.d.l.	b.d.l.	b.d.l.	b.d.l.	b.d.l.	b.d.l.
Mn	b.d.l.	b.d.l.	b.d.l.	b.d.l.	b.d.l.	b.d.l.	b.d.l.	b.d.l.	b.d.l.	b.d.l.	b.d.l.	b.d.l.	b.d.l.	b.d.l.	b.d.l.	b.d.l.	b.d.l.	b.d.l.
Mn3+	b.d.l.	b.d.l.	b.d.l.	b.d.l.	b.d.l.	b.d.l.	b.d.l.	b.d.l.	b.d.l.	b.d.l.	b.d.l.	b.d.l.	b.d.l.	b.d.l.	b.d.l.	b.d.l.	b.d.l.	b.d.l.
Mg	2.69	2.67	2.72	2.70	2.66	2.70	2.72	2.65	2.61	2.63	2.66	2.63	2.65	2.79	2.66	2.69	2.65	2.60
Ca	0.06	0.05	0.05	0.05	0.05	0.06	0.05	0.06	0.06	0.06	0.05	0.06	0.06	0.01	0.07	0.06	0.05	0.06
Na	b.d.l.	b.d.l.	b.d.l.	b.d.l.	b.d.l.	b.d.l.	b.d.l.	b.d.l.	b.d.l.	b.d.l.	b.d.l.	b.d.l.	b.d.l.	b.d.l.	b.d.l.	b.d.l.	b.d.l.	b.d.l.
K	b.d.l.	b.d.l.	b.d.l.	b.d.l.	b.d.l.	b.d.l.	b.d.l.	b.d.l.	b.d.l.	b.d.l.	b.d.l.	b.d.l.	b.d.l.	b.d.l.	b.d.l.	b.d.l.	b.d.l.	b.d.l.
Sum	7.97	7.98	7.99	7.98	7.97	7.98	7.98	7.98	7.97	7.98	7.99	7.99	7.97	8.00	7.98	7.98	7.99	7.98

Table A.1.20: compositional (in wt%) transect in garnet megablast DM17-13 (part 2)

S.	DM171 3-1A L20	DM171 3-1A L21	DM171 3-1A L22	DM171 3-1A L23	DM171 3-1A L24	DM171 3-1A L25	DM171 3-1C L01	DM171 3-1C L02	DM171 3-1C L03	DM171 3-1C L04	DM171 3-1C L05	DM171 3-1C L06	DM171 3-1C L07	DM171 3-1C L08	DM171 3-1C L09	DM171 3-1C L10	DM171 3-1C L11	DM171 3-1C L12
Na2O	b.d.l.	b.d.l.	b.d.l.	b.d.l.	b.d.l.	b.d.l.	b.d.l.	b.d.l.	b.d.l.	b.d.l.	b.d.l.	b.d.l.	b.d.l.	b.d.l.	b.d.l.	b.d.l.	b.d.l.	b.d.l.
MgO	25.30	25.02	25.70	26.09	26.24	26.47	27.36	27.36	27.06	26.83	26.55	26.37	26.47	27.04	26.99	26.83	26.71	27.08
Al2O3	24.96	25.02	24.98	24.96	25.10	25.31	25.46	25.37	25.57	25.28	25.25	25.24	25.14	25.25	25.02	25.51	25.24	25.31
SiO2	43.53	43.67	43.84	43.46	43.79	43.48	43.99	43.94	43.87	43.80	43.63	43.87	44.13	44.45	44.08	43.93	44.07	44.15
K2O	b.d.l.	b.d.l.	b.d.l.	b.d.l.	b.d.l.	b.d.l.	b.d.l.	b.d.l.	b.d.l.	b.d.l.	b.d.l.	b.d.l.	b.d.l.	b.d.l.	b.d.l.	b.d.l.	b.d.l.	b.d.l.
CaO	0.76	0.81	0.59	0.51	0.72	0.51	0.31	0.35	0.60	0.60	0.99	1.26	0.77	0.56	0.63	0.73	0.92	0.84
TiO2	0.05	0.03	b.d.l.	b.d.l.	0.05	0.06	0.02	b.d.l.	b.d.l.	b.d.l.	0.01	0.05	0.01	0.03	b.d.l.	0.03	0.08	0.04
Cr2O3	b.d.l.	b.d.l.	0.05	0.03	b.d.l.	b.d.l.	b.d.l.	0.04	b.d.l.	b.d.l.	0.03	0.01	b.d.l.	0.04	b.d.l.	b.d.l.	0.02	b.d.l.
Mno	0.02	0.06	0.05	0.05	0.07	0.03	0.01	0.02	b.d.l.	0.05	0.03	0.08	0.01	b.d.l.	b.d.l.	0.01	0.01	0.05
FeO	5.06	5.25	4.79	3.83	3.78	3.53	2.55	2.84	2.96	3.23	3.33	3.77	3.25	3.02	3.02	3.01	3.23	3.28
Sum	99.68	99.86	99.99	98.93	99.76	99.38	99.70	99.91	100.06	99.78	99.82	100.65	99.79	100.39	99.74	100.04	100.28	100.75
Si	3.00	3.01	3.01	3.00	3.00	2.99	2.99	2.99	2.98	2.99	2.98	2.99	3.01	3.01	3.01	2.99	3.00	2.99
Ti	b.d.l.	b.d.l.	b.d.l.	b.d.l.	b.d.l.	b.d.l.	b.d.l.	b.d.l.	b.d.l.	b.d.l.	b.d.l.	b.d.l.	b.d.l.	b.d.l.	b.d.l.	b.d.l.	b.d.l.	b.d.l.
Al	2.03	2.03	2.02	2.03	2.03	2.05	2.04	2.03	2.05	2.04	2.04	2.02	2.02	2.02	2.01	2.05	2.02	2.02
Cr	b.d.l.	b.d.l.	b.d.l.	b.d.l.	b.d.l.	b.d.l.	b.d.l.	b.d.l.	b.d.l.	b.d.l.	b.d.l.	b.d.l.	b.d.l.	b.d.l.	b.d.l.	b.d.l.	b.d.l.	b.d.l.
Fe2+	0.29	0.30	0.27	0.22	0.22	0.20	0.15	0.16	0.17	0.18	0.19	0.21	0.19	0.17	0.17	0.17	0.18	0.19
Fe3+	b.d.l.	b.d.l.	b.d.l.	b.d.l.	b.d.l.	b.d.l.	b.d.l.	b.d.l.	b.d.l.	b.d.l.	b.d.l.	b.d.l.	b.d.l.	b.d.l.	b.d.l.	b.d.l.	b.d.l.	b.d.l.
Mn	b.d.l.	b.d.l.	b.d.l.	b.d.l.	b.d.l.	b.d.l.	b.d.l.	b.d.l.	b.d.l.	b.d.l.	b.d.l.	b.d.l.	b.d.l.	b.d.l.	b.d.l.	b.d.l.	b.d.l.	b.d.l.
Mn3+	b.d.l.	b.d.l.	b.d.l.	b.d.l.	b.d.l.	b.d.l.	b.d.l.	b.d.l.	b.d.l.	b.d.l.	b.d.l.	b.d.l.	b.d.l.	b.d.l.	b.d.l.	b.d.l.	b.d.l.	b.d.l.
Mg	2.60	2.57	2.63	2.69	2.68	2.71	2.78	2.78	2.74	2.73	2.71	2.68	2.69	2.73	2.75	2.72	2.71	2.73
Ca	0.06	0.06	0.04	0.04	0.05	0.04	0.02	0.03	0.04	0.04	0.07	0.09	0.06	0.04	0.05	0.05	0.07	0.06
Na	b.d.l.	b.d.l.	b.d.l.	b.d.l.	b.d.l.	b.d.l.	b.d.l.	b.d.l.	b.d.l.	b.d.l.	b.d.l.	b.d.l.	b.d.l.	b.d.l.	b.d.l.	b.d.l.	b.d.l.	b.d.l.
K	b.d.l.	b.d.l.	b.d.l.	b.d.l.	b.d.l.	b.d.l.	b.d.l.	b.d.l.	b.d.l.	b.d.l.	b.d.l.	b.d.l.	b.d.l.	b.d.l.	b.d.l.	b.d.l.	b.d.l.	b.d.l.
Sum	7.98	7.97	7.98	7.98	7.98	7.99	7.98	7.99	7.99	7.99	8.00	8.00	7.97	7.98	7.99	7.99	7.99	8.00

Table A.1.20: compositional (in wt%) transect in garnet megablast DM17-13 (part 3)

S.	DM1713-1C L13	DM1713-1C L14	DM1713-1C L15	DM1713-1C L16	DM1713-1C L17	DM1713-1C L18	DM1713-1C L19	DM1713-1C L20	DM1713-1C L21	DM1713-1C L22	DM1713-1C L23	DM1713-1C L24	DM1713-1C L25
Na2O	b.d.l.	b.d.l.	b.d.l.	b.d.l.	b.d.l.	b.d.l.	b.d.l.	b.d.l.	b.d.l.	b.d.l.	b.d.l.	b.d.l.	b.d.l.
MgO	26.41	26.41	26.99	26.41	26.60	26.38	26.35	26.04	25.49	26.21	25.93	26.19	26.42
Al2O3	25.13	25.13	25.48	25.32	25.33	25.37	25.27	25.19	25.19	25.44	25.13	25.25	25.19
SiO2	43.77	43.85	44.09	43.69	43.76	43.37	43.58	44.16	43.54	43.47	43.39	43.68	43.66
K2O	b.d.l.	b.d.l.	b.d.l.	b.d.l.	b.d.l.	b.d.l.	b.d.l.	b.d.l.	b.d.l.	b.d.l.	b.d.l.	b.d.l.	b.d.l.
CaO	0.91	1.33	0.81	1.06	1.03	1.17	1.27	1.34	1.63	1.40	1.51	1.55	1.34
TiO2	b.d.l.	0.06	b.d.l.	0.04	0.01	b.d.l.	0.02	0.06	0.09	0.01	0.07	b.d.l.	0.03
Cr2O3	b.d.l.	b.d.l.	b.d.l.	0.01	0.02	0.02	b.d.l.	0.02	0.04	b.d.l.	0.02	0.03	b.d.l.
Mno	0.02	0.04	0.07	0.03	b.d.l.	0.03	0.03	0.06	0.06	b.d.l.	0.04	b.d.l.	0.02
FeO	3.32	3.24	3.32	3.45	3.26	3.47	3.28	3.54	3.68	3.47	3.39	3.23	3.33
Sum	99.56	100.06	100.76	100.00	100.02	99.81	99.80	100.41	99.71	100.00	99.48	99.93	99.99
Si	3.00	2.99	2.99	2.99	2.99	2.97	2.98	3.01	2.99	2.97	2.98	2.99	2.98
Ti	b.d.l.	b.d.l.	b.d.l.	b.d.l.	b.d.l.	b.d.l.	b.d.l.	b.d.l.	b.d.l.	b.d.l.	b.d.l.	b.d.l.	b.d.l.
Al	2.03	2.02	2.03	2.04	2.04	2.05	2.04	2.02	2.04	2.05	2.04	2.04	2.03
Cr	b.d.l.	b.d.l.	b.d.l.	b.d.l.	b.d.l.	b.d.l.	b.d.l.	b.d.l.	b.d.l.	b.d.l.	b.d.l.	b.d.l.	b.d.l.
Fe2+	0.19	0.18	0.19	0.20	0.19	0.20	0.19	0.20	0.21	0.20	0.19	0.18	0.19
Fe3+	b.d.l.	b.d.l.	b.d.l.	b.d.l.	b.d.l.	b.d.l.	b.d.l.	b.d.l.	b.d.l.	b.d.l.	b.d.l.	b.d.l.	b.d.l.
Mn	b.d.l.	b.d.l.	b.d.l.	b.d.l.	b.d.l.	b.d.l.	b.d.l.	b.d.l.	b.d.l.	b.d.l.	b.d.l.	b.d.l.	b.d.l.
Mn3+	b.d.l.	b.d.l.	b.d.l.	b.d.l.	b.d.l.	b.d.l.	b.d.l.	b.d.l.	b.d.l.	b.d.l.	b.d.l.	b.d.l.	b.d.l.
Mg	2.70	2.69	2.73	2.69	2.71	2.69	2.69	2.64	2.61	2.67	2.66	2.67	2.69
Ca	0.07	0.10	0.06	0.08	0.08	0.09	0.09	0.10	0.12	0.10	0.11	0.11	0.10
Na	b.d.l.	b.d.l.	b.d.l.	b.d.l.	b.d.l.	b.d.l.	b.d.l.	b.d.l.	b.d.l.	b.d.l.	b.d.l.	b.d.l.	b.d.l.
K	b.d.l.	b.d.l.	b.d.l.	b.d.l.	b.d.l.	b.d.l.	b.d.l.	b.d.l.	b.d.l.	b.d.l.	b.d.l.	b.d.l.	b.d.l.
Sum	7.99	7.99	8.00	7.99	7.99	8.00	8.00	7.98	7.98	8.00	7.99	7.99	8.00

APPENDIX A2

LA-ICP-MS ANALYSIS

GARNET

Table A.2.1: REE compositional transect in garnet megablast DM17-35

S. (Notes)	La (ppm)	Ce (ppm)	Pr (ppm)	Nd (ppm)	Sm (ppm)	Eu (ppm)	Gd (ppm)	Tb (ppm)	Dy (ppm)	Ho (ppm)	Er (ppm)	Tm (ppm)	Yb (ppm)	Lu (ppm)
DM17-35-5A-g1	b.d.l.	b.d.l.	b.d.l.	0.02	0.57	0.25	9.17	3.09	23.70	5.13	15.29	2.10	13.04	1.75
DM17-35-5A-g2	b.d.l.	b.d.l.	b.d.l.	0.03	0.46	0.19	7.23	2.40	18.61	3.99	13.00	1.73	11.81	1.75
DM17-35-5A-g3	0.07	0.06	0.02	0.04	0.47	0.18	6.30	1.81	14.29	3.01	9.38	1.30	8.35	1.20
DM17-35-5A-g4	b.d.l.	b.d.l.	b.d.l.	0.03	0.50	0.20	6.42	1.91	15.23	3.25	9.85	1.36	9.06	1.25
DM17-35-5A-g5	b.d.l.	0.01	b.d.l.	0.02	0.26	0.11	3.94	1.30	11.28	2.59	8.28	1.15	7.74	1.09
DM17-35-5A-g6	b.d.l.	b.d.l.	b.d.l.	b.d.l.	b.d.l.	b.d.l.	b.d.l.	b.d.l.	b.d.l.	b.d.l.	b.d.l.	b.d.l.	b.d.l.	b.d.l.
DM17-35-5A-g7	b.d.l.	b.d.l.	b.d.l.	0.02	0.18	0.09	3.05	0.99	8.93	1.91	5.40	0.74	4.83	0.62
DM17-35-5A-g8	0.09	0.22	0.03	0.08	0.12	0.05	1.33	0.59	6.67	1.90	7.30	1.36	11.22	1.77
DM17-35-5A-g9	b.d.l.	b.d.l.	b.d.l.	0.03	0.54	0.21	6.87	1.97	15.30	3.31	10.08	1.29	8.20	1.09
DM17-35-5A-g10	0.01	0.01	b.d.l.	0.03	0.48	0.21	6.30	1.89	13.70	2.84	8.51	1.15	7.24	0.92
DM17-35-5A-g11	0.10	0.06	0.01	0.04	0.31	0.12	5.29	1.74	15.06	3.62	11.93	1.66	12.37	1.82
DM17-35-5A-g12	b.d.l.	0.01	b.d.l.	b.d.l.	b.d.l.	b.d.l.	b.d.l.	b.d.l.	b.d.l.	b.d.l.	b.d.l.	b.d.l.	b.d.l.	b.d.l.
DM17-35-3A-g1	0.01	0.01	b.d.l.	0.05	0.56	0.14	2.79	0.62	4.91	1.06	3.45	0.53	3.85	0.61
DM17-35-3A-g2	b.d.l.	b.d.l.	b.d.l.	0.05	0.46	0.12	2.51	0.61	4.66	0.86	2.56	0.35	2.16	0.27
DM17-35-3A-g3	0.01	0.01	b.d.l.	0.06	0.45	0.11	1.79	0.46	3.42	0.73	2.21	0.29	2.09	0.27
DM17-35-3A-g4	b.d.l.	b.d.l.	b.d.l.	0.04	0.53	0.12	3.18	0.90	7.36	1.49	4.90	0.72	4.68	0.62
DM17-35-3A-g5	0.01	0.01	b.d.l.	0.03	0.29	0.09	3.06	0.88	7.48	1.77	5.78	0.87	5.75	0.86
DM17-35-3A-g6	b.d.l.	b.d.l.	b.d.l.	0.04	0.25	0.10	2.68	0.85	6.99	1.67	5.57	0.79	5.57	0.90
DM17-35-3A-g7	b.d.l.	0.01	b.d.l.	0.02	0.30	0.10	3.57	1.14	9.56	2.25	7.14	1.06	7.05	1.02
DM17-35-3A-g8	b.d.l.	b.d.l.	b.d.l.	0.02	0.30	0.10	3.00	0.85	7.69	1.70	5.49	0.79	6.47	0.95
DM17-35-3A-g9	b.d.l.	0.01	b.d.l.	0.03	0.48	0.12	2.60	0.68	5.25	1.18	3.63	0.58	3.91	0.54
DM17-35-3A-g10	0.09	0.07	0.01	0.06	0.25	0.05	1.80	0.55	4.94	1.32	4.43	0.74	6.06	1.02
DM17-35-3A-g11	0.01	0.02	b.d.l.	0.02	0.44	0.12	3.83	1.23	10.61	2.54	8.30	1.18	8.06	1.12
DM17-35-3A-g12	b.d.l.	b.d.l.	b.d.l.	0.01	0.32	0.09	2.38	0.66	5.99	1.55	5.54	0.77	6.24	0.91
DM17-35-1A-g1	0.01	0.02	b.d.l.	0.02	0.23	0.10	3.99	1.56	13.95	3.51	11.77	1.69	12.12	1.87
DM17-35-1A-g2	b.d.l.	b.d.l.	b.d.l.	b.d.l.	b.d.l.	b.d.l.	b.d.l.	b.d.l.	b.d.l.	b.d.l.	b.d.l.	b.d.l.	b.d.l.	b.d.l.
DM17-35-1A-g3	b.d.l.	b.d.l.	b.d.l.	0.04	0.43	0.17	7.46	2.50	19.80	4.43	13.38	1.76	11.40	1.56
DM17-35-1A-g4	0.01	0.02	b.d.l.	0.02	0.20	0.09	4.47	1.49	13.31	3.29	10.82	1.53	10.61	1.67
DM17-35-1A-g5	b.d.l.	b.d.l.	b.d.l.	b.d.l.	b.d.l.	b.d.l.	b.d.l.	b.d.l.	b.d.l.	b.d.l.	b.d.l.	b.d.l.	b.d.l.	b.d.l.
DM17-35-1A-g6	b.d.l.	b.d.l.	b.d.l.	0.02	0.24	0.10	3.85	1.38	12.04	2.67	8.26	1.14	7.89	1.14
DM17-35-1A-g7	0.05	0.06	0.01	0.06	0.31	0.12	4.45	1.63	14.52	3.42	10.53	1.50	10.13	1.45
DM17-35-1A-g8	b.d.l.	b.d.l.	b.d.l.	0.02	0.32	0.16	5.68	1.97	17.18	3.95	12.67	1.75	11.94	1.72
DM17-35-1A-g9	b.d.l.	b.d.l.	b.d.l.	b.d.l.	b.d.l.	b.d.l.	b.d.l.	b.d.l.	b.d.l.	b.d.l.	b.d.l.	b.d.l.	b.d.l.	b.d.l.
DM17-35-1A-g10	0.03	0.02	b.d.l.	0.03	0.29	0.13	5.39	1.72	14.49	3.19	9.21	1.28	8.53	1.23
DM17-35-1A-g11	0.02	0.06	0.01	0.05	0.21	0.08	3.23	1.14	11.28	2.79	9.39	1.31	9.06	1.31
DM17-35-1A-g12	b.d.l.	b.d.l.	b.d.l.	0.04	0.41	0.16	6.32	2.11	18.79	4.26	13.42	1.82	12.35	1.71

Table A.2.2: REE compositional transect in garnet megablast DMG4-6

S. (notes)	La (ppm)	Ce (ppm)	Pr (ppm)	Nd (ppm)	Sm (ppm)	Eu (ppm)	Gd (ppm)	Tb (ppm)	Dy (ppm)	Ho (ppm)	Er (ppm)	Tm (ppm)	Yb (ppm)	Lu (ppm)
DMG4-6-g1	b.d.l.	b.d.l.	b.d.l.	0.04	0.47	0.22	8.12	3.81	37.68	8.73	27.10	3.88	26.25	3.62
DMG4-6-g2	b.d.l.	b.d.l.	b.d.l.	0.01	0.38	0.17	5.68	2.44	22.43	5.19	16.09	2.31	15.13	2.07
DMG4-6-g3	b.d.l.	b.d.l.	b.d.l.	0.01	0.37	0.14	4.22	1.82	17.16	3.90	11.86	1.66	10.78	1.38
DMG4-6-g4	b.d.l.	b.d.l.	b.d.l.	b.d.l.	0.38	0.18	5.56	2.21	20.10	4.72	14.63	2.07	13.48	1.83
DMG4-6-g5	b.d.l.	b.d.l.	b.d.l.	0.04	0.38	0.20	6.54	2.57	25.09	5.49	17.52	2.35	15.46	2.12
DMG4-6-g6	b.d.l.	b.d.l.	b.d.l.	0.03	0.24	0.14	4.70	1.86	17.63	3.83	11.97	1.63	10.66	1.43
DMG4-6-g7	b.d.l.	b.d.l.	b.d.l.	0.02	0.38	0.16	4.80	1.98	18.79	4.13	11.82	1.58	9.87	1.23
DMG4-6-g8	b.d.l.	b.d.l.	b.d.l.	0.03	0.32	0.12	4.00	1.71	16.14	3.60	10.68	1.37	8.33	1.11
DMG4-6-g9	b.d.l.	0.00	b.d.l.	0.01	0.34	0.16	5.27	2.22	20.01	4.40	12.59	1.62	10.14	1.20
DMG4-6-g10	b.d.l.	b.d.l.	b.d.l.	0.02	0.32	0.17	5.26	2.18	20.09	4.47	12.84	1.70	10.63	1.37
DMG4-6-g11	b.d.l.	b.d.l.	b.d.l.	b.d.l.	0.40	0.18	6.50	2.75	25.49	5.39	15.21	1.82	10.54	1.26
DMG4-6-g12	b.d.l.	b.d.l.	b.d.l.	b.d.l.	0.27	0.14	4.61	2.18	19.51	4.14	11.18	1.37	7.78	0.90
DMG4-6-A-g13	b.d.l.	b.d.l.	b.d.l.	0.02	0.39	0.18	7.18	3.41	32.76	7.35	22.18	2.83	18.48	2.39
DMG4-6-A-g14	b.d.l.	b.d.l.	b.d.l.	0.01	0.26	0.13	4.58	1.87	17.01	3.81	10.89	1.40	8.93	1.08
DMG4-6-A-g15	0.01	0.01	b.d.l.	0.04	0.29	0.14	4.66	1.98	19.26	4.56	14.64	1.92	12.94	1.74
DMG4-6-B-g1	b.d.l.	b.d.l.	b.d.l.	b.d.l.	0.48	0.25	8.49	4.03	35.19	7.24	19.64	2.50	14.29	1.75
DMG4-6-B-g2	0.01	0.02	b.d.l.	0.04	0.32	0.17	6.22	2.80	24.16	4.76	12.36	1.47	8.68	1.02
DMG4-6-B-g3	0.09	0.07	0.02	0.10	0.43	0.19	7.15	3.22	28.28	5.76	15.13	1.86	10.57	1.32
DMG4-6-B-g4	0.10	0.08	0.02	0.09	0.44	0.20	6.55	2.97	24.54	4.64	11.64	1.41	8.25	0.99
DMG4-6-B-g5	b.d.l.	b.d.l.	b.d.l.	b.d.l.	0.36	0.18	7.31	3.00	25.78	4.99	13.43	1.64	10.40	1.30
DMG4-6-B-g6	b.d.l.	b.d.l.	b.d.l.	b.d.l.	0.20	0.09	3.67	1.73	14.67	2.71	6.61	0.81	4.74	0.56
DMG4-6-B-g7	b.d.l.	b.d.l.	b.d.l.	0.01	0.20	0.13	4.39	1.81	14.19	2.40	6.48	0.75	5.04	0.69
DMG4-6-B-g8	b.d.l.	b.d.l.	b.d.l.	0.02	0.33	0.16	5.60	2.20	15.79	2.83	7.33	0.88	5.69	0.71
DMG4-6-B-g9	b.d.l.	b.d.l.	b.d.l.	b.d.l.	0.41	0.21	6.64	2.57	19.70	3.72	10.30	1.38	8.25	1.14
DMG4-6-B-g10	b.d.l.	b.d.l.	b.d.l.	0.02	0.37	0.16	6.31	2.42	18.52	3.70	9.81	1.29	8.43	1.12
DMG4-6-B-g11	b.d.l.	b.d.l.	b.d.l.	0.02	0.45	0.21	7.05	2.86	20.95	4.13	11.08	1.40	9.10	1.25
DMG4-6-B-g12	b.d.l.	b.d.l.	b.d.l.	0.02	0.37	0.18	6.51	2.76	22.90	4.62	12.77	1.67	10.31	1.38
DMG4-6-B-g13	b.d.l.	b.d.l.	b.d.l.	0.02	0.30	0.14	4.41	1.51	10.93	2.05	5.62	0.69	4.04	0.55
DMG4-6-B-g14	b.d.l.	b.d.l.	b.d.l.	0.02	0.42	0.22	7.22	2.57	19.34	3.67	9.93	1.30	7.70	1.09
DMG4-6-B-g15	0.01	0.01	b.d.l.	0.03	0.38	0.16	6.32	2.77	23.74	4.66	12.25	1.42	8.16	0.99
DMG4-6-B-g16	b.d.l.	0.02	b.d.l.	0.01	0.29	0.12	4.10	1.58	10.99	2.03	4.94	0.64	3.75	0.49
DMG4-6-B-g17	b.d.l.	b.d.l.	b.d.l.	0.03	0.31	0.14	5.75	2.27	17.58	3.38	8.71	1.03	6.07	0.79
DMG4-6-B-g18	b.d.l.	b.d.l.	b.d.l.	0.01	0.24	0.11	3.08	1.23	8.52	1.54	4.34	0.57	3.59	0.50
DMG4-6-B-g19	b.d.l.	b.d.l.	b.d.l.	0.01	0.35	0.15	5.74	2.37	18.29	3.40	9.52	1.30	7.78	1.04
DMG4-6-B-g20	b.d.l.	b.d.l.	b.d.l.	0.03	0.47	0.21	7.09	2.65	19.46	3.65	10.25	1.33	8.50	1.16

Table A.2.3: REE compositional transect in garnet megablast DM17-13

S. (notes)	La (ppm)	Ce (ppm)	Pr (ppm)	Nd (ppm)	Sm (ppm)	Eu (ppm)	Gd (ppm)	Tb (ppm)	Dy (ppm)	Ho (ppm)	Er (ppm)	Tm (ppm)	Yb (ppm)	Lu (ppm)
DM17-13-A-g1	0.00	0.00	0.00	0.03	0.90	0.50	17.38	7.93	87.90	25.48	97.40	15.91	115.00	16.00
DM17-13-A-g2	0.00	0.00	0.00	0.03	0.62	0.35	13.15	5.62	62.60	18.37	73.90	12.56	95.70	14.07
DM17-13-A-g4	0.01	0.02	0.01	0.06	0.86	0.47	17.66	7.52	79.40	21.95	83.10	13.44	98.00	14.32
DM17-13-A-g5	0.00	0.00	0.00	0.03	1.10	0.68	25.36	10.56	110.85	30.53	117.40	19.62	152.00	23.12
DM17-13-A-g6	0.00	0.00	0.00	0.02	0.94	0.47	17.97	7.50	78.60	21.99	85.80	15.03	116.40	17.88
DM17-13-A-g7	0.00	0.00	0.00	0.06	1.32	0.69	27.09	11.43	119.70	32.91	126.70	21.29	164.30	24.27
DM17-13-A-g8	0.00	0.00	0.00	0.07	1.46	0.83	31.20	12.60	133.00	36.60	140.50	24.10	185.90	28.59
DM17-13-A-g9	0.00	0.00	0.00	0.05	1.20	0.67	25.82	11.54	139.70	43.88	180.00	31.48	252.80	39.97
DM17-13-A-g10	0.00	0.00	0.00	0.05	1.15	0.66	25.58	11.13	117.10	31.51	110.70	16.94	117.70	15.88
DM17-13-B-g1	0.00	0.00	0.00	0.02	0.89	0.62	23.87	10.89	105.70	26.34	86.77	12.53	86.74	11.92
DM17-13-B-g2	0.00	0.00	0.00	0.04	0.85	0.55	21.86	9.46	85.40	20.62	65.85	9.42	65.32	9.03
DM17-13-B-g3	0.00	0.00	0.00	0.02	0.67	0.41	16.72	7.34	67.96	15.96	50.10	6.79	44.22	5.73
DM17-13-B-g4	0.00	0.00	0.00	0.04	0.90	0.58	21.06	8.91	82.58	19.63	63.23	8.80	58.89	7.91
DM17-13-B-g5	0.00	0.00	0.00	0.04	0.75	0.42	15.23	6.42	58.60	13.15	41.62	5.73	39.33	5.51
DM17-13-B-g7	0.00	0.01	0.00	0.03	0.78	0.41	13.47	4.51	36.28	7.77	23.52	3.08	19.81	2.64
DM17-13-B-g8	0.00	0.00	0.00	0.05	1.23	0.60	19.15	6.36	51.23	11.22	35.47	5.03	33.48	4.54
DM17-13-B-g9	0.00	0.00	0.00	0.06	1.18	0.65	21.59	7.39	62.11	13.76	44.24	6.30	41.64	5.53
DM17-13-B-g10	0.00	0.00	0.00	0.06	1.06	0.56	19.26	7.11	60.91	13.93	44.64	6.44	43.99	5.92
DM17-13-B-g11	0.00	0.00	0.00	0.07	1.09	0.57	16.93	5.69	48.06	12.30	44.40	7.08	51.71	7.58
DM17-13-B-g13	0.00	0.00	0.00	0.07	1.31	0.63	20.55	6.95	56.61	12.29	39.80	5.43	37.07	4.84
DM17-13-C-g1	0.00	0.00	0.00	0.02	0.79	0.49	16.06	6.21	54.30	13.64	49.05	7.90	57.28	7.86
DM17-13-C-g2	0.00	0.00	0.00	0.04	0.63	0.40	12.13	4.57	40.03	10.21	36.95	6.04	41.68	5.73
DM17-13-C-g3	0.00	0.00	0.00	0.03	0.77	0.43	14.63	5.62	54.71	13.99	52.56	8.54	62.11	8.84
DM17-13-C-g4	0.00	0.00	0.00	0.03	0.59	0.31	9.59	4.12	40.20	10.38	39.18	6.37	46.09	6.99
DM17-13-C-g5	0.00	0.00	0.00	0.03	0.70	0.33	10.34	3.80	36.09	9.14	34.43	5.34	37.55	5.40
DM17-13-C-g6	0.00	0.00	0.00	0.04	0.73	0.39	12.93	4.67	41.47	10.08	34.84	5.22	34.77	4.64
DM17-13-C-g7	0.00	0.00	0.00	0.04	0.64	0.33	9.20	4.01	36.20	8.31	28.54	4.14	28.07	3.86
DM17-13-C-g8	0.00	0.00	0.00	0.05	0.90	0.44	13.41	4.69	37.77	8.50	28.02	4.03	27.70	3.68
DM17-13-C-g9	0.00	0.00	0.00	0.04	0.78	0.45	14.28	5.08	42.96	9.35	29.03	4.07	25.93	3.29
DM17-13-C-g10	0.00	0.00	0.00	0.03	0.94	0.46	14.20	5.11	41.80	9.10	28.60	4.05	26.84	3.51
DM17-13-C-g11	0.00	0.00	0.00	0.03	0.66	0.33	10.86	4.48	38.91	8.57	28.11	4.06	26.37	3.59
DM17-13-C-g12	0.00	0.00	0.00	0.05	0.88	0.49	15.50	5.46	47.22	10.32	32.75	4.52	28.76	3.64
DM17-13-C-g13	0.00	0.00	0.00	0.06	0.70	0.33	11.72	4.96	46.20	10.40	35.50	5.29	38.17	5.38
DM17-13-C-g14	0.00	0.00	0.00	0.03	0.53	0.29	8.38	3.35	30.17	6.69	22.70	3.26	22.08	2.95
DM17-13-C-g15	0.00	0.00	0.00	0.02	0.55	0.35	9.96	3.44	29.84	6.93	24.47	3.56	24.86	3.36
DM17-13-C-g16	0.00	0.00	0.00	0.04	0.84	0.45	14.30	5.10	43.82	10.56	35.75	5.18	35.94	4.66
DM17-13-C-g17	0.00	0.00	0.00	0.05	0.96	0.50	16.18	5.64	46.75	9.83	30.86	4.35	28.75	3.74
DM17-13-C-g18	0.00	0.00	0.00	0.00	0.56	0.31	9.96	4.60	44.96	10.02	31.99	4.73	33.46	4.69
DM17-13-C-g19	0.00	0.00	0.00	0.03	0.67	0.39	15.86	7.85	81.20	18.93	56.40	7.31	43.75	5.57
DM17-13-C-g20	0.00	0.00	0.00	0.04	0.55	0.27	10.49	5.47	61.70	15.32	45.32	5.47	30.72	3.56
DM17-13-C-g21	0.04	0.09	0.01	0.12	0.89	0.37	10.64	3.35	27.50	5.94	16.38	1.81	10.32	1.18
DM17-13-C-g22	0.00	0.00	0.00	0.06	0.64	0.30	9.23	3.38	29.85	7.50	26.54	4.13	29.96	4.37
DM17-13-C-g23	0.02	0.05	0.01	0.08	0.47	0.26	8.15	3.34	35.49	11.33	47.15	7.96	60.68	9.01

Table A.2.4: minor elements from garnet megablast DM17-35

S. (note)	P (ppm)	Ti (ppm)	V (ppm)	Cr (ppm)	Mn (ppm)	Y (ppm)	Zr (ppm)	Hf (ppm)	Ca (ppm)
DM17-35-5A-g4	667.7	410	13.07	9.14	92.1	97.82	4.21	0.053	3869
DM17-35-5A-g5	618.2	30.6	10.1	9.54	85.4	73.35	3.56	0.074	3361
DM17-35-5A-g3	695.7	49.3	12.24	10.24	95.28	88.49	4.49	0.043	3624
DM17-35-5A-g2	693.2	50.3	14.91	7.15	88.9	116.58	3.99	0.038	3740
DM17-35-5A-g7	381.1	29.1	7.58	13.22	70.03	56.96	2.18	0.022	2980
DM17-35-5A-g1	745.4	80.5	15.81	6.66	115.7	149.03	4.62	0.063	4163
DM17-35-5A-g8	513	12.09	4.02	7.57	181.8	55.1	1.95	0.025	3757
DM17-35-5A-g11	699.6	32.8	9.6	9.67	113.76	94.85	4	0.058	3347
DM17-35-3A-g1	715.6	62.4	14.84	14.22	130	33.83	8.11	0.087	2765
DM17-35-3A-g2	764.1	73.8	19.18	10.86	66.41	27.46	2.54	0.012	2772
DM17-35-3A-g10	760.9	29	8.22	13.1	209.9	39.62	6.57	0.098	3187
DM17-35-3A-g3	667	73.7	11.77	9.53	88.7	22.6	6.04	0.07	2432
DM17-35-3A-g9	589.6	69.1	13.37	12.77	84.97	35.92	5.73	0.067	2533
DM17-35-3A-g11	579.3	50.9	12.6	9.65	91.8	74.36	4.87	0.075	3096
DM17-35-3A-g4	562.8	61.9	13.42	13.79	81.48	47.61	6.26	0.041	2671
DM17-35-3A-g6	546	34.1	9.39	11.01	99.57	49.94	3.63	0.059	2685
DM17-35-3A-g5	519.5	39.3	10.41	10.26	69.95	52.57	3.34	0.048	2652
DM17-35-3A-g7	661.3	31.5	9.47	10.22	91.93	64.56	4.08	0.048	3327
DM17-35-1A-g1	629.9	30	8.58	9.77	111.12	91.55	3.24	0.047	3176
DM17-35-1A-g3	726.6	48.8	13.73	9.63	75.36	123.53	4.17	0.071	3796
DM17-35-1A-g4	684.8	26.7	8.39	10.55	118.02	85.47	3.46	0.026	3307
DM17-35-1A-g7	611.5	36.9	10.53	11.03	129.9	92.81	3.13	0.042	3272
DM17-35-1A-g11	591.1	20.6	5.23	6.81	178.7	73.71	2.72	0.033	3373
DM17-35-1A-g6	502.1	49	9.36	11.89	101.69	75.9	2.51	0.035	3123
DM17-35-1A-g8	632.6	43.6	11.81	12.31	87	111.48	3.28	0.039	3626
DM17-35-1A-g10	809	43.9	12.55	11.6	80.7	87.6	4.99	0.126	3333

Table A.2.5: minor elements from garnet megablast DMG4-6

S. (notes)	P (ppm)	Ti (ppm)	V (ppm)	Cr (ppm)	Mn (ppm)	Y (ppm)	Zr (ppm)	Hf (ppm)	Ca (ppm)
DMG4-6-g5	610.00	84.50	5.66	9.80	135.70	161.80	3.22	0.03	6820.00
DMG4-6-g6	435.40	59.30	6.44	5.66	135.80	115.60	1.49	0.02	6100.00
DMG4-6-g7	513.00	91.10	5.09	18.40	135.30	122.31	2.26	0.03	6290.00
DMG4-6-g8	410.80	49.90	6.07	4.17	136.27	105.01	1.52	0.03	5890.00
DMG4-6-g9	469.10	64.40	4.08	5.42	135.80	130.74	2.13	0.04	6160.00
DMG4-6-g10	470.00	65.30	4.93	5.10	136.87	130.80	1.99	0.02	6130.00
DMG4-6-g11	718.30	71.30	3.78	7.37	137.60	158.70	4.35	0.08	6130.00
DMG4-6-g12	392.20	50.70	3.28	3.19	143.30	125.77	1.25	0.03	5660.00
DMG4-6-A-g13	700.60	48.70	5.85	12.14	124.20	208.20	3.98	0.04	6050.00
DMG4-6-A-g14	433.40	45.60	4.02	3.64	132.70	113.50	1.62	b.d.l.	5960.00
DMG4-6-A-g15	521.00	134.00	6.52	9.17	131.80	129.90	3.51	0.03	5770.00
DMG4-6-B-g1	682.00	410.00	7.55	8.19	153.00	214.60	3.90	0.06	6900.00
DMG4-6-B-g2	719.70	50.50	9.01	8.75	142.10	139.70	3.80	0.07	6040.00
DMG4-6-B-g3	669.90	64.00	9.41	10.32	144.90	167.80	3.16	0.04	6492.00
DMG4-6-B-g4	702.90	86.20	8.17	8.92	137.90	140.80	3.86	0.05	6450.00
DMG4-6-B-g5	684.50	98.60	7.25	9.81	140.30	149.90	3.56	0.04	6010.00
DMG4-6-B-g6	398.80	43.00	6.40	2.44	133.29	80.76	0.88	b.d.l.	4800.00
DMG4-6-B-g7	512.90	39.10	7.83	4.02	115.05	75.96	1.62	0.03	4990.00
DMG4-6-B-g8	633.10	85.60	6.35	6.88	106.82	85.03	2.91	0.03	5260.00
DMG4-6-B-g9	727.00	94.70	8.67	10.26	104.35	109.70	3.36	0.04	5540.00
DMG4-6-B-g10	705.70	64.90	11.03	9.28	105.58	104.60	3.04	0.03	5350.00
DMG4-6-B-g11	743.70	91.70	10.20	12.18	107.80	121.51	3.56	0.03	5470.00
DMG4-6-B-g12	738.50	81.60	12.17	11.12	110.90	131.86	3.79	0.04	5290.00
DMG4-6-B-g13	571.30	60.90	7.17	4.06	97.20	61.24	2.45	0.04	4560.00
DMG4-6-B-g14	716.60	122.50	8.73	11.55	95.40	107.71	3.97	0.03	5240.00
DMG4-6-B-g16	509.50	41.70	5.15	10.27	77.83	60.47	2.17	0.01	4480.00
DMG4-6-B-g17	675.90	58.20	7.39	7.31	97.52	98.68	3.46	0.03	5060.00
DMG4-6-B-g18	376.00	46.00	6.20	3.22	95.50	47.26	1.19	0.03	3910.00

Table A.2.6: minor elements from garnet megablast DM17-13

sample (notes)	P (ppm)	Ti (ppm)	V (ppm)	Cr (ppm)	Mn (ppm)	Y (ppm)	Zr (ppm)	Hf (ppm)	Ca (ppm)
DM17-13-A-g1	356	81.9	12.06	2.83	414.8	737.6	1.325	b.d.l.	4534
DM17-13-A-g2	239.1	68.7	9.15	2.69	406.3	539.6	0.675	b.d.l.	4028
DM17-13-A-g4	325.1	91.6	10.59	3.6	378.2	639.6	1.088	b.d.l.	4410
DM17-13-A-g5	440.1	67.3	15.67	5.96	393.6	893.4	2.08	0.019	5096
DM17-13-A-g6	329.8	82.2	10.91	4.13	393.6	650.8	1.15	b.d.l.	4459
DM17-13-A-g7	442.5	95.9	15.61	3.97	388.9	963.9	2.12	0.025	5306
DM17-13-A-g8	479.9	147.7	14.57	6.51	363.4	1065.2	2.44	0.028	5372
DM17-13-A-g9	477.8	71.4	11.37	6.88	245.7	1247.6	2.71	0.012	5192
DM17-13-A-g10	527.8	145.2	15.84	5.3	402.6	937.2	2.95	b.d.l.	5916
DM17-13-B-g1	578.6	143.9	15.48	8.55	326.2	805.5	3.15	0.024	6641
DM17-13-B-g2	646	119.3	14.82	8.21	278.9	627.1	3.21	b.d.l.	7046
DM17-13-B-g3	655.2	b.d.l.	26.7	15	286.3	491.5	3.85	0.071	6195
DM17-13-B-g4	550.9	82.8	13.46	9.27	250	598.5	2.87	0.028	5754
DM17-13-B-g5	702.7	104.7	14.69	7.74	242.5	402.5	b.d.l.	0.0085	7328
DM17-13-B-g7	338.4	65.4	11.37	11.07	212.1	241.8	3.52	0.036	8289
DM17-13-B-g8	451.9	145.1	16.12	8.79	234.4	351.9	5.78	0.079	8971
DM17-13-B-g9	443.7	151	16.4	10.65	260.1	429.1	4.84	0.073	9164
DM17-13-B-g10	467.8	148.7	16.66	10.81	246.3	427.1	4.73	0.065	9163
DM17-13-B-g11	452.6	111.5	15.03	13.31	228.7	367.4	4.75	0.083	9205
DM17-13-C-g13	470	87.4	12.15	6.18	218.6	327.8	4.24	0.096	9450
DM17-13-C-g14	383	74.1	10.45	14.39	279.8	206.1	3.03	0.061	8683
DM17-13-C-g15	432.2	91.3	11.07	5.46	251.2	213.6	3.64	0.054	6395
DM17-13-C-g16	427.5	98.3	11.68	9.41	263.6	323.4	3.87	0.085	5850
DM17-13-C-g7	406	112	9.33	8.03	271.2	255	5.9	0.166	8179
DM17-13-C-g6	416.7	108.2	9.93	8.69	268.5	310.5	3.57	0.073	5732
DM17-13-C-g17	454.7	98.2	10.86	7.62	215.7	310.8	4.6	0.101	3979
DM17-13-C-g18	649.8	96.3	10.52	7.41	200.5	306.7	6.16	0.108	6990
DM17-13-C-g19	456.7	92.5	6.84	7.23	84.57	587.9	3.09	0.043	1602
DM17-13-C-g20	537.7	108	8.26	4.34	22.77	469.2	5.46	0.096	744
DM17-13-C-g21	575.7	155.3	11.27	7.4	15.36	170.7	8.19	0.153	2080
DM17-13-C-g22	378.3	108.4	5.54	4.57	38.87	216.8	4.36	0.076	1366
DM17-13-C-g23	305	66.3	5.33	10.51	30.08	324.6	2.82	0.081	1262

APPENDIX A3

LA-ICP-MS ANALYSIS

RUTILE

Table A.3.1: trace elements composition in rutile inclusions from garnet megablast DM17-35 (part 1)

S. (notes)	Sc (ppm)	Zn (ppm)	Rb (ppm)	Y (ppm)	Zr (ppm)	Nb (ppm)	Mo (ppm)	Sn (ppm)	Sb (ppm)	Yb (ppm)	Hf (ppm)
DM17_35_1a_p1	4.32	4.12	b.d.l.	0.21	178.51	3987.00	13.25	591.40	15.33	0.01	9.25
DM17_35_1a_p2	4.70	3.48	b.d.l.	0.25	178.60	4066.00	13.02	594.00	17.77	0.01	8.92
DM17_35_1a_p3	9.00	4.15	1.19	4.80	176.30	4094.00	11.35	588.60	11.64	1.27	8.99
DM17_35_1a_p4	2.80	3.23	b.d.l.	0.11	244.20	2706.00	12.62	347.50	4.01	b.d.l.	5.66
DM17_35_1a_p5	5.84	3.46	b.d.l.	0.15	219.20	3631.00	12.96	566.10	7.79	b.d.l.	8.71
DM17_35_1a_p6	1.73	4.80	b.d.l.	0.13	233.60	2938.00	13.26	465.50	5.31	b.d.l.	9.48
DM17_35_1a_p7	2.48	3.23	b.d.l.	0.16	188.50	3858.00	13.21	584.80	13.91	b.d.l.	9.07
DM17_35_1a_p8	1.83	3.19	b.d.l.	0.13	201.50	3829.00	13.61	626.90	6.48	b.d.l.	10.91
DM17_35_1a_p9	1.98	6.10	0.02	0.16	221.70	345b.d.l.	13.78	630.80	11.75	b.d.l.	10.91
DM17_35_1a_p10	3.06	4.49	0.03	0.14	216.60	3839.00	13.14	607.00	6.42	b.d.l.	9.83
DM17_35_1a_p11	4.25	3.96	b.d.l.	0.14	218.60	4254.00	12.19	870.60	6.35	b.d.l.	10.04
DM17_35_1a_p12	5.41	3.17	b.d.l.	0.13	195.60	4169.00	12.43	726.70	7.38	b.d.l.	9.74
DM17_35_1a_p13	1.61	3.23	b.d.l.	0.13	255.70	3658.00	13.36	604.90	4.35	b.d.l.	8.00
DM17_35_1a_p14	2.37	3.40	b.d.l.	0.17	218.50	281b.d.l.	13.96	580.40	14.07	b.d.l.	10.23
DM17_35_1a_p15	2.94	3.44	0.56	1.62	217.30	2833.00	13.76	584.10	14.87	0.27	10.21
DM17_35_1a_p16	2.18	3.19	b.d.l.	0.12	291.60	4394.00	12.95	846.80	2.40	b.d.l.	11.95
DM17_35_1a_p17	8.04	2.97	b.d.l.	0.16	185.40	4133.00	12.47	624.10	8.53	0.01	9.96
DM17_35_1a_p18	4.12	3.28	b.d.l.	0.13	196.00	3601.00	13.78	590.70	6.33	b.d.l.	10.77
DM17_35_1a_p19	5.61	3.17	b.d.l.	0.14	178.30	3893.00	13.18	591.50	11.81	b.d.l.	9.53
DM17_35_1a_p20	3.80	3.17	1.00	0.53	181.80	4065.00	12.74	583.50	17.89	0.02	8.74
DM17_35_1a_p21	2.27	2.75	b.d.l.	0.12	234.70	3312.00	13.05	600.10	5.53	b.d.l.	9.28
DM17-35-3A-p1	2.29	2.94	b.d.l.	0.12	278.00	5339.00	11.55	149b.d.l.	4.29	b.d.l.	10.37
DM17-35-3A-p3	8.88	2.25	b.d.l.	0.14	167.89	4085.00	12.33	582.00	19.65	b.d.l.	7.77
DM17-35-3A-p4	6.79	2.33	b.d.l.	0.12	181.50	3877.00	13.44	550.30	7.49	b.d.l.	10.22
DM17-35-3A-p5	7.54	2.24	b.d.l.	0.12	209.10	4642.00	12.89	885.00	6.67	b.d.l.	11.06
DM17-35-3A-p10	7.79	2.05	b.d.l.	0.12	187.80	353b.d.l.	13.65	548.80	8.87	b.d.l.	10.36

Table A.3.2: transition metals and trace elements composition in rutile inclusions from garnet megablast DM17-35 (part 1)

sample name (notes)	Ta (ppm)	W (ppm)	Pb (ppm)	Th (ppm)	U (ppm)	Al (ppm)	Si (ppm)	P (ppm)	V (ppm)	Cr (ppm)	Mn (ppm)	Fe (ppm)	Co (ppm)	Ni (ppm)
DM17_35_1a_p1	296.90	213.90	2.38	0.09	3.39	385.70	4023.00	b.d.l.	1494.00	189.80	b.d.l.	1159.00	0.01	8.10
DM17_35_1a_p2	397.20	248.20	0.23	0.18	3.53	380.40	3488.00	b.d.l.	1547.00	181.10	b.d.l.	118b.d.l.	b.d.l.	7.59
DM17_35_1a_p3	751.00	265.50	17.80	0.06	3.23	930b.d.l.	2030b.d.l.	28.20	1505.10	166.20	11.80	356b.d.l.	0.20	6.86
DM17_35_1a_p4	224.10	156.40	0.06	b.d.l.	2.08	598.00	3751.00	b.d.l.	1235.00	147.50	b.d.l.	1044.00	b.d.l.	7.40
DM17_35_1a_p5	245.40	184.50	0.22	b.d.l.	3.01	362.90	4347.00	b.d.l.	1304.00	153.40	b.d.l.	1346.00	0.01	7.30
DM17_35_1a_p6	388.00	180.40	0.27	b.d.l.	2.06	559.00	3599.00	b.d.l.	1482.00	143.40	b.d.l.	1054.00	0.01	7.13
DM17_35_1a_p7	242.40	216.00	0.07	0.03	2.70	343.10	3863.00	b.d.l.	1567.00	155.10	b.d.l.	131b.d.l.	0.01	6.15
DM17_35_1a_p8	303.10	214.70	0.03	0.01	2.13	36b.d.l.	3934.00	b.d.l.	1526.00	174.40	b.d.l.	1229.20	0.01	7.31
DM17_35_1a_p9	211.70	265.10	0.47	b.d.l.	1.97	738.00	544b.d.l.	b.d.l.	1784.00	144.50	0.58	101b.d.l.	0.03	8.43
DM17_35_1a_p10	208.90	176.80	0.07	b.d.l.	2.10	483.00	3598.00	b.d.l.	133b.d.l.	152.00	b.d.l.	1408.00	0.01	7.12
DM17_35_1a_p11	476.90	182.40	0.10	b.d.l.	2.43	361.00	420b.d.l.	b.d.l.	1150.40	176.80	b.d.l.	1875.00	0.09	7.03
DM17_35_1a_p12	485.40	187.60	0.06	0.01	2.60	294.20	402b.d.l.	b.d.l.	1129.20	158.00	b.d.l.	1808.00	0.02	6.58
DM17_35_1a_p13	216.30	153.40	0.05	b.d.l.	1.95	369.00	435b.d.l.	b.d.l.	1199.30	156.50	0.37	1437.00	0.02	7.37
DM17_35_1a_p14	195.00	216.10	0.05	0.02	2.25	1031.00	3991.00	b.d.l.	1685.00	157.90	b.d.l.	1011.70	0.01	6.42
DM17_35_1a_p15	248.80	229.70	6.70	0.02	2.35	272b.d.l.	870b.d.l.	16.90	172b.d.l.	157.60	1.20	153b.d.l.	0.05	6.66
DM17_35_1a_p16	485.10	161.90	0.04	b.d.l.	1.93	398.30	350b.d.l.	b.d.l.	1307.00	173.20	b.d.l.	1834.00	0.02	6.90
DM17_35_1a_p17	448.20	208.60	1.01	0.01	3.23	351.00	4656.00	7.40	1052.40	155.60	0.76	1772.00	0.01	6.31
DM17_35_1a_p18	201.00	181.80	0.08	b.d.l.	3.27	215.50	3699.00	b.d.l.	1080.60	160.60	b.d.l.	1757.00	0.02	8.30
DM17_35_1a_p19	224.70	219.50	0.08	0.01	3.59	213.40	3576.00	b.d.l.	986.90	159.90	b.d.l.	1889.00	0.01	6.41
DM17_35_1a_p20	354.20	249.90	11.60	2.18	5.00	1089.00	432b.d.l.	b.d.l.	1412.00	167.40	b.d.l.	1107.90	0.17	6.64
DM17_35_1a_p21	224.30	173.70	0.05	b.d.l.	2.28	1155.00	3746.00	b.d.l.	1849.00	146.80	b.d.l.	740.10	0.01	6.09
DM17-35-3A-p1	510.40	171.20	0.06	b.d.l.	3.23	527.10	417b.d.l.	b.d.l.	1377.00	170.10	0.54	2029.00	0.02	6.42
DM17-35-3A-p3	337.50	264.00	0.31	0.11	2.31	463.50	3873.00	b.d.l.	1272.40	151.80	b.d.l.	1098.20	0.01	6.34
DM17-35-3A-p4	255.10	231.40	0.05	0.01	3.28	334.70	3835.00	b.d.l.	1156.10	192.30	b.d.l.	1355.00	0.01	6.27
DM17-35-3A-p5	656.50	179.20	0.05	b.d.l.	2.40	404.90	3876.00	b.d.l.	1252.00	149.80	b.d.l.	1463.00	0.01	5.59
DM17-35-3A-p10	147.00	201.50	0.06	b.d.l.	3.02	425.30	3883.00	b.d.l.	1200.20	161.10	b.d.l.	1060.40	0.01	5.70

Table A.3.3: trace elements composition in rutile inclusions from garnet megablast DM17-35 (part 2)

S (notes)	Sc (ppm)	Zn (ppm)	Rb (ppm)	Y (ppm)	Zr (ppm)	Nb (ppm)	Mo (ppm)	Sn (ppm)	Sb (ppm)	Yb (ppm)	Hf (ppm)
DM17-35-3A-p23	2.16	2.27	b.d.l.	0.12	181.80	3002.00	13.49	592.50	12.99	b.d.l.	9.43
DM17-35-3A-p21	3.09	2.11	b.d.l.	0.11	245.10	3068.00	14.31	453.30	7.72	b.d.l.	10.80
DM17-35-3A-p22	1.29	2.32	b.d.l.	0.11	246.10	2771.00	14.65	483.70	5.35	b.d.l.	10.84
DM17-35-3A-p6	8.55	3.33	b.d.l.	0.13	207.70	4037.00	12.57	600.40	7.90	b.d.l.	9.55
DM17-35-3A-p15	3.41	2.52	b.d.l.	0.13	288.10	4195.00	12.45	903.60	3.05	b.d.l.	11.97
DM17-35-3A-p14	3.59	2.40	b.d.l.	0.12	294.00	4114.00	12.86	698.00	2.07	b.d.l.	12.77
DM17-35-3A-p13	21.21	2.03	0.22	0.25	187.70	417b.d.l.	8.58	722.00	24.28	0.01	8.03
DM17-35-3A-p12	2.84	2.42	b.d.l.	0.13	210.30	3009.00	13.80	527.40	8.86	b.d.l.	11.00
DM17-35-3A-p7	6.07	1.97	b.d.l.	0.14	177.70	4034.00	13.03	609.20	11.15	b.d.l.	9.78
DM17-35-3A-p9	2.66	92.60	6.20	0.51	202.90	444b.d.l.	13.58	637.00	19.84	b.d.l.	10.22
DM17-35-3A-p16	1.36	2.08	0.05	0.11	262.00	2751.00	14.13	442.10	6.89	b.d.l.	9.36
DM17-35-3A-p18	1.53	1.84	b.d.l.	0.12	201.40	3704.00	13.91	554.80	6.62	b.d.l.	11.13
DM17-35-3A-p19	2.17	2.07	b.d.l.	0.11	255.20	3324.00	13.98	425.10	4.02	b.d.l.	8.89
DM17-35-3A-p20	4.02	4.60	b.d.l.	0.15	271.70	4047.00	12.62	642.80	3.30	b.d.l.	12.08
DM17-35-5A-p8	2.06	1.85	b.d.l.	0.12	280.60	3996.00	12.31	695.80	2.78	b.d.l.	11.84
DM17-35-5A-p10	2.45	1.84	b.d.l.	0.11	250.20	2227.00	13.71	341.30	6.14	b.d.l.	5.02
DM17-35-5A-p11	2.46	2.36	b.d.l.	0.30	198.50	3836.00	14.05	657.70	14.23	0.01	9.53
DM17-35-5A-p13	2.09	2.23	0.06	0.90	243.10	3647.00	14.31	628.90	5.59	0.10	11.51
DM17-35-5A-p14	5.70	1.78	b.d.l.	0.13	190.40	4504.00	13.25	979.00	9.57	b.d.l.	9.57
DM17-35-5A-p15	4.17	1.93	b.d.l.	0.14	218.40	4969.00	11.97	1383.00	8.81	b.d.l.	10.19
DM17-35-5A-p16	2.14	1.77	b.d.l.	0.12	252.30	2782.00	13.14	376.70	3.68	b.d.l.	6.81
DM17-35-5A-p17	6.22	2.30	b.d.l.	0.20	175.40	3722.00	13.57	616.70	10.80	0.03	9.88
DM17-35-5A-p1	5.52	2.04	b.d.l.	0.13	261.90	3017.00	9.68	465.60	5.83	b.d.l.	9.03
DM17-35-5A-p3	2.89	1.87	b.d.l.	0.24	222.90	4336.00	11.84	322.50	10.89	b.d.l.	6.51
DM17-35-5A-p4	2.37	1.80	b.d.l.	0.13	221.40	4712.00	11.39	316.40	6.80	b.d.l.	6.33
DM17-35-5A-p5	4.63	2.38	b.d.l.	0.13	274.00	4176.00	13.40	679.50	3.23	b.d.l.	12.65
DM17-35-5A-p6	2.12	2.01	2.28	0.28	251.80	3552.00	13.26	593.60	6.28	b.d.l.	11.20

Table A.3.4: transition metals and trace elements composition in rutile inclusions from garnet megablast DM17-35 (part 2)

sample name (notes)	Ta (ppm)	W (ppm)	Pb (ppm)	Th (ppm)	U (ppm)	Al (ppm)	Si (ppm)	P (ppm)	V (ppm)	Cr (ppm)	Mn (ppm)	Fe (ppm)	Co (ppm)	Ni (ppm)
DM17-35-3A-p23	362.40	229.90	83.00	b.d.l.	2.14	281.40	2938.00	b.d.l.	1567.00	148.40	b.d.l.	753.00	0.03	5.80
DM17-35-3A-p21	313.90	387.50	0.04	b.d.l.	2.18	378.90	3566.00	b.d.l.	1445.00	163.60	b.d.l.	949.00	b.d.l.	5.13
DM17-35-3A-p22	280.10	273.50	0.03	b.d.l.	2.18	294.00	3999.00	b.d.l.	1614.00	192.50	0.64	889.00	0.01	6.24
DM17-35-3A-p6	369.40	223.10	0.69	b.d.l.	2.34	56b.d.l.	3657.00	b.d.l.	1273.00	166.70	b.d.l.	1342.00	0.01	5.46
DM17-35-3A-p15	447.90	162.70	0.08	b.d.l.	1.91	256.10	3694.00	b.d.l.	1137.30	164.30	b.d.l.	1907.00	0.01	6.65
DM17-35-3A-p14	483.70	158.00	0.11	b.d.l.	5.19	298.50	3625.00	b.d.l.	1115.00	155.00	b.d.l.	1813.00	0.04	6.25
DM17-35-3A-p13	389.10	384.50	2.03	0.13	1.53	548.00	3943.00	b.d.l.	840.30	120.60	0.34	172b.d.l.	0.04	5.72
DM17-35-3A-p12	133.11	213.10	0.72	0.01	2.52	43b.d.l.	3756.00	b.d.l.	1426.10	171.30	b.d.l.	807.00	0.01	5.50
DM17-35-3A-p7	170.40	224.80	0.07	b.d.l.	3.88	247.20	3622.00	b.d.l.	1268.50	155.50	b.d.l.	1645.00	0.01	6.02
DM17-35-3A-p9	372.50	250.30	1.74	0.55	8.80	2720b.d.l.	1570b.d.l.	b.d.l.	1571.00	178.50	0.68	1738.00	0.82	12.70
DM17-35-3A-p16	558.60	258.90	0.08	b.d.l.	2.21	349.00	3632.00	b.d.l.	1644.00	146.60	b.d.l.	844.30	b.d.l.	6.48
DM17-35-3A-p18	248.70	187.90	0.04	b.d.l.	1.92	559.50	3947.00	b.d.l.	1520.90	161.50	0.50	810.50	b.d.l.	5.49
DM17-35-3A-p19	276.30	167.60	0.07	b.d.l.	1.97	308.30	3584.00	b.d.l.	1499.00	157.70	b.d.l.	1147.00	0.01	6.15
DM17-35-3A-p20	448.50	177.40	0.62	b.d.l.	3.10	57b.d.l.	395b.d.l.	b.d.l.	1284.00	162.10	0.99	1567.00	0.06	47.00
DM17-35-5A-p8	469.10	167.80	0.07	b.d.l.	3.41	426.80	3722.00	b.d.l.	1347.60	153.60	b.d.l.	1399.80	0.01	5.50
DM17-35-5A-p10	96.84	271.40	0.03	b.d.l.	2.05	431.00	3534.00	3.15	1537.20	96.60	b.d.l.	854.90	0.01	5.82
DM17-35-5A-p11	376.60	224.30	1.96	0.15	2.47	531.00	3471.00	21.00	1616.00	158.80	b.d.l.	1101.00	0.02	5.73
DM17-35-5A-p13	272.20	195.00	8.70	0.07	2.40	231b.d.l.	747b.d.l.	12.10	1649.80	163.00	1.55	1196.00	0.07	5.59
DM17-35-5A-p14	448.70	239.40	0.05	b.d.l.	3.19	507.30	3433.00	b.d.l.	1297.80	145.40	b.d.l.	1226.00	0.01	6.46
DM17-35-5A-p15	777.50	202.90	0.07	b.d.l.	2.31	393.30	3641.00	4.30	1426.80	106.90	b.d.l.	1953.00	0.02	6.34
DM17-35-5A-p16	176.50	145.49	0.14	b.d.l.	7.14	288.40	3745.00	b.d.l.	1817.10	136.00	0.49	924.60	0.01	5.36
DM17-35-5A-p17	233.50	207.30	1.05	0.02	3.23	276.40	3613.00	7.80	1198.90	149.10	b.d.l.	1784.00	0.19	5.25
DM17-35-5A-p1	203.63	178.80	1.77	0.01	2.75	307.00	3957.00	b.d.l.	1299.90	224.50	0.63	1057.90	0.01	6.62
DM17-35-5A-p3	249.20	368.40	0.34	0.02	4.80	554.00	3592.00	b.d.l.	1380.80	215.10	b.d.l.	1061.00	0.01	5.79
DM17-35-5A-p4	474.00	404.80	0.10	0.02	5.12	568.30	3428.00	3.50	1415.00	232.40	b.d.l.	1202.90	0.01	5.84
DM17-35-5A-p5	469.00	171.50	0.51	b.d.l.	2.03	481.60	373b.d.l.	b.d.l.	1258.70	161.10	b.d.l.	1555.00	0.01	6.61
DM17-35-5A-p6	335.20	236.10	0.11	0.64	2.24	989.00	507b.d.l.	b.d.l.	1557.00	155.90	b.d.l.	1211.30	0.03	5.76

Table A.3.5: trace elements composition in rutile inclusions from garnet megablast DMG4-6

S. (notes)	Sc (ppm)	Zn (ppm)	Rb (ppm)	Y (ppm)	Zr (ppm)	Nb (ppm)	Mo (ppm)	Sn (ppm)	Sb (ppm)	Yb (ppm)	Hf (ppm)
DMG4-6-A-p1	22.81	2.20	b.d.l.	0.15	188.00	4217.00	16.35	570.50	12.53	b.d.l.	8.57
DMG4-6-A-p2	7.64	3.73	b.d.l.	23.66	225.80	3589.00	10.40	469.50	5.53	2.41	5.76
DMG4-6-A-p3	14.75	3.72	0.19	14.10	171.60	5308.00	20.24	831.00	19.54	0.15	8.13
DMG4-6-A-p4	3.80	3.05	1.47	0.18	276.70	4805.00	8.47	999.00	8.91	b.d.l.	11.50
DMG4-6-A-p5	7.97	3.42	b.d.l.	0.27	178.90	4799.00	11.52	1552.00	11.71	0.03	9.44
DMG4-6-A-p6	5.64	3.55	b.d.l.	0.15	184.30	5051.00	11.79	853.00	14.93	b.d.l.	10.33
DMG4-6-A-p7	3.36	2.00	b.d.l.	0.14	257.80	4712.00	8.21	884.00	11.13	b.d.l.	10.96
DMG4-6-A-p8	4.49	2.03	b.d.l.	0.13	189.70	3656.00	7.60	493.20	9.47	b.d.l.	10.35
DMG4-6-A-p9	3.78	2.70	1.21	16.44	224.60	5167.00	9.48	1068.00	11.65	0.59	11.21
DMG4-6-A-p10	4.21	1.91	b.d.l.	0.15	227.70	4447.00	9.76	872.00	12.92	b.d.l.	11.13
DMG4-6-A-p11	3.14	5.27	b.d.l.	0.12	255.30	3857.00	7.38	467.10	10.03	b.d.l.	6.82
DMG4-6-A-p12	5.98	2.88	b.d.l.	0.19	271.80	5522.00	9.69	892.00	28.69	0.02	12.93
DMG4-6-A-p13	5.25	2.36	b.d.l.	0.13	303.10	5322.00	8.13	924.00	19.54	b.d.l.	13.81
DMG4-6-A-p14	4.06	2.33	b.d.l.	0.14	219.10	5076.00	1b.d.l.	91b.d.l.	12.65	b.d.l.	11.96
DMG4-6-A-p15	3.10	1.91	b.d.l.	0.14	277.40	4266.00	8.41	674.80	10.03	b.d.l.	9.77
DMG4-6-A-p16	2.44	2.53	b.d.l.	0.12	230.70	3773.00	12.17	453.20	8.90	b.d.l.	10.65
DMG4-6-B-p1	2.62	6.29	0.04	0.37	289.00	872b.d.l.	3.38	1127.00	3.92	b.d.l.	8.57
DMG4-6-B-p2	2.69	2.20	b.d.l.	0.13	261.70	6783.00	4.35	1345.00	5.62	b.d.l.	10.99
DMG4-6-B-p3	2.54	2.12	b.d.l.	0.12	271.90	6007.00	4.57	1594.00	13.38	b.d.l.	10.61
DMG4-6-B-p4	10.92	2.30	b.d.l.	0.35	199.60	4231.00	6.20	804.00	9.23	b.d.l.	7.36
DMG4-6-B-p5	1.76	4.82	b.d.l.	0.15	245.80	3635.00	4.93	646.00	8.95	b.d.l.	7.52
DMG4-6-B-p6	2.51	2.60	b.d.l.	0.13	218.50	3516.00	5.74	611.60	6.36	b.d.l.	6.42
DMG4-6-B-p7	7.14	2.83	b.d.l.	5.60	250.60	5328.00	5.88	2632.00	11.15	0.34	15.80
DMG4-6-B-p8	1.83	1.82	b.d.l.	0.24	210.30	3246.00	5.38	401.00	8.29	b.d.l.	5.84
DMG4-6-B-p9	1.78	2.10	b.d.l.	0.11	268.30	3299.00	4.07	684.70	5.19	b.d.l.	6.55
DMG4-6-B-p10	1.38	3.15	b.d.l.	0.14	174.60	3142.00	5.28	516.00	5.33	b.d.l.	5.00
DMG4-6-B-p11	1.60	2.53	b.d.l.	0.12	184.30	3151.00	4.67	570.30	4.85	b.d.l.	4.84
DMG4-6-B-p12	2.04	2.41	b.d.l.	0.86	265.10	4017.00	3.44	1656.00	5.74	0.07	10.74
DMG4-6-B-p14	3.78	2.95	0.03	0.55	134.17	4295.00	10.11	476.20	7.32	0.03	4.73
DMG4-6-B-p15	4.21	2.22	b.d.l.	0.20	131.80	4295.00	10.01	493.30	7.67	b.d.l.	4.67
DMG4-6-B-p16	4.15	11.43	b.d.l.	0.19	178.40	365b.d.l.	8.97	86b.d.l.	11.47	b.d.l.	8.53
DMG4-6-B-p17	14.71	57.30	0.52	109b.d.l.	195.90	952b.d.l.	10.25	417b.d.l.	11.25	8.40	11.68

Table A.3.6: transition metals and trace elements composition in rutile inclusions from garnet megablast DMG4-6

sample name (notes)	Ta (ppm)	W (ppm)	Pb (ppm)	Th (ppm)	U (ppm)	Al (ppm)	Si (ppm)	P (ppm)	V (ppm)	Cr (ppm)	Mn (ppm)	Fe (ppm)	Co (ppm)	Ni (ppm)
DMG4-6-A-p1	497.00	389.00	0.13	0.29	6.94	845.00	3365.00	b.d.l.	1354.00	109.60	b.d.l.	769.00	0.01	5.17
DMG4-6-A-p2	206.60	307.90	0.20	b.d.l.	10.70	1929b.d.l.	3722b.d.l.	122.50	1502.00	179.80	22.59	755b.d.l.	0.39	4.83
DMG4-6-A-p3	450.30	344.60	2.99	6.50	17.30	114b.d.l.	3354.00	218.00	759.20	140.80	b.d.l.	95b.d.l.	0.28	5.40
DMG4-6-A-p4	460.60	586.90	0.97	0.11	18.90	116b.d.l.	403b.d.l.	b.d.l.	1676.00	218.10	b.d.l.	542.50	0.02	5.00
DMG4-6-A-p5	446.10	385.40	1.53	0.59	30.49	727.00	308b.d.l.	5.40	1546.00	204.00	b.d.l.	745.00	0.02	5.34
DMG4-6-A-p6	338.50	326.00	0.13	0.10	6.86	858.00	2884.00	b.d.l.	821.00	139.20	b.d.l.	1406.00	0.01	4.36
DMG4-6-A-p7	299.90	316.30	0.09	0.01	5.37	1178.00	3349.00	b.d.l.	790.40	138.30	b.d.l.	795.30	0.01	4.78
DMG4-6-A-p8	322.20	335.20	0.16	b.d.l.	9.33	463.20	323b.d.l.	b.d.l.	1613.00	178.90	b.d.l.	384.40	b.d.l.	4.24
DMG4-6-A-p9	270.20	324.20	1.68	0.21	6.48	1812.00	4902.00	342.00	842.00	135.50	b.d.l.	1033.00	0.04	4.66
DMG4-6-A-p10	295.20	328.00	0.14	0.08	7.23	841.00	3172.00	b.d.l.	869.00	153.30	b.d.l.	803.00	0.02	4.80
DMG4-6-A-p11	328.90	365.80	0.18	b.d.l.	6.79	203b.d.l.	3308.00	b.d.l.	1266.00	174.00	b.d.l.	630.70	0.03	4.27
DMG4-6-A-p12	611.20	357.10	0.65	b.d.l.	8.85	563.30	3744.00	b.d.l.	757.00	126.20	b.d.l.	3025.00	0.01	4.39
DMG4-6-A-p13	611.10	364.00	0.24	b.d.l.	14.04	976.00	3408.00	b.d.l.	749.00	126.70	b.d.l.	2441.00	0.02	5.43
DMG4-6-A-p14	170.40	398.60	0.14	0.02	6.80	1049.00	3094.00	b.d.l.	80b.d.l.	139.10	b.d.l.	887.00	0.02	4.79
DMG4-6-A-p15	312.50	361.30	0.11	b.d.l.	6.27	644.50	3428.00	5.30	134b.d.l.	17b.d.l.	b.d.l.	611.10	0.01	4.26
DMG4-6-A-p16	189.80	337.30	0.55	b.d.l.	29.87	639.00	3507.00	b.d.l.	1456.00	142.90	b.d.l.	1544.00	b.d.l.	4.98
DMG4-6-B-p1	901.00	2179.00	1.02	b.d.l.	21.92	254b.d.l.	3347.00	b.d.l.	2207.00	240.10	b.d.l.	3588.00	0.15	4.50
DMG4-6-B-p2	525.60	976.00	0.40	b.d.l.	21.12	606.90	4984.00	4.90	195b.d.l.	225.90	b.d.l.	240b.d.l.	0.02	5.51
DMG4-6-B-p3	404.30	596.10	0.43	0.01	24.10	678.00	626b.d.l.	b.d.l.	1834.00	197.50	b.d.l.	1989.00	0.02	5.04
DMG4-6-B-p4	273.80	395.50	0.31	4.33	13.55	1949.00	668b.d.l.	b.d.l.	1454.00	177.30	b.d.l.	1538.00	0.01	4.35
DMG4-6-B-p5	236.00	278.00	0.69	0.02	28.40	272b.d.l.	6667.00	14.20	1927.00	135.90	b.d.l.	804.20	0.04	4.42
DMG4-6-B-p6	142.40	223.90	0.41	b.d.l.	22.94	574.00	601b.d.l.	b.d.l.	1672.00	114.00	b.d.l.	675.80	0.01	5.57
DMG4-6-B-p7	384.00	75b.d.l.	4.70	0.19	15.98	153b.d.l.	653b.d.l.	77.00	2014.00	136.00	b.d.l.	945.00	0.04	6.52
DMG4-6-B-p8	354.00	495.00	0.58	0.16	32.03	1425.00	684b.d.l.	5.50	1695.00	105.70	b.d.l.	652.90	0.01	5.37
DMG4-6-B-p9	113.24	200.40	0.95	b.d.l.	54.59	477.50	6264.00	b.d.l.	2848.00	155.60	b.d.l.	787.00	b.d.l.	4.65
DMG4-6-B-p10	93.70	196.30	0.50	0.03	26.61	564.50	632b.d.l.	b.d.l.	1848.00	168.70	b.d.l.	153b.d.l.	0.01	4.36
DMG4-6-B-p11	102.90	169.70	0.79	0.01	44.11	373.40	5916.00	b.d.l.	1799.00	165.50	b.d.l.	961.00	b.d.l.	4.37
DMG4-6-B-p12	142.60	219.80	0.18	b.d.l.	8.37	181b.d.l.	823b.d.l.	13.00	2183.00	166.30	b.d.l.	125b.d.l.	0.05	4.86
DMG4-6-B-p14	342.80	397.40	0.65	0.03	15.95	161b.d.l.	686b.d.l.	6.80	135b.d.l.	213.50	b.d.l.	219b.d.l.	0.09	4.78
DMG4-6-B-p15	318.20	405.10	0.33	0.19	16.31	120b.d.l.	619b.d.l.	b.d.l.	1342.00	218.50	b.d.l.	1794.00	0.04	5.20
DMG4-6-B-p16	338.00	376.20	0.30	0.21	2.01	349b.d.l.	661b.d.l.	b.d.l.	2033.00	107.30	b.d.l.	1446.00	0.29	5.03
DMG4-6-B-p17	1377.00	283.90	34.70	242b.d.l.	182b.d.l.	843b.d.l.	986b.d.l.	230b.d.l.	2001.00	141.00	b.d.l.	1967.00	0.61	6.90

Table A.3.7 trace elements composition in rutile inclusions from garnet megablast DM17-13

sample name (notes)	Sc (ppm)	Zn (ppm)	Rb (ppm)	Y (ppm)	Zr (ppm)	Nb (ppm)	Mo (ppm)	Sn (ppm)	Sb (ppm)	Yb (ppm)	Hf (ppm)
DM17-13-C-p2	51.98	3.41	0.13	0.51	151.30	6642.00	4.36	483.80	4.43	0.05	6.77
DM17-13-C-p3	6.88	2.43	b.d.l.	0.13	137.10	766b.d.l.	4.44	638.00	2.77	b.d.l.	6.35
DM17-13-C-p4	19.31	2.91	b.d.l.	0.13	150.50	7256.00	6.65	494.60	2.52	b.d.l.	6.24
DM17-13-C-p5	2.34	2.91	b.d.l.	0.34	148.10	7593.00	15.42	355.80	1.51	0.02	6.97
DM17-13-C-p6	7.06	2.46	b.d.l.	0.13	140.50	7292.00	7.64	544.00	2.76	b.d.l.	6.02
DM17-13-C-p7	7.23	5.41	b.d.l.	0.13	171.40	804b.d.l.	3.24	671.00	2.60	b.d.l.	6.61
DM17-13-C-p8	7.88	3.08	b.d.l.	0.14	131.60	7381.00	5.39	592.00	3.01	b.d.l.	5.68
DM17-13-C-p9	12.89	2.62	b.d.l.	0.14	143.20	8117.00	3.76	781.00	2.51	b.d.l.	6.06
DM17-13-C-p10	5.33	2.81	b.d.l.	0.16	140.40	838b.d.l.	3.03	837.00	2.44	0.01	6.54
DM17-13-C-p11	5.10	3.23	b.d.l.	0.13	131.70	799b.d.l.	3.53	723.00	2.56	b.d.l.	5.87
DM17-13-C-p12	4.80	2.64	b.d.l.	0.14	150.60	7957.00	3.86	691.00	2.31	b.d.l.	6.46
DM17-13-C-p13	4.77	2.11	0.05	0.31	146.10	786b.d.l.	3.53	658.00	2.52	0.02	6.40
DM17-13-C-p14	6.40	2.37	b.d.l.	0.13	136.20	8986.00	2.65	868.00	2.56	b.d.l.	6.88
DM17-13-C-p15	6.00	2.60	b.d.l.	0.12	141.90	8104.00	3.06	736.20	2.15	b.d.l.	6.45
DM17-13-C-p16	6.26	7.60	b.d.l.	0.15	132.90	794b.d.l.	3.64	785.00	2.64	b.d.l.	6.20
DM17-13-C-p17	4.89	2.69	b.d.l.	0.12	126.90	7244.00	4.71	529.00	2.56	b.d.l.	5.85
DM17-13-C-p18	5.01	2.49	b.d.l.	0.12	133.60	730b.d.l.	5.90	575.00	2.82	b.d.l.	5.91
DM17-13-C-p19	5.04	2.43	b.d.l.	0.14	144.20	773b.d.l.	3.70	587.00	2.35	b.d.l.	7.32
DM17-13-C-p20	5.08	2.62	b.d.l.	0.13	14b.d.l.	787b.d.l.	3.23	583.80	2.54	b.d.l.	6.05
DM17-13-C-p21	6.18	13.90	b.d.l.	0.28	161.60	855b.d.l.	2.99	859.00	1.96	0.04	7.43
DM17-13-C-p22	8.19	2.64	b.d.l.	0.13	154.80	8011.00	4.15	727.00	2.03	b.d.l.	7.07
DM17-13-C-p23	7.22	3.42	b.d.l.	0.19	132.80	7893.00	2.89	695.40	2.63	0.01	6.30
DM17-13-C-p24	7.14	2.76	b.d.l.	0.14	137.30	835b.d.l.	2.97	753.00	2.66	b.d.l.	6.50
DM17-13-C-p25	7.96	2.67	b.d.l.	0.14	153.60	8168.00	3.02	874.00	2.15	b.d.l.	7.04
DM17-13-C-p26	2.13	2.43	b.d.l.	0.52	150.60	7646.00	11.74	451.10	1.54	0.03	6.90
DM17-13-C-p27	2.62	2.41	b.d.l.	0.20	15b.d.l.	7192.00	19.90	331.90	1.53	0.01	6.73
DM17-13-C-p28	2.00	2.67	0.03	0.21	143.10	770b.d.l.	11.73	338.70	1.49	0.01	6.63
DM17-13-C-p29	5.06	2.39	b.d.l.	0.59	151.90	8088.00	3.75	379.60	2.09	0.12	7.09
DM17-13-B-p2	25.45	3.04	b.d.l.	0.23	145.30	7424.00	3.43	534.00	2.61	0.02	5.90
DM17-13-B-p3	18.12	3.19	b.d.l.	0.14	148.70	9191.00	3.87	1289.00	2.00	b.d.l.	6.62
DM17-13-B-p4	6.68	2.96	b.d.l.	0.15	138.50	8165.00	3.84	814.00	1.89	b.d.l.	6.05
DM17-13-B-p6	6.23	2.89	b.d.l.	0.14	150.70	8081.00	10.49	1483.00	1.30	b.d.l.	6.69
DM17-13-B-p7	7.18	4.17	b.d.l.	0.13	144.70	984b.d.l.	3.75	1403.00	1.27	b.d.l.	6.61
DM17-13-B-p8	6.47	3.73	b.d.l.	0.12	152.20	1356b.d.l.	2.41	3474.00	1.11	b.d.l.	7.74
DM17-13-B-p10	18.91	3.14	b.d.l.	0.19	151.50	8022.00	2.88	451.10	1.89	0.01	6.40
DM17-13-B-p11	11.64	2.95	b.d.l.	1.65	146.70	5686.00	4.21	423.00	2.09	0.06	4.57
DM17-13-B-p12	6.98	4.50	b.d.l.	0.13	132.50	784b.d.l.	2.44	499.00	1.79	b.d.l.	5.52
DM17-13-B-p14	9.14	8.55	1.08	0.48	138.10	4226.00	7.15	305.90	3.25	0.02	3.22

Table A.3.8: transition metals and trace elements composition in rutile inclusions from garnet megablast DM17-13

sample name (notes)	Ta (ppm)	W (ppm)	Pb (ppm)	Th (ppm)	U (ppm)	Al (ppm)	Si (ppm)	P (ppm)	V (ppm)	Cr (ppm)	Mn (ppm)	Fe (ppm)	Co (ppm)	Ni (ppm)
DM17-13-C-p2	512.70	74b.d.l.	0.55	0.06	1.31	1555.00	3683.00	b.d.l.	1276.00	142.10	b.d.l.	1393.00	0.01	5.30
DM17-13-C-p3	687.90	1377.00	0.02	b.d.l.	0.87	1655.00	3676.00	b.d.l.	1345.00	83.00	b.d.l.	1994.00	0.01	4.84
DM17-13-C-p4	617.80	715.00	0.01	b.d.l.	0.69	142b.d.l.	366b.d.l.	b.d.l.	1277.00	120.70	b.d.l.	1744.00	0.01	4.82
DM17-13-C-p5	678.80	723.70	0.15	0.01	5.99	2294.00	3506.00	b.d.l.	107b.d.l.	82.80	b.d.l.	322.20	b.d.l.	4.13
DM17-13-C-p6	590.40	886.00	0.06	b.d.l.	3.15	1772.00	3812.00	b.d.l.	1281.00	114.30	b.d.l.	966.00	0.01	3.98
DM17-13-C-p7	536.50	1774.00	0.06	b.d.l.	2.78	2168.00	3603.00	b.d.l.	149b.d.l.	115.00	b.d.l.	1276.00	0.02	4.96
DM17-13-C-p8	596.90	981.00	0.08	b.d.l.	4.37	1833.00	354b.d.l.	b.d.l.	1428.00	120.10	b.d.l.	1174.00	0.01	4.15
DM17-13-C-p9	630.70	162b.d.l.	0.06	b.d.l.	3.27	207b.d.l.	3523.00	b.d.l.	1495.00	83.90	b.d.l.	849.00	0.02	4.74
DM17-13-C-p10	618.80	1688.00	0.06	b.d.l.	2.31	264b.d.l.	359b.d.l.	b.d.l.	1423.00	61.70	b.d.l.	695.00	0.02	4.91
DM17-13-C-p11	599.00	1569.00	0.04	b.d.l.	2.39	2197.00	3403.00	b.d.l.	139b.d.l.	92.20	b.d.l.	659.00	0.01	4.38
DM17-13-C-p12	602.10	1503.00	0.05	b.d.l.	2.03	2093.00	3601.00	b.d.l.	1627.00	98.20	b.d.l.	510.90	0.01	4.46
DM17-13-C-p13	653.10	1566.00	1.27	b.d.l.	4.86	2301.00	368b.d.l.	b.d.l.	1584.10	91.60	b.d.l.	518.00	0.01	5.48
DM17-13-C-p14	670.40	2049.00	0.05	b.d.l.	2.38	2542.00	334b.d.l.	b.d.l.	113b.d.l.	46.10	b.d.l.	871.00	0.01	5.07
DM17-13-C-p15	625.60	153b.d.l.	0.05	b.d.l.	2.35	2098.00	333b.d.l.	b.d.l.	1106.00	60.38	b.d.l.	775.20	0.02	5.82
DM17-13-C-p16	567.20	1485.00	0.06	b.d.l.	2.64	275b.d.l.	354b.d.l.	b.d.l.	1494.00	87.50	b.d.l.	622.00	0.03	5.48
DM17-13-C-p17	486.10	684.00	0.08	b.d.l.	4.98	1629.00	3252.00	b.d.l.	1459.00	149.20	b.d.l.	736.00	0.01	5.81
DM17-13-C-p18	607.70	693.30	0.10	b.d.l.	5.32	1637.00	3481.00	5.60	1502.00	132.00	b.d.l.	732.00	0.01	5.44
DM17-13-C-p19	419.30	187b.d.l.	0.13	b.d.l.	6.00	220b.d.l.	3493.00	b.d.l.	1642.00	125.50	b.d.l.	764.00	0.01	4.61
DM17-13-C-p20	465.90	2196.00	0.11	b.d.l.	5.96	2036.00	3553.00	b.d.l.	1646.00	127.70	b.d.l.	889.60	b.d.l.	5.04
DM17-13-C-p21	598.20	1534.00	0.08	b.d.l.	3.47	384b.d.l.	369b.d.l.	b.d.l.	1404.00	78.00	b.d.l.	1173.00	0.09	4.74
DM17-13-C-p22	629.30	1451.00	0.02	b.d.l.	1.48	2024.00	3313.00	b.d.l.	1525.00	78.70	b.d.l.	594.10	0.01	5.50
DM17-13-C-p23	591.70	1423.00	0.30	b.d.l.	7.91	296b.d.l.	449b.d.l.	b.d.l.	1412.00	73.70	b.d.l.	571.00	0.03	4.30
DM17-13-C-p24	611.90	1704.00	0.14	b.d.l.	7.69	2342.00	3537.00	b.d.l.	1474.00	71.40	b.d.l.	555.20	0.01	5.52
DM17-13-C-p25	479.90	1558.00	0.07	b.d.l.	3.77	2036.00	3141.00	b.d.l.	1288.00	74.80	b.d.l.	1148.00	0.02	5.53
DM17-13-C-p26	612.80	867.00	0.17	0.01	6.93	2316.00	3415.00	b.d.l.	1226.00	81.70	b.d.l.	434.20	b.d.l.	4.55
DM17-13-C-p27	674.30	605.60	0.09	0.01	3.58	2602.00	3479.00	b.d.l.	1054.00	79.80	b.d.l.	948.00	0.01	5.35
DM17-13-C-p28	682.90	631.40	0.78	b.d.l.	3.29	2153.00	3479.00	b.d.l.	1057.00	75.70	0.62	1036.00	0.01	5.18
DM17-13-C-p29	743.40	663.70	1.37	0.10	3.35	794b.d.l.	401b.d.l.	b.d.l.	1086.00	86.20	0.93	1159.00	0.02	4.39
DM17-13-B-p2	393.70	941.00	3.60	0.12	0.76	144b.d.l.	375b.d.l.	b.d.l.	1088.00	137.30	b.d.l.	2008.00	b.d.l.	5.30
DM17-13-B-p3	529.50	510.60	0.22	b.d.l.	0.53	1512.00	345b.d.l.	b.d.l.	1136.00	62.60	b.d.l.	2184.00	0.01	4.62
DM17-13-B-p4	431.90	1159.00	2.85	0.02	2.26	1403.00	3675.00	b.d.l.	1111.00	87.00	b.d.l.	2124.00	0.01	5.63
DM17-13-B-p6	494.30	429.30	0.06	b.d.l.	3.12	137b.d.l.	3749.00	b.d.l.	111b.d.l.	77.80	b.d.l.	1877.00	0.02	6.10
DM17-13-B-p7	764.00	803.00	0.02	b.d.l.	1.33	1852.00	374b.d.l.	b.d.l.	1201.00	77.80	b.d.l.	2086.00	0.02	5.90
DM17-13-B-p8	718.10	344.30	0.04	b.d.l.	1.92	2533.00	352b.d.l.	b.d.l.	1269.00	57.10	b.d.l.	2068.00	0.04	6.80
DM17-13-B-p10	445.40	92b.d.l.	0.02	0.01	0.71	1472.00	3778.00	b.d.l.	1124.00	131.30	b.d.l.	1636.00	b.d.l.	6.35
DM17-13-B-p11	159.80	563.50	0.29	5.74	1.35	1291.00	3828.00	b.d.l.	149b.d.l.	185.90	b.d.l.	570.50	0.02	5.45
DM17-13-B-p12	403.10	1432.00	0.04	b.d.l.	1.87	1748.00	351b.d.l.	b.d.l.	1749.00	135.30	b.d.l.	809.00	0.01	4.73
DM17-13-B-p14	135.00	1522.00	0.83	0.66	0.85	316b.d.l.	495b.d.l.	b.d.l.	1173.00	148.00	b.d.l.	1002.00	0.10	5.53